Thesis for the degree of Doctor of Philosophy

High-temperature superconducting magnetometers for on-scalp MEG

Silvia Ruffieux

CHALMERS

Department of Microtechnology and Nanoscience – MC2
Quantum Device Physics Laboratory
Chalmers University of Technology
Göteborg, Sweden 2020

High-temperature superconducting magnetometers for on-scalp MEG
Silvia Ruffieux
ISBN 978-91-7905-356-7

Doktorsavhandlingar vid Chalmers tekniska högskola
Ny serie nr 4823
ISSN 0346-718X

Quantum Device Physics Laboratory
Department of Microtechnology and Nanoscience – MC2
Chalmers University of Technology
SE–412 96 Göteborg
Sweden
Telephone: + 46 (0)31 772 1000

Cover:
Top left: AFM image of the microbridges forming the Josephson junctions in a bicrystal grain boundary SQUID. *Bottom left*: Voltage modulation of a SQUID as a function of flux and bias current. *Top center*: SQUIDs in the 7-channel system. *Center*: 7-channel system placed to record from the author's head. *Bottom center*: Resonance shift in a KIM when applying a dc magnetic field. *Top left*: Micrograph of a fabricated prototype integrated flux transformer device. *Top left*: Simulation of the sheet current density in a SQUID washer coupled to a flux transformer input coil.

Printed by Chalmers Reproservice
Göteborg, Sweden 2020

High-temperature superconducting magnetometers for on-scalp MEG
Silvia Ruffieux
Department of Microtechnology and Nanoscience – MC2
Chalmers University of Technology
Göteborg, Sweden 2020

Abstract

In the growing field of on-scalp magnetoencephalography (MEG), brain activity is studied by non-invasively mapping the magnetic fields generated by neuronal currents with sensors that are flexibly placed in close proximity to the subject's head. This thesis focuses on high-temperature superconducting magnetometers made from $YBa_2Cu_3O_{7-x}$ (YBCO), which enables a reduction in the sensor-to-room temperature standoff distance from roughly 2 cm (for conventional MEG systems) down to 1 mm. Because of the higher neuromagnetic signal magnitudes available to on-scalp sensors, simulations predict that even a relatively low-sensitivity (higher noise) full-head on-scalp MEG system can extract more information about brain activity than conventional systems.

In the first part of this thesis, the development of high critical temperature (high-T_c) superconducting quantum interference device (SQUID) magnetometers for a 7-channel on-scalp MEG system is described. The sensors are single layer magnetometers with a directly coupled pickup loop made on 10 mm × 10 mm substrates using bicrystal grain boundary Josephson junctions. We found that the kinetic inductance strongly varies with film quality and temperature. Determination of all SQUID parameters by combining measurements and inductance simulations led to excellent agreement between experimental results and theoretical predictions. This allowed us to perform an in-depth magnetometer optimization. The best magnetometers achieve a magnetic field noise level of 44 fT/$\sqrt{\text{Hz}}$ at 78 K. Fabricated test SQUIDs provide evidence that noise levels below 30 fT/$\sqrt{\text{Hz}}$ are possible for high quality junctions with fairly low critical currents and in combination with the optimized pickup loop design. Different feedback methods for operation in a densely-packed on-scalp MEG system were also investigated. Direct injection of current into the SQUID loop was identified as the best on-chip feedback method with feedback flux crosstalk below 0.5%. By reducing the operation temperature, the noise level can be further reduced, however, the effective area also decreases because of the decreasing kinetic inductance contribution. We present a method that allows for one-time sensor calibration independent of temperature.

In the second part, the design, operation, and performance of the constructed 7-channel on-scalp MEG system based on the fabricated magnetometers is presented. With a dense (2 mm edge-to-edge) hexagonal head-aligned array, the system achieves a small sensor-to-head standoff distance of 1-3 mm and dense spatial sampling. The magnetic field noise levels are 50-130 fT/$\sqrt{\text{Hz}}$ and the sensor-to-sensor feedback flux crosstalk is below 0.6%. MEG measurements with the system demonstrate the feasibility of the approach and indicate that our on-scalp MEG system allows retrieval of information unavailable to conventional MEG.

In the third part, two alternative magnetometer types are studied for the next generation system. The first alternative is magnetometers based on Dayem bridge junctions instead of bicrystal grain boundary junctions. With a magnetometer based on the novel grooved Dayem bridge junctions, a magnetic field noise level of 63 fT/$\sqrt{\text{Hz}}$ could be achieved, which shows that Dayem bridge junctions are starting to become a viable option for single layer magnetometers. The second alternative are high-T_c SQUID magnetometers with an inductively coupled flux transformer. The best device with bicrystal grain boundary junctions reaches a magnetic field noise level below 11 fT/$\sqrt{\text{Hz}}$ and outperforms the best single layer device for frequencies above 20 Hz.

In the last part, the potential of kinetic inductance magnetometers (KIMs) is investigated. We demonstrate the first high-T_c KIMs, which can be operated in fields of 9-28 µT and achieve a noise level of 4 pT/$\sqrt{\text{Hz}}$ at 10 kHz.

Keywords: high-T_c SQUID, magnetoencephalography, on-scalp MEG, magnetometer, SQUID optimization, multi-channel system, crosstalk, SQUID magnetometer calibration, kinetic inductance, kinetic inductance magnetometer.

To my love Jonathan
my little sunshine Felicia
and the heart beating below mine

"The mind is not a book, to be opened at will and examined at leisure. Thoughts are not etched on the inside of skulls, to be perused by any invader. The mind is a complex and many-layered thing, Potter. Or at least most minds are..."
J.K.Rowling

Acknowledgement

The past five years have been among the best of my life (so far) and I consider myself very lucky to have found this PhD position. The time here would not have been half as great if it were not for the people by my side and I would like to thank them for being there.

First of all, I would like to thank my supervisors Dag Winkler, Alexei Kalaboukhov, and Justin Schneiderman for giving me the opportunity to work on this interesting and diverse project. Dag, you were a great source of ideas and you gave me a lot of freedom in planning my PhD and deciding what to do. Thank you also for bringing us to the weekly innebandy training – your priorities are an inspiration. Alex, your broad scientific expertise has been invaluable. Although you were constantly busy with experiments or fabrication (or running from one to another), you always found some time to help me and give me advice. I appreciate your logical way of thinking and reasoning. Thank you also for 'healing' my SQUIDs with a CeO_2 buffer layer. Thank you, Justin, for bringing the medical aspect into my PhD project and giving the superconducting sensors a greater purpose. I very much enjoyed that my project has a useful application. Thank you also for the advice and polishing my writing – your comments generally significantly improved my written work.

Next I would like to thank my friends and colleagues in the SQUID lab – Maxim Chukharkin, Minshu Xie, Christoph Pfeiffer and Sobhan Sepehri – as well as the YBCO team – Edoardo Trabaldo, Eric Wahlberg (Andersson), Riccardo Arpaia, Marco Arzeo, Floriana Lombardi, Thilo Bauch – for making my PhD very enjoyable and fun. Thank you also for the advice, the common measurements, the help in the lab and the cleanroom, and the common conference visits. Maxim, I am very grateful that you introduced me to the art of fabricating high-temperature superconducting devices, taught me cleanroom techniques, and generously shared your knowledge about YBCO SQUID magnetometers. I very much enjoyed working together, including your life wisdom, encouragements when films were bad, and comments such as "There is no magic – you just don't understand it yet. Try again." Minshu, I have learned a lot from you and enjoyed our discussions, measurements and cleanroom visits. Thank you also for introducing me to the inductance simulation – it has been of great use to me. Chris, thank you for the great teamwork getting the 7-channel system to work and being my friend also outside of work. Figuring out why things were not working was much more fun together. Sobhan, you were my

friend here from day one. I will always remember our road trip together through the US. Thank you also for taking care of 3-month-old Felicia while I was teaching.

I would like to thank Visa Vesterinen from VTT Finland for his two month visit at Chalmers where we measured kinetic inductance magnetometers (KIMs) together. Thank you for teaching me how to read out KIMs, answering all my questions (also after you left), introducing me to lab instrument control, and for being the postdoc I wished we had. Kiitos!

This work would not have been possible without the support of the cleanroom staff at MC2 and their dedication to keeping the equipment running. I would especially like to thank Niclas Lindvall for the help with electron beam lithography and the nice conversations (and leaving me a tidy office), Henrik Frederiksen for the big help with the DCA system and especially the YBCO PLD system, Mats Hagberg for maintenance of the argon ion milling system (including getting rid of algae in the water cooling system with me), and finally Johan Karl Andersson for help with the laser writer. I normally learned most about the systems when they failed, and you were all there to solve my problems and teach me more about the tools.

Thank you, Lars Jönsson, for your excellent work on the cryostats, and the quick and elegant fixes to make my measurements work. I appreciate the administrative support from Debora (Debbie) Perlheden, Susannah Carlsson, Maria Tremblay, Linda Brånell, Annika Holtringer, and the IT support from Henric Fjellstedt.

I would like to thank Bushra Riaz, Elin Eriksson Hagberg, Elena Orekhova, Lau Andersen, Daniel Lundqvist, Karin Westin for the MEG measurements and the meetings. Then, I would like to thank John Clarke and Michael Faley for their visits and valuable SQUID advice.

A general thank you goes to all the past and present members of QDP for the lunch company, interesting discussions, and Friday fika. I thank my fellow *Quantum mums* Ida-Maria Svensson, Laure Bruhat, Floriana, Janine Splettstösser, and Giovanna Tancredi for the advice and support, as well as the Swedish system for allowing me to combine family and career this well. Thank you SQUID SQUID – Chris, Sobhan, Minshu, Jonathan, Dag, Bogdan Karpiak, Bing Zhao – for the good runs, and the innebandy team – Gustav Andersson, Jan-Åke Wiman, Dag, Chris, Eric, Debbie, Ida-Maria, Laure, Claudia Ramirez, and Angelika Bernhofer for the fun games and lunches.

I would also like to thank my family and friends back home for their support and visits to Sweden. Special thanks goes to my dad and Ria for the yearly trips to Finnish Lapland.

Finally, I would like to thank my beloved husband Jonathan and daughter Felicia for reminding me that the important things in life happen above 77 K. Thank you, Jonathan, for the help with simulations (including SQUID I-V curve simulations while waiting for northern lights in Lapland), introducing me to regular expressions and git, and most of all for the happiness you create in my life. Felicia, you are a wonderful daughter and make me smile every day. Thank you!

Gotland, August 2020

Publications

Publications to be included in the thesis:
* These authors contributed equally to this work.

A **Feedback solutions for low crosstalk in dense arrays of high-T_c SQUIDs for on-scalp MEG**
S. Ruffieux, M. Xie, M. Chukharkin, C. Pfeiffer, A. Kalaboukhov, D. Winkler and J. F. Schneiderman
Supercond. Sci. Technol. **30**, 054006 (2017)

B **The role of kinetic inductance on the performance of YBCO SQUID magnetometers**
S. Ruffieux, A. Kalaboukhov, M. Xie, M. Chukharkin, C. Pfeiffer, S. Sepehri, J. F. Schneiderman and D. Winkler
Supercond. Sci. Technol. **33**, 025007 (2020)

C **A 7-channel high-T_c SQUID-based on-scalp MEG system**
C. Pfeiffer*, **S. Ruffieux***, L. Jönsson, M. Chukharkin, A. Kalaboukhov, M. Xie, D. Winkler and J. F. Schneiderman
IEEE T. Bio-Med. Eng. **67**, 1483-1489 (2020)

D **Improved coupling of nanowire-based high-T_c SQUID magnetometers - simulation and experiments**
M. Xie, M. Chukharkin, **S. Ruffieux**, J. F. Schneiderman, A. Kalaboukhov, M. Arzeo, T. Bauch, F. Lombardi and D. Winkler
Supercond. Sci. Technol. **30**, 115014 (2017)

E **Properties of grooved Dayem bridge based $YBa_2Cu_3O_{7-\delta}$ superconducting quantum interference devices and magnetometers**
E. Trabaldo, **S. Ruffieux**, E. Andersson, R. Arpaia, D. Montemurro, J. Schneiderman, A.Kalaboukhov, D. Winkler, F. Lombardi, and T. Bauch
Appl. Phys. Lett **116**, 132601 (2020)

F **Magnetic field sensing with the kinetic inductance of a high-T_c superconductor**
V.Vesterinen, **S. Ruffieux**, A. Kalaboukhov, H. Sipola, M. Kiviranta, D. Winkler, J. F. Schneiderman and J. Hassel
AIP Adv. **9**, 045217 (2019)

Other publications that are outside the scope of this thesis:

I **On-scalp MEG**
J. F. Schneiderman, **S. Ruffieux**, C. Pfeiffer and B. Riaz
In: S. Supek & C. J. Aine (eds) Magnetoencephalography. *Springer*, Cham (2019)

II **Similarities and differences between on-scalp and conventional in-helmet magnetoencephalography recordings**
L. M. Andersen*, R. Oostenveld*, C. Pfeiffer, **S. Ruffieux**, V. Jousmäki, M. Hämäläinen, J. F. Schneiderman and D. Lundqvist
PLOS ONE **12**, 7, e178602 (2017)

III **On-scalp MEG sensor localization using magnetic dipole-like coils: A method for highly accurate co-registration**
C. Pfeiffer, **S. Ruffieux**, L. M. Andersen, A. Kalaboukhov, D. Winkler, R. Oostenveld, D. Lundqvist, J.F. Schneiderman
NeuroImage **212**, 116686 (2020)

IV **On-scalp MEG SQUIDs are sensitive to early somatosensory activity unseen by conventional MEG**
L. M. Andersen, C. Pfeiffer, **S. Ruffieux**, B. Riaz, D. Winkler, J. F. Schneiderman and D. Lundqvist
NeuroImage **221**, 117157 (2020)

V **Detection of interictal epileptiform discharges: A comparison of on-scalp MEG and conventional MEG measurements**
K. Westin, C. Pfeiffer, L. M. Andersen, **S. Ruffieux**, G. Cooray, A. Kalaboukhov, D. Winkler, M. Ingvar, J. Schneiderman and D. Lundqvist
Clin. Neurophysiol. **131**, 1711-1720 (2020)

Abbreviations and constants

Abbreviations

ac	Alternating current
AEF	Auditory evoked field
AFM	Atomic force microscopy
BOLD	Blood oxygenation level-dependent
BC	Bicrystal
CMP	Chemical mechanical polishing
CT	Computed tomography
dc	Direct current
GBJ	Grain boundary junction
GDB	Grooved Dayem bridge
ECG	Electrocardiography
EEG	Electroencephalography
FFL	Flux-locked loop
FFT	Fast Fourier transform
FIB	Focused ion beam
fMRI	Functional magnetic resonance imaging
FT	Flux transformer
FWHM	Full-width-half-maximum
High-T_c	High critical temperature superconducting
HTS	High-temperature superconductor
IED	Interictal epileptiform discharge
JJ	Josephson junction
KIM	Kinetic inductance magnetometer
Low-T_c	Low critical temperature superconducting
LTS	Low-temperature superconductor
MCG	Magnetocardiography
MEG	Magnetoencephalography
MKID	Microwave kinetic inductance detector
MRI	Magnetic resonance imaging
MSR	Magnetically shielded room
NatMEG	The Swedish national facility for magnetoencephalography

NDE	Non destructive evaluation
OPM	Optically pumped magnetometer
PCB	Printed circuit board
RCSJ	Resistively and capacitively shunted junction
rf	Radio frequency
RSJ	Resistively shunted junction
PET	Positron emission tomography
PLD	Pulsed laser deposition
SEF	Somatosensory evoked field
SEM	Scanning electron microscopy
f SERF	Spin-exchange relaxation-free
SPECT	Single-photon emission computed tomography
SNR	Signal-to-noise ratio
SQUID	Superconducting quantum interference device
STO	$SrTiO_3$
VNA	Vector network analyzer
YBCO	$YBa_2Cu_3O_{7-x}$
XRD	X-Ray diffraction

Constants

h	Planck constant	$h \approx 6.63 \times 10^{-34}$ Js
$\hbar$	Reduced Planck constant	$\hbar = h/2\pi \approx 1.06 \times 10^{-34}$ Js
e	Elementary charge	$e \approx 1.60 \times 10^{-19}$ C
m_e	Electron mass	$e \approx 9.11 \times 10^{-31}$ kg
Φ_0	Magnetic flux quantum	$\Phi_0 = h/2e \approx 2.07 \times 10^{-15}$ Wb
k_B	Boltzmann's constant	$k_B \approx 1.38 \times 10^{-23}$ J/K
μ_0	Vacuum permeability	$\mu_0 \approx 4\pi \times 10^{-7}$ H/m
ϵ_0	Vacuum permittivity	$\epsilon_0 \approx 8.85 \times 10^{-12}$ F/m
c	Speed of light in vacuum	$c \approx 3.00 \times 10^{8}$ m/s

A list of symbols can be found in Appendix A.

Contents

1

Introduction

The average human brain contains an estimated 68 billion neurons and a similar number of non-neuronal cells [1]. Around 20 billion of these neurons are in the neocortex [2], which is the part of the brain involved in higher-order brain functions such as conscious thought, sensory perception, generation of motor commands, language, and spatial reasoning. Each neuron in the neocortex has approximately 7000 synapses connecting it to other neurons, which results in an enormous total number of neocortical synapses in the order of 10^{14} [3]. The sheer complexity of the human brain is a challenge, and powerful technologies are required to gain a better understanding of the brain and treat it in disease.

Several neuroimaging modalities have been developed to obtain a window into the brain without penetrating the skull [4, 5]. They can be divided into two broad categories: structural and functional imaging technologies. Structural neuroimaging technologies allow one to distinguish between different tissues (e.g. bone, grey matter, white matter, cerebrospinal fluid). The two main structural neuroimaging technologies are computed tomography (CT), which merges a series of X-ray images to create cross-sectional images [6], and magnetic resonance imaging (MRI), which combines strong magnetic fields and radio frequency (rf) waves to generate 3D images [7].

Functional neuroimaging technologies, on the other hand, measure neural activity in the brain. This is done either directly by sampling the electromagnetic field generated by neural activity or indirectly by imaging the metabolic processes that are modulated by brain activity. The two direct functional neuroimaging methods are electroencephalography (EEG), which measures the electric potential with electrodes placed on the scalp, and magnetoencephalography (MEG), which samples the magnetic field using a sensor array around the head. The most commonly used indirect functional neuroimaging technologies are functional magnetic resonance imaging (fMRI), positron emission tomography (PET) and single-photon emission computed tomography (SPECT) [8]. fMRI generates a brain map corresponding to blood flow to active neurons via the blood oxygenation level-dependent (BOLD) contrast with MRI [9, 10], while PET and SPECT rely on different types of radioactive tracers [8]. A comparison of these five functional neuroimaging technologies is given in Fig. 1.1.

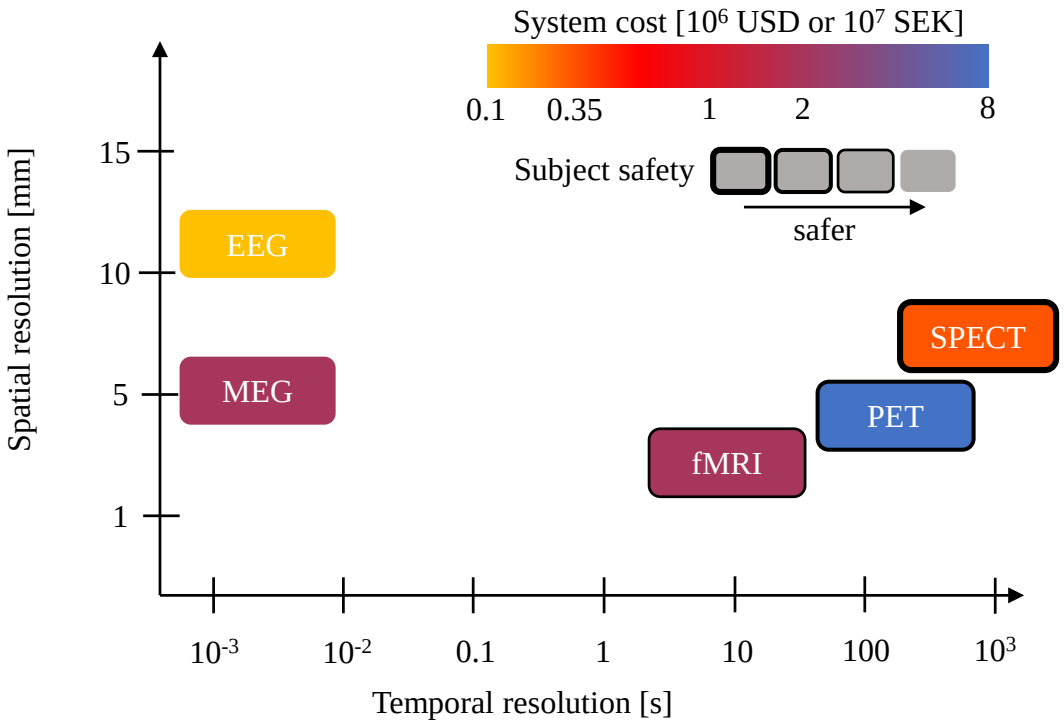

Figure 1.1: Comparison of different functional neuroimaging methods in terms of spatial and temporal resolution as well as system cost and invasiveness. The data were taken from Ref. [8]. System costs are approximate and strongly depend on the specifications.

In this project we focus on the direct functional neuroimaging method MEG. It combines excellent temporal resolution with good spatial resolution while being totally passive, and thus safe (no radioactive tracers or high magnetic fields). Both MEG and EEG signals are created by postsynaptic currents in the pyramidal neurons of the cerebral cortex [11]. A detectable MEG signal is created by 10 000 to 50 000 pyramidal cells firing synchronously [12]. Although MEG and EEG signals have the same source, the two modalities are not redundant [13, 14]. In contrast to EEG signals, MEG signals are virtually undistorted by the skull and scalp, especially in the case of shallow sources [15]. This simplifies source localization and leads to a better spatial resolution for MEG than for EEG. MEG has contributed significantly towards the understanding of sensory processing, motor planning and action, cognition, language perception and production, social interaction, and various brain disorders [16]. Clinically, MEG is nowadays used for epilepsy (diagnosis of epilepsy and localization of epileptic foci) and pre-operative evaluation, while applications on the horizon include stroke, chronic pain, traumatic brain injury, dementia and Parkinson's disease [14].

The first magnetoencephalogram was recorded by D. Cohen in 1968 with an induction coil magnetometer that had one million turns of copper wire wound around a removable ferrite rod core [17]. He measured the magnetic fields generated by alpha rhythm currents, which are relatively strong compared to other brain activity,

contained in the narrow frequency band of 8-13 Hz, and can simply be modulated by closing or opening the eyes. As their peak-to-peak signal amplitude of around 70 fT (fT = 10^{-15} T) is roughly one billionth of that of the earth magnetic field ($\approx$ 50 µT), the measurements were performed in a multilayer magnetically shielded room (MSR). Nonetheless, the signal-to-noise ratio (SNR) was poor and the MEG signal had to be extracted by averaging 2500 times and using the EEG signal as a trigger reference.

MEG technology made a leap forward when the induction coil was replaced by a superconducting quantum interference device (SQUID) invented just a few years earlier at the Ford Research Labs [18]. The SQUID consists of a superconducting loop interrupted by one or two weak links, the Josephson junctions [19]. It is a very sensitive magnetic flux sensor and allowed D. Cohen in 1972 to record magnetoencephalograms of the alpha rhythm without noise averaging [20].

After the first MEG recordings, MEG systems developed from single-channel detectors (that require manual mechanical scanning over the area of interest) to full-head systems with around 100 channels in the early 1990s [21–24]. State-of-the-art systems nowadays include hundreds of SQUID sensors and are commercially available from MEGIN (Croton Healthcare), CTF systems, Compumedics, Ricoh, and Tristan Tech. These systems contain three main components: SQUID sensors with their electronics, flux transformers that couple the neuromagnetic field to the SQUIDs, and a dewar containing liquid helium. Additionally, MEG systems are located inside a magnetically shielded room to reduce environmental noise. The SQUIDs and flux transformers are made from low critical temperature (low-T_c) superconductors, which is why they need to be cooled to liquid helium temperatures (4 K = -269 °C). The flux transformer can be configured to create a magnetometer (measuring magnetic field) or a gradiometer (measuring differences in magnetic field). Typical white noise spectral densities of low-T_c SQUID sensors in state-of-the-art MEG systems are below 5 fT/$\sqrt{\text{Hz}}$ for magnetometers and below 5 fT/(cm$\sqrt{\text{Hz}}$) for gradiometers [25]. The sensors are arranged inside a fixed helmet and insulated from the room temperature environment with a thick layer of superinsulation and vacuum. The helium boil-off requires the dewar to be refilled weekly, which is expensive and requires trained personnel. Recently, closed-cycle cryocoolers for helium recycling have been developed, which enables MEG operation without helium refills, thus drastically reducing the helium costs [26, 27].

The advent of novel magnetic sensor technologies operating at higher temperatures has opened up the possibility of getting rid of liquid helium cooling altogether. For example, SQUIDs made from high critical temperature (high-T_c) superconductors can be cooled with cheap and abundant liquid nitrogen instead [28]. Optically pumped magnetometers (OPMs, also known as atomic magnetometers or spin-exchange relaxation-free (SERF) magnetometers), on the other hand, do not require any cryogenics, but need to be heated to reach the sensitivities required for MEG [29, 30]. Several groups have demonstrated the feasibility of MEG recordings with high-T_c SQUIDs [28, 31–35] and OPMs [36–39].

In 2012 two groups took advantage of the reduced thermal requirements of high-T_c SQUIDs [40] and OPMs [41], and showed that these sensor technologies allowed for a significant reduction in the sensor-to-scalp distance. This idea lead to the birth of the growing field of *on-scalp MEG* in which the MEG sensors are flexibly placed directly

on the scalp. In conventional (low-T_c SQUID) MEG systems the sensor-to-scalp distance is at best ∼2 cm [13, 25]. The neuromagnetic field intensity decreases at least as $1/r^2$ with the distance r between the source and the sensor [14]. Placing the sensors closer to the scalp thus leads to higher signal magnitudes available to the sensors. Varying head sizes and shapes require that the sensors can be placed flexibly in order to provide minimal standoff distance everywhere on the scalp for everyone. Additionally, the sensor spacing should be approximately the distance of the sensors to the closest sources, meaning that the sensors in on-scalp MEG systems should be more densely packed than in conventional MEG systems [42, 43]. The advantages of full-head on-scalp MEG (besides higher signal amplitudes) are improved sampling of the entire brain, reduction of start-up/running costs related to liquid helium cooling, and potentially higher spatial resolution [44–47]. However, on-scalp MEG is still in its infancy and full-head systems have yet to be built to demonstrate the full potential of on-scalp MEG. A more detailed introduction to on-scalp MEG is given in Publication I.

The work in this thesis is part of the *NeuroSQUID*[1] project that aims to develop multichannel on-scalp MEG based on high-T_c SQUIDs. Several other groups have been working on building multichannel on-scalp MEG systems during the time of my PhD and all of these systems are based on OPMs [48–51]. OPMs have the advantage that they do not need any cryogenics but have to be heated instead, which facilitates the fabrication of flexible and lightweight MEG systems immensely. Low-noise OPMs are furthermore much simpler to fabricate than high-T_c SQUID magnetometers. Nonetheless, high-T_c SQUIDs have several advantages over OPMs. First, the bandwidth of MEG OPMs is typically chosen to be less than 200 Hz due to the intrinsic trade-off between the bandwidth and the sensitivity [30, 52]. SQUIDs, on the other hand, are broad-band sensors and the bandwidth is usually only limited by the readout electronics to the kHz range, but can easily be increased to the MHz range if needed [53]. Second, SQUIDs have a sensitive area over which the measured magnetic field is averaged, while OPMs have a sensitive volume. This means that the standoff distance for OPMs does not only depend on the thickness of the insulation needed to protect the head from the heated cell, but also on the size of the vapor cell. Decreasing the vapor cell volume, however, decreases the sensitivity [30]. Third, OPMs require low background magnetic fields for operation in the ultra-sensitive SERF regime, which limits their dynamic range. Often a standard MSR is not enough and active field cancellation is required [49, 50].

High-T_c SQUIDs and OPMs are not the only possible on-scalp MEG sensor technologies. Alternative magnetometer technologies include diamond nitrogen-vacancy (NV) center-based magnetometers [54–56], magnetoelectric sensors [57], magnetoresistive or mixed sensors [58, 59], and kinetic inductance magnetometers (KIMs) [60]. Both diamond NV center magnetometers and magnetoelectric sensors are room temperature sensors, which allow for minimal standoff distances. However, diamond NV center magnetometers have so far mainly been used for nanoscale detection of nuclear spins [55], and a macroscopic sensor has yet to be demonstrated, although a very promising sensitivity of 3 $\mathrm{fT}/\sqrt{\mathrm{Hz}}$ has been theoretically predicted [54]. A magnetoelectric sensor operating at room temperature has been constructed,

[1] Knut and Alice Wallenberg foundation project KAW 2014.0102

but the noise level of a few pT/$\sqrt{\text{Hz}}$ is still too high for MEG [57]. Suitable noise levels of around 100 fT/$\sqrt{\text{Hz}}$ were demonstrated with a giant magnetoresistive (GMR) sensor coupled to a high-T_c superconducting pickup loop [58]. Like high-T_c SQUIDs, this mixed sensor requires cooling, but the fabrication process is simpler. Nonetheless, white and low frequency noise is higher than in SQUIDs. A simpler fabrication process is also offered by KIMs, which even allow for frequency multiplexing, but as a superconducting sensor, they also require cryogenics [60]. A noise level of 30 fT/$\sqrt{\text{Hz}}$ has been reached with a low-T_c superconducting KIM [60], but for on-scalp MEG a high-T_c superconducting version would be required. Since high-T_c KIMs can be fabricated in a similar way as high-T_c SQUIDs, my PhD project not only focused on high-T_c SQUID magnetometers for on-scalp MEG, but also included KIMs.

1.1 Thesis objectives and outline

The aim of this thesis is to describe the development of high-temperature superconducting magnetometers for multichannel on-scalp MEG. The first step from single-channel systems made earlier in our group [40, 61] towards full-head coverage was chosen to be a densely-packed 7-channel system. I first describe the development of single layer high-T_c SQUID magnetometers with a directly coupled pickup loop and bicrystal grain boundary Josephson junctions for the said system (Paper A and Paper B). Then I present the assembled 7-channel on-scalp MEG system (Paper C), which is being used for MEG measurements (Paper II-Paper V). Next, I describe the development of magnetometers for the next generation on-scalp MEG system with more channels. First, the possibility of replacing the bicrystal grain boundary junctions with Dayem bridge junctions is investigated (Paper D and Paper E). Second, the development of improved sensors with inductively coupled flux transformers is described. Lastly, we demonstrate the first high-T_c KIMs (Paper F) and evaluate the feasibility of this sensor for multichannel on-scalp MEG.

The outline of my PhD thesis is the following:
Chapter 2 introduces the theoretical background and methods used to design, operate, characterize, and optimize our high-T_c SQUID magnetometers and KIMs. **Chapter 3** describes how these devices are fabricated in the Nanofabrication Laboratory cleanroom at Chalmers. **Chapter 4** details the work done on single layer high-T_c SQUID magnetometers with bicrystal grain boundary Josephson junctions. **Chapter 5** describes the 7-channel on-scalp MEG system built and summarizes the MEG measurements performed with it. The benefits of this system and possible improvements for future high-T_c SQUID-based on-scalp MEG systems are discussed. **Chapter 6** reports on the development of the next generation high-T_c SQUID magnetometers and includes both Dayem bridge-based magnetometers and magnetometers with an inductively coupled multilayer flux transformers. **Chapter 7** covers the work done on the second type of magnetic field detector, the high-T_c KIM. Finally, **chapter 8** summarizes the main results of the thesis and provides an outlook for future work.

2

Theoretical background and methods

This chapter provides the theoretical background for the work presented in this thesis and describes the main ideas behind the methods used. First, an introduction into superconductivity is given and the two main ingredients for the SQUID are explained: flux quantization and Josephson junctions. A detailed description of the dc SQUID follows covering the basic operation principle, simulations of SQUID behaviour, noise in SQUIDs and ways to minimize noise, and lastly how to readout SQUIDs using a flux-locked loop. The focus is always on high-T_c SQUIDs. Next, we move from SQUIDs as flux-to-voltage transducers to magnetometers measuring magnetic fields and present two different methods to couple to magnetic field. Since inductance is a key parameter for all superconducting magnetometers, an introduction into geometric and kinetic inductance is given, followed by a description of the inductance simulation method used and a way to measure inductance. Lastly, the operation principle of the KIM is introduced and important formulas describing the behaviour of the KIM are given. For more information on superconductivity, SQUIDs, and applications see for example Refs. [19, 62–65], on which this chapter is based.

2.1 Superconductivity

Superconductivity was discovered by the Dutch physicist H. Kamerlingh Onnes in 1911, three years after he successfully liquefied helium for the first time [66]. He found that the electrical resistance of mercury (Hg) at 3 K was zero - at least within measurement limits [67]. Later that year he observed that the transition between the superconducting and the normal state occurred abruptly at a temperature of 4.2 K [68]. The temperature of the transition is called the critical temperature T_c and it is a material-specific property of superconductors. Nowadays, 31 elements are known to be superconducting at ambient pressure with niobium (Nb) having the highest T_c = 9.25 K [69].

Perfect conductivity is the first characteristic property of superconductors; the second is the so-called Meissner effect. In 1933, W. Meissner and R. Ochsenfeld found that magnetic fields are completely expelled from the inside of a superconductor

when it is cooled below T_c [70]. Their experiment showed that superconductors were more than just perfect conductors, they also exhibit perfect diamagnetism.

The two characteristic properties of superconductors can be described by the London equations, which were proposed by the brothers F. and H. London in 1935 [71]. They relate the superconducting current density $\boldsymbol{J}$ to the electric field $\boldsymbol{E}$ and the magnetic field $\boldsymbol{B}$ within the superconductor:

$$\frac{\partial \boldsymbol{J}}{\partial t} = \frac{n_s e^{*2}}{m^*}\boldsymbol{E} \tag{2.1a}$$

$$\boldsymbol{\nabla} \times \boldsymbol{J} = -\frac{n_s e^{*2}}{m^*}\boldsymbol{B}, \tag{2.1b}$$

where n_s is the number density of superconducting carriers (superfluid density), e^* is the effective charge and m^* the effective mass (which are typically assumed to be twice the value for single electrons, i.e. $m^* = 2m_e$, where m_e is the electron mass, and $e^* = -2\mathrm{e}$, where e is the elementary charge. The first London equation implies that the electric field accelerates the superconducting electrons without resistance, and thus describes perfect conductivity. Applying Ampere's law, $\boldsymbol{\nabla} \times \boldsymbol{B} = \mu_0 \boldsymbol{J}$, to the second London equation gives the Helmholtz equation for the magnetic field:

$$\boldsymbol{\nabla}^2 \boldsymbol{B} = \frac{1}{\lambda^2}\boldsymbol{B} \quad \text{with} \quad \lambda := \sqrt{\frac{m^*}{\mu_0 n_s e^{*2}}}, \tag{2.2}$$

where μ_0 is the vacuum permeability. This equation predicts an exponential decay of the magnetic field $\boldsymbol{B}$ inside the superconductor from its value at the surface. The characteristic length scale of this decay is given by the London penetration depth λ. The magnetic field in the bulk is expelled by screening currents that flow in a thin region at the surface of the superconductor. However, if the applied magnetic field is too large, then superconductivity breaks down. Superconductors can be classified according to how this breakdown occurs. In type-I superconductors, superconductivity is abruptly destroyed when the applied field rises above the critical field H_c. In type-II superconductors there are two critical fields. When the applied field is greater than the lower critical field H_{c1}, magnetic flux vortices penetrate the material, but the electrical resistance remains zero. Supercurrents circulate around the cores of the flux vortices, which are also known as Abrikosov vortices after A. A. Abrikosov, who first predicted their existence [72]. At the upper critical field H_{c2} the flux vortex density becomes too large and superconductivity breaks down. The different states are illustrated in Fig. 2.1.

In 1950, V. L. Ginzburg and L. Landau postulated a phenomenological model to describe the macroscopic behaviour of superconductors, which is now known as the Ginzburg-Landau theory [73]. They introduced the order parameter Ψ, which is zero above T_c and takes the form of a complex wave function below T_c:

$$\Psi = \sqrt{n_s} e^{i\delta}, \tag{2.3}$$

where δ is the superconducting phase, and the amplitude is determined by the superfluid density n_s. Ginzburg-Landau theory can be used to explain whether a superconductor is type I or type II.

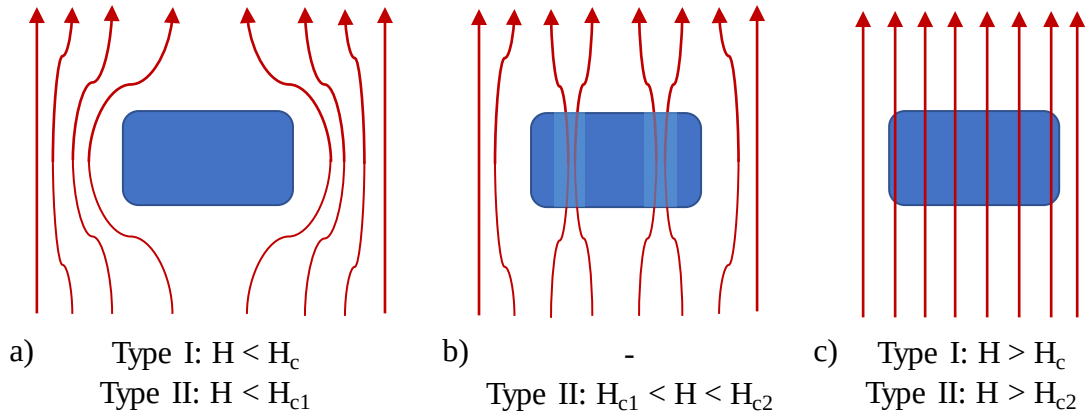

Figure 2.1: Illustration of type I and type II superconductors in a magnetic field.

The first microscopic theory of superconductivity was presented in 1957 by J. **B**ardeen, L. **C**ooper, and J. R. **S**chrieffer and is now known as the BCS theory [74]. According to their theory, electrons at the Fermi surface with opposite spin and momentum may overcome Coulomb repulsion in the presence of an attractive potential and at sufficiently low temperatures. For conventional superconductors this attractive potential is given by electron-phonon interactions, that is interactions of electrons with crystal lattice vibrations. As a result, electrons can pair up into so-called *Cooper pairs*, which are bosons, and can thus condense into the same quantum state - unlike single electrons that are fermions. The collective quantum state can be described by the wave function given in Eq. (2.3). The minimum energy required to break up a Cooper pair is the superconducting energy gap.

The discovery of high-temperature superconductivity in 1986 opened up a new research field: J. Bednorz and K. Müller found superconductivity at around 30 K in the Ba-La-Cu-O system, well above the highest T_c known at the time (23 K) [75]. Just a few months later the first superconductor with a critical temperature above the boiling point of liquid nitrogen (77 K) was found: $YBa_2Cu_3O_{7-x}$ (YBCO) with T_c = 92 K [76]. Many other superconductors with a similar crystal structure followed with T_c up to 133 K at ambient pressures [77]. These superconductors belong to a class of ceramics called *copper oxides*, or *cuprates*, and the superconducting properties are attributed to the copper-oxide (CuO_2) layers [78]. They are called unconventional superconductors because they can not be fully described by the BCS theory and a complete theory for superconductivity in cuprates is still missing. Cuprates are type II superconductors and have large upper critical fields - sometimes above 100 T [78]. The crystal structure is highly anisotropic and it is difficult to fabricate wires or devices because they are ceramics. Although there are superconductors with higher T_c than YBCO, it is one of the most used cuprate superconductors in practical applications and the high-T_c superconductor used throughout this thesis.

In the last 2 decades several other types of superconductors with relatively high T_c were identified. In 2001, magnesium diboride (MgB_2) was found to be a conventional superconductor with T_c = 39 K [79]. In 2006, another class of unconventional superconductors was discovered: the iron-based superconductors [80]. The critical

temperature increased quickly from the initial 4 K [80] via 26 K in 2008 [81] to above 100 K in 2015 for a single unit cell layer FeSe film [82]. The record for the highest T_c is at the moment held by lanthanum hydride (LaH_{10}) at ultra-high pressures (170-200 GPa) with a T_c of 250-260 K [83, 84]. This material is predicted to be a room temperature superconductor at even higher pressures [85].

The field of superconductivity has a large range of applications [86], which can be divided into three main areas: magnets, electric power applications, and electronic devices. Superconducting magnets can generate large magnetic fields and are widely used in MRI systems, but also in particle accelerators and to confine plasma in fusion reactors. Electric power applications include cables, generators, energy storage, fault-current limiters, and transformers [87]. Superconducting electronic devices are used for sensing, metrology, signal processing, digital electronics, and quantum computing. The key ingredient for superconducting electronic devices is usually flux quantization or the Josephson effect, which are both discussed herein after a short description of the high-temperature superconductor YBCO.

2.1.1 The high-temperature superconductor YBCO

Cuprate superconductors have a layered crystal structure in common, where conducting CuO_2 planes alternate with insulating charge-carrier reservoirs along the crystallographic c-axis direction. The crystal structure of YBCO is shown in Fig. 2.2. The YBCO unit cell consists of three perovskite cells on top of each other, where the center position is either occupied by a Y atom (center) or a Ba atom (top and bottom). The CuO_2 planes are located above and below the Y atom and are responsible for superconductivity, while the CuO chains in the b direction act as charge reservoirs and are extremely sensitive to oxygen doping.

The symmetry, the lattice parameters, and the critical temperature of $YBa_2Cu_3O_{7-x}$ depend on the oxygen content $n = 7 - x$ per unit cell and the hole doping p (number

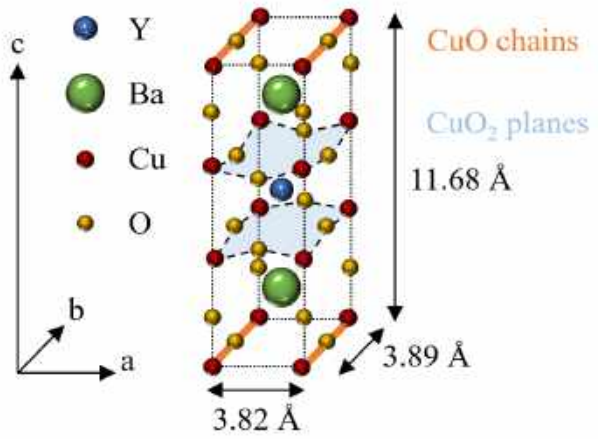

Figure 2.2: Unit cell of YBCO. The CuO_2 planes are highlighted in blue and the CuO chains in orange. The doping changes the number of oxygen atoms in the CuO chains, which affects the symmetry, the lattice parameters and T_c. The lattice parameters are here shown for optimal doping. Figure adapted from Ref. [78].

of holes per copper atom in the CuO_2 planes). At zero doping ($p = 0$, $n = 6.0$), YBCO is an antiferromagnetic insulator with tetragonal crystal structure. By adding oxygen (increasing n), the CuO chains form and the crystal symmetry changes to orthorhombic. Superconductivity appears at $p = 0.05$ ($n = 6.4$) and the critical temperature of these *underdoped* films increases until the maximum is reached for an *optimal doping* of $p = 0.16$ ($n \approx 6.9$) and decreases again for *overdoped* films [88]. For optimal doping, the lattice parameters are a = 3.82 Å, b = 3.89 Å, and c = 11.68 Å [78].

As a consequence of the layered crystal structure, properties such as the electrical resistivity, the penetration depth or the critical current density are very different in the ab-plane as compared to the c-axis direction. Single-crystalline YBCO thin films with their c-axis normal to the substrate can be epitaxially grown using a substrate with suitable lattice parameters. These c-axis YBCO films have been found to exhibit high critical current densities in the ab plane and SQUIDs fabricated from them show acceptable low frequency flux noise [19]. Because research efforts generally have been focused on YBCO, the film qualities achieved for YBCO are higher than for other HTS compounds, and consequently most HTS electronic devices are fabricated from epitaxial c-axis YBCO films [19].

2.2 Flux quantization

Magnetic flux quantization in a superconducting ring is a striking demonstration of the macroscopically observable quantum mechanical properties of the superconducting state. It can be derived using the classical canonical momentum $\boldsymbol{p}$ of a particle with effective mass m^* and charge e^* in the presence of a magnetic field $\boldsymbol{B}$ [63]:

$$\boldsymbol{p} = m^* \boldsymbol{v_s} + e^* \boldsymbol{A}, \tag{2.4}$$

where $\boldsymbol{A}$ is the vector potential with $\boldsymbol{B} = \boldsymbol{\nabla} \times \boldsymbol{A}$ and $\boldsymbol{v_s}$ is the velocity. The connection to the quantum mechanical description is that the momentum density $n_s \boldsymbol{p}$ is the expectation value of the canonical momentum operator $-i\hbar\boldsymbol{\nabla}$ operating on the wave function (2.3) describing the superconducting state:

$$n_s \boldsymbol{p} = \langle \Psi | - i\hbar \boldsymbol{\nabla} | \Psi \rangle, \tag{2.5}$$

where $\hbar$ is the reduced Planck constant. From this equation we obtain $\boldsymbol{p} = \hbar \boldsymbol{\nabla} \delta$. Eq. (2.4) can now be rewritten using that the superconducting current density is given by $\boldsymbol{J} = n_s e^* \boldsymbol{v_s}$:

$$\boldsymbol{p} = \hbar \boldsymbol{\nabla} \delta = \frac{m^*}{n_s e^*} \boldsymbol{J} + e^* \boldsymbol{A} = e^* (\mu_0 \lambda^2 \boldsymbol{J} + \boldsymbol{A}). \tag{2.6}$$

Integration of this equation around a path C lying within a superconductor and surrounding a non-superconducting hole gives:

$$\hbar \oint_C \boldsymbol{\nabla} \delta \cdot d\boldsymbol{r} = e^* \oint_C (\mu_0 \lambda^2 \boldsymbol{J} + \boldsymbol{A}) d\boldsymbol{r}. \tag{2.7}$$

In order for the wave function to be single valued, the integral on the left side needs to be an integer multiple of 2π:

$$\oint_C \boldsymbol{\nabla}\delta \cdot d\boldsymbol{r} = 2\pi n, \quad n \in \mathbb{Z}. \tag{2.8}$$

The integral on the right hand side of Eq. (2.7) is called London's *fluxoid*. For an integration path deep inside the superconductor, $\boldsymbol{J} = 0$, and we obtain with the help of Stokes' theorem:

$$e^* \oint_C (\mu_0 \lambda^2 \boldsymbol{J} + \boldsymbol{A}) d\boldsymbol{r} = e^* \oint_C \boldsymbol{A} \cdot d\boldsymbol{r} = e^* \iint_S (\boldsymbol{\nabla} \times \boldsymbol{A}) d\boldsymbol{s} = e^* \iint_S \boldsymbol{B} \cdot d\boldsymbol{s} = e^* \Phi, \tag{2.9}$$

where Φ is the flux enclosed by the path. Recombining the two sides of Eq. (2.7) gives:

$$\Phi = \frac{2\pi n \hbar}{e^*} = \frac{nh}{e^*}, \tag{2.10}$$

meaning that flux is quantized in units of $h/|e^*|$. First experiments on flux quantization [89, 90] found $|e^*| = 2e$ in line with BCS theory. The value of the basic quantum of magnetic flux is therefore $\Phi_0 = h/2e = 2.07 \cdot 10^{-15}$ Wb. Each Abrikosov vortex in a type II superconductor contains exactly one flux quantum.

2.3 Josephson junctions

A Josephson junction consists of two superconductors separated by a weak link as illustrated in Fig. 2.3. If the potential barrier is small enough, the two wave functions overlap and Cooper pairs can tunnel between the two superconductors without dissipation.

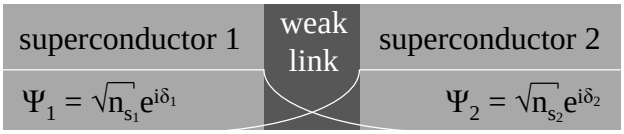

Figure 2.3: A Josephson junction is made from two superconductors separated by a weak link. The white lines indicate the wave function of the two superconductors.

In 1962, B. Josephson theoretically predicted the behaviour of this device [91] and his predictions were soon after experimentally confirmed [92, 93]. B. Josephson presented two equations, one for the superconducting current I_s and one for the voltage V across the junction, both as a function of the phase difference of the wave functions on each side of the junction, $\delta = \delta_2 - \delta_1$. The first Josephson equation is:

$$I_s = I_0 \sin(\delta), \tag{2.11}$$

where I_0 is the maximum supercurrent (critical current) the junction can withhold without developing a voltage drop across it. This equation describes the dc Josephson

effect. When a Josephson junction is biased with a dc current, the voltage across it remains zero up to the critical current I_0. When the bias current is further increased, the junction switches into a resistive state and a non-zero averaged voltage develops across the junction. The voltage depends on the derivative of the phase difference as described by the second Josephson equation:

$$V = \frac{\hbar}{2e}\frac{\partial \delta}{\partial t} = \frac{\Phi_0}{2\pi}\frac{\partial \delta}{\partial t}. \tag{2.12}$$

When the junction is instead biased with a constant average voltage, integrating Eq. (2.12) shows that the phase difference linearly depends on time, $\delta = (2e/\hbar)Vt + \delta_0$. Substituting this into Eq. (2.11) gives an oscillating supercurrent $I_s = I_0 \sin(2\pi f t + \delta_0)$ with the frequency $f = (2e/h)V = 483.6$ GHz/mV. The junction thus acts as a voltage-to-frequency converter. This effect is known as the ac Josephson effect. If one instead applies microwave radiation at a constant frequency, the junction acts as a frequency-to-voltage converter, which is used in the Josephson voltage standard in metrology [94].

2.3.1 RCSJ model

A common way of modeling a Josephson junction is with the resistively and capacitively shunted junction (RCSJ) model [95, 96]. The equivalent circuit of this model is shown in Fig. 2.4a.

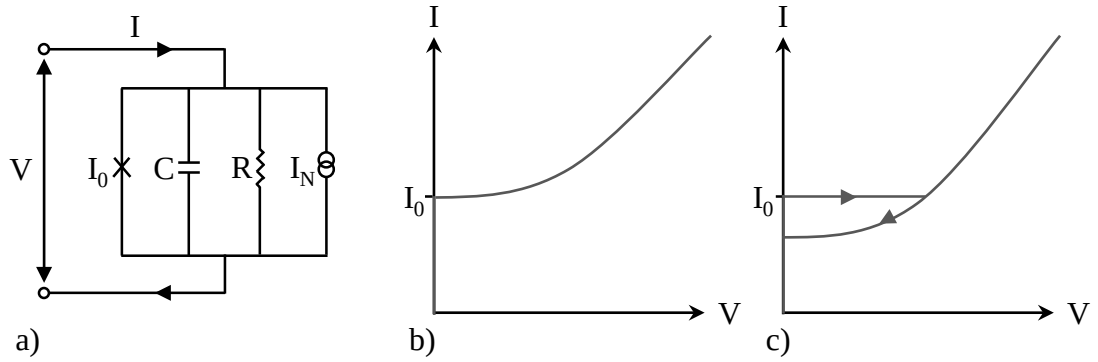

Figure 2.4: a) Equivalent circuit used in the RCSJ model. b) I-V characteristic of a non-hysteretic Josephson junction with $\beta_c \ll 1$. c) I-V characteristic of a hysteretic Josephson junction with $\beta_c \gtrsim 1$.

The total junction current I is given by the sum of the supercurrent I_s, the displacement current $C \cdot dV/dt$ in the shunting capacitor with capacitance C, the current V/R through the shunting resistor with resistance R, and the noise current I_n of the resistor. This sum can be written with the help of the Josephson Eqs. (2.11) and (2.11) as

$$I = C\frac{\Phi_0}{2\pi}\frac{\partial^2 \delta}{\partial t^2} + \frac{1}{R}\frac{\Phi_0}{2\pi}\frac{\partial \delta}{\partial t} + I_0 \sin(\delta) + I_n. \tag{2.13}$$

By introducing the so-called Stewart-McCumber parameter $\beta_c = 2\pi I_0 R^2 C/\Phi_0$ and the normalized time $\tau = t/\omega_c$, where $\omega_c = 2\pi I_0 R/\Phi_0$ is the characteristic frequency,

the differential equation can be simplified to

$$\frac{I}{I_0} = \beta_c \ddot{\delta} + \dot{\delta} + \sin(\delta) + \frac{I_n}{I_0}. \tag{2.14}$$

The dot denotes the derivative with respect to normalized time. Numerical solutions can be obtained for any β_c and even the effect of noise can be simulated (see for example Ref. [97]). It is possible to obtain an analytical solution in the case of very small $\beta_c \ll 1$ and no noise. The capacitance term is then negligible and Eq. (2.14) can be integrated. The average voltage V across the junction is obtained as:

$$V = 0 \qquad \text{for} \quad I \leq I_0, \tag{2.15a}$$

$$V = R\sqrt{I^2 - I_0^2} \qquad \text{for} \quad I > I_0. \tag{2.15b}$$

The current-voltage (I-V) characteristic of such a junction is shown in Fig. 2.4b. For $\beta_c \gtrsim 1$, the I-V characteristic becomes hysteretic (see Fig. 2.4c). For high-T_c junctions, the limit $\beta_c \ll 1$ is often obtained and the RCSJ model reduces to the RSJ model [64].

2.3.2 HTS Josephson junctions

A successful Josephson junction technology for SQUIDs offers a nonhysteretic I-V characteristic close to the prediction of the RSJ model, controllable and reproducible parameters (I_0, R, C), a high I_0R product, high yield, high stability, and low noise [64]. While such technologies are available using low-T_c materials like niobium and aluminum, the hunt for a HTS Josephson junction technology fulfilling (most of) these requirements is still ongoing. The problems are mainly related to the cuprate's anisotropic crystal structure and that their superconducting properties are highly susceptible to structural and chemical changes on atomic length scales. The latter is because cuprates have a very small *coherence length* ξ – the order parameter decays over a length scale of just a few nm [78].

Several useful high-T_c Josephson junction technologies have been developed. Soon after the discovery of superconductivity in YBCO, devices fabricated from polycrystalline YBCO films provided the first evidence that grain boundaries act as junctions [98]. This property is used in bicrystal grain boundary junctions (GBJs) and step-edge junctions (see Fig. 2.5a&b), which are the junction types that are nowadays usually employed in HTS biomagnetometers [99].

Bicrystal GBJs rely on a bicrystal substrate, which is obtained by bonding together two crystals with their crystal lattices rotated along the substrate normal by a certain misorientation angle θ. The junction is created by growing an epitaxial high-T_c film on the bicrystal substrate and patterning a microbridge across the grain boundary [100–102]. This leads to a grain boundary also in the superconducting film and the critical current density of the junction decreases exponentially with increasing θ [101]. Substrates with different angles (e.g. 24°, 30°, or 36°) are commercially available, but they are expensive (above 200 € for a 10 mm × 10 mm substrate). The straightforward fabrication makes these junctions reliable, however, the junction properties strongly depend on the bicrystal quality, and their placement is constrained [64].

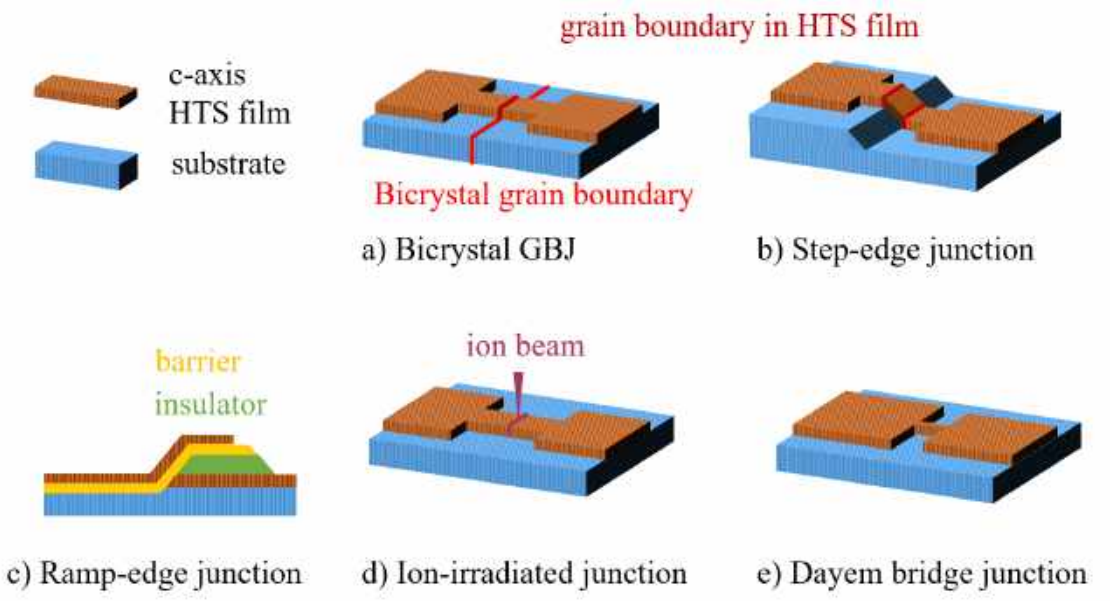

Figure 2.5: Different types of HTS Josephson junctions.

Step-edge junctions are fabricated by first etching a step into the single-crystal substrate and then growing an epitaxial high-T_c film that is patterned into a microbridge across the step. Depending on the step angle and substrate material, the film changes its orientation at the step, and one or two grain boundaries are formed [102]. The best results are achieved using MgO with its c-axis aligned to the substrate normal (referred to as MgO 001) because the YBCO film grows c-axis orientated also on the 45° slope of the step [103–105]. Step-edge junctions often have a higher I_0R product than bicrystal GBJs, and they can be placed wherever on the substrate, but the junction properties strongly depend on the microstructure of the etched step [103–105].

Although grain boundary junctions are the most commonly used HTS junction type nowadays, several groups rely on junctions without grain boundaries such as ramp-edge junctions, ion-damage junctions, and Dayem bridge junctions, which are shown in Fig. 2.5c-e.

Ramp-edge junctions require the complicated fabrication of an epitaxial tri-layer where the two superconductors are separated by a thin barrier [106–108]. The current transport is along the a-b-planes of the c-axis orientated films, and one can thus take advantage of the larger coherence length is in this direction as compared to the c-axis direction [64]. The top electrode shields the magnetic field component normal to the film surface, which may be an advantage when operating the device in unshielded environments [108]. However, the junction properties strongly depend on the interface quality and the fabrication process is complex [106–108].

Ion-irradiated junctions are fabricated by locally exposing the HTS film to an ion beam and thus creating a region of suppressed superconductivity [109–112]. The film properties can be tuned from superconducting via conducting to insulating by increasing the irradiation dose [111, 113]. The junction can either be defined by irradiation through a narrow slit in a resist mask [110] or using a focused ion beam

(FIB) with which the junction can be written directly [109, 111, 112]. The narrowest junction barriers can be achieved using helium FIB with a beam diameter of 0.5 nm [111, 112]. Ion irradiation can also be used to define the remaining device structure by turning parts insulating that one would otherwise have to etch away [109, 110, 114]. In the case of FIB, however, this is a very slow process. The advantages of ion-irradiated junctions are that their properties can be tuned with the ion dose and that they can be freely positioned on the substrate. However, helium FIB junctions rely on very thin films ($\lesssim 50$ nm) so that the ion beam can fully penetrate, and they are operated at temperatures below 77 K, possibly because of comparatively low I_0R products at 77 K [111, 115].

Dayem bridge or nanowire junctions are thin film constrictions in the form of nanobridges [116]. Josephson-like behaviour has been obtained for YBCO nanobridges with dimensions smaller than the effective penetration depth [117, 118]. The junction properties can be controlled by varying the cross section of the bridge – high quality YBCO nanowires with cross sections of 50 nm $\times$ 50 nm have been fabricated [119]. The advantages of Dayem bridges are that they can be placed freely on the substrate and that they can be fabricated with a single e-beam exposure requiring no alignment. However, thin films of approximately 50 nm are required, and instead of a single and well-defined RSJ-like resistance parameter R, the nanobridge is characterized by a bias-dependent dynamic resistance [120].

Which junction technology is best depends on the device that should be made. Nonetheless, most often one does not have the luxury of picking the most suitable junction technology, but one is limited to at best a few junction types that the group can successfully fabricate. In our case these are bicrystal GBJs and Dayem bridge junctions. The suitability of these junction technologies for SQUID magnetometers will be discussed in more detail later.

2.4 DC SQUIDs

A SQUID consists of a superconducting loop interrupted by one or two Josephson junctions. A SQUID with one junction is called an rf SQUID, while a SQUID with two junctions in parallel is called a dc SQUID. SQUIDs used for MEG are mainly dc SQUIDs and this is the type of SQUID used throughout this thesis. An illustration of a dc SQUID can be found in Fig. 2.6a.

SQUIDs are very sensitive flux-to-voltage converters. Their operation principle can be understood using the example of a symmetric SQUID. An input current I to the SQUID splits into two currents I_1 and I_2, one for each arm of the SQUID loop. In the absence of external flux, I_1 and I_2 are equal. If the external flux Φ is increased, a circulating current J is created to guarantee flux quantization in the superconducting loop. This circulating current increases the current in one of the arms, $I_1 = I/2 + J$, and decreases it in the other, $I_2 = I/2 - J$. As soon as the current in one of the arms exceeds the critical current I_0 of that junction, a voltage appears. The voltage V across the SQUID thus depends on the circulating current, which in turn depends on the external flux. Fig. 2.6b shows the typical I-V characteristic of a symmetric dc SQUID for two different external flux values. When the SQUID is biased with a constant current I_b above the critical current of the SQUID, $I_c = 2I_0$, the voltage V

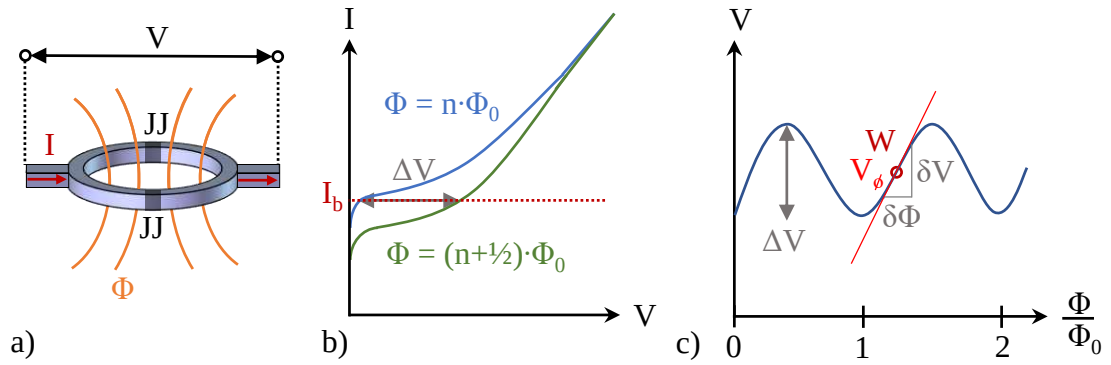

Figure 2.6: a) Schematic of a dc SQUID. Josephson junctions are marked as JJ. b) Typical I-V characteristic of a symmetric dc SQUID. c) SQUID voltage V as a function of normalized applied flux Φ/Φ_0 for a constant bias current I_b.

oscillates as a function of flux Φ (see Fig. 2.6c). The period of oscillation is exactly one flux quantum because of flux quantization in the SQUID loop.

In order to use the SQUID as a sensitive flux-to-voltage converter, a working point with a large voltage output δV to a small change in flux $\delta\Phi$ needs to be chosen, i.e. a point on the $V(\Phi)$ curve with a large slope $|\partial V/\partial\Phi|_I$. The maximal value of $|\partial V/\partial\Phi|_I$ is called the transfer function V_Φ. In practise, the working point is usually found by first choosing the bias current with the largest voltage modulation ΔV and then setting the external flux to get the point in the center of the slope, which corresponds to $\Phi = (n \pm \frac{1}{4})\Phi_0$ in the case of the symmetric SQUID. This working point W is shown in Fig. 2.6c. For sinusoidal voltage modulation, V_Φ and ΔV are related by $V_\Phi = \pi\Delta V/\Phi_0$.

SQUIDs can be used to sense any quantity that can be transduced into a magnetic flux. This includes magnetic fields, magnetic field gradients, electrical currents, voltages, and displacements. SQUIDs are widely used in several applications including biomagnetism, non-destructive evaluation (NDE), geophysics, SQUID microscopy, quantum information, and basic physics [62, 65, 86, 121]. Most SQUIDs employed in biomagnetism are used in MEG systems, however, they can also be used for measuring magnetic signals from other organs such as the heart, the stomach and intestines, the lungs, muscles, and peripheral nerves. Another useful biomedical application of SQUIDs is biosensing utilizing magnetic markers [122]. High-T_c SQUIDs are mainly used for biomagnetism, NDE, geophysics, and SQUID microscopy [64, 99].

2.4.1 Basic equations for SQUID simulations

Modeling of SQUID behaviour can give valuable insights into how a SQUID should be designed. The model used here was first described and simulated in Ref. [123] and consists of two resistively shunted Josephson junctions connected in parallel as shown in Fig. 2.7. The input current I splits up into two currents I_1 and I_2, one for each SQUID arm. The circulating current is defined to be $J = (I_2 - I_1)/2$. The currents through the two Josephson junctions can then be written with the help of

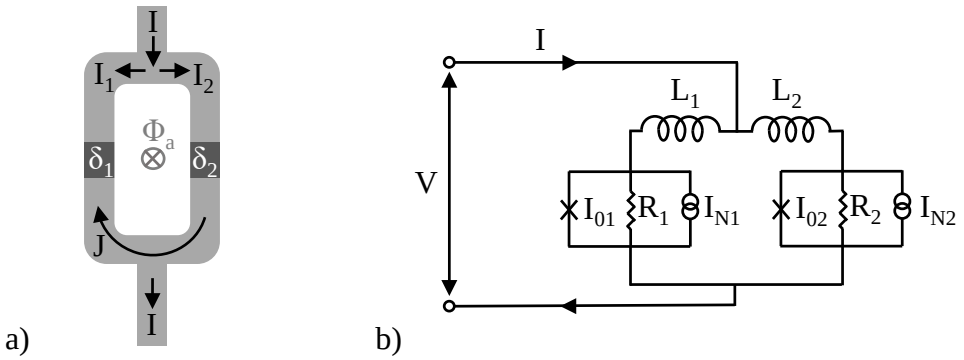

Figure 2.7: a) Schematic of a dc SQUID showing the currents and phase differences used in the model. b) RSJ model equivalent circuit for the dc SQUID.

Eq. (2.13) as:

$$I_1 = \frac{I}{2} - J = \frac{1}{R_1}\frac{\Phi_0}{2\pi}\frac{\partial\delta_1}{\partial t} + I_{01}\cdot\sin(\delta_1) + I_{N1} \tag{2.16a}$$

$$I_2 = \frac{I}{2} + J = \frac{1}{R_2}\frac{\Phi_0}{2\pi}\frac{\partial\delta_2}{\partial t} + I_{02}\cdot\sin(\delta_2) + I_{N2} \tag{2.16b}$$

The capacitive term in the RCSJ model is neglected here because β_c is small for high-T_c Josephson junctions.

Because of flux quantization in the superconducting loop, the phase differences δ_1 and δ_2 (both modulo 2π) differ by

$$\delta_1 - \delta_2 = 2\pi\frac{\Phi_T}{\Phi_0}, \tag{2.17}$$

where Φ_T is the total flux threading the SQUID loop. The total flux is the sum of the applied flux Φ_a and the fluxes created by the currents I and J. It can be written as:

$$\Phi_T = \Phi_a + LJ + (L_2 - L_1)I/2. \tag{2.18}$$

For convenience, we switch to dimensionless units, which are written in lower case letters. All currents are normalized to the average junction critical current $I_0 = (I_{01} + I_{02})/2$, resistances to twice the parallel resistance $R = 2(\frac{1}{R_1} + \frac{1}{R_2})^{-1}$, voltages to I_0R, flux to Φ_0, and time to $1/\omega_c = \Phi_0/(2\pi I_0 R)$; refer to Appendix A for definitions of all symbols. To describe the asymmetry in the resistances, the critical currents and the inductances, we define the asymmetry parameters $\alpha_R = (R_1 - R_2)/(R_1 + R_2)$, $\alpha_I = (I_{02} - I_{01})/(2I_0)$ and $\alpha_L = (L_2 - L_1)/L$, where the inductance L includes the mutual inductance M between the two SQUID arms: $L = L_1 + L_2 - 2M$. The case of the symmetric SQUID is obtained when all the asymmetry parameters are zero. Finally, we need to define one more parameter, the screening parameter $\beta_L = 2I_0L/\Phi_0$, which is of great importance as we will soon see.

Eqs. (2.16) - (2.18) can be expressed as:

$$i_1 = \frac{i}{2} - j = (1-\alpha_R)\dot{\delta_1} + (1-\alpha_I)\sin(\delta_1) + i_{N1} \tag{2.19a}$$

$$i_2 = \frac{i}{2} + j = (1+\alpha_R)\dot{\delta_2} + (1+\alpha_I)\sin(\delta_2) + i_{N2} \tag{2.19b}$$

$$\delta_1 - \delta_2 = 2\pi\phi_a + \pi\beta_L j + \pi\beta_L\alpha_L i/2 \tag{2.19c}$$

Furthermore, the normalized voltage v across the SQUID can be obtained using [123]:

$$v = \frac{1+\alpha_L}{2}\dot{\delta_1} + \frac{1-\alpha_L}{2}\dot{\delta_2}. \tag{2.20}$$

The main purpose of using this model here is to study the effect of the screening parameter, the asymmetry parameters, and noise on the critical current modulation, the current-voltage characteristics, and the voltage modulation with flux.

2.4.2 Critical current modulation

For sufficiently low input currents i, the voltage v across the SQUID is zero and so are the time derivatives. In the noise free case Eqs. (2.19) reduce to:

$$i = (1-\alpha_I)\sin(\delta_1) + (1+\alpha_I)\sin(\delta_2) \tag{2.21a}$$

$$2j = -(1-\alpha_I)\sin(\delta_1) + (1+\alpha_I)\sin(\delta_2) \tag{2.21b}$$

$$\delta_2 = \delta_1 - 2\pi\phi_a - \pi\beta_L j - \pi\beta_L\alpha_L i/2. \tag{2.21c}$$

The largest current producing zero voltage across the SQUID is called the critical current i_c and depends on ϕ_a, β_L, α_I and α_L, but not on α_R because we are in the superconducting state. In the special case of a symmetric SQUID with negligible inductance ($\beta_L = 0$), the equations can easily be solved analytically yielding $i_c(\phi_a) = 2|\cos(\pi\phi_a)|$. To obtain the critical current modulation curve $I_c(\phi_a)$ for different choices of β_L, α_I and α_L, we numerically solve Eqs. (2.19) using the locus method described in Ref. [124]. The resulting $i_c(\phi_a)$ curve for the symmetric SQUID is shown in Fig. 2.8a for different values of β_L. The maximal critical current $i_{c,max} = 2$ is obtained for integer ϕ_a, while the minimal value $i_{c,min}$ is obtained for half-integer ϕ_a. The critical current modulation depth $\Delta i_c = i_{c,max} - i_{c,min}$ decreases rapidly with increasing β_L as plotted in Fig. 2.8b.

The effect of α_I and α_L on the $i_c(\phi_a)$ curves is shown in Fig. 2.9. The maximal value $i_{c,max} = 2$ is always attained for some value of ϕ_a, but not necessarily at integer ϕ_a. The critical current modulation depth is not affected by α_L, but decays with increasing α_I.

2.4.3 Current-voltage characteristics

We now switch to the case of nonzero voltage across the SQUID. It is again possible to obtain an analytical solution for the current-voltage characteristic of the noise free symmetric SQUID with $\beta_L = 0$. The average voltage $\bar{v}$ is given by $\bar{v} = \sqrt{(i/2)^2 - \cos^2(\pi\phi_a)}$ for currents i above the critical current $i_c = 2|\cos(\pi\phi_a)|$, and zero below.

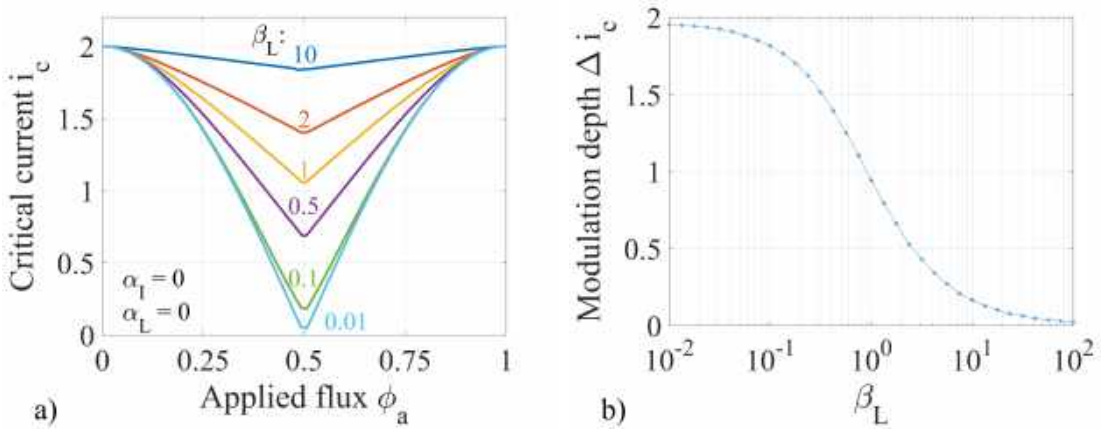

Figure 2.8: a) Simulated critical current modulation curves $i_0(\phi_a)$ for different values of β_L for the symmetric SQUID. b) Simulated critical current modulation depth as a function of β_L.

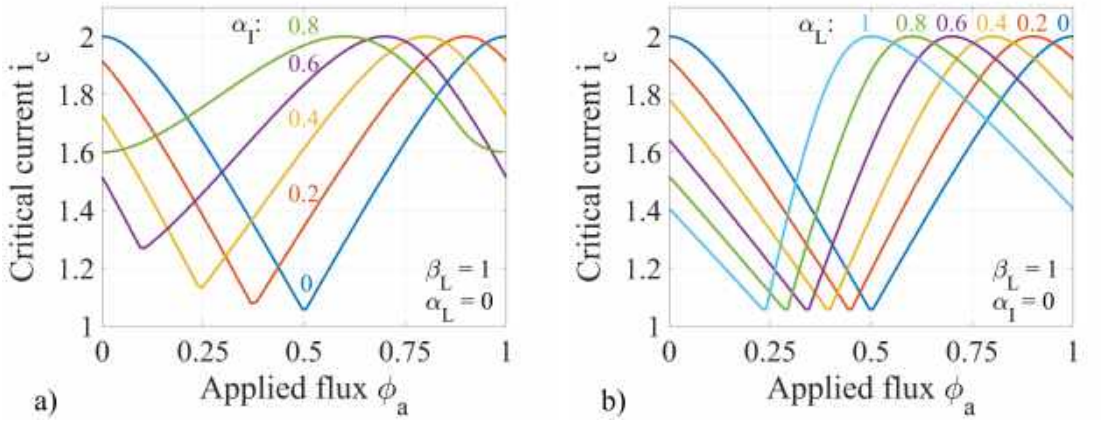

Figure 2.9: Simulated critical current of a SQUID vs. applied flux as a function of a) critical current asymmetry α_I and b) inductance asymmetry α_L. Both plots are for $\beta_L = 1$.

The $i - \bar{v}$ characteristics for general values β_L, α_L, α_I and α_R can be obtained by calculating the average voltage $\bar{v}$ for every input current i and applied flux ϕ_a of interest. The voltage v and the circulating current j oscillate in time and fulfill:

$$j(\tau) = \frac{\delta_1 - \delta_2 - 2\pi\phi_a}{\pi\beta_L} - \frac{\alpha_L i}{2} \tag{2.22a}$$

$$\dot{\delta}_1(\tau) = \frac{i/2 - j - (1-\alpha_I)\sin(\delta_1) + i_{N1}}{1-\alpha_R} = v_1 \tag{2.22b}$$

$$\dot{\delta}_2(\tau) = \frac{i/2 + j - (1+\alpha_I)\sin(\delta_2) + i_{N2}}{1+\alpha_R} = v_2 \tag{2.22c}$$

$$v(\tau) = \frac{1+\alpha_L}{2}\dot{\delta}_1 + \frac{1-\alpha_L}{2}\dot{\delta}_2, \tag{2.22d}$$

which is obtained by rearranging Eqs. (2.19) - (2.20). We start with the noise free case (i.e. $i_{N1} = 0 = i_{N2}$) and solve the differential equations by integrating stepwise

in time using the 4th order Runge-Kutta method. A timestep $\Delta\tau = 2\pi/100$ and 10^4 time units were used.

The resulting $i - \bar{v}$ curve for the symmetric SQUID with $\beta_L = 1$ is plotted for five different ϕ_a values in Fig. 2.10a. The $i - \bar{v}$ curve for $\phi_a = 0$ can be described by $\bar{v} = \sqrt{(i/2)^2 - 1}$, which is plotted in black. The $i - \bar{v}$ curve for $\phi_a = 0$ is independent of β_L as indicated by the black curve in Fig. 2.10b. For asymmetric SQUIDs the situation is more complicated as the lowest average voltage $\bar{v}_{min}$ for a specific current is no longer simply obtained for $\phi_a = 0$, but for varying ϕ_a. However, the curve $\bar{v}_{min}(i)$ can still be described by $\bar{v}_{min}(i) = \sqrt{(i/2)^2 - 1}$ as indicated in Fig. 2.10c for the case of large inductance asymmetry $\alpha_L = 0.8$.

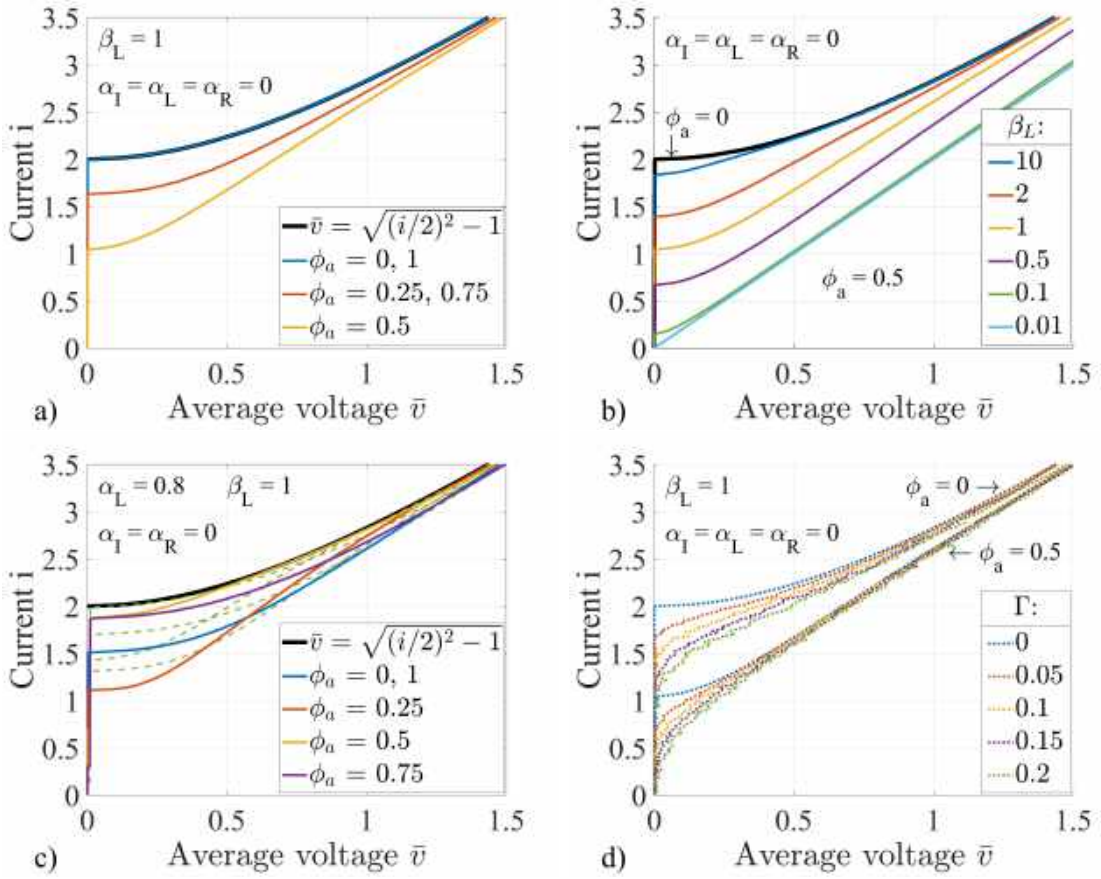

Figure 2.10: Simulated $i - \bar{v}$ characteristics for different ϕ_a values and combinations of β_L, α_L, α_I and α_R as indicated in each graph. The black curves correspond to $\bar{v} = \sqrt{(i/2)^2 - 1}$. The noise free case is shown in a) - c), while d) shows the effect of increasing noise.

The largest voltage modulation depth $\Delta v = \bar{v}_{max}(i) - \bar{v}_{min}(i)$ is obtained for $i = 2$. Same as the critical current modulation depth Δi_c, Δv decreases rapidly with increasing β_L: for low $\beta_L < 0.1$, $\Delta v \approx 1$, while for $\beta_L = 2$, $\Delta v \approx 0.5$ (see Fig. 2.10b).

For devices operating at a temperature $T \approx 77$ K, noise has an appreciable effect. Noise can be modeled using the Nyquist noise current I_N with a white voltage spectral density $S_V = 4k_BTR$, where k_B is the Boltzmann constant. This corresponds in dimensionless units to $s_V = 4\Gamma$, where $\Gamma = 2\pi k_b T/I_0\Phi_0$ is the noise parameter. As

in Ref. [123], we approximate the two random noise currents $i_{N1,2} = v_{N1,2}/(1 \mp \alpha_R)$ using trains of voltage pulses each of duration $\Delta\tau$ and random amplitude v_k. The values v_k are chosen to be Gaussian-distributed with zero mean and $\langle v_k^2 \rangle = 2\Gamma/\Delta\tau$. The integration of Eq. (2.22) is performed in the same way as in the noise free case, however, the number of time units has to be increased to 10^5 to obtain fairly smooth $i - \bar{v}$ curves.

Noise results in rounding of the $i - \bar{v}$ curve for small voltages as shown in Fig. 2.10d for the case of the symmetric SQUID with $\beta_L = 1$. The voltage modulation depth also decays with increasing Γ, and the bias current with the largest Δv is below the SQUID critical current $i_c = 2$. In order to avoid serious degradation of the modulation depth, $\Gamma < 0.2$ has been suggested [125], which corresponds to $I_0 > 17$ µA at 77 K.

Noise rounding complicates the extraction of the SQUID critical current $I_c = 2I_0$ from the measured current-voltage characteristics. Often a voltage criterion such as $I_c = max(I \text{ with } V(I) < 2 \text{ µV})$ is used, however, this leads to underestimation of I_c. We instead extract I_c by fitting the measured $V_{min}(I)$ curve with the function $V_{min}(I) = R_n\sqrt{I^2 - I_c^2}$, where $R_n = R/2$ denotes the SQUID normal resistance. This function corresponds to the black curves shown in Fig. 2.10 and is valid for fairly high currents where the effect of noise rounding is negligible. The inverse slope $\partial V/\partial I$ of any I-V curve goes asymptotically towards the SQUID normal resistance R_n. However, this happens rather slowly - the estimated $R_n^{est} = \partial V/\partial I$ for $I = 3I_c$ is still 6% higher than the actual R_n. We therefore obtain both I_c and R_n from the fit $V_{min}(I) = R_n\sqrt{I^2 - I_c^2}$. In order to get a good fit, we try to measure the I-V characteristics of our SQUIDs to at least $I = 3I_c$, but the electronics used limits the current to 250 µA. Additionally, measured I-V curves can show *excess currents*, which are defined by the current axis intercept of a linear fit to the I–V curve at large currents [126, 127]. Excess currents are not described with the RSJ model used to model SQUID behavior and we consequently replace I_c with the reduced SQUID critical current $I_c^* = I_c - I_{ex}$ when comparing measurement results with theoretical predictions.

2.4.4 Voltage modulation with flux

Voltage-flux characteristics can be obtained with exactly the same method as used for the $i - \bar{v}$ characteristics, but by sweeping the applied flux and fixing the bias current. The simulated $\bar{v} - \phi_a$ characteristics for the symmetric SQUID with $\beta_L = 1$ are shown in Fig. 2.11. The voltage is modulated with a period of Φ_0. In the noise free case (see Fig. 2.11a), the $\bar{v} - \phi_a$ curves contain sharp features for bias currents up to the SQUID critical current. These features are rounded when noise is introduced and the $\bar{v} - \phi_a$ curves appear more sinusoidal (see Fig. 2.11b). Moreover, voltage modulation already arises for lower bias currents than in the noise free case, and the maximum voltage modulation is now obtained for a bias current below the SQUID critical current.

These simulations show that the SQUID works as a sensitive flux-to-voltage transducer. The transfer function V_Φ is defined as the maximum slope of the voltage-flux curve. Extensive simulations have been made to describe V_Φ as a function of β_L

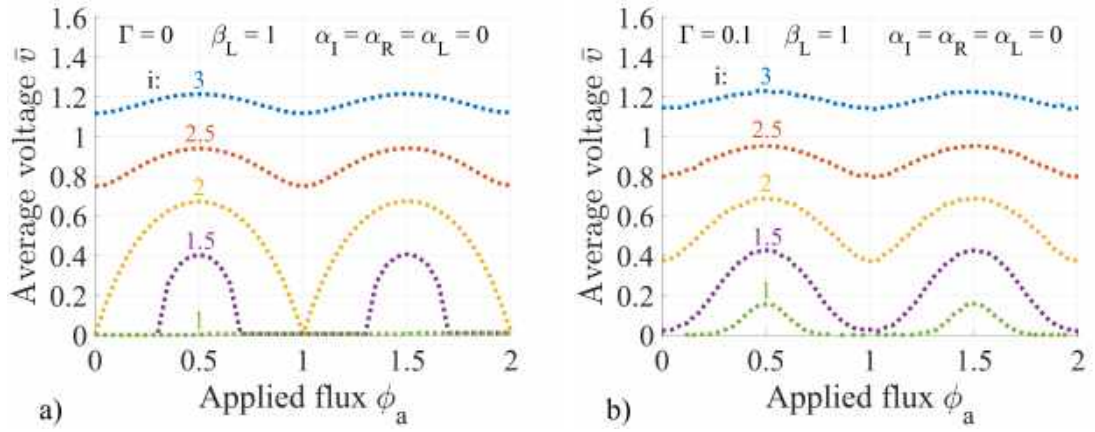

Figure 2.11: Simulated $\bar{v} - \phi_a$ characteristics as a function of bias current i for the symmetric SQUID with $\beta_L = 1$. The noise free case is shown in a), while b) shows the effect of noise ($\Gamma = 0.1$).

and Γ [64, 97, 128]. A commonly used expression is [129]:

$$V_\Phi = \frac{4}{\Phi_0} \cdot \frac{I_c R_n}{1+\beta_L} \cdot exp(-2.75\Gamma\beta_L) = \frac{4}{\Phi_0} \cdot \frac{I_c R_n}{1+\beta_L} \cdot exp\left(-3.5\pi^2 \frac{k_B T L}{\Phi_0^2}\right). \quad (2.23)$$

However, this formula does not take the effect of asymmetries into account. While an inductance asymmetry only leads to a horizontal shift of the $\bar{v} - \phi_a$ characteristics by $-\alpha_L \beta_L i/4$ [123], a current or resistance asymmetry leads to a shift and a tilt of the $\bar{v} - \phi_a$ curve and thus a higher slope on one side of the curve [130]. This is shown in Fig. 2.12. It has been found that for high-T_c SQUIDs with $\beta_L \leq 5$, V_Φ mostly decreases with increasing α_I [115].

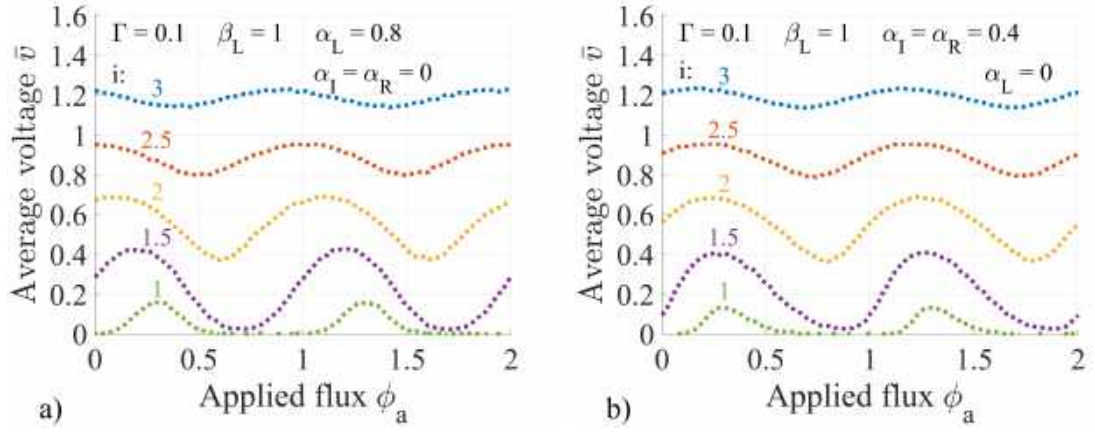

Figure 2.12: The effect of asymmetry on the simulated $\bar{v} - \phi_a$ characteristics of a SQUID with $\beta_L = 1$. a) Effect of inductance asymmetry: $\alpha_L = 0.8$. b) Effect of current and resistance asymmetry $\alpha_I = \alpha_R = 0.4$.

The transfer function is not only modified by asymmetries, but also by resonances. SQUIDs made on $SrTiO_3$ (STO) substrates are often affected by resonances [131].

This is because STO has a large relative permittivity $\epsilon_r \approx 1930$ at 77 K, which leads to a large parasitic capacitance distributed along the SQUID inductance. This results in standing waves along the SQUID slit of length l_{sl} and resonances at specific voltages given by [131]:

$$V_n^{res} = f_n \Phi_0 = (2n-1)\frac{c}{4l_{sl}}\sqrt{\frac{2}{\epsilon_r + 1}}\Phi_0, \quad n \in \mathbb{N} \tag{2.24}$$

where c is the speed of light in vacuum.

2.4.5 Noise in high-T_c SQUIDs

The noise spectrum of a SQUID is characterized by two different types of noise: frequency independent white noise and low frequency 1/f-like noise (also called *flicker* noise). The frequency where the 1/f-like noise disappears in the white noise is called the 1/f corner.

White noise

The white noise is produced by thermal Nyquist noise currents in the shunt resistors which generate a white voltage noise across the SQUID and a white current noise around the SQUID loop [64, 132]. The intrinsic high-T_c SQUID voltage noise (amplitude spectral density) can be written as [132–134]:

$$S_{V,sq}^{1/2} = \sqrt{\frac{12 k_B T}{R}\left[R_d^2 + \frac{(LV_\Phi)^2}{4}\right]}, \tag{2.25}$$

where $R_d = \partial V/\partial I$ is the dynamic resistance at the point of operation. In order to obtain a formula that only depends on the SQUID parameters I_c, $R_n = R/2$, and L, we assume that $R_d \approx \sqrt{2}R_n$ and V_Φ is given by Eq. (2.23) [134]. When performing noise measurements, the noise of the preamplifier needs to be taken into account as well. For our readout electronics this is $S_{V,el}^{1/2} = 0.4\ \mathrm{nV}/\sqrt{\mathrm{Hz}}$. The total voltage noise is then given by $S_V^{1/2} = \sqrt{S_{V,sq} + S_{V,el}}$.

The total equivalent magnetic flux noise (amplitude spectral density) is calculated from the voltage noise using the transfer function:

$$S_\Phi^{1/2} = \frac{S_V^{1/2}}{V_\Phi}. \tag{2.26}$$

Combining Eqs. (2.25) and (2.23) with the above assumptions, the dependence of the flux noise on the SQUID parameters I_c, R_n and L can be plotted. This is useful to optimize the SQUID noise performance, however, several groups have found discrepancies between the measured and theoretically predicted V_Φ or $S_\Phi^{1/2}$ values [64, 133, 135, 136]. In any case, the SQUID performance strongly depends on the SQUID inductance L because V_Φ degrades rapidly with increasing L [128, 129]. The total flux noise as a function of inductance is shown in Fig. 2.13a for different combinations of I_c and R_n. Although low flux noise levels can be achieved with a small SQUID

inductance, we will later see that inductance is important to increase the magnetic field sensitivity of a magnetometer. Extensive numerical simulations have found that the best SQUID magnetometer performance is usually obtained for $\beta_L = I_c L/\Phi_0 \approx 1$ [123]. Furthermore, higher $I_c R_n$ products lead to lower flux noise levels, and junction technologies with high $I_c R_n$ products are thus favourable.

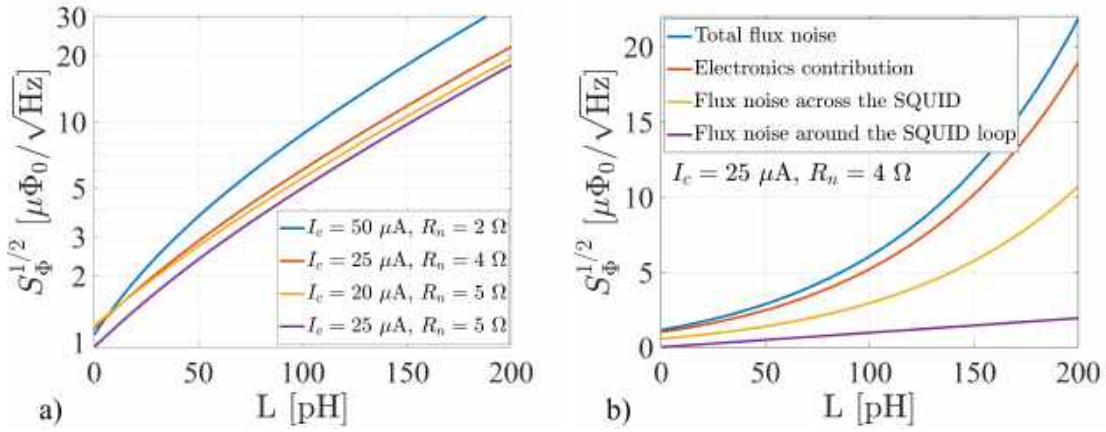

Figure 2.13: White flux noise as a function of inductance. a) Total flux noise for different combinations of I_c and R_n. b) Contributions to the flux noise for the case $I_c = 25$ μA and $R_n = 4$ Ω.

In Fig. 2.13b the different contributions to the flux noise for the case $I_c = 25$ μA and $R_n = 4$ Ω are shown separately. The dominant contribution is from the electronics, followed by the flux noise across the SQUID (described by the first term in Eq. (2.25) divided by V_Φ), while the flux noise around the SQUID loop (described by the second term in Eq. (2.25) divided by V_Φ) is negligible. This represents the typical case for our SQUIDs. At 77 K the flux noise across the SQUID is larger than the electronics noise for $R_n > 12.5$ Ω.

1/f-like noise

The second type of noise is 1/f-like noise, which refers to low frequency noise with a power spectral density that scales roughly with the inverse of the frequency. For high-T_c SQUIDs this noise generally dominates over the white noise at low frequencies, which is problematic because the low frequency range is of great interest for MEG. In high-T_c SQUIDs the two main sources of 1/f-like noise are critical current fluctuations and thermally activated motion of flux vortices [19].

Fluctuations in the critical current of the junctions are caused by electrons being trapped at defects in the tunnel barrier and their subsequent release [137]. The critical current fluctuation in the two junctions can appear in-phase or out-of-phase. The in-phase fluctuations appear as voltage noise across the SQUID and lead to a voltage offset in the $V - \Phi$ characteristics, while the out-of-phase fluctuations appear as flux noise and cause a shift in flux. Both types of critical current fluctuations can be reduced substantially using a suitable readout scheme [53].

Flux hopping between different pinning sites are the second source of 1/f-like noise. When a superconducting film is cooled below its transition temperature, flux

can be trapped as vortices in defects called pinning centers. When the thermal energy is larger than the pinning energy, the flux can hop between neighboring pinning centers, which induces a random telegraph signal. There are several ways to reduce this type of noise [138]. First, the low frequency noise decreases drastically when the crystalline quality of the film improves, hence making optimization of the YBCO film growth an essential part of the noise reduction process [139]. Second, it is possible to introduce artificial pinning centers and holes to control and limit the vortex motion [140, 141]. Third, narrow linewidth structures can prevent the trapping of vortices during cooling given that the magnetic field is below the threshold field [142]:

$$B_T = \frac{\pi \Phi_0}{4w^2}, \tag{2.27}$$

where w is the linewidth of the structure. Cooling in the Earth's magnetic field thus requires linewidths below 5.7 µm. Nonetheless, even with narrow linewidths it can be helpful to slowly cool the device in low magnetic fields. Fourth, large and fast changes in the applied field should be avoided also when the sensor is cold as the induced circulating currents can drive flux vortices into the film. A flux dam can be used to limit the circulating current [143–145]. A theoretical prediction for the threshold current I_T above which massive flux entry into a superconducting strip occurs is given by [146]:

$$I_T = 2.4621 \cdot I_c \cdot \left(\frac{2\Phi_0}{\mu_0 \cdot w \cdot I_c} \right)^{1/4}, \tag{2.28}$$

where w is the width of the strip and I_c its critical current.

2.4.6 DC SQUID readout

We have seen that a SQUID acts as a sensitive flux-to-voltage transducer when biased at a working point with a large slope $\partial V/\partial \Phi$. Small changes in flux lead to a linear voltage output signal. For larger changes ($\Phi_a \geq \Phi_0/\pi$), however, the output becomes strongly distorted because the $V - \Phi$ curve is periodic and not linear. To linearize the output signal and increase the dynamic range, the SQUID is operated in a flux-locked loop (FLL), where a negative feedback flux is applied to the SQUID to keep it at its working point [53]. The circuit diagram for a FLL with direct readout is shown in Fig. 2.14. A small change in flux Φ_a creates a change in voltage across the SQUID. This voltage change is amplified, integrated and fed back as a current through a feedback coil which induces a flux into the SQUID. The feedback flux $\Phi_f = -\Phi_a$ compensates the flux change and the SQUID is brought back to its working point.

The output of the integrator V_{out} is proportional to Φ_a and can thus be used as the output signal of the FLL. The proportionally constant $V_\Phi^{FLL} = |V_{out}/\Phi_a|$ is known as the FLL transfer function and can easily be derived. The feedback resistor R_f turns the output V_{out} into a feedback current $I_f = V_{out}/R_f$. The feedback coil with mutual inductance M_f to the SQUID converts the feedback current into a flux $\Phi_f = M_f \cdot I_f = -\Phi_a$. The FLL transfer function is thus:

$$V_\Phi^{FLL} = \frac{R_f}{M_f}. \tag{2.29}$$

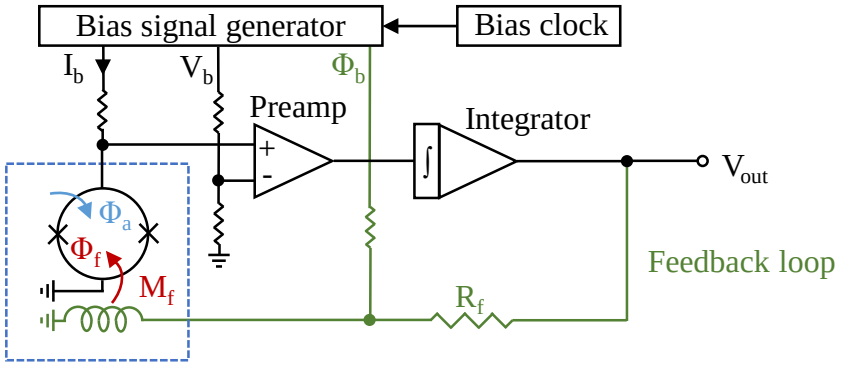

Figure 2.14: Circuit diagram for direct SQUID readout with bias reversal and flux-locked loop. Components inside the blue box are at cryogenic temperatures. Green components are used to convert the output voltage V_{out} into the feedback flux Φ_f. Adapted from Ref. [53].

The total flux noise of a SQUID can easily be determined by measuring the total voltage noise in FLL mode $S_{V,FLL}^{1/2}$ and dividing by the FLL transfer function:

$$S_\Phi^{1/2} = \frac{S_{V,FLL}^{1/2}}{V_\Phi^{FLL}}. \tag{2.30}$$

This is more stable than measuring the noise in open loop configuration where a change in flux moves the SQUID away from its working point thus changing $\partial V/\partial\Phi$. The flux noise is nonetheless strongly dependent on the transfer function V_Φ because $S_{V,FLL}^{1/2} = S_V^{1/2} \cdot V_\Phi^{FLL}/V_\Phi$.

Additionally to the operation in a flux-locked loop, high-T_c SQUIDs are typically operated using a technique called *ac bias reversal* to reduce 1/f-like noise from critical current fluctuations. The polarity of the bias current I_b is switched periodically at a frequency well above the corner frequency of the 1/f-like noise obtained with dc bias. Both in-phase and out-of-phase fluctations can be treated with ac bias reversal [53].

For the readout of our SQUIDs we use a commercially available direct readout SQUID electronics *SEL-1* from Magnicon GmbH, Hamburg, Germany. The electronics allows for operation in a FLL with ac bias reversal.

2.5 High-T_c SQUID magnetometers

SQUIDs are very sensitive flux detectors, however, the magnetic field sensitivity of bare SQUIDs is rather limited. The effective area A_{eff} describes a magnetometer's ability to convert a change in magnetic field δB into a change in flux $\delta\Phi$: $A_{eff} = \delta\Phi/\delta B$. The effective area of a magnetometer is measured using a calibrated Helmholtz coil to generate a well-defined magnetic field. In order to get a reliable result, we vary the amplitude of the applied field δB and measure the output flux Φ_{out} in FLL mode. The effective area is then obtained with a linear fit: $\Phi_{out}(\delta B) = A_{eff} \cdot \delta B$.

Once A_{eff} is known, the equivalent magnetic field noise (amplitude spectral density) of the magnetometer can be calculated:

$$\sqrt{S_B} = \frac{\sqrt{S_\Phi}}{A_{eff}}. \tag{2.31}$$

The effective area of a SQUID can be increased by increasing the SQUID loop dimensions, but this also results in a higher SQUID inductance, which leads to more flux noise. More effective methods to increase the effective area and produce sensitive magnetometers are thus required.

2.5.1 Magnetometers with a directly coupled pickup loop

A commonly used approach for high-T_c SQUIDs is to couple a pickup loop directly to the SQUID [147–149]. The equivalent circuit for this method is shown in Fig. 2.15a. A change in the magnetic field δB leads to a change of the flux in the pickup loop: $\delta\Phi_p = A_p \cdot \delta B$, where A_p is the effective area of the pickup loop. This flux change induces a circulating current $I_p = \delta\Phi_p / L_p$ in the pickup loop with inductance L_p. Because of the galvanic coupling to the SQUID loop, the current flowing in the coupling inductance L_c creates a flux in the SQUID loop: $\delta\Phi_s^c = L_c \cdot I_p$. The change in magnetic field also directly changes the flux in the SQUID: $\delta\Phi_s = A_s \cdot \delta B$, where A_s is the bare SQUID effective area. This flux is much smaller than the flux coupled into the SQUID via the pickup loop, and of opposite sign. The effective area of a directly coupled magnetometer is thus:

$$A_{eff} = \frac{-\delta\Phi_s + \delta\Phi_s^c}{\delta B} = -A_s + \frac{L_c}{L_p} \cdot A_p \approx \frac{L_c}{L_p} \cdot A_p. \tag{2.32}$$

The last approximation is valid in the typical case where the effective area of the SQUID is negligible. The magnetometer effective area scales proportionally with the outer dimension D of the pickup loop because $A_p \propto D^2$ and $L_p \propto D$ [19]. The magnetometer effective area can thus be increased by increasing the size of the pickup loop. This type of magnetometer is simple to make as it only requires a single layer of superconducting film. However, it suffers from a large inductance mismatch L_c/L_p.

Nonetheless, impressive magnetic field noise levels have been reached with such directly-coupled high-T_c SQUID magnetometers at 77 K. As early as in 1995, Lee *et al.* reported a bicrystal SQUID magnetometer with a directly coupled pickup loop (D = 9.3 mm) reaching a white noise level of 35 fT$\sqrt{\text{Hz}}$ and a low frequency noise level of 65 fT/$\sqrt{\text{Hz}}$ at 1 Hz [150]. Ludwig *et al.* presented a magnetometer of the same type (D = 9 mm) with a white noise level of 24 fT$\sqrt{\text{Hz}}$ and a 1/f corner frequency of 4 Hz [151]. With a larger pickup loop (D = 19 mm), Cantor *et al.* achieved a white noise of 10 fT/$\sqrt{\text{Hz}}$ at 10 kHz increasing to 26 fT/$\sqrt{\text{Hz}}$ at 1 Hz [152]. Using step-edge junctions instead of bicrystal grain boundary junctions, Glyantsev *et al.* achieved 20 fT/$\sqrt{\text{Hz}}$ at 1 kHz (and large 1/f-like noise at lower frequencies) with a rather small (D = 8 mm) directly coupled pickup loop thanks to a large junction resistance of 10 Ω [153].

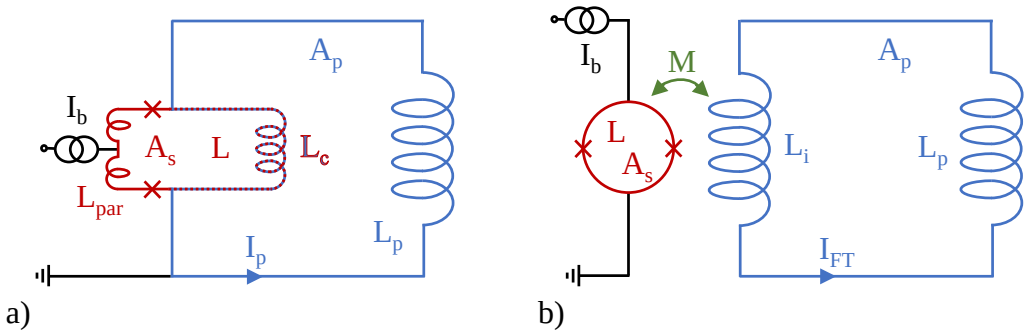

Figure 2.15: Equivalent circuit of a SQUID magnetometer with a) a directly coupled pickup loop and b) an inductively coupled flux transformer. The SQUID loop is colored red and Josephson junctions are marked with crosses.

2.5.2 Magnetometers with an inductively coupled flux transformer

Larger effective areas can be achieved by inductively coupling a flux transformer to the SQUID loop [154, 155] as shown in Fig. 2.15b. The flux transformer consists of a large-area pickup loop and a small multi-turn input coil that is placed above the SQUID. A change in magnetic field again leads to a change in flux in the pickup looop of the flux transformer: $\delta\Phi_{FT} = \delta B \cdot A_p = I_{FT} \cdot (L_i + L_p)$, where A_p and L_p is the pickup loop effective area and inductance, respectively, and L_i is the input coil inductance. The current I_{FT} induced in the flux transformer couples to the SQUID through the mutual inductance M between the input coil and the SQUID loop: $\delta\Phi_s^c = M \cdot I_{FT}$. The mutual inductance is given by $M = k\sqrt{LL_i}$, where k is the coupling coefficient and L is the SQUID inductance. Taking again also the direct flux change $\delta\Phi_s$ in the SQUID into account, the total magnetometer effective area can be written as:

$$A_{eff} = \frac{\pm\delta\Phi_s + \delta\Phi_s^c}{\delta B} = \pm A_s + \frac{M}{L_i + L_p} \cdot A_p \approx \frac{k\sqrt{LL_i}}{L_i + L_p} \cdot A_p. \tag{2.33}$$

Whether the SQUID effective area increases or decreases the magnetometer effective area depends on the winding sense of the input coil. Assuming that the coupling coefficient k does not depend on L_i, the largest A_{eff} is achieved for $L_i = L_p = L_{FT}$:

$$A_{eff} \approx \frac{k}{2}\sqrt{\frac{L}{L_{FT}}} \cdot A_p. \tag{2.34}$$

The inductively coupled flux transformer magnetometer effective area thus scales as $D^{1.5}$, where D is again the outer dimension of the pickup loop.

Flux transformers are standard for low-T_c SQUIDs, and both thin-film and wire-wound flux transformers are being used [19]. In contrast, high-T_c flux transformers are much less common and they are always thin-film devices (again, because YBCO is a ceramic). To fabricate the multi-turn input coil, two superconducting layers separated by an insulating layer are required. Fabrication of multilayer high-T_c

superconducting structures with low 1/f-like noise is difficult and has only been achieved by a few groups [99]. The SQUID and the flux transformer can either be made on the same chip (integrated device) or on different chips that are pressed together (flip-chip device). Flip-chip devices have the advantage that the yield of good magnetometers is higher as one can pick a good SQUID and a good flux transformer. However, the two chips need to be aligned and the distance between them is larger than in the integrated case. Integrated devices often suffer from resonances caused by a parasitic capacitance between the input coil and the SQUID washer [64].

Several groups have achieved excellent noise levels with high-T_c SQUID magnetometers with an inductively coupled flux transformer at 77 K. Danstsker *et al.* fabricated a flip-chip magnetometer with a white noise level of 8.5 fT/$\sqrt{\text{Hz}}$ and 27 fT/$\sqrt{\text{Hz}}$ at 1 Hz using bicrystal grain boundary junctions and a 9 mm × 9 mm pickup loop for the flux transformer [142]. With an integrated device, Drung *et al.* achieved 9.7 fT$\sqrt{\text{Hz}}$ at 1 kHz and 53 fT$\sqrt{\text{Hz}}$ at 1 Hz for a 8.3 mm × 8.6 mm pickup loop [32]. The lowest noise level at 77 K was reached by Faley *et al.* with a flip chip flux transformer with a 16 mm × 16 mm pickup loop: 3.5 fT$\sqrt{\text{Hz}}$ above 10 Hz and 7 fT$\sqrt{\text{Hz}}$ at 1 Hz [156]. This noise level is comparable to that of low-T_c SQUID magnetometers.

2.6 Inductance of thin superconducting films

Inductance is a key parameter when optimizing the performance of a SQUID magnetometer. Inductance is also essential for the operation of the kinetic inductance magnetometer. In thin superconducting films, two types of inductances have to be taken into account. First, there is the geometric inductance L^{Geo}, which is associated with the energy stored in the magnetic field $\boldsymbol{B} = \boldsymbol{\nabla} \times \boldsymbol{A}$ generated by the current $\boldsymbol{I}$ with current density $\boldsymbol{J}$ in the superconductor [157]:

$$E_{Geo} = \frac{1}{2} L^{Geo} \boldsymbol{I}^2 = \frac{1}{2} \iiint_V (\boldsymbol{J} \cdot \boldsymbol{A}) dV. \tag{2.35}$$

The geometric inductance depends on the shape of the inductor and approximate formulas for some common designs used in this thesis are given in Appendix B.

Second, there is the kinetic inductance L^{Kin}, which is associated with the kinetic energy of the charge carriers (the Cooper pairs):

$$E_{Kin} = \frac{1}{2} L^{Kin} \boldsymbol{I}^2 = \iiint_V (\frac{1}{2} n_s m^* \boldsymbol{v_s}^2) dV = \frac{1}{2} \mu_0 \lambda^2 \iiint_V \boldsymbol{J}^2 dV, \tag{2.36}$$

where the last equality is obtained using $\boldsymbol{J} = n_s e^* \boldsymbol{v_s}$ and the definition of the London penetration depth λ as was done for Eq. (2.6). For a thin superconducting strip with thickness $t < \lambda$, width w, and length l, the current density is uniform ($\boldsymbol{J} = \boldsymbol{I}/wt$) and the kinetic inductance of the strip is given by:

$$L^{Kin}_{strip} = \mu_0 \frac{l}{wt} \lambda^2. \tag{2.37}$$

The kinetic inductance can dominate over the geometric inductance in thin superconducting structures with a linewidth comparable to λ.

In contrast to L^{Geo}, L^{Kin} is temperature dependent because of the temperature dependence of the London penetration depth, which in the case of YBCO has been found to obey [158, 159]:

$$\lambda(T) = \frac{\lambda_0}{\sqrt{1-(T/T_c)^2}}, \tag{2.38}$$

where T is the operation temperature, T_c the critical temperature of the film, and λ_0 is the London penetration depth at 0 K. Measured values for λ_0 in c-axis orientated YBCO films are around 180 - 250 nm, and strongly depend on film quality [158, 160–162].

The kinetic inductance furthermore depends on the superconducting current I_s in a nonlinear way [163, 164]:

$$L^{Kin}(I_s) = L^{Kin}(0)\left(1+\frac{I_s^2}{I^{*2}}\right), \tag{2.39}$$

where I^* is the characteristic nonlinearity parameter whose scale is of the order of the film's critical current. The kinetic inductance nonlinearity is negligible for SQUIDs as I_s is much smaller than the critical current. KIMs, on the other hand, are based on this nonlinearity.

2.6.1 Inductance simulation

While empirical inductance formulas are useful for inductance estimations and for understanding the scaling behaviour, we rely on numerical simulations of the inductances in our devices. The method used was developed by Khapaev, who implemented it in the software package 3D-MLSI [165]. We instead use the COMSOL Multiphysics software (COMSOL Inc., Stockholm, Sweden) as the finite element method (FEM) solver because it allows us to directly import CAD designs, which makes the simulation of complicated structures such as flux transformer input coils easier. As many results in this thesis were obtained using the inductance simulation, it will be explained in more detail now; the full derivation of the formulas can be found in Refs. [157, 165, 166].

The main idea is to first calculate the current density $\boldsymbol{J}$ by numerically solving the London equation $\mu_0\lambda^2\boldsymbol{\nabla}\times\boldsymbol{J}=\boldsymbol{B}$ (compare with Eq. (2.1b)) and the Maxwell equation $\boldsymbol{\nabla}\times\boldsymbol{B}=\mu_0\boldsymbol{J}$. Next, the geometric and the kinetic energy are calculated using Eqs. (2.35) and (2.36). Lastly, the inductance values are extracted from the calculated energies. The boundary conditions for the current define if the self-inductance of a hole or the mutual inductance between two holes is calculated. The whole procedure needs to be repeated for each selection of boundary conditions.

The calculation of the current density and the energies can be simplified because the circuits of interest can be approximated by several 2D layers. Assume we have N_l superconducting layers separated by dielectric layers as shown in Fig. 2.16a. Let the m^{th} superconducting layer occupy a surface domain S_m in the xy-plane, have a thickness t_m, a London penetration depth λ_m and be positioned at a height h_m, thus

occupying a space domain $V_m = S_m \times [h_m - t_m/2, h_m + t_m/2]$. Each superconducting layer can be treated as two dimensional if $t_m \ll l$ and $t_m \leq \lambda_m$, where l is the typical lateral size of the circuit in plane, and the thickness of the dielectric layers is also much smaller than l. In this case the current density $\boldsymbol{J_m}$ of the m^{th} layer can be replaced by the sheet current density $j_m = t_m \cdot J_m$. The sheet current density can be described by a stream function $u_m(\boldsymbol{r})$, which is defined as:

$$j_{m,x} = \frac{\partial u_m(\boldsymbol{r})}{\partial y} \quad \text{and} \quad j_{m,y} = -\frac{\partial u_m(\boldsymbol{r})}{\partial x}. \tag{2.40}$$

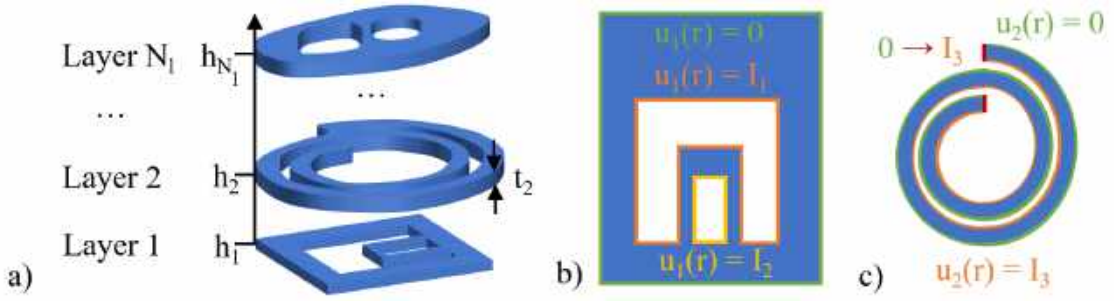

Figure 2.16: a) Sketch of the N_l superconducting layers. b) Boundary conditions for holes. c) Boundary conditions for a terminal. The red lines indicates a linear change from 0 on the green side to I_3 on the orange side.

With the N_l stream functions, solving the London and Maxwell equations mentioned above reduces to solving the following N_l differential equations [165]:

$$\frac{\lambda_m^2}{t_m} \boldsymbol{\nabla}^2 u_m(\boldsymbol{r_0}) = \frac{1}{4\pi} \sum_{n=1}^{N_l} \iint_{S_n} (\boldsymbol{\nabla} u_n(\boldsymbol{r}) \cdot \boldsymbol{\nabla} G_{mn}(\boldsymbol{r}, \boldsymbol{r_0})) \cdot d\boldsymbol{r}, \tag{2.41}$$

in which the kernels G_{mn} have the form:

$$G_{mn}(\boldsymbol{r}, \boldsymbol{r_0}) = \begin{cases} 1/\sqrt{|\boldsymbol{r} - \boldsymbol{r_0}|^2 + (h_m - h_n)^2}, & n \neq m. \\ \frac{1}{2}\left(\frac{1}{|\boldsymbol{r}-\boldsymbol{r_0}|} + \frac{1}{\sqrt{|\boldsymbol{r}-\boldsymbol{r_0}|^2 + t_m^2}}\right), & n = m. \end{cases} \tag{2.42}$$

The boundary conditions for the stream functions are provided by the N_h circulating currents I_k around the holes and the current distribution defined by the excited currents through the N_t input and output terminals. On the boundary of hole k in the m^{th} layer, $u_m(\boldsymbol{r}) = I_k$ as shown in Fig. 2.16b. This type of boundary condition is used for the SQUID loop and the pickup loop. For the flux transformer input coil we use an input and output terminal instead. The boundary conditions are set as shown in Fig. 2.16c. The stream function is zero on one side of the conductor and equal to the current passing through it on the other side. At the input and output terminal the stream function changes linearly. Reversing the two sides of the conductor switches the direction of the current. On all other boundaries (e.g. the outer edge of the superconducting layer) the stream function is zero.

Once the stream function is known, the geometric and kinetic energies associated with the current distribution can be calculated. Using the stream function, the geometric energy from Eq. (2.35) can be written as:

$$E_{Geo} = \frac{\mu_0}{8\pi} \sum_{n=1}^{N_l} \sum_{m=1}^{N_l} \iint_{S_n} d\boldsymbol{r_n} \iint_{S_m} (\boldsymbol{\nabla} u_n(\boldsymbol{r_n}) \cdot \boldsymbol{\nabla} u_m(\boldsymbol{r_m}))\, G_{mn}(\boldsymbol{r_m}, \boldsymbol{r_n}) d\boldsymbol{r_m} \quad (2.43)$$

and the the kinetic energy from Eq. (2.36) as:

$$E_{Kin} = \frac{\mu_0}{2} \sum_{m=1}^{N_l} \iint_{S_m} \frac{\lambda_m^2}{t_m} (\boldsymbol{\nabla} u_m(\boldsymbol{r_m}))^2 d\boldsymbol{r_m}. \quad (2.44)$$

As the boundary problem is linear, the full energy is a positive quadratic form with respect to the current vector $\boldsymbol{I} = (I_1, ..., I_N)^T$, where $N = N_h + N_t$. Hence there exists an $N \times N$ inductance matrix $\boldsymbol{L}$ fulfilling:

$$E = E_{Kin} + E_{Geo} = \frac{1}{2} \langle \boldsymbol{L}\boldsymbol{I}, \boldsymbol{I} \rangle. \quad (2.45)$$

The diagonal elements L_{ii} correspond to the self-inductance associated with the current I_i and can be calculated by setting all other currents to zero when solving the differential Eqs. (2.41) and calculating the energy E, hence $L_{ii} = 2E/I_i^2$. The off-diagonal elements L_{ij} correspond to the mutual inductance between the structures associated with I_i and I_j and can be calculated by setting all currents to zero except I_i and I_j when solving the boundary problem and calculating E. The mutual inductance is given by $L_{ij} = (2E - L_{ii}I_i^2 - L_{jj}I_j^2)/2I_iI_j$. Since the kinetic and geometric energies can be calculated separately, the kinetic and geometric inductance contributions can be extracted individually.

Lastly, this simulation tool can not only be used to extract inductances and to visualize current distributions, but one can also numerically calculate the effective area. To get the effective area A_{eff}^i of the i^{th} hole in layer n, the magnetic moment M_m is calculated [167]:

$$M_m = \frac{1}{2} \iint_V (\boldsymbol{r} \times \boldsymbol{J}) d\boldsymbol{r} = \frac{1}{2} \iint_{S_n} (x \cdot j_{n,y} - y \cdot j_{n,x})\, dxdy = I_i \cdot A_{eff}^i. \quad (2.46)$$

Again all currents except I_i are set to zero.

2.6.2 Inductance measurement

Parts of the SQUID inductance can be easily measured by directly injecting a current I_{inj} into the SQUID loop as shown in Fig. 2.17. In this configuration, flux is coupled into the SQUID via the injected current instead of an externally applied flux. For a constant bias current I_b, the SQUID voltage V is modulated by I_{inj} with a periodicity $\Delta I_{inj} = \Phi_0/(L_3 + L_4)$ [123]. The inductance $L_3 + L_4$ can thus be extracted by finding the current needed to couple one flux quantum into the SQUID.

The very same configuration is also used for a magnetometer with a directly coupled pickup loop. The circulating current in the pickup loop is in that case the injected current and the voltage modulation periodicity is Φ_0/L_c, where L_c is the coupling inductance between the SQUID and pickup loop.

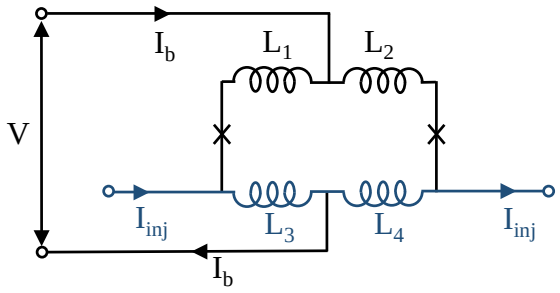

Figure 2.17: Equivalent circuit for direct injection of a current I_{inj} into the SQUID loop as used in inductance measurements and with a directly coupled pickup loop.

2.7 Kinetic inductance magnetometers

The kinetic inductance magnetometer (KIM) is a superconducting magnetometer that does not require Josephson junctions, but instead relies on the current nonlinearity of the kinetic inductance as described by Eq. (2.39). The first KIM was demonstrated in 2014 using NbN as the superconductor [60], and similar smaller devices based on TiN [168] and NbTiN [169] followed. These three disordered low-T_c superconductors are used due to their high kinetic inductance and resilience to large background magnetic fields [169]. Independent of the material used, the operation principle and readout is the same.

2.7.1 Operation principle

Same as SQUIDs, KIMs take advantage of flux quantization. Consider a thin superconducting loop with an area A and an inductance L that is composed of the kinetic inductance L_k and the geometric inductance L_g (i.e. $L = L_k + L_g$). When a magnetic field is applied, a screening current I_s is created in the loop to satisfy the flux quantization condition

$$(L_k + L_g)I_s = B_0 A + m\Phi_0, \tag{2.47}$$

where B_0 is the average orthogonal field ($B_0 = \Phi_a/A$, where Φ_a is the flux threading the loop) and m an integer. The screening current modifies L_k due to the current nonlinearity of the kinetic inductance, $L_k = L_{k0}(1+(I_s/I^*)^2)$, where $L_{k0} = L_k(I_s = 0)$. The change in inductance is measured with the help of an LC resonance circuit. For this purpose, an interdigital capacitor C is placed in parallel with the loop, and the resulting resonator is coupled to a transmission line with a coupling capacitor C_C as depicted in Fig. 2.18a.

The total inductance of the resonator is $L_{tot} = (L_k + L_g)/4 + L_{par}$, where L_{par} is the parasitic inductance of the central line. The resonator's resonance frequency f_r is determined by

$$f_r = \frac{\omega_r}{2\pi} = \frac{1}{2\pi\sqrt{L_{tot}(C + C_c)}}. \tag{2.48}$$

As the magnetic field and consequently I_s increases, the resonance shifts to lower frequencies because of the increase in L_k. However, the screening current can not be

increased indefinitely; at some point I_s either exceeds the critical current I_c of the thin loop and the KIM resets, or I_s exceeds the threshold current I_T for flux entry into the loop (Eq. (2.28)) and flux is trapped instead.

2.7.2 Transmission measurement

The resonance is characterized by transmission measurements with the equivalent circuit shown in Fig. 2.18b. The transmission parameter S_{21} is given by

$$S_{21} = \frac{2V}{V_{in}} = \frac{2Z}{2Z + Z_0}, \tag{2.49}$$

where V is the output voltage for a certain input voltage V_{in}, $Z_0 = 50\ \Omega$ is the characteristic readout impedance, and Z is the impedance of the resonator. For frequencies f near the resonance, the latter is determined by [170]

$$Z = \frac{Z_0 Q_e}{2Q_i}\left(1 + 2iQ_i\frac{f - f_r}{f_r}\right). \tag{2.50}$$

Here, Q_i is the internal quality factor describing the superconductor losses with the help of the resistance R_i (which depends on material, design, temperature, and magnetic field), and Q_e is the external quality factor describing the coupling to the transmission line. The total quality factor of the loaded resonator $Q_t = (Q_i^{-1} + Q_e^{-1})^{-1}$ determines the resonance width $\Delta f = f_r/Q_t$ (full width at half maximum (FWHM)), which also defines the bandwidth $\Delta f/2$ of the resonator [163, 168].

An illustration of a typical S_{21} measurement can be found in Fig. 2.18c. Fitting the measured S_{21} as a function of frequency allows extraction of the resonance frequency and all three quality factors. To fit the S_{21} curves we use the following equation that takes both inductive and capacitive coupling, as well as an impedance

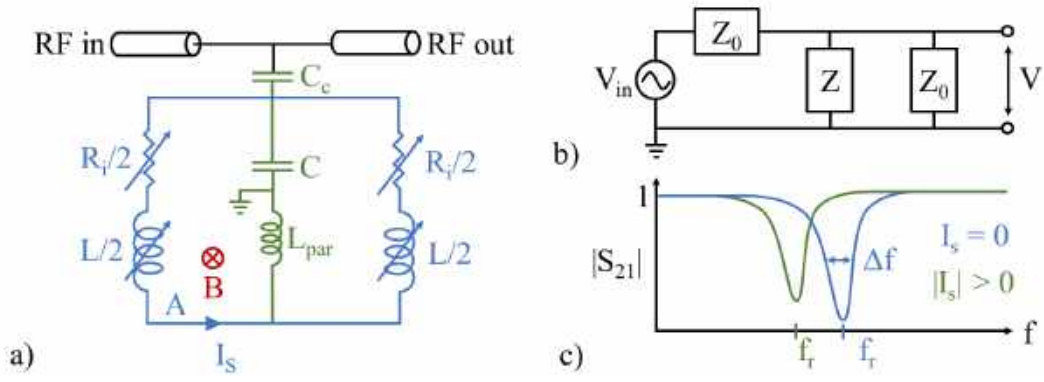

Figure 2.18: a) Equivalent circuit of a KIM (blue and green) coupled to a transmission line (black). The superconducting loop is colored blue. b) Equivalent circuit for the measurement of the transmission parameter S_{21}. c) Illustration of a typical $|S_{21}|$ measurement as a function of frequency for zero screening current (blue). Increasing $|I_s|$ shifts the resonance to lower frequencies. The width Δf of the resonance defines the bandwidth of the KIM.

mismatch in the feedline into account [171, 172]:

$$S_{21} = a_1 \left(1 + a_2 \frac{f - f_r}{f_r}\right) \left(1 - \frac{\frac{Q_t}{|Q_c|} e^{i\theta}}{1 + 2iQ_t \frac{f - f_r}{f_r}}\right) e^{i(\phi_f f + \phi_0)}. \tag{2.51}$$

Here, a_1 is the transmission amplitude away from resonance, a_2 allows us to account for a potential linear variation in the transmission close to the resonance, and ϕ_f and ϕ_0 account for the propagation delay to and from the sample. The complex-valued quality factor $Q_c = |Q_c|e^{-i\theta}$ is related to Q_e via $1/Q_e = Re[1/Q_c]$.

2.7.3 Responsivity

An important value characterizing the magnetometer's performance is its responsivity $\partial V/\partial B_0$ to a change in magnetic field. At the resonance, the responsivity can be approximated as [60]:

$$\left|\frac{\partial V}{\partial B_0}\right|_{f=f_r} = \left|\frac{\partial V}{\partial L_k}\frac{\partial L_k}{\partial I_S}\frac{\partial I_S}{\partial \Phi_a}\frac{\partial \Phi_a}{\partial B_0}\right|_{f=f_r} = \frac{V_{in}Q_t^2}{4Q_e L_{tot}} \frac{I_S}{I^{*2}\left(1 + 3\left(\frac{I_S}{I^*}\right)^2 + \frac{L_g}{L_{k0}}\right)} A. \tag{2.52}$$

Different parameters can be tuned in order to reach a high responsivity. First, a decent kinetic inductance fraction $\alpha_k = L_{k0}/(L_{k0} + L_g)$ is essential and can be achieved with film thicknesses and linewidths smaller than λ, and by using materials with a large λ. The term $3(I_s/I^*)^2$ is maximal for $I_s = I_c$, where $3(I_c/I^*)^2 \approx 0.5$ [163], meaning that for $1/\alpha_k \gg 3(I_s/I^*)^2$ – which is the case except for large α_k – the responsivity is roughly proportional to α_k. Thinner films and narrower linewidths also lead to lower I^*, and thus increases the responsivity.

Second, the responsivity is first-order magnetic field-insensitive at $I_s = 0$ and grows with increasing I_s. A dc magnetic field bias can be used to operate the magnetometer at a point with high responsivity.

Third, increasing V_{in} leads to a higher responsivity, however, the excitation voltage also generates an rf current in the loop with an amplitude I_{rf}. When the current $I_{rf}/2 + I_s$ in one of the loop arms reaches I_c or I_T, the responsivity can no longer be increased. Furthermore, the kinetic inductance nonlinearity gives rise to Duffing oscillator behavior: increasing the readout power distorts the resonance until it eventually bifurcates [173]. Additionally, both V_{in} and V are limited by the readout electronics.

Forth, a high Q_i indicating low internal dissipation is desired. The resistive part of the superconductor rf surface impedance R_i grows with increasing operation temperature T and I_s, and depends on film quality [60, 174, 175]. Dielectric losses due to the substrate may also play a role [174].

Fifth, a larger loop area leads to a larger responsivity, but also a larger inductance, although the ratio A/L_{tot} improves with loop size – same as in the case of SQUID pickup loops. Besides fabrication limits, the upper bound on the KIM loop size is given by the requirement that the magnetometer must appear as a lumped element at the resonance frequency and thus needs to have smaller dimensions than the carrier wavelength λ_c [176]:

$$\sqrt{A} \ll \lambda_c = \frac{c}{f_r \sqrt{(1 + \epsilon_r)/2}}. \tag{2.53}$$

Since f_r is not fixed, this can also be seen as a condition limiting the resonance frequency. The latter can be adjusted with the capacitance $C + C_c$, but is also limited by the readout electronics.

To compare different magnetometers, it can be an advantage to study the normalized responsivity

$$\left| \frac{1}{V} \frac{\partial V}{\partial B_0} \right|_{f=f_r} \approx \frac{Q_i^2 I_s \alpha_k A}{2(Q_i + Q_e) L_{tot} I^{*2}}, \tag{2.54}$$

which is obtained using $V(f_r) = V_{in} Q_t / (2Q_i)$ based on Eqs. (2.49) and (2.50), and assumes $1/\alpha_k \gg 3(I_s/I^*)^2$.

2.7.4 KIM readout

The readout of the KIM is shown schematically in Fig. 2.19. The resonator is excited using an rf carrier with a frequency corresponding to the resonance frequency $f_r(I_s)$, where I_s has been set to correspond to an operation point with high responsivity. The resonator encodes the applied magnetic field signal into the rf domain, where the signal appears as sidebands to the carrier signal. The resulting transmitted signal is amplified and demodulated down to dc with an IQ mixer. Both the in-phase (I) and quadrature (Q) components of the signal are further amplified and filtered, and finally the data is acquired using analog-to-digital converters. For the demodulation, a branch of the rf carrier input signal is used as the local oscillator. Optionally, a second branch of the rf carrier can be used to cancel the carrier signal before the first amplifier. This allows one to increase V_{in} without saturating the readout electronics, however, both the amplitude and phase of the cancellation signal need to be adjusted to interferometrically cancel the carrier signal after it has travelled through the resonator.

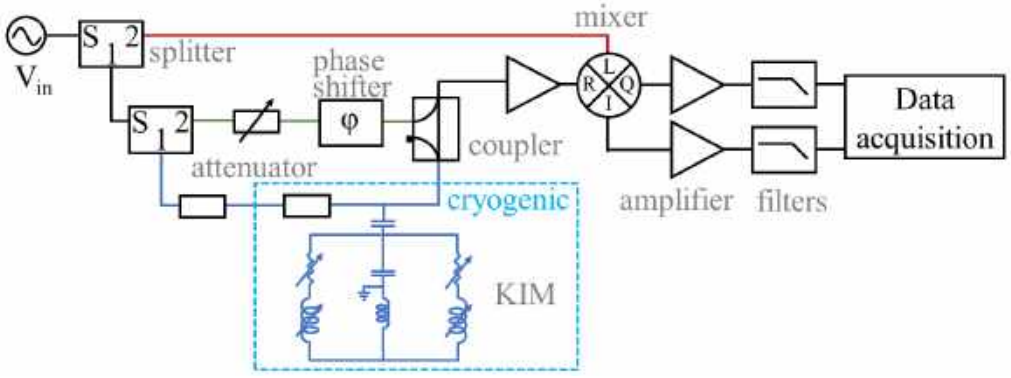

Figure 2.19: KIM readout scheme designed by Visa Vesterinen. The branch of the carrier signal going to the KIM is shown in blue, the branch for the local oscillator in red, and the branch for carrier cancellation in green.

This setup can also be used to measure S_{21}, $|\partial V/\partial B_0|$ if a magnetic ac probe tone is supplied, and the noise spectrum if a fast Fourier transform (FFT) is performed on a time trace of the complex output voltage.

The carrier signal travels nearly unperturbed off-resonance where $|S_{21}| \approx 1$. Several resonators with different resonance frequencies can thus be coupled to the same transmission line allowing for frequency multiplexed readout [163, 176]. Such a readout has been demonstrated for thousands of microwave kinetic inductance detectors (MKIDs)[177], which are very similar to KIMs.

2.7.5 KIM noise

The magnetic field sensitivity of the KIM is constrained by several noise sources. As for SQUIDs, thermal noise leads to a white noise spectrum, which in the case of the KIM can be estimated as [60]:

$$S_B^{1/2} = \sqrt{8k_bTZ_0Q_e(2Q_i + Q_e)}\frac{L_{tot}I^{*2}}{Q_tQ_iI_sV_{in}A}\left[\frac{1}{\alpha_k} + 3\left(\frac{I_s}{I^*}\right)^2\right]. \tag{2.55}$$

This formula is obtained using $S_B^{1/2} = S_V^{1/2}/(\sqrt{2}|\partial V/\partial B_0|)$, where $S_V^{1/2}$ is the voltage noise of the resonator coupled to the amplifier, and the factor $1/\sqrt{2}$ comes from the assumption that the noise power is evenly distributed into the two quadratures. Other sources of noise include generation-recombination noise from quasiparticle dynamics, electromagnetic interference, and noise added by the readout electronics [60, 176]. The KIM is only sensitive to external rf interference with frequencies around the resonance frequency. The frequencies of these peaks in the demodulated spectra depend on the carrier frequency used, which allows identification of the peaks.

3

Fabrication of high-temperature superconducting devices

This chapter describes how our high-T_c SQUID magnetometers and KIMs are fabricated. First, suitable substrates for the epitaxial growth of YBCO films are discussed. Then the growth of high-quality YBCO films and their characterization is described. We continue with how the devices are patterned and show examples of fabricated structures. The chapter ends with a description of the fabrication of multi-layer structures for flux transformer input coils.

3.1 Epitaxial growth and suitable substrates

High-quality c-axis orientated YBCO films are often a key component for achieving low-noise YBCO devices. Such films can be fabricated by epitaxial growth on a suitable substrate. To minimize defects, one usually chooses substrates that have lattice parameters very close to those of YBCO, as well as comparable thermal expansion coefficients, which is why $SrTiO_3$ (STO) and $LaAlO_3$ (LAO) are frequently selected [19, 64]. Other common substrates are Al_2O_3 (sapphire), yttria-stabilized zirconia (YSZ), $NdGaO_3$ and MgO [19].

For our SQUIDs we use STO, which has a cubic perovskite structure below 110 K with a lattice parameter a = 3.905 Å, and thus a very small tensile lattice mismatch with YBCO (a = 3.82 Å and b = 3.89 Å) [178]. It is furthermore possible to buy bicrystal substrates made from STO. In this project we use bicrystals with a misorientation angle of 22.6° from Shinkosha, Japan [178].

Single crystal STO substrates are used for flip-chip flux transformers because STO can also be used as the insulating layer between the two superconducting YBCO films. Both the first and the second YBCO film can thus be grown on the same type of crystal, which simplifies the growth of low-noise multilayers.

As mentioned in §2.4.4, STO has a large relative permittivity at low temperatures: $\epsilon_r \approx 1930$ at 77 K [131], which leads to resonances in the SQUID. The large relative permittivity and loss tangent ($tan(\delta) = 2.5 \cdot 10^{-4}$ at 77 K [179]) make STO unsuitable for high-frequency applications. For the fabrication of KIMs we therefore use r-cut

sapphire or MgO (110) instead, which both have low relative permittivity (sapphire: $\epsilon_r = 9.3$ and $\epsilon_{rz} = 11.3$ anisotropic, MgO: $\epsilon_r = 9.6$) and low dielectric loss tangents ($< 4 \cdot 10^{-6}$) [179]. Achieving high-quality films on MgO (110) is more complicated than on STO because of the larger lattice mismatch. For good YBCO films on sapphire, a YSZ and CeO_2 buffer layer is needed, which complicates the fabrication process. Except for the very first KIM fabricated in the beginning of my PhD, all KIMs were fabricated on MgO (110) substrates because the YBCO deposition was continuously optimized for this type of substrate by other members in our group making YBCO nanowires.

3.2 YBCO thin films

Several methods exist to grow YBCO films: pulsed laser deposition (PLD), rf or dc sputtering, thermal or electron beam evaporation, and metalorganic chemical vapor deposition (CVD) [180]. We deposit YBCO films with PLD, which has the advantages that the film stoichiometry (composition) is close to that of the YBCO target, the contamination level is low, and the deposition rate is high.

3.2.1 Growth of YBCO films with pulsed laser deposition

Growing high-quality films with PLD is an art – I have spent around one third of my PhD growing and optimizing our YBCO films. This is because there are many deposition parameters that can be optimized, the film growth depends on the substrate and the buffer layer used, and the results varied over time thus making reoptimization necessary.

Pictures and a schematic of our PLD system is shown in Fig. 3.1. The PLD chamber is part of a cluster deposition system from DCA, Finland, that also includes a metal sputter chamber and an oxide sputter chamber. The three chambers are connected through a vacuum buffer line thus enabling *in-situ* deposition of several layers of metals and oxides.

The PLD film deposition principle is the following. First, the clean substrate is placed upside down into the hole of a wafer carrier, where it is held only at its four corners. This allows the substrate to be heated from above via radiation heating, and the film to be deposited from below. We have carriers for 5 mm × 5 mm and 10 mm × 10 mm substrates. Eventual buffer layers are deposited first, which will be described later. Then the carrier is loaded via the vacuum buffer line onto the manipulator in the PLD chamber. The chamber is backfilled with oxygen to the deposition pressure p_{dep} and the substrate is heated to the deposition temperature T_{dep}.

Once T_{dep} is reached, the distance d_{dep} between the substrate and target is set, and the target rotation and sweeping is started. The deposition itself is done using a pulsed KrF excimer laser beam with a wavelength of 248 nm and a pulse duration of 20 ns. For the pulse frequency we first used 10 Hz, but we found that the YBCO film surface improves when reducing the pulse frequency to 5 Hz, which was subsequently used. The laser beam is regulated by an aperture and focused with a lens onto the target. The energy E_{dep} of the laser after the aperture is the last deposition

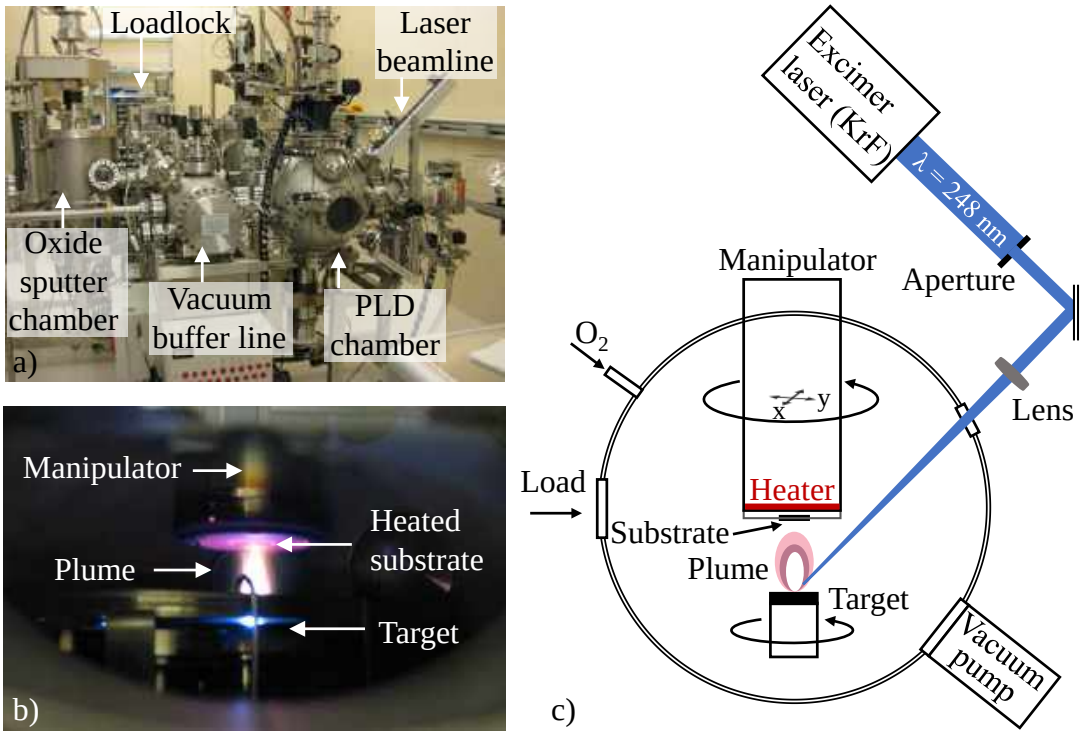

Figure 3.1: Pulsed laser deposition (PLD) system. a) Photograph of the cluster deposition system including the PLD chamber. b) Photograph showing the inside of the chamber during the deposition. c) Schematic of the PLD system.

parameter that was varied. It defines the energy density for the 4 mm^2 laser spot on the target. The target material is ablated by the pulsed laser beam, forms a plasma plume and condenses on the heated substrate placed above the target. To improve the uniformity of the film deposition, the manipulator is rotated during the deposition. In the case of a 10 mm × 10 mm substrate, we furthermore use a meander sweep to cover also the edges of the substrate. The sweep parameters need to be adjusted such that the manipulator does not hit the laser beam, which can be a problem for small d_{dep}. In order to avoid ablating from a single spot on the target, we also rotate and sweep the target. The number of pulses defines the film thickness: 2000 pulses corresponds to roughly 150 nm.

After the deposition, the film is slowly (5-10 °C/min) cooled down to room temperature. The oxygen diffusion at higher temperatures determines the doping level of the YBCO film. In the first half of my PhD, we filled the chamber with 640 Torr oxygen and post annealed the film at a temperature of 550 °C for one hour. We later found that better films can be obtained using the deposition pressure instead, and cooling down without waiting one hour. In this case the whole procedure including heating, deposition and cool down takes 3 hours.

The YBCO film quality depends on the substrate type used and the deposition parameters T_{dep}, p_{dep}, d_{dep}, and E_{dep}. Optimization of the YBCO film growth was done by depositing and characterizing test films on single crystal substrates until a good film was obtained. For each film, one deposition parameter was changed

Table 3.1: Latest optimized YBCO PLD deposition parameters used for different device types. BC stands for bicrystal and FT for flux transformer.

Device	SQUID	SQUID	FT	KIM	KIM
Substrate	STO BC	STO BC	STO	Al_2O_3 (r-cut)	MgO (110)
Buffer layer	-	CeO_2	-	YSZ & CeO_2	-
T_{dep} [°C]	750	805	805	790	740
p_{dep} [mBar]	1.6	1.2	1.2	0.6	1.0
d_{dep} [mm]	52.5	58	58	60	54
E_{dep} [mJ]	63	58	58	53	58

based on the characterization results. Generally, higher critical temperatures were obtained for higher T_{dep} and p_{dep}, but increasing these values often led to worse surface morphology. Adjusting p_{dep} changes the shape of the plume and thus requires readjustment of d_{dep} and E_{dep}. The 10 mm × 10 mm substrates typically required higher T_{dep} than the smaller ones. Furthermore, the heat absorption properties of single crystals and bicrystals seem to be different, meaning that in some cases T_{dep} had to be corrected when we switched from test films to the bicrystals. In the beginning of my PhD we furthermore tried to improve the uniformity of the heat absorption by first depositing an amorphous YBCO layer on the backside of the substrate, which meant an additional deposition. As we did not notice any change, and films improved mainly thanks to increasing p_{dep}, the amorphous YBCO layer was skipped. The optimized deposition parameters for the latest deposited films are summarized in Table 3.1 for different device types.

3.2.2 YBCO film characterization

The quality of the YBCO films was assessed using optical microscopy, atomic force microscopy (AFM), superconducting critical temperature (T_c) measurements, and in rare cases x-ray diffraction (XRD). Optical microscopy images of YBCO films with different types of surfaces are shown in Fig. 3.2. Good surfaces show only a few particulates, which are microscopic particles that were ejected by the target and are commonly observed for PLD [180]. The particulate density is lower for the first few depositions after repolishing the target, however, we choose to repolish the target only if really necessary to avoid having to reoptimize the YBCO film growth. Bad surfaces have lots of dots and outgrowths, which are often a-axis orientated grains forming above the c-axis orientated YBCO [180].

The surface can be studied in more detail using AFM. Good surfaces as in Fig. 3.3a&b have an average roughness $Ra \approx 2$ nm and show characteristic c-axis spiral-like islands, while dots and a-axis grains along with a rougher surface ($Ra \approx 5$ nm in Fig. 3.3c indicate bad surface morphology.

As long as the film surfaces were good, critical temperature measurements determined which deposition parameters were best. The critical temperature was established from either susceptibility or resistance measurements as a function of temperature. The susceptibility measurement setup consists of two coils between which the sample can be placed. During the cooldown, the mutual inductance of the

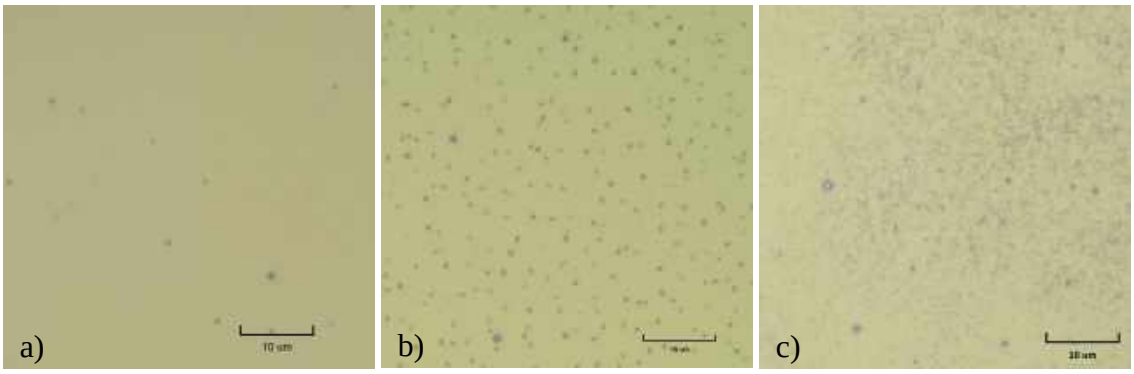

Figure 3.2: Optical microscopy images of YBCO films made on STO substrates. a) Good surface with a few particulates. b) Bad surface with lots of dots. c) Very bad surface with lots of outgrowths.

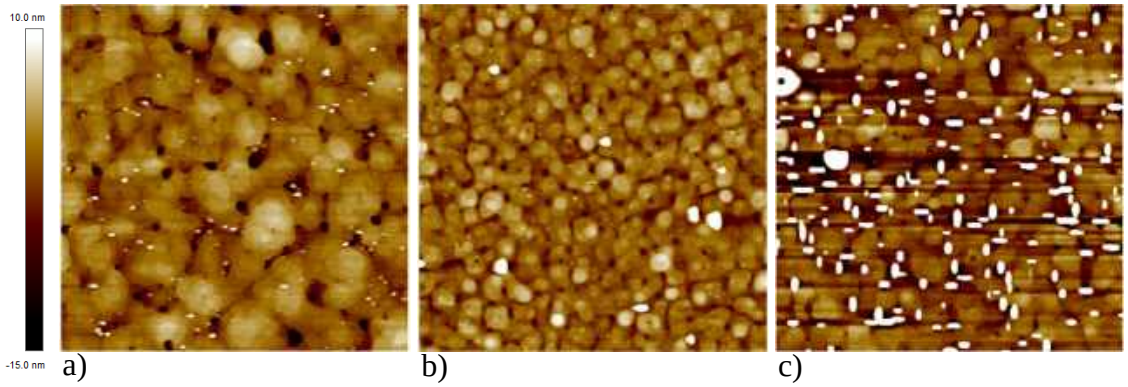

Figure 3.3: AFM images of YBCO films made on STO substrates. a) Good surface with c-axis spiral-like islands. b) Good surface with smaller islands. c) Bad surface with a-axis grains. Each image spans an area of 5 µm × 5 µm and the color scale for all images is shown to the left.

coils is monitored by applying a sinusoidal signal to one of the coils and measuring the induced signal in the other coil. Screening currents in the superconductor alter the mutual inductance at the transition temperature and below. Susceptibility measurements provide information about the quality of the whole film and a narrow transition at a high temperature is desired. Fig. 3.4 shows susceptibility measurements for films made with different deposition pressures during one optimization round.

Resistance measurements, on the other hand, provide information on the quality of the best current path through the film. In contrast to susceptibility measurements, resistance measurements can also be used for patterned devices and they indicate whether the structure goes fully superconducting or if there is a residual resistance. Resistance measurements as a function of temperature were made with a 4-point measurement in a physical property measurement system (PPMS) or later in a dipstick, which is quicker and gives the same results, but had to be set up first. Example resistance measurements from recent films with very high T_c are shown in Fig. 3.4. The figure shows that even for the same deposition parameters, the critical

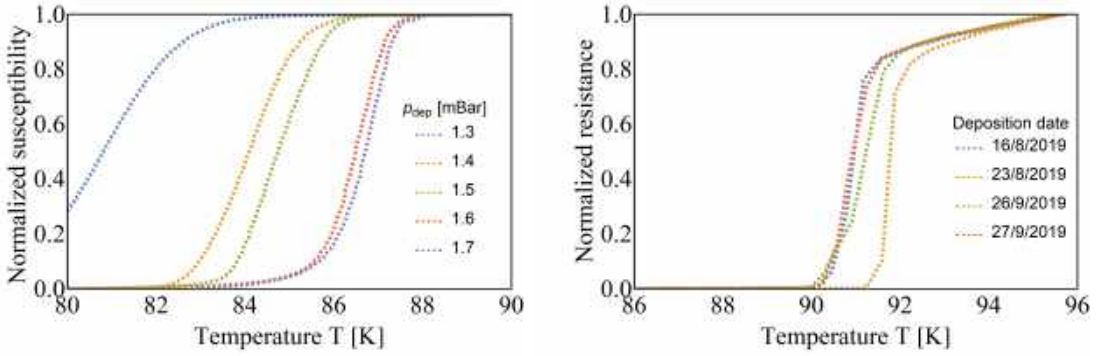

Figure 3.4: Critical temperature measurements. a) Susceptibility measurements for test films deposited at different oxygen pressures p_{dep} and with constant $T_{dep} = 750$ °C, $d_{dep} = 52.5$ mm, and $E_{dep} = 63$ mJ. The critical temperature increases with increasing p_{dep}, but the surface starts to deteriorate above $p_{dep} = 1.6$ mBar. b) Resistance measurements for YBCO films made on different days on single crystal STO substrates with the deposition parameters in Table 3.1.

temperatures can vary over time. In one PLD parameter optimization round, one should do either susceptibility or resistance measurements as the two can not be compared to each other.

In the beginning of my PhD we had problems obtaining YBCO films with high T_c. Two new high-density YBCO targets were bought and installed, but this did not change the situation much. We then figured out that we had to substantially increase p_{dep} (from 0.6 mBar to 1.6 mBar in the late 2016 to early 2017 optimization round). This was partly found thanks to XRD measurements. From XRD measurements, the c-axis parameter can be calculated, which is related to the oxygen content per unit cell [181]. During the last two years we have had stable deposition parameters and very good YBCO films on STO with T_c above 90 K as shown in Fig. 3.4b.

3.2.3 Deposition of buffer and insulating layers

One or several buffer layers can be used to improve the epitaxial growth of YBCO on substrates with large lattice mismatch or to prevent chemical reactions between YBCO and some substrates like sapphire [182]. For the KIM made on sapphire, a YSZ and a CeO_2 buffer layer was used. In the case of bicrystal substrates, buffer layers can furthermore help improve the junction properties. The use of a CeO_2 buffer layer on bicrystal substrates used to be common in our group, but was omitted by the time I started my PhD. During my PhD we then found that the junction properties could be significantly improved with the help of a CeO_2 buffer layer and all bicrystal grain boundary junctions thereafter were made using such a CeO_2 buffer layer.

YSZ and a CeO_2 buffer layers are deposited in the oxide sputtering chamber of our cluster deposition system. The same system is also used to sputter the STO insulating layer for multilayer flux transformers. The deposition parameters for all three materials are given in Table 3.2.

Table 3.2: Oxide sputtering deposition parameters.

Material	YSZ	CeO_2	STO
Deposition temperature T_{dep} [°C]	780	750	650
Deposition pressure p_{dep} [mBar]	0.02	0.1	0.1
Ar flow [sccm]	1	100	75
O_2 flow [sccm]	9	25	25
Distance to target d_{dep} [mm]	28	30	28
Presputtering time t_{pre} [min]	10	10	5
Deposition time t_{dep} [min]	30	20	40

3.2.4 In-situ gold

To achieve a low contact resistance between YBCO and the metal used for contact pads, the metal layer should be deposited in-situ or after only a brief exposure to air [183]. We use gold deposited in-situ in the metal chamber of the DCA cluster system for this purpose. The gold layer is sputtered at room temperature at a pressure of 5 µbar and a power of 40 W for 30 s after 30 s of presputtering. The whole procedure takes less than 5 min. The gold layer furthermore protects the YBCO film from oxygen outdiffusion and chemical reactions during patterning, but it needs to be removed after fabrication of the contact pads because the gold shunts the Josephson junctions in the case of SQUIDs or can affect the high frequency properties in the case of KIMs. For devices with very thin films, removing the gold can be problematic, which is why the gold in these cases was either kept or no in-situ gold was deposited at all, as will be discussed later.

3.3 Device patterning

The general patterning procedure for single layer SQUID magnetometers and KIMs is illustrated in Fig. 3.5. The YBCO film including eventual in-situ gold is patterned with photolithography using a laser writer and argon ion milling.

First, the photoresist is spun onto the sample and baked on a hotplate. The design is transferred to the photoresist by directly exposing the latter with a laser writer DWL 2000 from Heidelberg instruments, Germany. The photoresist is then developed and baked on a hotplate. The structures that should be kept are covered by photoresist (negative design). The pattern is transferred from the photoresist mask to the YBCO film through argon ion milling with an Oxford Ionfab 300 Plus ion beam etching system from Oxford instruments, United Kingdom. For the etching, the beam voltage is set to 300 V and the beam current to 15 mA, which leads to a current density of 0.1 mA/cm^2 for the 15 cm diameter circular beam. The etching is performed at an angle of 30° to the substrate normal and the sample is rotated at 3 rpm to avoid the buildup of redeposited material. Secondary ion mass spectroscopy (SIMS) is used for endpoint detection, i.e. the process is stopped when we detect a drop in the Y and Ba signal and a rise in the Sr, Mg or Ce signal depending on the substrate or buffer layer used. In the case of STO, overetching can be

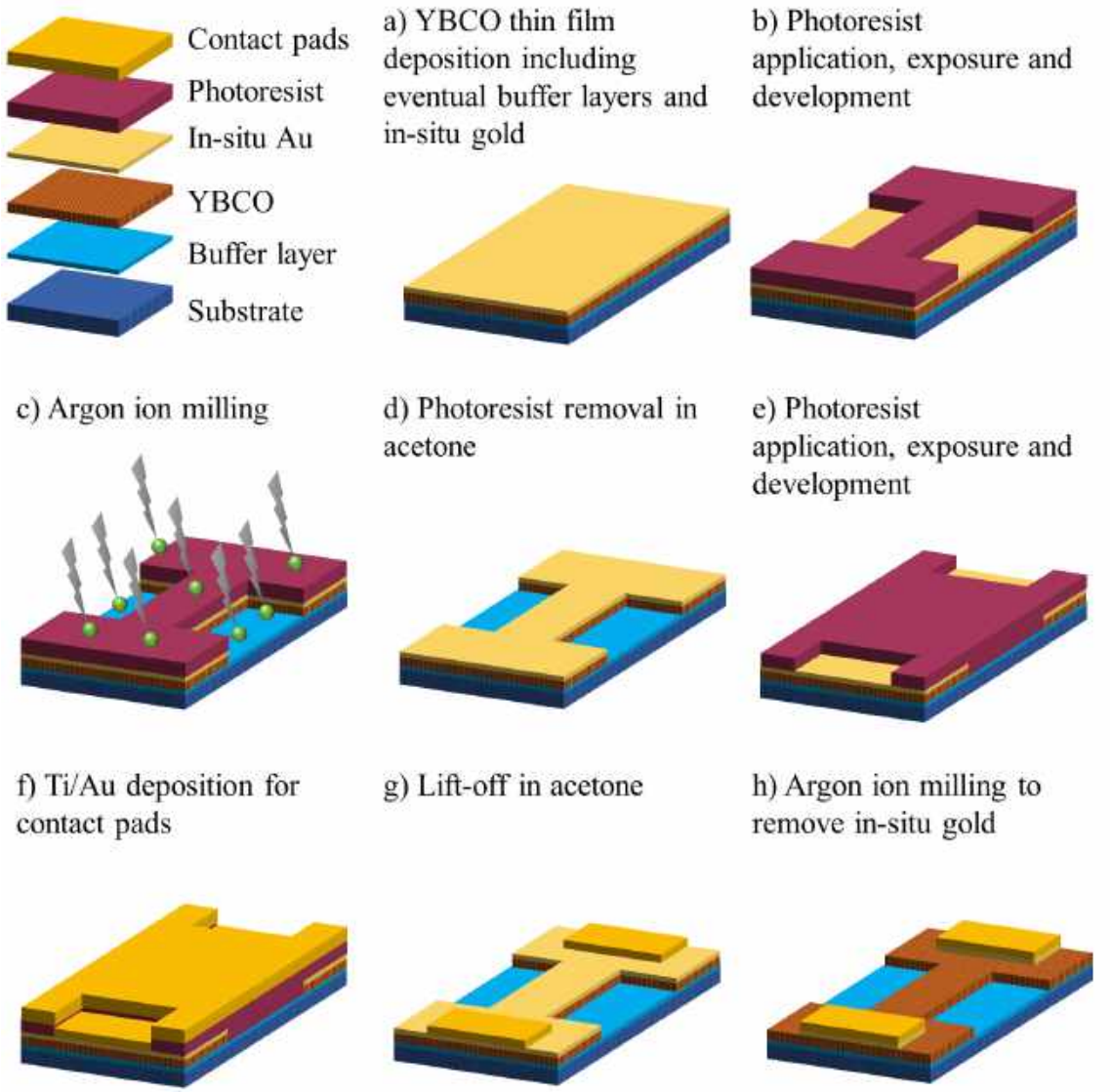

Figure 3.5: Step-by-step illustration of the fabrication process using a photoresist mask.

problematic because STO becomes semiconducting, which shunts dc measurements. The photoresist mask is removed in acetone.

After patterning the device, gold contact pads are made with a lift-off process. A new photoresist mask is applied, exposed and developed in the same manner as before. This time holes are opened in the photoresist where contact pads should be made (positive design). We first deposit a 15 nm thin Ti layer to improve adhesion and then deposit a 100 nm thick gold layer. Both depositions are done without breaking vacuum using an MS150 sputterer from FHR, Germany. The lift-off is then performed in acetone, which removes the photoresist and the metals on top of it. In case of an in-situ gold layer, the sample is etched for 4 min using argon ion milling with the same parameters as above to remove the in-situ gold.

3.3.1 Alignment to the grain boundary

In the case of bicrystal grain boundary junctions, the device design needs to be aligned to the grain boundary. The grain boundary of the first 10 bicrystals from Shinkosha was very smooth and hardly visible with optical microscopy. We therefore etched 100 nm deep alignment marks with argon ion milling into the bare substrates as shown in Fig. 3.6a. Three alignment marks were used: one in the center, one on the left and one on the right side (both 400 µm from the edge where photolithography was still possible). The coordinates of the grain boundary were then found with AFM (see Fig. 3.6b) and used for the laser writer alignment. The grain boundary crossed the patterned microbridges in all cases, see for an example Fig. 3.6c.

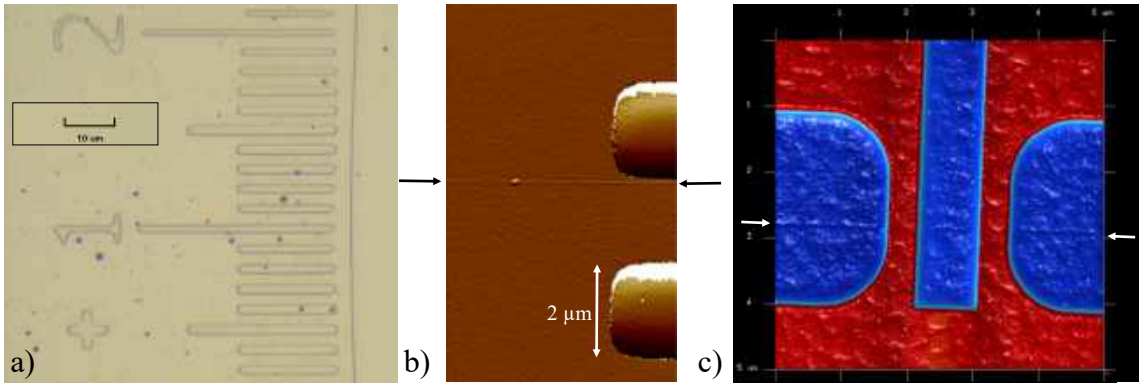

Figure 3.6: Alignment to the grain boundary. The grain boundary is marked with arrows. a) Micrograph of part of the alignment marks etched into the substrate. The grain boundary at + 1.3 is not visible with optical microscopy. b) AFM image of the grain boundary close to the alignment marks. c) AFM image of a SQUID with the grain boundary crossing the 0.5 µm wide YBCO film at two places to form Josephson junctions. The substrate is colored blue, the YBCO red, and the grain boundary marked with white arrows.

The transparency of the bare substrates made optical focusing of the laser writer on the surface difficult. However, it was unclear if the grain boundary would be detectable once a film was grown, and the idea was that the alignment marks could be reused even after repolishing the substrates. It turned out that the alignment marks were also removed by polishing, but it was possible to find the grain boundary with AFM using alignment marks etched into the YBCO down to the substrate, hence this was done for repolished substrates instead.

The grain boundary of the 20 bicrystal substrates from the second batch was very clearly visible with optical microscopy and the alignment marks were instead made using only photoresist and no etching. The same photoresist as used for the magnetometer design is used for the alignment marks, which makes the process very short and simple. First, the alignment marks are exposed with the laser writer and developed. Then, the coordinates of the grain boundary with respect to the alignment marks are determined and used to expose the design directly after. The only limitation is that the position of the alignment marks needs to be chosen in such a way that the alignment marks do not interfere with the device design as they are made in the same photoresist and are thus part of the final pattern.

3.3.2 Narrow linewidth structures

The very high critical current densities of the bicrystal junctions made microbridges with a width around, or even below, 1 µm necessary. To fabricate such narrow structures, a carbon (C) mask instead of a photoresist mask was used. This allows fabrication of clearly defined structures as shown in Fig. 3.7. Using the laser writer and a carbon mask, it was possible to achieve good structures with widths down to 0.7 µm as shown in Fig. 3.7a. However, the linewidth is generally larger than in the design (design value 0.3 µm in this case) and variations can be expected. With e-beam lithography, the width from the design corresponds to the top width of the microbridge, and reproducible results are obtained (see for example the 0.5 µm wide bridges in Fig. 3.6c). A carbon mask and e-beam lithography is also used by my colleagues to fabricate the nanowire-based SQUIDs characterized in this thesis. These junctions have widths down to ∼50 nm.

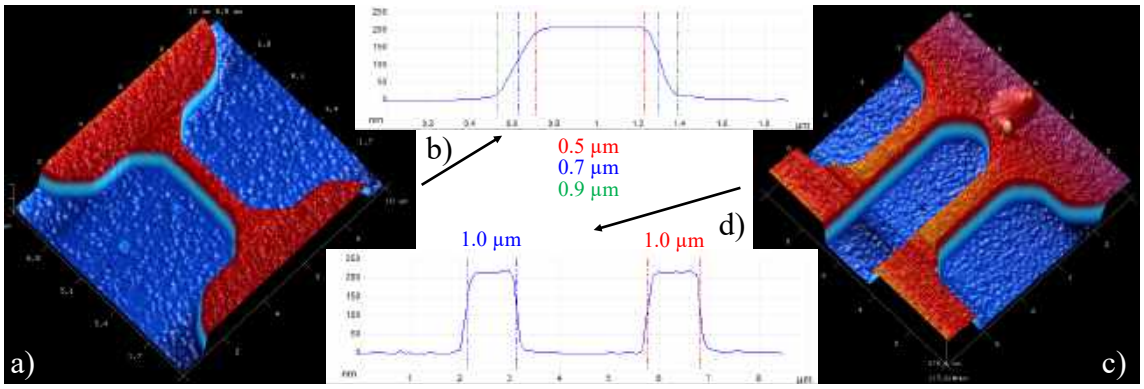

Figure 3.7: AFM images of microbridges pattered with a carbon mask and using a laser writer. a) 3D image of the narrowest microbridge achieved with the laser writer. b) Height profile across the center of the microbridge in a), which is narrowest at the top and widest at the bottom. The width at half the height is used to define the junction width. c) 3D image of the junctions of a SQUID. d) Height profile across the center of the two junctions in c). They both have a width of 1.0 µm.

The device patterning process with a carbon mask is shown in Fig. 3.8. The preparation of the carbon mask takes several more steps than the preparation of the photoresist mask (steps b1 to b5 for the carbon mask compared to step b for the photoresist mask). First, a carbon layer with a thickness of around 100 nm is deposited with PLD in a dedicated chamber. Second, the resist (photoresist or e-beam resist) is applied, exposed and developed. The opposite pattern as in the case of a photoresist etching mask is used. Third, a 12 nm thick chromium (Cr) layer is evaporated with an e-beam evaporator from Kurt J. Lesker Company, United States. Forth, the resist and Cr is lifted-off. Fifth, the pattern is transferred from the Cr mask to the carbon by 25 min of oxygen plasma etching in a reactive ion etcher from Plasma-Therm, United States. We use a power of 50 W, a pressure of 100 mTorr, and an oxygen flow of 10 sccm. The patterned carbon mask is then used for argon ion milling as before. The Cr layer is removed during argon ion milling, while the carbon mask remaining after ion milling is removed with another round of oxygen plasma etching.

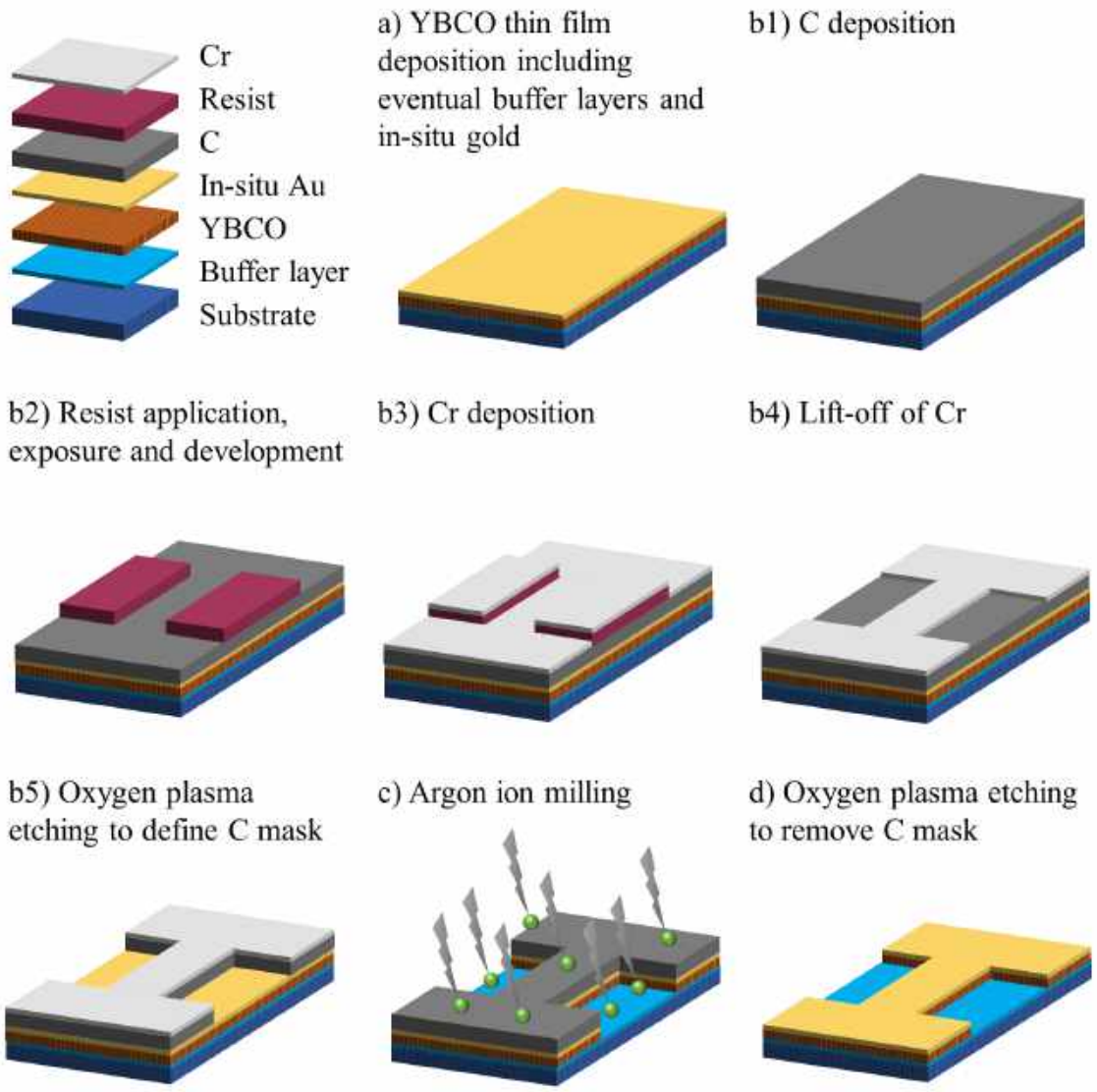

Figure 3.8: Step-by-step illustration of the device patterning process using a carbon mask.

Using a carbon mask turned out to be advantageous also for the fabrication of KIMs. One reason is that during the laser writer exposure, only the narrow lines belonging to the KIM design had to be exposed, which leads to less focusing errors than exposing everything except these few lines. In the case where no in-situ gold is used, the carbon may cause less chemical reactions with the YBCO than the photoresist.

3.4 Multilayer structures

The fabrication of superconducting multi-turn input coils requires at least two superconducting layers separated by an insulating layer. We use YBCO-STO-YBCO as discussed earlier. At two points, the two superconducting layers need to be

connected through windows in the insulator called *vias*. Furthermore, the top YBCO needs to be grown over the patterned bottom YBCO at so-called *crossovers*. An illustration of both structures is given in Fig. 3.9. Fabrication of these two high-T_c superconducting structures is complicated because both the bottom and top YBCO film should be c-axis orientated, and the supercurrent should flow along the a-b plane and not along the c-axis direction where the critical current density is substantially reduced. Additionally, steep slopes need to be avoided to prevent the formation of grain boundaries, which also reduce the critical current density. The bottom YBCO film and the insulating layer thus need to have very shallow slopes. Furthermore, the presence of outgrowths and particulates on the surface of the bottom YBCO film can lead to shorts between the two superconducting layers.

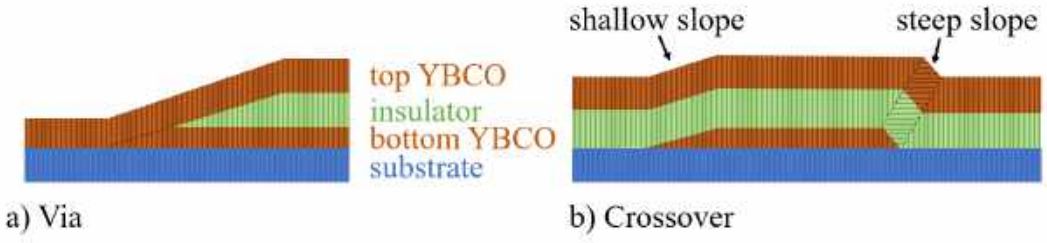

Figure 3.9: Illustration of high-T_c superconducting multilayer structures: a) via and b) crossover. In order to prevent the formation of grain boundaries, steep slopes need to be avoided.

The process for making high-T_c superconducting multilayer structures presented here was developed by my colleague Maxim Chukharkin [184]. It is based on chemical-mechanical polishing (CMP), which allows fabrication of both very shallow slopes and removal of particles potentially causing shorts [185]. Other methods to make shallow slopes include ion milling at low incidence angles – normally in combination with post exposure baking of the photoresist mask to get shallow resist edges – and chemical etching using a solution containing bromine (Br) [186–188]. While we also make use of ion milling with post exposure baking to pattern the YBCO before polishing, we do not use Br solutions because Br is highly toxic and forbidden in most university environments, including ours [184].

An illustration of the step-by-step process used to fabricate vias and crossovers in YBCO-STO-YBCO multilayers is shown in Fig. 3.10. First, a 225 nm thick YBCO film is grown on the STO substrate and a photoresist mask is prepared as before. After development, the photoresist is post exposure baked on a hotplate at 140 °C for 5 min to achieve edges with a slope around 24° [184]. Argon ion milling is then performed with the same parameters as before, except for the etching angle, which is now 45°. AFM confirmed that this results in slopes with an angle of 24° as described in Ref. [184].

The second step is CMP: the substrate is glued with heated wax to a 4 inch glass wafer carrier with several satellite substrates to ensure uniform pressure during the polishing. We use a CMP polishing and lapping tool PM5 from Logitech, Switzerland, and the Logitech SF1 polishing suspension, which is an alkaline colloidal silica. The suspension is continuously dripped onto the rotating table of the polishing tool. The

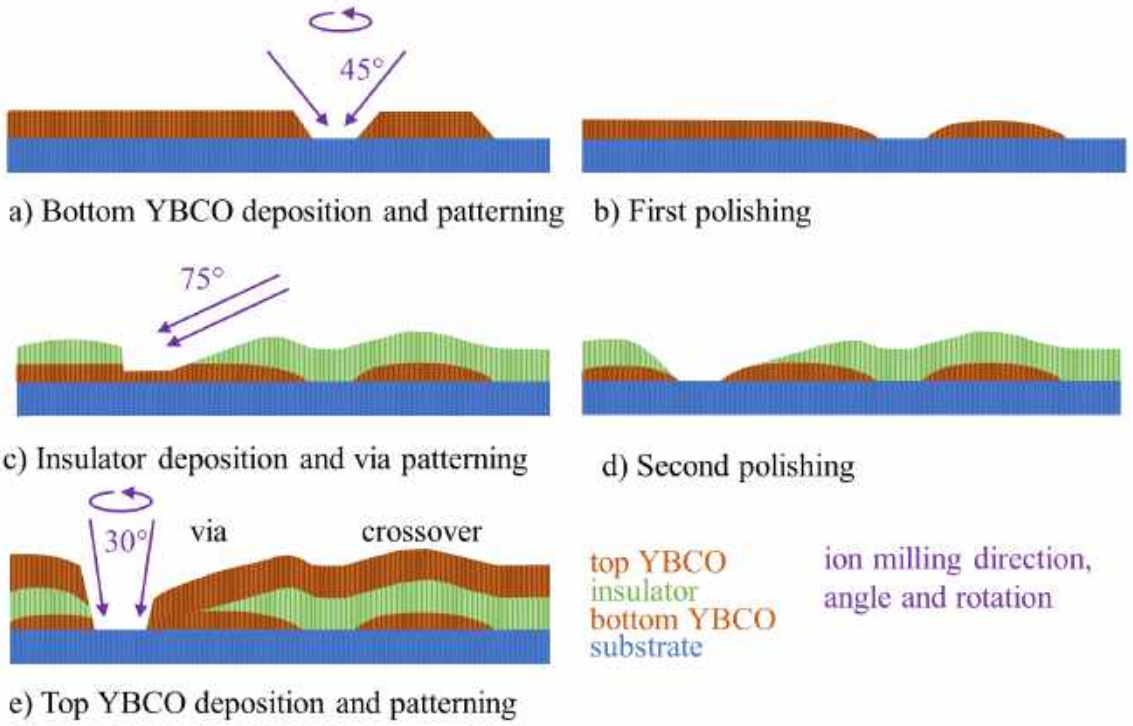

Figure 3.10: Step-by-step illustration of the multilayer fabrication process. A via is made to the left and a crossover to the right. Thicknesses and angles are not to scale.

wafer carrier is placed with the substrate down on the wet polishing pad and moved around with an arm. The etching rate depends on several parameters including the rotation speed and the weight on the wafer carrier. We use 10 rpm and a weight of 400 g on top of the 120 g wafer carrier. The progress is checked under the microscope after every minute. For example, AFM images show that on one sample a slope of around 3° and a film thickness of 135 nm was achieved after 4 min of CMP. The thickness can already be estimated with optical microscopy from the color of the YBCO film – thinner films are redder.

Third, a 120 nm STO insulating layer is deposited with the deposition parameters in Table 3.2. The photoresist mask is prepared without post exposure baking. Instead, the window for the via is argon ion milled at an angle of 75° to the substrate normal without rotating the substrate. To speed the process up, the beam current is increased from 15 mA to 20 mA – the other etching parameters remain the same. The etching is done for three times 75 min with two breaks to avoid overheating. After 160 min an Y and Ba signal was detected; we etch into the YBCO, but not through it. Micrographs of fabricated vias at this stage can be found in Fig. 3.11a-c.

Forth, the window is polished with CMP for 30 s the same way as in the second step. This results in a shallow slope for the bottom YBCO - STO window, and removes the remaining YBCO at the bottom of the window.

Lastly, a thick layer (6000 pulses, ca 450 nm) of YBCO is deposited and the input coil is patterned with standard photolithography and argon ion milling. For

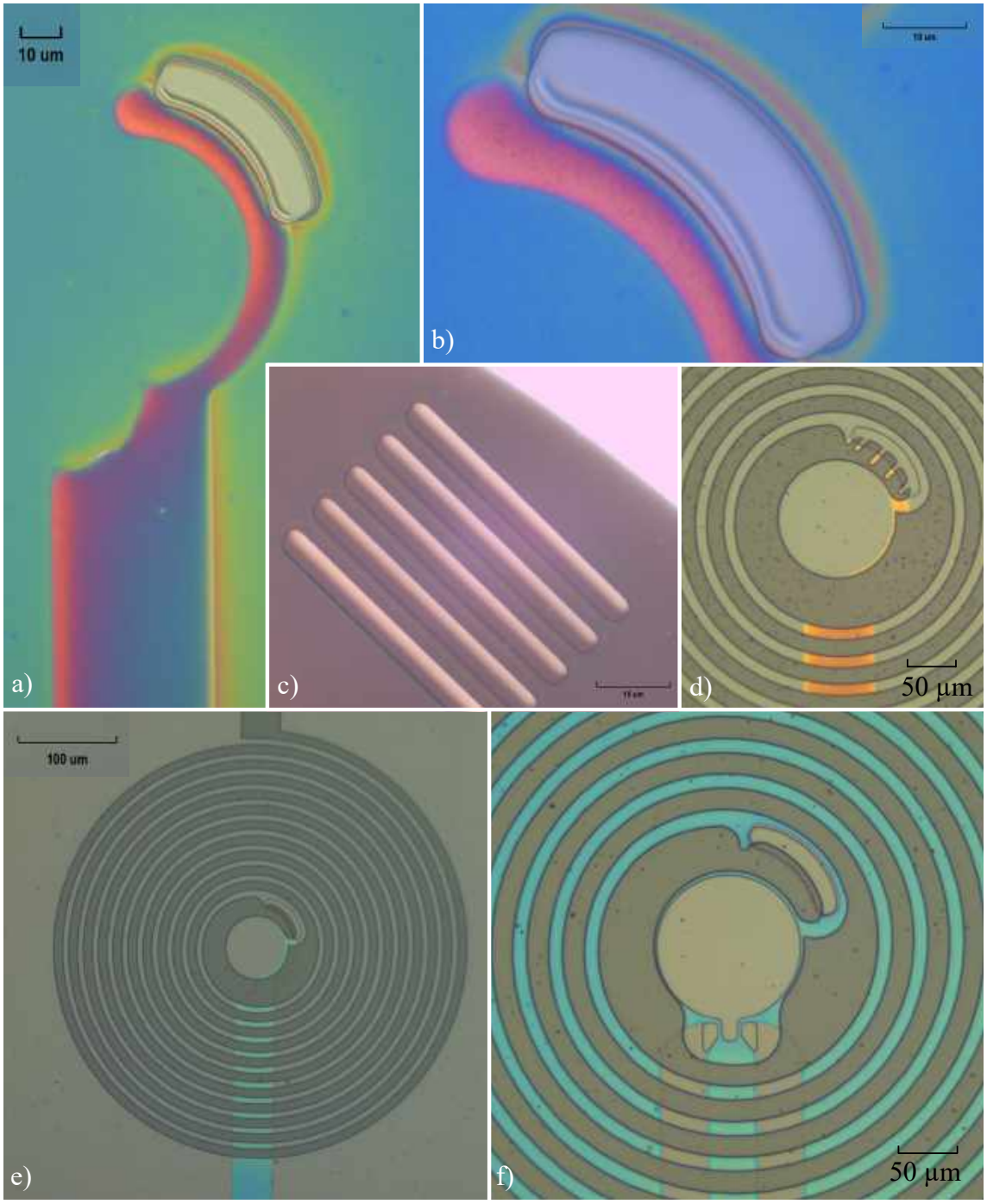

Figure 3.11: Micrographs of HTS multilayer structures after ion milling the window (a-c) and the final input coils (d-f). The ion milling direction is in all images towards the northeast. a) Bottom YBCO film (red/purple) and window in the STO for the via (white). b) Close-up of the via in a). c) Backlight image of a fabricated via outside of the input coil. The thickness of the YBCO (grey) decreases in northeast direction for each ion milled window. d) Flip-chip type flux transformer input coil with a via in the center and crossovers where the top YBCO film (dark grey) crosses the bottom YBCO film (orange). e) Another flux transformer input coil with thicker bottom YBCO (blue/green) film than in d). f) Integrated type flux transformer input coil (grey) with the bottom YBCO (blue) in the form of a washer SQUID.

the via we only use the very shallow edge in the ion milling direction of the third fabrication step in Fig. 3.10 and remove the YBCO above the ion milled window with the steeper slopes. Examples of the final multilayer structures can be found in Fig. 3.11d-f.

4

SQUID magnetometers for the 7-channel system

In this chapter the results obtained for single layer high-T_c SQUID magnetometers with a directly coupled pickup loop and bicrystal grain boundary Josephson junctions are summarized. The sensors for the 7-channel on-scalp MEG system were chosen to be of this type because such sensors were successfully implemented in single-channel systems [40].

First, the magnetometer design is presented, followed by an evaluation of different feedback methods that allow the sensors to be operated in a densely-packed multi-channel on-scalp MEG system. The results of this evaluation have been published in Paper A. Next, the characterization of the fabricated magnetometers is described, followed by a detailed description of the SQUID and pickup loop optimization performed. Several of the important lessons learnt have been published in Paper B and will be expanded on here. After presentation of the achieved noise levels at 78 K, the temperature dependence is studied in more detail. The chapter ends with a conclusion and outlook.

4.1 Design for the 7-channel system

The sensor design for the 7-channel system is shown in Fig. 4.1. It is based on the design of the magnetometers that were previously used in the single-channel cryostats [40]. The main components are the SQUIDs, the pickup loop, the feedback, the heater, and the contact pads.

The high-T_c SQUID consists of a loop with a linewidth of 4 µm and a hole size of 60 µm × 3 µm – see Fig. 4.1a. Based on Eq. (2.27), this narrow linewidth should prevent flux from being trapped in the SQUID during the cooldown. The Josephson junctions are formed where the 6 µm long microbridges cross the grain boundary of the STO bicrystal substrate. The width of the microbridge is adjusted to tailor the critical current of the junctions.

For redundancy, two SQUIDs with different junction widths are fabricated on each magnetometer chip and the better SQUID is selected. The two SQUIDs are

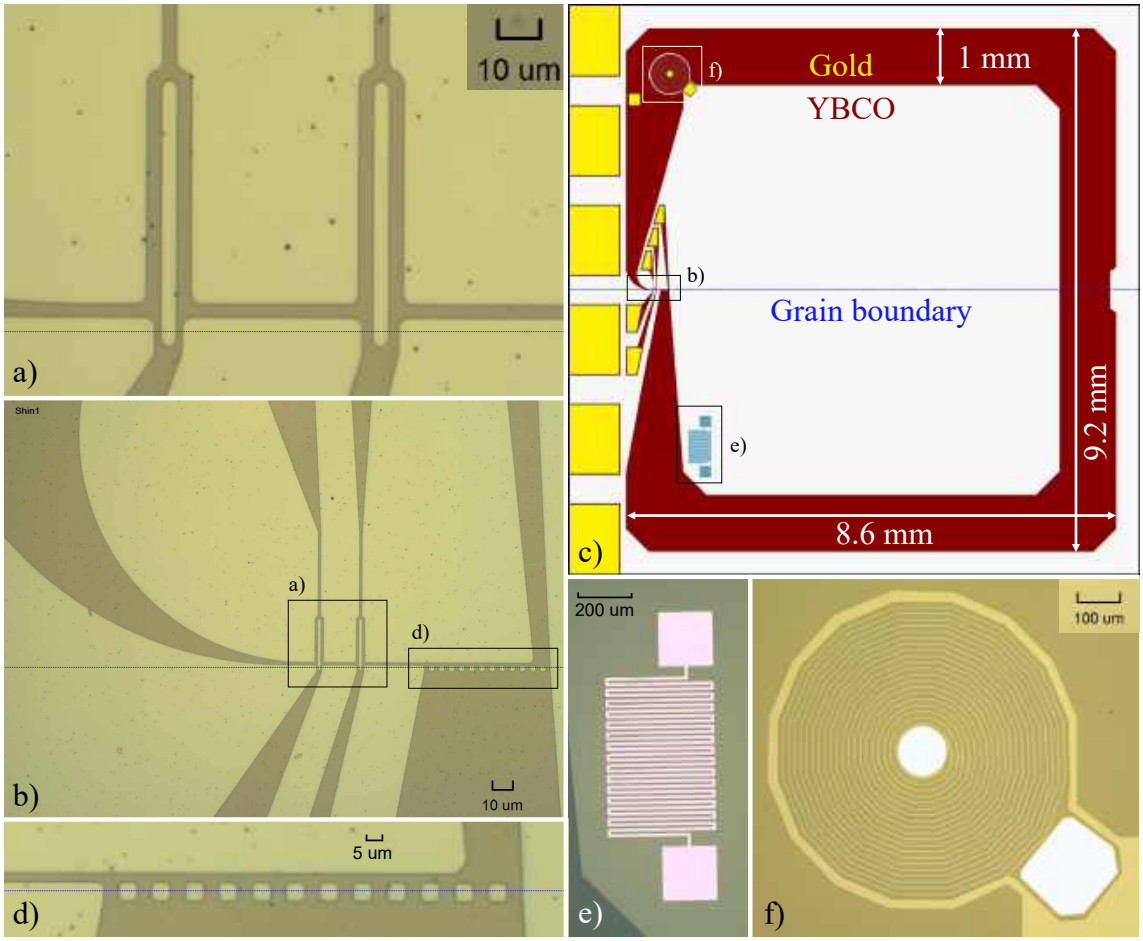

Figure 4.1: Single layer high-T_c SQUID magnetometer for the 7-channel system. a) Micrograph of two bicrystal grain boundary SQUIDs. The grain boundary is marked in blue. b) Micrograph showing the SQUIDs coupled to the pickup loop. c) Design of the magnetometer on a 10 mm × 10 mm bicrystal substrate. d) Micrograph showing the 6 µm × 6 µm holes in the pickup loop along the grain boundary. e) Micrograph of the on-chip heater. f) Micrograph of the on-chip superconducting feedback coil.

coupled to the same pickup loop as shown in Fig. 4.1b. The elongated hairpin design maximizes the coupling to the pickup loop and minimizes the parasitic inductance, which will be discussed in more detail later. In principle, more redundant SQUIDs could be coupled to the pickup loop, however, each SQUID increases the pickup loop inductance L_p and requires additional contact pads for the readout. In this design each SQUID has two contact pads that allow for symmetric SQUID biasing.

Since the effective area of the magnetometer grows linearly with the outer dimension of the pickup loop, a large pickup loop is wanted [19]. However, the size is limited by the available bicrystal substrate dimensions, and in our case the PLD deposition system, which is why we use 10 mm × 10 mm bicrystal substrates. Furthermore, the sensor spacing in a MEG system should be approximately the distance of the sensors to the closest sources [42, 43], i.e. around 1 cm (the distance between the scalp and the outermost active layer of an adult human's brain) plus

the sensor-to-scalp standoff distance [40], meaning that 10 mm × 10 mm substrates are a reasonable choice.

The pickup loop has outer dimensions of 9.2 mm × 8.6 mm and a linewidth of 1 mm as shown in Fig. 4.1c. In order to obtain well-defined YBCO edges to minimize flux trapping, the outer edge of the substrate is avoided. One substrate edge is furthermore used for contact pads that allow to connect to the cryostat wiring from the side.

The pickup loop crosses the grain boundary at two places. As flux can be trapped in defects that are more likely along the grain boundary, we reduce the number of possible pinning centers by patterning 6 µm × 6 µm holes into the YBCO film along the grain boundary – see Fig. 4.1d. The structure furthermore acts as a flux dam limiting the maximal circulating current [143]. The critical current of the flux dam can be adjusted by varying the length of the part crossing the grain boundary.

If too much flux has been trapped, the YBCO film can be heated above its critical temperature and re-cooled to expel trapped flux. For this purpose, a platinum heater has been placed on the chip as shown in Fig. 4.1e.

Lastly, the design includes two on-chip feedback solutions, which will be discussed in more detail next.

4.2 Feedback solutions

To operate the SQUID in a flux-locked loop as described in §2.4.6, a feedback coil is needed. Previously, our group has used wire-wound copper coils, which were made by hand. In the case of single channel cryostats, the coils were placed around the sapphire piece holding the SQUID. This solution does not compromise the standoff distance, nor does it reduce the cooling area. However, it is impractical in densely-packed multi-channel systems due to space limitations – an on-chip solution is thus preferable. Additionally, in multi-channel systems the flux generated by the feedback coil can also couple into neighboring magnetometers thus leading to unwanted crosstalk [189]. Feedback flux crosstalk is defined by the ratio of (unwanted) flux Φ_{12} coupled into the sensing SQUID 1 by the feedback of SQUID 2 and the (wanted) flux Φ_{22} coupled into the exciting SQUID 2:

$$C_{12} = \frac{\Phi_{12}}{\Phi_{22}}. \tag{4.1}$$

In Paper A we evaluate two on-chip feedback solutions in terms of coupling, noise, and feedback flux crosstalk. The first solution is the superconducting coil shown in Fig. 4.1f placed in one corner of the pickup loop. The second solution is direct injection of current into the SQUID loop using the configuration shown in Fig. 4.2a.

We find that both solutions provide sufficient coupling for operation in a FLL without adding additional noise. Feedback flux crosstalk measurements between two magnetometers as a function of distance show values below 5% for the superconducting coil and below 0.5% for direct injection – see Fig. 4.3. The measured crosstalk values depend on the effective area of the magnetometers, meaning that C_{12} and C_{21} are not necessarily the same. We furthermore found that crosstalk arising from the wires carrying the feedback current can be an issue. Wire crosstalk can be identified by

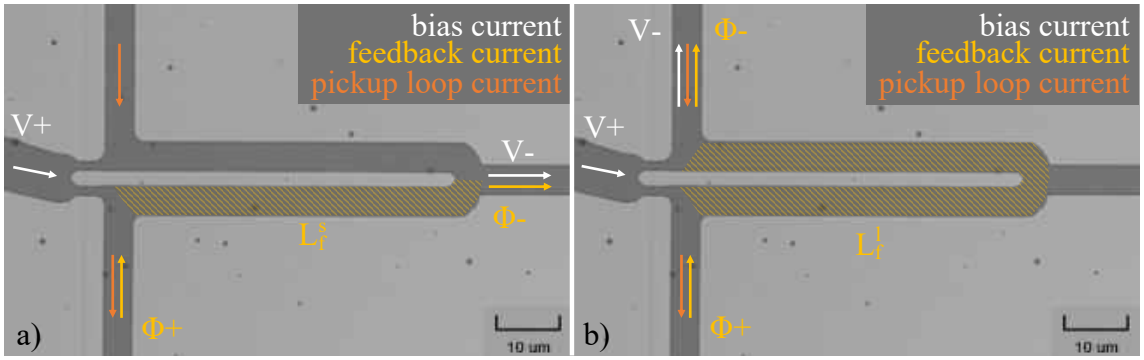

Figure 4.2: Wiring configurations for direct injection of current. The feedback coupling inductance is shaded yellow. The Josephson junctions are now to the left where the YBCO film crosses the visible grain boundary. a) Short direct injection with feedback coupling inductance L_f^s and symmetric SQUID biasing (the inductances of both SQUID arms are roughly equal). b) Long direct injection with feedback coupling inductance $L_f^l = L_c \approx 2L_f^s$ and asymmetric SQUID biasing.

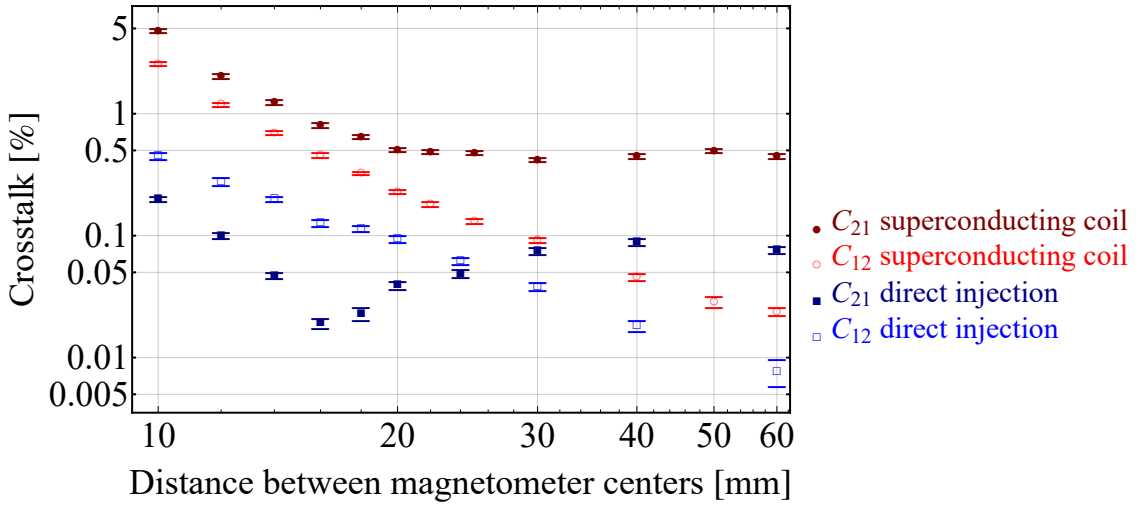

Figure 4.3: Feedback flux crosstalk as a function of distance between the magnetometer centers as presented in Paper A. At the minimal distance of 10 mm the two substrates touch each other.

the fact that the crosstalk does not decrease with the distance between the sensors. Based on the results obtained in Paper A, we decided to use direct injection as the feedback method for the 7-channel magnetometers.

When using direct injection feedback, two things are important in practice. First, the connections for the SQUID bias and the feedback current need to be done via separate contact pads. Using the same contact pad results in a voltage offset in the SQUID output signal that is dependent on the feedback current. This is due to the contact resistance. Second, when using the direct readout SQUID electronics *SEL-1* from Magnicon with the four wire scheme, the polarity of the connections matters because the voltage offset for operation in a FLL can otherwise not be compensated.

In the four wire scheme, two wires are used to bias and readout the SQUID ($V+$ and $V-$) and two are for the feedback ($\Phi+$ and $\Phi-$). Since $V-$ and $\Phi-$ correspond to the ground, they need to be on the same side of the junctions.

We refer to the wiring configuration shown in Fig. 4.2a as *short direct injection*. This type was chosen in order to bias the SQUID symmetrically, however, less than half of the SQUID loop inductance constitutes the feedback coupling inductance L_f^s. Using the configuration shown in Fig. 4.2b instead, the feedback coupling inductance can be roughly doubled. With such *long direct injection*, the feedback current takes the same path as the current from the pickup loop, meaning the feedback coupling inductance L_f^l and the pickup loop coupling inductance L_c are the same. This is also advantageous as it allows us to measure L_c using the same connections as for the feedback, and it is valuable for sensor calibration, as will be discussed in §4.5.2. The large inductance asymmetry α_L from the asymmetric biasing is moreover completely unproblematic as it only leads to a bias current dependent shift of the flux in the SQUID, but does not affect the modulation depth (see §2.4). Such a flux shift is also obtained from the feedback current and the signal current from the pickup loop as described in §2.6.2, and is thus unavoidable. Long direct injection is therefore preferable over short direct injection.

4.3 Magnetometer characterization

Before being placed into the 7-channel system, all fabricated magnetometers are characterized in a dipstick immersed in liquid nitrogen. An image of the setup is shown in Fig. 4.4a. The dipstick is filled with 0.8 bar helium exchange gas, which results in an operation temperature of ∼78 K. The measurements are performed inside our 2-layer MSR (consisting of 2 layers of mu-metal and one layer of copper-coated aluminum) from Vacuumschmeltze GmbH, Hanau, Germany. Except for the effective area measurements, the samples are placed inside a superconducting shield made of $Bi_{1.8}Pb_{0.26}Sr_2Ca_2Cu_3O_{10+x}$ (BPSCCO-2223) with a critical temperature of 110 K from Can Superconductors, Kamenice, Czech Republic. For the characterization we use a direct readout SQUID electronics as described in §2.4.6.

First, the SQUID voltage dependence on bias current I and flux Φ is measured. For this purpose, we apply a triangular current I_f to the feedback coil with an amplitude corresponding to at least one flux quantum. The resulting flux modulated voltage curve is recorded for different bias currents. Fig. 4.4b displays part of such a measurement showing the SQUID voltage modulation. The modulation period ΔI_f can be used to extract the feedback coupling inductance $M_f = \Phi_0/\Delta I_f$. In the case of long direct injection, this also yields the pickup loop coupling inductance L_c.

The $V(\Phi(I_f), I)$ data can then be used to plot the flux modulated I-V curve – see Fig. 4.4c for an example. Since noise rounding is significant, the I-V curves are fitted as described in §2.4.3 to obtain the SQUID critical current I_c, the SQUID normal resistance R_n, and the excess current I_{ex}. Taking excess currents into account turned out to be important to obtain better agreement between theoretical predictions and the measured values for the peak-to-peak voltage modulation depth ΔV, the transfer function V_Φ, and the flux noise $S_\Phi^{1/2}$.

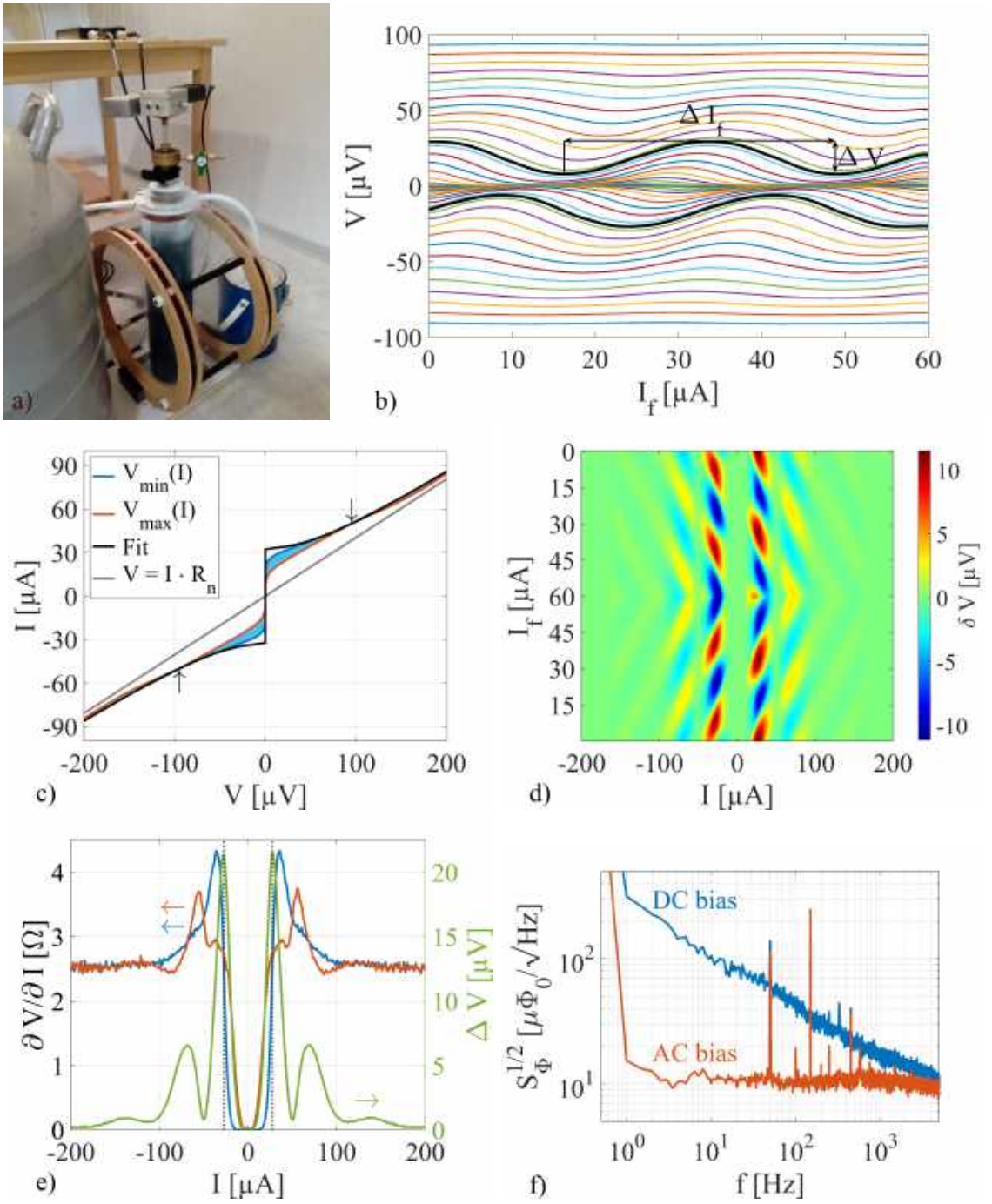

Figure 4.4: a) Photograph of the measurement setup. b) Flux modulated SQUID voltage curves for different bias currents between -50 µA and 50 µA in steps of 2 µA. The two curves with the largest voltage modulation depth ΔV are marked in black. The period ΔI_f corresponds to one flux quantum. c) Flux modulated I-V curve (light blue) with the two enveloping I-V curves highlighted in blue and orange, and a fit to obtain I_c, R_n, and I_{ex} in black. Arrows mark the position of the resonance. d) 2D color plot showing the deviation δV from the average voltage for a certain bias current as a function of applied flux. e) Left axis: dynamic resistance $\partial V/\partial I$ for the two enveloping I-V curves (blue and orange) in c) as a function of bias current. Right axis: modulation depth ΔV as a function of bias current. f) Equivalent flux noise spectrum of another device using dc bias and ac bias.

The $V(\Phi)$ curves for different bias currents can furthermore be used to identify the best working point for the SQUID. Different types of visualizations of the SQUID voltage modulation are given in Fig. 4.4b-d. In most cases the largest slope $|\partial V/\partial \Phi|_I = V_\Phi$ is obtained for the bias current leading to the largest ΔV, which simplifies manual SQUID tuning. The flux modulated voltage curves are not in all cases fully sinusoidal – for the measured SQUIDs we find that V_Φ and the maximal ΔV are related by $\Delta V = \alpha V_\Phi \Phi_0/\pi$ with α ranging from 0.8 to 1 (for sinusoidal curves $\alpha = 1$ is expected). Hence we determine V_Φ from the $V(\Phi)$ curves and do not only estimate it using $V_\Phi = \pi \Delta V/\Phi_0$. Calculating the dynamic resistance $\partial V/\partial I$ for the two enveloping I-V curves plotted blue and orange in Fig. 4.4c shows that the maximal modulation is obtained when the dynamic resistance of the two curves is equal – see Fig. 4.4e.

Many I-V curves show signs of resonances, which can be expected for SQUIDs made on STO substrates (see §2.4.4 and Ref. [131]). For the SQUID shown in Fig. 4.4c-e, a resonance is visible at $V_1^{res} \approx 96$ µV, which here corresponds to $I = 50$ µA. At that point the voltage modulation reaches a first minimum and then increases again. Using Eq. (2.24), a standing wave along the SQUID slit of length $l_{sl} \approx 52$ µm is predicted for this voltage, which is in line with the physical length of the SQUID slit without the microbridges and the lower half of the connection to the pickup loop. The second minimum in the voltage modulation depth can be explained by a second order resonance and occurs at a three times higher voltage. In the worst case the resonances can deteriorate the SQUID performance, however, in most cases the resonances appeared above the optimal operation point.

Once a good working point has been determined, the bias current I_b is set accordingly, the voltage offset V_b is compensated, and the SQUID is locked in a flux-locked loop. The transfer function V_Φ^{FLL} in the FLL can be measured directly by applying a triangular or sinusoidal current to the feedback coil with a peak-to-peak amplitude corresponding to one flux quantum and measuring the peak-to-peak output voltage in the FLL. We find that the measured values agree well with the expected ones from Eq. (2.29) using M_f as determined above and a feedback resistor with $R_f = 30$ kΩ.

Noise is measured in FLL mode using an FFT spectrum analyzer (Dynamic Signal Analyzer 35670A) from Keysight, Santa Rosa, USA. To obtain the flux noise spectra, we average 50 voltage noise spectra and divide by V_Φ^{FLL}. Fig. 4.4f shows how the 1/f-like noise from critical current fluctuations can be successfully reduced using ac bias reversal. We therefore always operate the SQUIDs with ac bias reversal at a frequency of 40 kHz, which is far above the signal frequencies of interest. In ac bias mode, not only the voltage offset needs to be adjusted before locking the SQUID in a FLL, but also the flux bias Φ_b to make the curves for positive and negative bias overlap at the chosen operation point.

Finally, to obtain the magnetic field noise and the sensor calibration, the effective area is measured as described in §2.5 using the calibrated Helmholtz coil shown in Fig. 4.4a. The calibration is performed without the superconducting shield. The effective area turned out to vary strongly between sensors and even different cooldowns of the same sensor, which will be discussed in more detail.

4.4 Magnetometer performance and optimization

Magnetometers were made in batches of one to three pieces. The design in each successive batch was slightly adjusted based on the results obtained from the previous magnetometers. For the first 7 magnetometers, the main adjustments concerned the junction width and film thickness to tune the junction parameters, which will be discussed first (§4.4.3). From these first 7 magnetometers it was furthermore found that the inductance varies strongly between different samples, even though the design was very similar. This led to the SQUID inductance investigation presented in Paper B and will be discussed in §4.4.2. The insights then allowed me to optimize the SQUID design (§4.4.3) and also the pickup loop design (§4.4.4). Finally, the magnetic field noise performance of the magnetometers is presented (§4.4.5).

4.4.1 Junction parameter tuning

The first magnetometer with a film thickness of 225 nm and junction widths of 1.5 µm (called Shin1L[1]) and 2.5 µm (called Shin1R) exhibited large SQUID critical currents $I_c \approx 450$ µA and $I_c \approx 700$ µA, respectively. This corresponds to a large junction critical current density $J_c \approx 62 - 67$ kA/cm^2 at 78 K. The following six magnetometers had lower – but still high – J_c with an average value of 24 kA/cm^2. Also, a large spread in J_c between these 6 magnetometers described by a standard deviation of 7 kA/cm^2 was found.

To obtain lower critical currents, narrow junctions with a width down to 1 µm were fabricated and the film thickness was decreased to 150 nm. Some fabricated junctions were furthermore trimmed with argon ion milling, which has previously been used to reduce I_c and increase R_n [190, 191]. A photoresist mask limited the ion milling to the junction region as shown in Fig. 4.5a. The ion milling was performed in several steps to see the progress. For Shin1L, I_c could be reduced from 450 µA to 22 µA, while R_n increased from 1.1 Ω to 6.7 Ω. This was achieved with 40 minutes of argon ion milling with the same parameters as for defining the SQUID. The process halved the initial junction thickness, but also reduced J_c to 7 kA/cm^2 and I_cR_n from almost 500 µV to around 150 µV at 78 K. An AFM image is shown in Fig. 4.5b. This approach proved to be well controllable, but requires additional fabrication steps and time.

The higher critical currents were often accompanied by excess currents. As an example, the I-V curve of SQUID Shin9R is shown in Fig. 4.5c. The fit yields $I_c = 81$ µA, $I_{ex} = 13$ µA, and $R_n = 2.5$ Ω. This gives a reduced critical current $I_c^* = 68$ µA, which is used instead of I_c in comparisons with theory. The voltage approaches the asymptotes defined by R_n and I_{ex} (purple lines in Fig. 4.5c) very slowly for high currents, which is why it is important to fit the curve. Current sweeps up to at least three times the critical current are desired to obtain a good fit. Otherwise I_{ex} and R_n can easily be overestimated.

[1] All magnetometers made on the bicrystals from Shinkosha were named "Shin" followed by a number for the substrate and "L" for the left SQUID or "R" for the right SQUID. Substrates that were repolished were named "ShinP" instead.

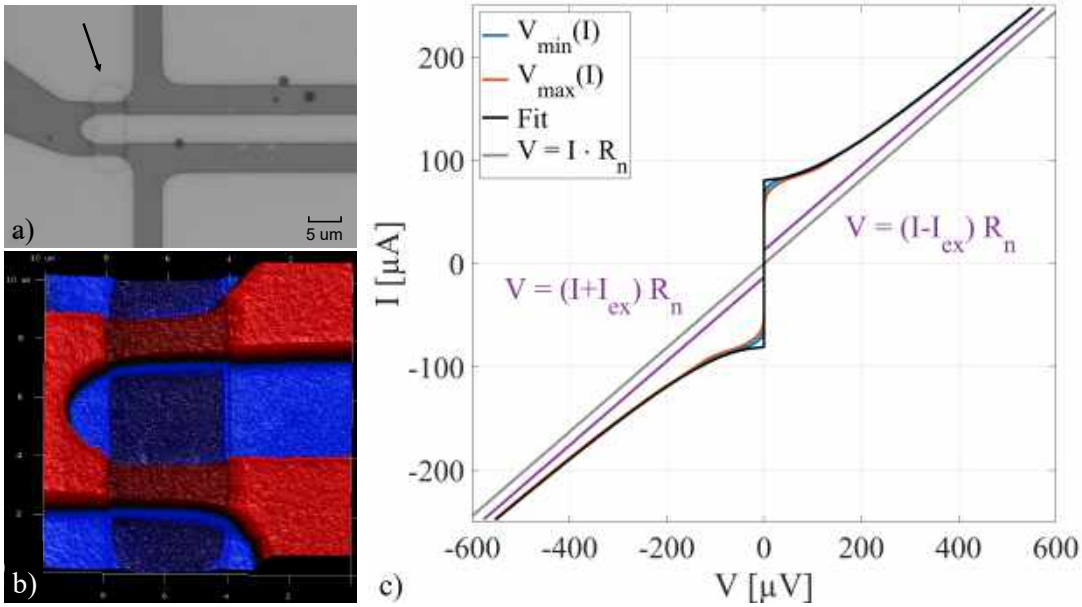

Figure 4.5: a) Micrograph showing the etched junction area of Shin1L. b) AFM image showing the same etched junction are with the YBCO in red and the STO substrate in blue. The darker areas are etched. c) *I*-*V* curve of magnetometer Shin9R with excess currents.

The solution to the problems with the very high J_c values and excess currents of up to 40% of I_c was found to be a CeO_2 buffer layer. The following 8 magnetometers with a buffer layer had an average $J_c = 4.7$ kA/cm^2 with a standard deviation of 3.5 kA/cm^2. The excess currents were all below 10 µA for SQUIDs with I_c up to 100 µA and in some cases even negative, which has also been found to be the case for step-edge junctions [104].

In Fig. 4.6 the measured $I_c^* R_n$ products of the SQUIDs on 15 fabricated magnetometers are plotted as a function of J_c^* with the measured I_c^* values given in different colors. A clear relationship between $I_c^* R_n$ and J_c^* can be seen with $I_c^* R_n$ increasing with increasing J_c^*. The same is the case when one replaces I_c^* with I_c. Gross *et al.* found a scaling behaviour $I_c R_n \propto J_c^p$ with $p = 0.5$ at 4.2 K for different HTS junction technologies and for J_c spanning more than 5 orders of magnitude [192]. The best fit for our magnetometers gives $p = 0.36$. Both the samples made without and with a buffer layer follow the same trend. Nonetheless, there is quite some spread and similar $I_c^* R_n$ values can be achieved with J_c^* varying by a factor 2 or even more.

Useful values of I_c^* around 30 µA were obtained with J_c^* between 2 and 7 kA/cm^2, which is more commonly achieved using a CeO_2 buffer layer. However, there is also a risk of obtaining very low J_c^* and I_c^* when using a CeO_2 buffer layer, resulting in low $I_c^* R_n$ products. We have found that the too low critical currents could be increased by annealing of the sample at 600 °C in a 650 Torr oxygen atmosphere for one hour. This type of reoxidation, however, affects the full sample, melts the gold on the contact pads, and in some cases turned out to be unstable over time, which is why it

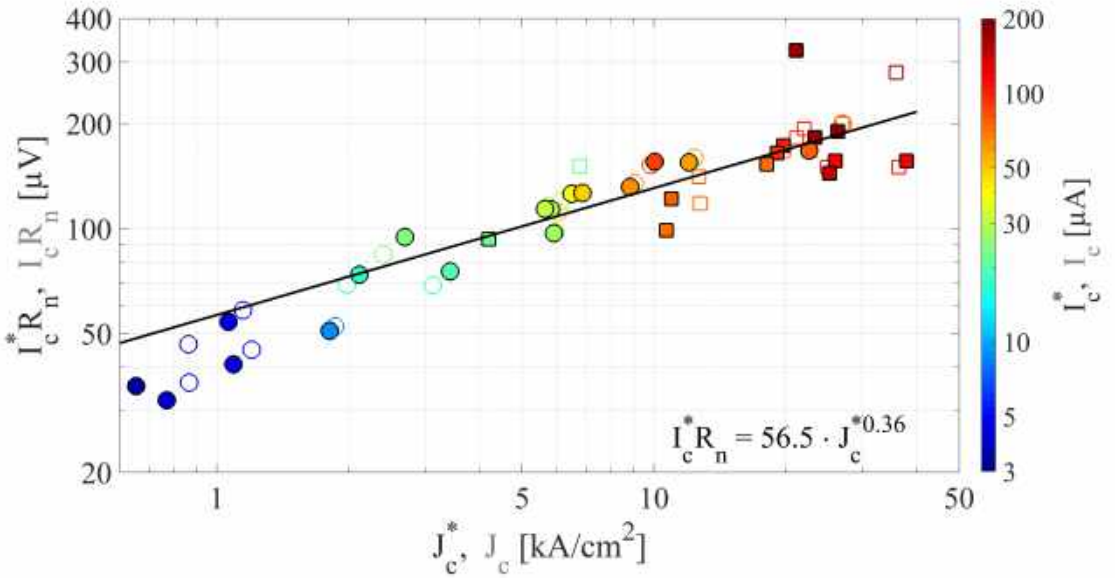

Figure 4.6: The measured $I_c^* R_n$ product of the SQUIDs on 15 fabricated magnetometers is plotted as a function of J_c^* with filled markers in the color corresponding to the measured I_c^* value. For comparison, the $I_c R_n$ product is plotted as a function of J_c with empty markers in the color of the measured I_c value. Square markers denote samples without a buffer layer, while circular markers denote samples with a CeO_2 buffer layer. A fit for $I_c^* R_n(J_c^*)$ is given in black.

was abandoned. Nonetheless, similar thermal annealing at much lower temperatures has been successfully used to tune the critical currents of low-T_c Josephson junctions [193, 194]. Instead of optimizing the annealing procedure, I focused on optimizing the YBCO film growth to obtain useful critical current densities without further treatment. Tuning of the critical currents was then mainly done by varying the junction width, which will be discussed in more detail later.

4.4.2 SQUID inductance investigation

While the junction parameters I_c and R_n of a SQUID are generally determined from its I-V curve, the SQUID inductance L is often only estimated from simulations and assumed to be constant for a device design used. However, in order to calculate the kinetic inductance contribution to the SQUID inductance, the London penetration depth λ of the film needs to be known. When operating the SQUID close to its critical temperature T_c (we often have $T > 0.8 \cdot T_c$), strong variations in λ can be expected as described by eq. (2.38). We have found that it is therefore not enough to simply assume a certain λ, but measurements are necessary.

In Paper B we combine inductance simulations and measurements to determine the full SQUID inductance. As detailed in Paper B, this is done by splitting the SQUID inductance into the coupling inductance L_c, which is mainly determined by the part of the SQUID loop shared with the pickup loop, and the parasitic inductance L_{par}, which is mainly determined by the microbridges forming the junctions plus the electrode and current injection lines. Both inductances consist of a geometric

inductance and a kinetic inductance contribution. While the earlier is independent of λ, the latter is proportional to the Pearl penetration length $\lambda_p = \lambda^2/t$, where t is the film thickness (see §2.6.1). For the geometric inductances L_c^{Geo} and L_{par}^{Geo} it is thus possible to directly use the simulated values. The kinetic coupling inductance contribution L_c^{Kin} is obtained by subtracting L_c^{Geo} from the L_c value measured with direct injection of current. The resulting L_c^{Kin} can be compared with the simulated value for a certain λ_p to extract the real λ_p. The latter can then be used to also scale the simulated value of L_{par}^{Kin} accordingly, and thus find all SQUID inductance contributions. Lastly, λ can also be calculated – given that the film thickness is known.

This method is used in Paper B to calculate the different inductance contributions for 10 SQUIDs made on 2 samples with slightly different T_c. Sample A furthermore has no buffer layer, while a CeO_2 buffer layer was used for sample B[2]. On each sample, 5 SQUIDs with different SQUID loop lengths l_{sq} from 10 µm to 50 µm were chosen. As shown in Fig. 4.7, increasing the loop length leads to a linear increase in L_c and is thus an effective way to adjust the inductance. Comparing two SQUIDs with the same l_{sq} but made on different samples shows that the kinetic inductance contributions are much higher for sample A than sample B. On average, the total SQUID inductances for sample A SQUIDs are twice as large as for sample B SQUIDs, thus clearly demonstrating that inductance measurements are necessary to obtain a trustworthy SQUID inductance estimation.

We attribute the larger kinetic inductance contributions for sample A to its lower T_c, although the two samples also differ in the use of a buffer layer. A comparison of the first 7 magnetometers made without a buffer layer shows that the film with the highest $T_c = 89.9$ K (width 1.0 K) has the lowest $\lambda = 450$ nm at 78 K, while the film with the lowest $T_c = 87.3$ K (width 2.0 K) has the largest $\lambda = 730$ nm at 78 K. We therefore conclude that λ is mainly determined by T_c and not the presence of a buffer layer, although the buffer layer may have an effect on the film quality. For the following 8 magnetometers with buffer layer a London penetration depth between 360 nm and 600 nm was measured at ∼78 K.

The large differences in the measured L_c between magnetometers also explains the differences in the effective area A_{eff} found as A_{eff} is proportional to L_c for negligible SQUID effective area, see §2.5. It is therefore critical that A_{eff} is measured for each magnetometer and not just assumed to be constant for a specific design.

4.4.3 SQUID optimization

With all the SQUID parameters determined, it is possible to compare the measured values with theoretical predictions and optimize the sensor performance. This will be described in the following.

[2]The original purpose of Shin12 (called sample A in Paper B) was to find the optimal SQUID loop length and junction width, and the sample thus contains 48 SQUIDs for which these two parameters are varied. Alexei Kalaboukhov then suggested to check if the junction properties could be improved with a CeO_2 buffer layer. A second sample, Shin13 (called sample B in Paper B), with identical design but using a CeO_2 buffer layer was fabricated. In between the fabrication of these two samples, the YBCO film growth was reoptimized, and a better film quality could be reached for Shin13. This was also the case for other YBCO films without a buffer layer.

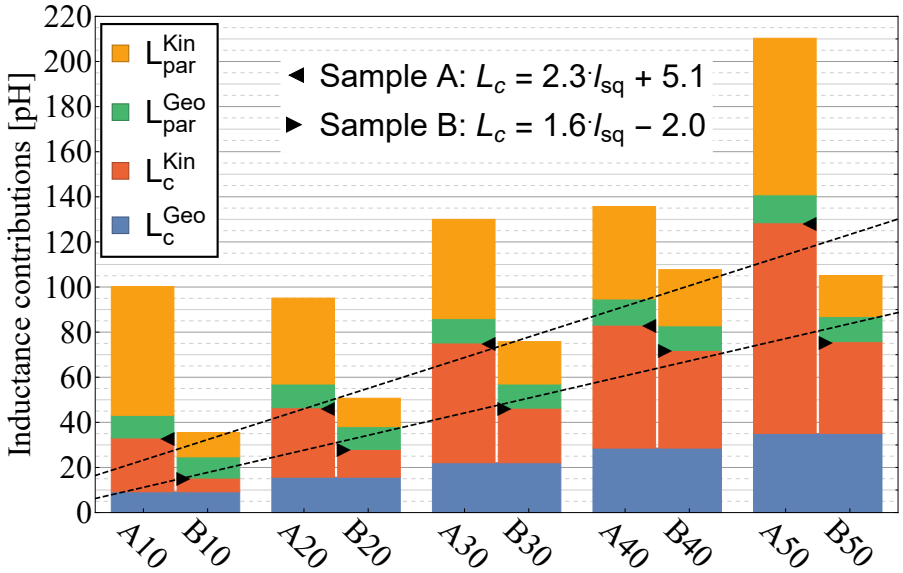

Figure 4.7: Inductance contributions of 10 SQUIDs made on two samples A (left bar) and B (right bar) with increasing SQUID loop length l_{sq} from 10 µm to 50 µm. The triangles mark the measured L_c and the lines are a separate linear fit for $L_c(l_{sq})$ for the two samples with the formula given in the figure.

SQUID performance dependence on inductance

We begin by studying the dependence of the transfer function V_Φ and the flux noise S_Φ on the inductance. This has been done in Paper B for the 10 SQUIDs presented earlier. As discussed in §2.4.5, V_Φ decreases rapidly with increasing L, which consequently leads to an increase in the flux noise. Fig. 4.8a shows the measured V_Φ in normalized form for better comparison with the prediction from Eq. (2.23). Note that the reduced critical current I_c^* is used instead of I_c as explained earlier. The measured values exhibit the expected exponential decrease with increasing L and fit the prediction well – especially in the case of sample B. Deviations may be due to resonances and asymmetries.

In Fig. 4.8b the total flux noise measured in FLL mode is shown as a function of L. The total flux noise is furthermore split into the electronics contribution $S_{\Phi,el}^{1/2} = S_{V,el}^{1/2}/V_\Phi$ with $S_{V,el}^{1/2} = 0.4$ nV/$\sqrt{\text{Hz}}$ for our electronics, and the intrinsic SQUID noise $S_{\Phi,sq}^{1/2} = \sqrt{S_\Phi - S_{\Phi,el}}$. The dominant contribution depends on the individual SQUID. For comparison, the theoretical values for the total flux noise based on the equations in §2.4.5 are plotted as black dots. For half of the SQUIDs, the difference between predicted and measured flux noise is less than 10%, while on average the measured values are 24% larger than predicted. Additionally, we plot the predicted flux noise for three different values of I_c^* representing the measured range and fix $I_c^* R_n$ to the average value of 108 µV. This clearly shows that lower critical currents are favourable, but that would also mean narrower junctions with larger L_{par}. This trade-off will be studied later in this section.

The SQUID with the lowest $L = 35$ pH has an impressively low total flux noise of 2.6 µΦ_0/$\sqrt{\text{Hz}}$ at 78 K with an intrinsic SQUID noise contribution of 1.5 µΦ_0/$\sqrt{\text{Hz}}$.

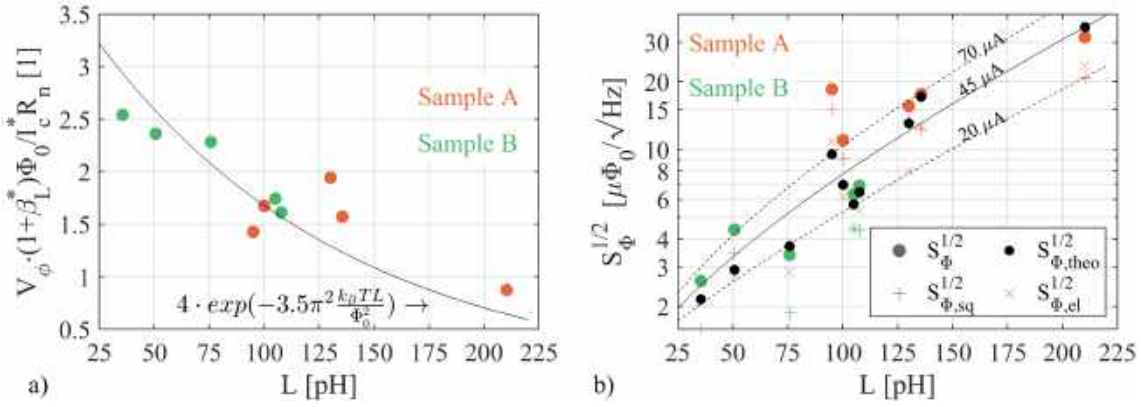

Figure 4.8: a) Normalized transfer function V_Φ as a function of SQUID inductance. The black line is the prediction from Eq. (2.23). b) White flux noise $S_\Phi^{1/2}$ as a function of SQUID inductance. Colored dots denote the total measured flux noise, plus signs the intrinsic SQUID contribution, crosses the electronics contribution, and black dots the theoretical total flux noise. The three lines represent the theoretical total flux noise for three different I_c^* as indicated and fixed $I_c^* R_n = 108$ μV.

However, due to the trade-off between low flux noise and coupling, this SQUID does not constitute the best magnetometer. The performance of a SQUID magnetometer is characterized by its magnetic field noise $S_B^{1/2} = S_\Phi / A_{eff}$, where the effective area $A_{eff} \approx L_c \cdot A_p / L_p$ for a directly coupled pickup loop, see Eqs. (2.31) and (2.32). The magnetic field noise can thus be divided into a SQUID dependent factor (S_Φ / L_c) and a pickup loop dependent factor (L_p / A_p), meaning the SQUID and the pickup loop can be optimized individually. SQUID optimization – which we focus on here – thus boils down to minimizing S_Φ / L_c. For the 10 SQUIDs studied in Paper B, the SQUID with the lowest S_Φ / L_c of 74 μ$\Phi_0/\sqrt{\text{Hz}}$/nH has $l_{sq} = 30$ μm, $L_c = 46.3$ pH, and $S_\Phi^{1/2}$ = 3.4 μ$\Phi_0/\sqrt{\text{Hz}}$ (for comparison, the SQUID described above with the lowest $S_\Phi^{1/2}$ had $S_\Phi / L_c = 167$ μ$\Phi_0/\sqrt{\text{Hz}}$/nH). Nonetheless, for SQUIDs with $l_{sq} = 30 - 50$ μm, S_Φ / L_c varies only slightly with L_c, but also depends on L_{par}, I_c^* and R_n. The next complete magnetometer was made with two SQUIDs with $l_{sq} = 30$ μm, while the following 7 magnetometers had one SQUID with $l_{sq} = 30$ μm and one with $l_{sq} = 50$ μm to increase the chance of achieving a suitable L. In all cases the junction width was varied and the better SQUID was picked.

Parasitic inductance reduction

While the approach described above turned out to work well to achieve useful SQUID inductance values, further optimization is possible as outlined in Paper B and tested for sample ShinP8, which will be investigated here. To begin with, minimizing $S_\Phi^{1/2} / L_c$ means that a low L_{par} is wanted as it does not contribute to the coupling, but only reduces V_Φ. Several measures can be taken to reduce L_{par}. First, a good film quality with a high T_c leading to a low λ is necessary to achieve a low L_{par}^{Kin}. The SQUID inductance investigation showed that just a few K difference in T_c can

have a large effect on λ. A change in λ from 600 nm to 400 nm decreases the kinetic inductance by a factor of 2.25 – a significant amount.

Second, the length l_{JJ} of the microbridges forming the junctions should be minimized in order to reduce L_{par}. The length depends on the junction technology used and is in our case limited by the precision with which the design can be aligned with the grain boundary. Test SQUIDs demonstrate that both $l_{JJ} = 3$ µm and 1 µm (instead of the 6 µm used earlier) were feasible. The general design of these SQUIDs is shown in Fig. 4.9a and a micrograph of one SQUID can be seen in Fig. 4.9b. The alignment was done with the help of alignment marks etched into the YBCO film as described in §3.3.1. Gold crosses for alignment during electron beam lithography were then fabricated using the laser writer and the coordinates established with AFM. The grain boundary was found to be 150-250 nm away from its intended position, thus indicating very good alignment. Decreasing l_{JJ} reduces both the kinetic and geometric inductance contribution to L_{par} roughly linearly as plotted in Fig. 4.9c. The impact of reducing l_{sq} is even stronger for microbridges with smaller w_{JJ}.

Third, the SQUID slit width w_{sl} can be decreased to further reduce L_{par} as plotted in Fig. 4.9d. This also affects L_c, which decreases with decreasing w_{sl}. To reach the same L_c, a longer SQUID loop is thus necessary, which also comes with a slightly larger L_{par}. However, for equal L_c, the SQUID with the narrower slit nonetheless has the lower L_{par}. For both L_{par} and L_c it is mainly the geometric contribution that is affected. Using standard photolithography, a slit width below 1 µm could not be resolved. With electron beam lithography narrower slits are possible, and using a focused helium ion beam a slit width of 10 nm has been achieved [162]. The chance of shunting the SQUID loop by a defect grows for narrower slits, which is why $w_{sl} = 1$ µm was chosen for the fabricated SQUIDs.

Fourth, decreasing the linewidth w_{sq} of the SQUID loop and current injection lines further reduces L_{par} as plotted in Fig. 4.9e. However, in this case L_c is strongly affected, with L_c^{Kin} roughly doubling when halving w_{sq}. While L_c can be adjusted by reducing l_{sq}, the kinetic inductance fraction remains high and makes the total inductance more sensitive to changes in λ. Furthermore, narrower lines are more likely to be ruined by defects. For these reasons the linewidth of 4 µm was maintained.

Fifth, small reductions in L_{par} can be achieved with rounded corners as shown in Fig. 4.9a&b, however, for the 1 µm long microbridges the roundings at the junctions were left out as w_{JJ} might be affected. Also, increasing the electrode width w_{el} can slightly decrease L_{par}, but to avoid flux trapping, large film areas close to the SQUID should be avoided. Holes were patterned into the electrode to reduce the film width (see Fig. 4.9b).

Lastly, but nonetheless potentially very impactful, is the adjustment of the junction width w_{JJ} on L_{par}. Since the junction width also affects the critical current and the normal resistance, it can not be adjusted as freely as the other SQUID design parameters. We will now study this trade-off between low L_{par} but large I_c and low R_n for wide junctions, and opposite for narrow.

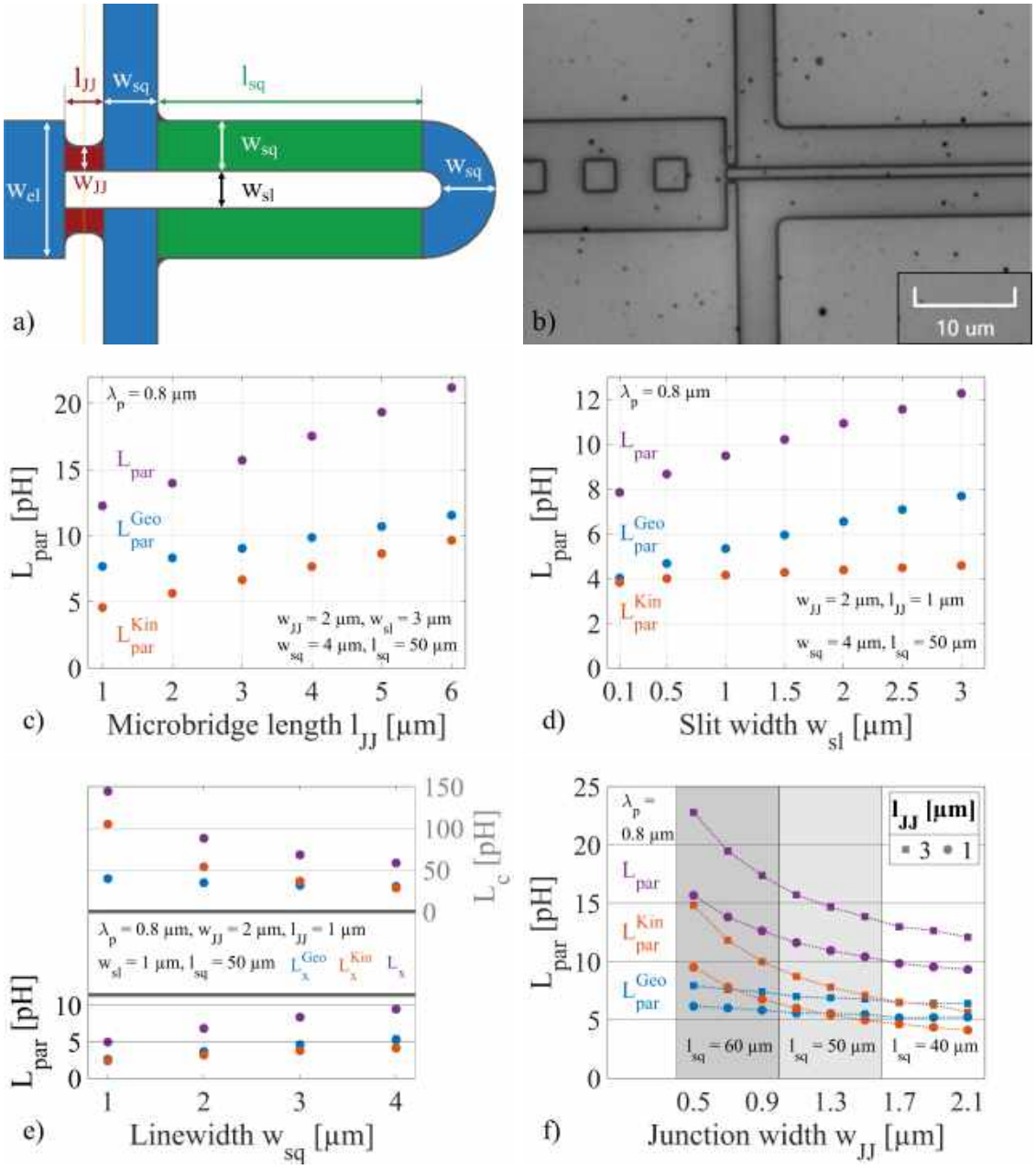

Figure 4.9: SQUID design and inductance simulation. a) SQUID design showing the varied parameters. The microbridges forming the junctions each have a length l_{JJ} and a width w_{JJ}. The SQUID loop has a linewidth w_{sq} and a slit width w_{sl}. The length l_{sq} of the green part of the SQUID loop is varied to adjust L_c. The electrode has a width $w_{el} = 11$ µm. Rounded corners are marked purple. b) Micrograph of a fabricated SQUID with $l_{JJ} = 1$ µm and $w_{JJ} = 0.5$ µm. c) Simulated L_{par} as a function of l_{sq} for the indicated parameters and no rounded corners. d) Simulated L_{par} as a function of w_{sl} for the indicated parameters and no rounded corners. e) Simulated L_{par} (bottom) and L_c (top) as a function of w_{sq} for the indicated parameters and no rounded corners. f) Simulated L_{par} as a function of w_{JJ} for the fabricated test SQUIDs on ShinP8. The SQUIDs have either $l_{JJ} = 3$ µm (squares) or $l_{JJ} = 1$ µm (circles) and the slit length is varied depending on w_{JJ} as indicated in the figure.

Junction width optimization

To find the optimal junction width, SQUIDs with w_{JJ} varying from 0.5 µm to 2.1 µm in steps of 0.2 µm were fabricated in the center of a substrate[3]. The rest of the film was protected with the intention to fabricate a full magnetometer once the optimal SQUID design was established from these test SQUIDs. One set of 9 such SQUIDs was made with $l_{JJ} = 3$ µm and another set with $l_{JJ} = 1$ µm. To counteract a larger β_L due to the larger I_c of wider junctions, the SQUID loop length was adjusted in groups of three SQUIDs as indicated in Fig. 4.9f. In the same figure the simulated L_{par} values for these SQUIDs are plotted. A clear increase in L_{par} for narrower junctions is observed.

All SQUIDs were characterized in a dipstick at an operation temperature of ∼78 K. Except for one SQUID with $l_{JJ} = 3$ µm and $w_{JJ} = 0.5$ µm, all SQUIDs were functional. The simulated values of L_{par} and L_c were again combined with the measured L_c values to determine λ_p and all SQUID inductance contributions. The measurements showed that $\lambda_p = 1.00 \pm 0.04$ µm, which means that the real kinetic inductance contributions are 25% larger than the simulated values that use $\lambda_p = 0.8$ µm. Assuming a uniform film thickness of 225 nm, one obtains $\lambda = 475 \pm 10$ nm. For these SQUIDs, the London penetration depth is rather uniform and differences in L_{par} are mainly due to varying w_{JJ} and l_{JJ}.

In Fig. 4.10a the SQUID critical current I_c, the reduced critical current I_c^*, and the excess current I_{ex} are plotted as a function of w_{JJ}. Excess currents are close to zero and slightly negative, meaning that I_c^* is typically slightly larger than I_c. A linear fit for $I_c^*(w_{JJ})$ is given in the figure, however, several values deviate considerably from this line. This illustrates one of the main problems with grain boundary junctions: even on the same film, w_{JJ} is not the only variable defining I_c and I_c^*, but local variations in the grain boundary properties also play a role. The fit predicts that I_c^* is zero for $w_{JJ} < 0.4$ µm. This was already the case for the SQUID with $w_{JJ} = 0.5$ µm and $l_{JJ} = 3$ µm.

The extracted SQUID normal resistance R_n is plotted as a function of w_{JJ} in Fig. 4.10b. A drastic increase in R_n is found for narrow junctions approaching 0.3 µm. Except for the three SQUIDs with I_c smaller than 15 µA, the resulting $I_c R_n$ and $I_c^* R_n$ products are roughly constant with 93 ± 8 µV and 99 ± 10 µV, respectively. The very narrow junctions are more prone to degradation. Fig. 4.10b also shows the SQUID dynamic resistance R_d at the operation point normalized by R_n. We measure $R_d/R_n = 1.1 \pm 0.2$, which is lower than $R_d/R_n = \sqrt{2}$ as assumed in §2.4.5. The ratio also seems to decrease for narrower junctions. The measured R_d is therefore used when calculating the theoretical SQUID noise based on Eq. (2.25).

Fig. 4.10c compares the measured transfer function with the theoretical one based on Eq. (2.23) using the measured I_c^*, R_n, and L values. Except for two SQUIDs with I_c^* smaller than 15 µA, the measured V_Φ reaches the predicted value or even slightly exceeds it. Good agreement with theory is also found for the total flux noise, see

[3] AFM images show that the width at half height quoted here is 0.1 µm larger than the designed value, which is achieved at the top of the film.

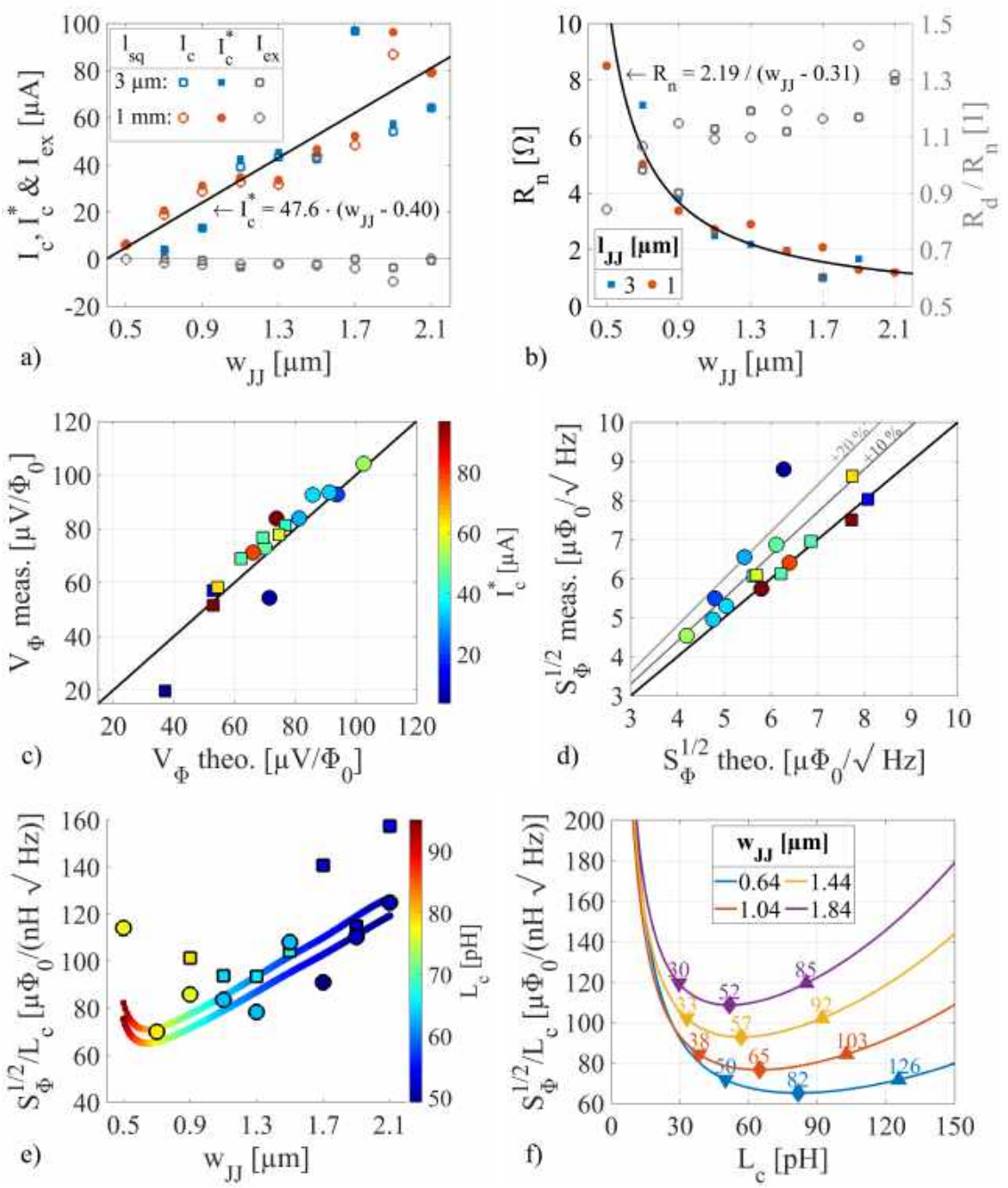

Figure 4.10: Optimization of the junction width w_{JJ}. Measured values of SQUIDs with $l_{JJ} = 3$ µm (1 µm) are indicated by squares (circles). a) Measured I_c (empty markers), I_c^* (filled markers), and I_{ex} (grey markers) as a function of w_{JJ} including a linear fit for $I_c^*(w_{JJ})$. b) Left axis: measured R_n with a linear fit for $1/R_n(w_{JJ}$. Right axis: measured R_d/R_n. c) Comparison of the measured and theoretical V_Φ. Equality is indicated with a line and I_c^* is given by the color scale. d) Comparison of the measured and theoretical flux noise, using the same color scale for I_c^*. Equality is indicated with the black line, while 10% and 20% higher measured noise values than predicted are given by grey lines. e) $S_\Phi^{1/2}/L_c$ as a function of w_{JJ} for the measured values (markers) as well as a theoretical prediction for $l_{JJ} = 3$ µm (top curve) and $l_{JJ} = 1$ µm (bottom curve). The color bar indicates L_c. f) Optimization of $S_\Phi^{1/2}/L_c$ as a function of L_c for 4 different w_{JJ} and $l_{JJ} = 1$ µm. Minima are indicated with diamonds, 10% higher values with triangles.

Fig. 4.10d. For several SQUIDs the measured flux noise is as predicted. Only in two cases with very low I_c the measured noise is more than 20% larger than predicted[4].

The lowest magnetic field noise (when directly coupled to a pickup loop) is reached with the SQUID with the lowest $S_\Phi^{1/2}/L_c$, which we will study now. Fig. 4.10e shows the measured $S_\Phi^{1/2}/L_c$ with filled markers. The lowest value $S_\Phi^{1/2}/L_c = 70$ $\mu\Phi_0/\sqrt{\text{Hz}}/\text{nH}$ is achieved with the SQUID with $l_{JJ} = 1$ µm and $w_{JJ} = 0.7$ µm. Generally, the SQUIDs with $l_{JJ} = 1$ µm show better performance than the SQUIDs with $l_{JJ} = 3$ µm and the same w_{JJ}, which is expected as L_{par} is smaller.

Since good agreement with theory was found in terms of noise, we can optimize $S_\Phi^{1/2}/L_c$ as a function of L_c for the different junction widths and lengths using the fitted dependencies of I_c^* and R_n on w_{JJ}, $R_d = 1.1R_n$, as well as an interpolation for L_{par}. For each of these $S_\Phi^{1/2}/L_c(L_c)$ curves the minimum is determined together with the associated L_c. These values are plotted in Fig. 4.10e as the two colorful curves, the lower being the one for $l_{JJ} = 1$ µm. From the lower curve it follows that the optimal junction width is 0.64 µm giving $S_\Phi^{1/2}/L_c = 65$ $\mu\Phi_0/\sqrt{\text{Hz}}/\text{nH}$. The best measured SQUID has a performance very close to this. Some measured $S_\Phi^{1/2}/L_c$ are below the theoretical curve because their measured I_c^* is lower than the fitted I_c^* value that was assumed for the theoretical curve.

Looking at the individual $S_\Phi^{1/2}/L_c(L_c)$ curves furthermore reveals that the minimum is very broad - see Fig. 4.10f showing 4 such curves for different junction widths and $l_{JJ} = 1$ µm. For $w_{JJ} = 0.64$ µm, the minimum is achieved for $L_c = 82$ pH, yet L_c values from 50 pH to 126 pH yield a $S_\Phi^{1/2}/L_c$ that is no more than 10% higher than the minimal value. The optimal L_c furthermore decreases with increasing junction width.

The minimum achieved for $w_{JJ} = 0.64$ µm suggests that low I_c^* values are best, however, there is also a risk that these narrow junctions have too low I_c^* and degraded $I_c^*R_n$ product. For the magnetometer made on the rest of the film on this substrate, slightly more conservative junction widths were thus chosen: 0.9 µm for the $l_{JJ} = 1$ µm SQUID called ShinP8L and 1.1 µm for the $l_{JJ} = 3$ µm SQUID called ShinP8R. While alignment to the grain boundary was again good for both SQUIDs, the $I_c^*R_n$ product was considerably reduced for ShinP8L with 55 µV ($I_c^* = 12.8$ µA, $R_n = 4.3$ Ω), but also slightly for ShinP8R with 80 µV ($I_c^* = 29.6$ µA, $R_n = 2.7$ Ω). The noise performance was nonetheless good with $S_\Phi^{1/2}/L_c = 141$ $\mu\Phi_0/\sqrt{\text{Hz}}/\text{nH}$ giving 57 $\text{fT}/\sqrt{\text{Hz}}$ for ShinP8L and $S_\Phi^{1/2}/L_c = 118$ $\mu\Phi_0/\sqrt{\text{Hz}}/\text{nH}$ giving 48 $\text{fT}/\sqrt{\text{Hz}}$ for ShinP8R, but much higher than the 28 $\text{fT}/\sqrt{\text{Hz}}$ predicted by the test SQUID with $S_\Phi^{1/2}/L_c = 70$ $\mu\Phi_0/\sqrt{\text{Hz}}/\text{nH}$.

The results highlight the importance of having a junction technology that allows one to reproducibly fabricate SQUIDs with low I_c^*, but still decent $I_c^*R_n$ products. For bicrystal Josephson junctions a solution may be to switch to a larger misorientation angle such as 30°-33° because SQUIDs made on such substrates have lower J_c but still achieve good I_cR_n products [195]. An alternative approach is to pattern wide junctions and trim the junction with argon ion milling as described in §4.4.1.

[4]One of these SQUIDs is not shown and has $I_c^* = 3.7$ µA, a measured $S_\Phi^{1/2} = 24.7$ $\mu\Phi_0/\sqrt{\text{Hz}}$, and a theoretical $S_\Phi^{1/2} = 12.2$ $\mu\Phi_0/\sqrt{\text{Hz}}$

4.4.4 Pickup loop optimization

Optimization of the pickup loop involves maximizing the pickup loop effective area to inductance ratio A_p/L_p. For a square pickup loop, $A_p = D \cdot d$, where D is the outer loop diameter and d the inner hole diameter [19]. The inductance depends on the pickup loop linewidth $w = (D - d)/2$ and decreases with increasing w, see Appendix B. The largest A_p/L_p is achieved for a wide pickup loop with $w > d$, where $L_p \approx 1.25\mu_0 d$ [64]. In practice, a slit is required were the SQUIDs are placed, and some space is occupied by contact pads and possibly a feedback coil and heater. The real values for A_p/L_p are thus lower.

Different pickup loop designs as displayed in Fig. 4.11 have been tested. Their A_p/L_p values have been obtained from measurements of A_{eff} and L_c using $A_p/L_p \approx A_{eff}/L_c$ and are summarized in Table 4.1. The L_c measurement is just an estimation as part of the injected current goes around the pickup loop instead of through the SQUID loop. The fraction of current going through the pickup loop depends on where the current is injected and the inductances of the two paths. The uncertainty is larger for wide pickup loops that have a lower inductance and thus a lower inductance mismatch. The current should be injected as close to the SQUID as possible to make a larger fraction of the current go through the SQUID loop.

Table 4.1: Pickup loop performance.

Design as shown in Fig. 4.11	Sensors Shin...	A_p/L_p [mm^2/nH]
a) with both coils	1	2.8
a) with big coil	3	3.0
a) without coils	5, 9	3.6-3.7
a) without coils, damaged edge	6-8	3.3-3.5
a) without coils, $\Phi-$ and $V-$ pads connected	16-19	3.9-4.2
b)	P20, P21, 24	4.5-5.0
c) with and without slits	14	5.4-5.6
d)	P8	5.1

The initial design with a 1 mm linewidth pickup loop as presented in §4.1 is not optimal in terms of A_p/L_p. The narrow linewidth was previously chosen to limit flux trapping during the cooldown. However, according to the calculation in Ref. [196], the indirect noise generated by vortices in the pickup loop is negligible compared to the intrinsic noise of the SQUID. This is due to the large inductance mismatch between the pickup loop and the SQUID loop. As a precaution, the wide loop of design b) was made in such a way that the initial design could be retrieved by etching parts of the pickup loop if necessary. No clear indication of higher noise due to flux trapping was found. A comparison of design c) before and after etching of slits to limit the pickup loop linewidth also showed no noticeable change in the noise properties, nor was A_p/L_p affected by more than the uncertainty from the slightly varying direct injection bonding positions.

Comparing magnetometers with different versions of design a) shows that leaving away the superconducting feedback coils increases A_p/L_p, which is due to a decrease

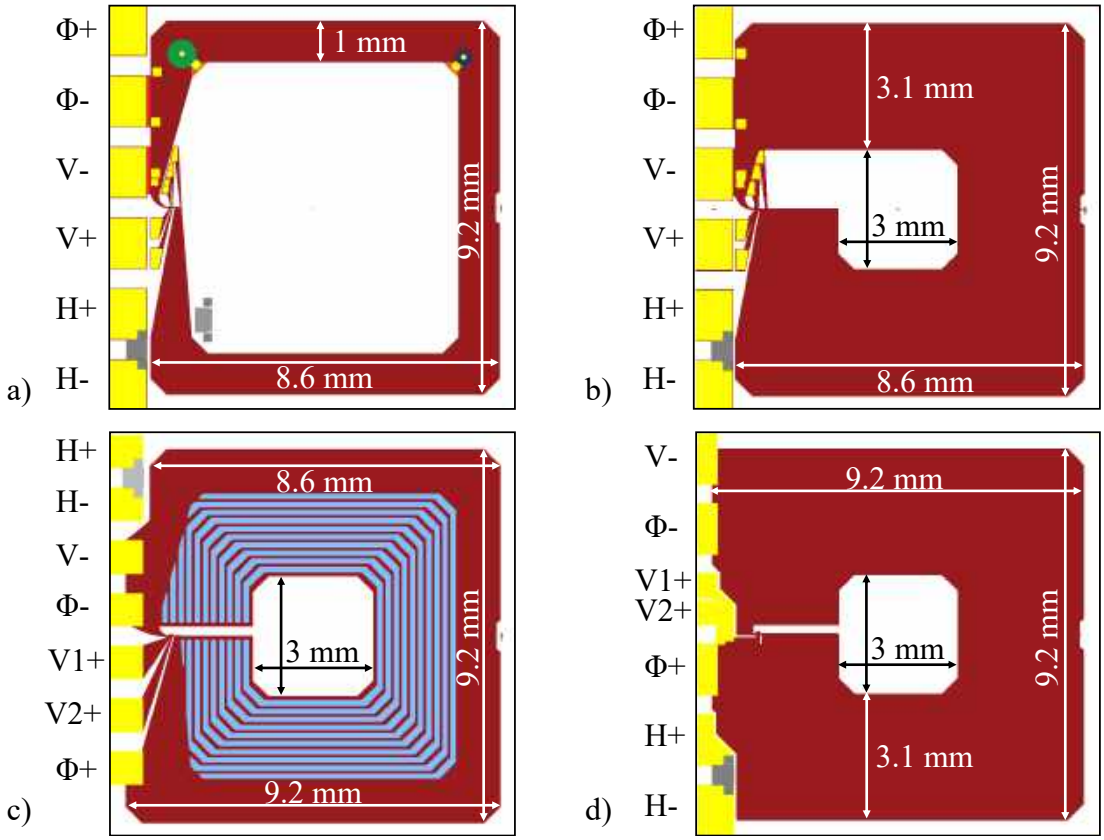

Figure 4.11: The different pickup loop designs and side contact pad layouts of the fabricated magnetometers. The YBCO pickup loop is shown in dark red, the gold contact pads in yellow and the heaters in grey. a) Thin loop magnetometer. The small superconducting feedback coil (blue) was removed and replaced with the orange colored film for magnetometers fabricated after Shin1, the big superconducting feedback coil (green) after Shin3. From Shin16 the side contact pads for $\Phi-$ and $V-$ were directly connected to the pickup loop (red). b) Wide loop magnetometer. c) Wide loop magnetometer with rearranged side contact pad configuration and no on-chip bonds. Etched slits are shown in light blue. d) Wide loop magnetometer with no on-chip bonds and a side contact pad layout that is suitable for the 7-channel system.

in L_p. Adding more film to the sides by connecting the $\Phi-$ and $V-$ side contact pads directly to the pickup loop leads to both a larger A_p and a lower L_p, and is thus advantageous[5]. In contrast, magnetometers Shin6-8 showed a reduction in A_p/L_p due to the damaged edges of the pickup loop decreasing the outer diameter D. The YBCO film of these magnetometers was sputtered by Ceraco (Ceraco ceramic coating GmbH, Ismaning, Germany) due to problems with our PLD system at that time, and the film did not cover the sample everywhere at the edges. Higher values of A_p/L_p can be obtained with the wide loop magnetometers, preferably by getting rid of the unnecessary contact pads inside the pickup loop and decreasing the gap size as was done in design c) and d). Simulations show that the positioning of the SQUIDs

[5]In earlier designs all edge contact pads were separated from the pickup loop by a 100 µm gap.

along the gap does not affect A_p/L_p, so the original position was maintained as it is a good compromise between higher film quality in the center and shorter contact pad connections on the side. A test sample furthermore showed that the side contact pad width could be reduced to 0.5 mm, which allowed the pickup loop to be increased in design d). The pickup loop with design d) nonetheless had a lower A_p/L_p than the one with design c). The reason for this is not understood, but may be related to the film quality also having an affect on A_p/L_p, for example through differently strong flux focusing. This may also be the reason for some of the differences in A_p/L_p for magnetometers with the same pickup loop design – besides the variations due to the direct injection bonding positions.

Additionally, the contact pad layout for operation in the 7-channel system was adjusted as shown in Fig. 4.11. The side contact pads $V+$, $V-$, $V1+$, and $V2+$ are for biasing and reading out the SQUID, $\Phi+$ and $\Phi-$ for applying the feedback current, and $H+$ and $H-$ for the heater. Designs a) and b) require on-chip bonds to connect the small contact pads to the large side contact pads used to connect the magnetometers to the cryostat wiring. By connecting $\Phi-$ and $V-$ directly to the pickup loop, two bonds could be avoided. Also, it turned out to be possible to make heaters very close to the edge of the sample. Moving the heater from inside the pickup loop to the edge removed two more bonds. The bond to $\Phi+$ can also be avoided by placing $\Phi+$ on the lower side of the pickup loop as in designs c) and d). This requires adjustments to the cryostat wiring, which were not done following the principle "never change a running system" (we had experienced problems with the wiring earlier). Lastly, the pad for $V+$ was split in two to choose one of the two SQUIDs. Both designs c) and d) do not require any on-chip bonds, however, design d) is more suitable for the 7-channel system because the sapphire wedges to which the SQUIDs are glued also contain 6 gold lines with the same spacing.

4.4.5 Magnetometer noise levels

Sixteen single layer high-T_c SQUID magnetometers with bicrystal Josephson junctions were fabricated. An overview of the measured white magnetic field noise levels in the dipstick at ∼78 K using the superconducting shield is given in Fig. 4.12. Each magnetometer contains 2 SQUIDs connected to the same pickup loop – the better SQUID is marked in blue. The SQUIDs that are currently employed in the 7-channel system are marked by stars. For each chip this is generally the SQUID with the better noise, but in some cases with very similar noise, the SQUID with the lower critical current was chosen instead. Fig. 4.12 furthermore shows that the achieved noise levels were generally lower when using a CeO_2 buffer layer.

The lowest white magnetic field noise level reached at ∼78 K in the dipstick is 44 fT$\sqrt{\text{Hz}}$ and was obtained for 3 magnetometers. The noise spectra of two of the magnetometers are shown in Fig. 4.13. The noise spectra of Shin14L is not shown because it contains several broad environmental noise peaks. The spectra for Shin16R contains sharp power line noise peaks at 100 Hz and harmonics. The noise peaks generally depend on the measurement day and are caused by nearby experiments and construction in the building. The low frequency noise can vary between magnetometers and mainly depends on how the sample is cooled down.

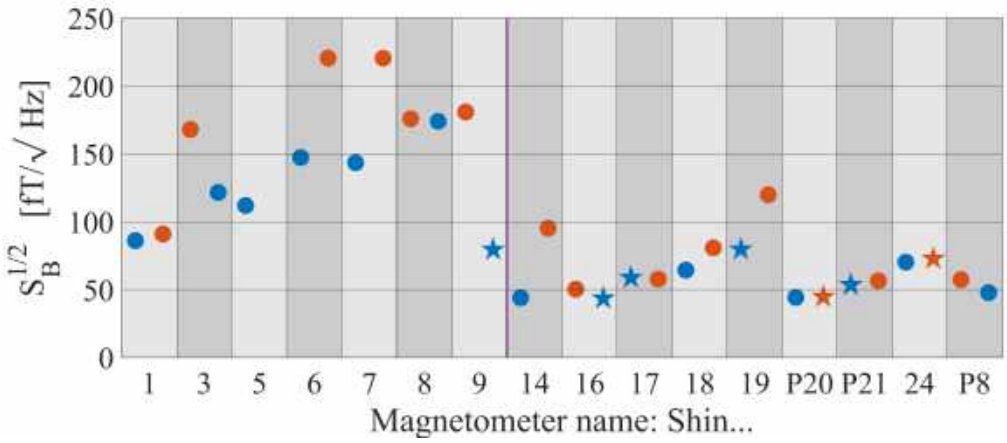

Figure 4.12: Measured white magnetic field noise levels of all fabricated magnetometers in chronological order. The better SQUID on each chip is colored blue. The SQUIDs currently operational in the 7-channel system are marked with a star. Magnetometers left of the purple line were fabricated without a buffer layer and to the right with.

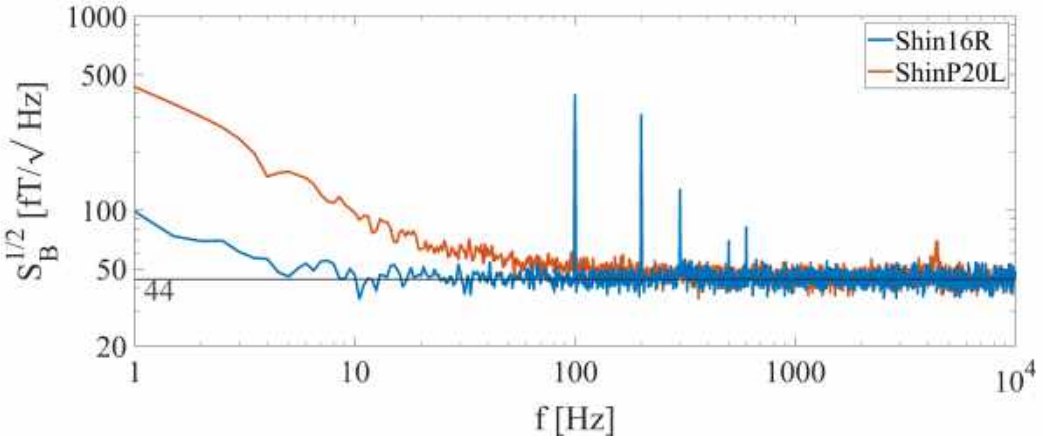

Figure 4.13: Magnetic field noise spectra of Shin16R and PShin20L measured in the dipstick at ∼78 K inside the superconducting shield.

The measured parameters for these three best magnetometers are summarized in Table 4.2. The low magnetic field noise level of Shin14L is mainly thanks to the good $A_p/L_p = 5.4$ mm^2/nH of the pickup loop, while Shin16R exhibits very good SQUID performance with $S_\Phi^{1/2}/L_c = 82$ μΦ$_0$/$\sqrt{\text{Hz}}$/nH. The best SQUID fabricated was a test SQUID with $S_\Phi^{1/2}/L_c = 70$ μΦ$_0$/$\sqrt{\text{Hz}}$/nH. Combining this SQUID with one of the better pickup loops fabricated suggests that a magnetic field noise level of 26-28 fT/$\sqrt{\text{Hz}}$ can be reached with this junction technology and substrate size. Unfortunately, I have not yet managed to fabricate such a good SQUID coupled to a wide pickup loop because of the difficulty of obtaining reproducible junction parameters.

Table 4.2: Measured parameters for the three best magnetometers with $S_B^{1/2} = 44$ fT/$\sqrt{\text{Hz}}$ at ∼78 K in the dipstick.

Name Shin	I_c [µA]	I_c^* [µA]	R_n [Ω]	$I_c^* R_n$ [µV]	I_b [µA]	ΔV [µV]	L_c [pH]	$S_\Phi^{1/2}$ [$\frac{\mu\Phi_0}{\sqrt{Hz}}$]	$S_\Phi^{1/2}/L_c$ [$\frac{\mu\Phi_0}{\sqrt{Hz}nH}$]	A_{eff} [mm^2]
14L	63.1	61.4	2.5	155	56.6	33	43.0	4.9	114	0.230
16R	31.0	30.4	3.7	114	28.4	25	75.0	6.1	82	0.292
P20L	25.0	28.1	3.4	95	21.2	25	53.4	5.7	106	0.264

4.5 Temperature dependence

Generally, the performance of a YBCO SQUID magnetometer can be improved by operating it at a lower temperature than 77 K. The $I_c^* R_n$ product, the modulation depth, and the transfer function increase, leading to lower noise levels. However, the magnetic field noise level does not decrease indefinitely. First, the effective area decreases when lowering the temperature because the kinetic inductance contribution to the coupling inductance decreases. This effect is significant and can not be ignored. Second, I_c^* increases with decreasing temperature and is often larger than the optimal value at that temperature. SQUID optimization is therefore preferably performed at the temperature the SQUID should later be operated at.

Here, I first present how we cool our high-T_c SQUID sensors placed inside an on-scalp MEG cryostat to temperatures below 77 K, then I discuss how temperature-independent sensor calibration can be achieved, and finally show the temperature dependence of several SQUID parameters including the magnetic field noise for an example SQUID.

4.5.1 Cooling on-scalp MEG sensors below 77 K

A very simple way to lower the operation temperature is to pump on the liquid nitrogen bath, which reduces the nitrogen vapor pressure and thus decreases the temperature of the nitrogen – see Fig. 4.14.

At 63 K the nitrogen undergoes a phase transition and becomes solid. Although it is possible to cool the nitrogen below 63 K by continuing pumping, Hales *et al.* found that while the temperature measured by a sensor immersed in the nitrogen further decreases, the temperature of a sensor placed on the outside of a base plate in direct thermal contact to the nitrogen remains at 63 K [199]. The reason is that the frozen nitrogen is fluffy like snow (or like cotton wool), and this consistency leads to a poor thermal contact with any surface. This also explains how a vacuum gap can easily form resulting in a thermal barrier [199]. The thermal barrier disappears as soon as the nitrogen melts.

To minimize the standoff distance, our high-T_c SQUID on-scalp MEG sensors are mounted on a sapphire plate in direct contact with the nitrogen bath, and we can therefore expect the lowest reachable operation temperature with pumping to be 63 K. In practise, we have measured a minimal temperature of 63 K on the sapphire plate, but the temperature on the SQUID chip can be several kelvins higher due

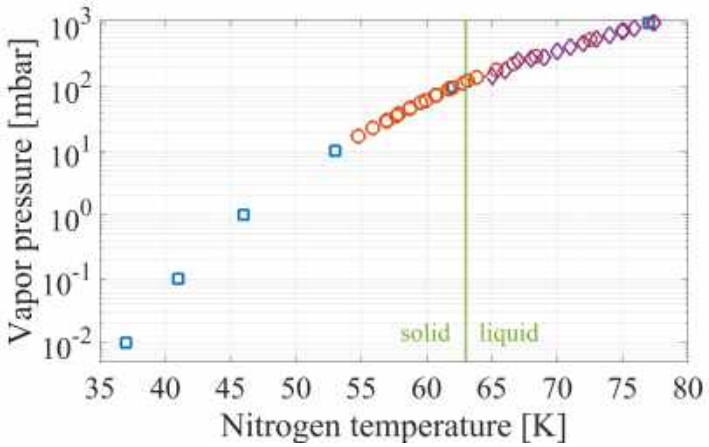

Figure 4.14: Relationship between nitrogen vapor pressure and the temperature of the nitrogen. Purple diamonds refer to values measured in our test cryostat, orange circles correspond to values from Ref. [197], and blue squares to values from Ref. [198]. The phase transition between solid and liquid at 63 K is marked by a green line.

to temperature gradients at the interfaces and the radiative heat load from room temperature.

4.5.2 Sensor calibration

High-T_c SQUID magnetometers are usually calibrated by measuring the effective area A_{eff}. However, A_{eff} is not a constant but varies with temperature because of the kinetic inductance contribution to L_c [159, 200]. Fig. 4.15a&b shows how L_c and A_{eff} measured for magnetometer Shin16R decrease when the temperature in the 7-channel cryostat is lowered. In the limited temperature range from 79 K to 72 K, L_c drops from 91 pH to 69 pH, which corresponds to a drop in λ from 490 nm to 380 nm, see Fig. 4.15c. The effective area of Shin16R follows L_c and decreases from 0.361 mm^2 to 0.284 mm^2. This 21% decrease clearly demonstrates that A_{eff} can not be measured at one temperature and used for sensor calibration at another temperature. A change in L_c is even noticeable between measurements in the dipstick with and without a superconducting shield. In principle, magnetometer calibration would therefore have to be performed at every operation temperature.

Since this is inconvenient, an alternative calibration approach has been developed. The approach is based on the operation of the magnetometer in a FLL with direct readout and using (long) direct injection of current into the SQUID loop for feedback. Note that this is how we normally operate the magnetometers during magnetic field measurements. The transfer function of a SQUID operated in a FLL with direct readout is according to Eq. (2.29) given by $V_\Phi^{FLL} = R_f/M_f$, where R_f is the feedback resistance (30 kΩ for the Magnicon electronics) and M_f the mutual inductance between the SQUID loop and the feedback coil. In the case of (long) direct injection into the SQUID loop, $M_f = L_c$, see §4.2. For calibration of a magnetometer, one is generally interested in the responsivity dV/dB (or its inverse). In our case the

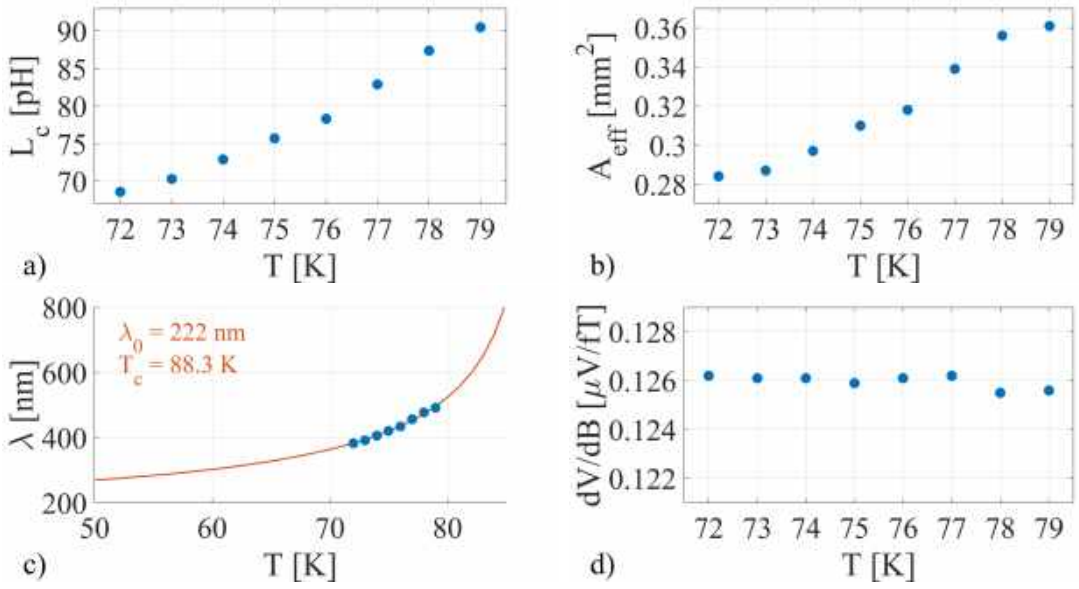

Figure 4.15: Temperature dependence of a) the coupling inductance, b) the effective area, c) the London penetration depth, and d) the responsivity. The sample is magnetometer Shin16R measured in the 7-channel cryostat.

responsivity can be calculated as:

$$\left(\frac{dV}{dB}\right)^{FLL} = \left(\frac{dV}{d\Phi}\right)^{FLL} \cdot \left(\frac{d\Phi}{dB}\right) = V_\Phi^{FLL} \cdot A_{eff} \approx \frac{R_f}{M_f} \cdot L_c \frac{A_p}{L_p} = R_f \cdot \frac{A_p}{L_p}, \quad (4.2)$$

which does not depend on L_c and thus temperature. The responsivity is measured with the same procedure as we use for A_{eff}: we vary the amplitude of a magnetic field applied with a calibrated Helmholtz coil and linearly fit the voltage response of the SQUID. This measurement gives directly $(dV/dB)^{FLL}$ and V_Φ^{FLL} does not need to be known (as it does when measuring A_{eff}). The responsivity of magnetometer Shin16R measured at different temperatures is shown in Fig. 4.15d. The responsivity varies less than 0.4% in the measured temperature range, thus making reliable one-time magnetometer calibration possible. This approach is now being used to calibrate all our single layer magnetometers. As a small part of the injected current again goes around the pickup loop (see also §4.4.4), the calibration needs to be redone every time the bonds on the chip or the sensor wiring is changed.

Totally unrelated to the calibration, I would like to point out that fitting the temperature dependence of λ shown in Fig. 4.15c with Eq. (2.38) allows the extraction of the low temperature London penetration depth λ_0 and the critical temperature T_c. In this case we find $\lambda_0 = 222 \pm 3$ nm and $T_c = 88.3 \pm 0.4$ K. Comparison of these parameters for different samples, or even SQUIDs on the same sample, may give some hints on how to achieve low λ values more reproducibly. To check the validity of Eq. (2.38), the temperature range needs to be extended and good knowledge of the sensor temperature needs to be guaranteed. The temperature stated here has been determined in a separate cooldown to avoid the introduction of noise and is the main source of uncertainty.

4.5.3 SQUID parameter temperature dependence

Lastly, we study how the performance of a SQUID depends on temperature T in the temperature range available by pumping on the test cryostat used. The SQUID presented here is a bare SQUID (no pickup loop) made on ShinP8 with a junction width $w_{JJ} = 0.9$ µm, a junction length $l_{JJ} = 1$ µm, a film thickness $t = 225$ nm, and a SQUID loop length $l_{sq} = 60$ µm. This SQUID was also part of the junction width optimization presented in §4.4.3.

Fig. 4.16a shows that I_c and I_c^* grow linearly with decreasing T. The $I_c^*(T)$ curve has a slope of -5.5 µA/K. The excess current is again slightly negative and becomes smaller with decreasing T.

The normal resistance is basically constant in this temperature range: $R_n = 3.61 \pm 0.07\ \Omega$. The dynamic resistance at the operation point (with the highest voltage modulation) R_d, on the other hand, increases when the SQUID is cooled. A strong increase can be found below 74 K where the resonance due to the STO substrate moves into the region with the highest voltage modulation. Contrarily, the maximal dynamic resistance of the I-V curve corresponding to integer flux seems unaffected by the resonance and grows continuously with decreasing T.

Both I_cR_n and $I_c^*R_n$ grow linearly with decreasing T, see Fig. 4.16c. The maximal voltage modulation depth first grows linearly too, but increases more rapidly below 73 K. This is probably again due to the resonance.

Fig. 4.16d shows how L, L_c, and L_{par} decrease with decreasing T because of the decreasing kinetic inductance contribution. The coupling inductance drops from 93 pH at 81 K to 55 pH at 68 K, while L drops from 111 pH to 65 pH. The parasitic inductance roughly halves in this temperature range. Again, one can calculate λ by combining the measured L_c and the simulated one. Fitting the temperature dependence with Eq. (2.38) gives $\lambda_0 = 199 \pm 2$ nm and $T_c = 86.4 \pm 0.2$ K.

The measured transfer function V_Φ shown in Fig. 4.16e follows the behaviour of the voltage modulation depth. The theoretical transfer function calculated using Eq. (2.23) predicts the behaviour well for temperatures above 73 K, but largely underestimates V_Φ at lower temperatures. This is again due to the resonance. The white flux noise level is shown in the same figure and decreases first rapidly when the SQUID is cooled, but then levels out. The theoretical curve based on the formulas in §2.4.5 and the measured I_c^*, R_n, R_d, and L predicts a faster decrease in noise at high temperatures than was measured, but approaches the measured values at lower temperatures. The decrease in flux noise from 12.5 $\mu\Phi_0/\sqrt{\text{Hz}}$ at 81 K to 3.7 $\mu\Phi_0/\sqrt{\text{Hz}}$ at 70 K is significant.

Lastly, we look at $S_\Phi^{1/2}/L_c$ for the SQUID, which is directly proportional to the magnetic field noise level, see Fig. 4.16f. Cooling causes again a large drop: $S_\Phi^{1/2}/L_c$ decreases from 134 $\mu\Phi_0/\sqrt{\text{Hz}}$/nH at 81 K to 66 $\mu\Phi_0/\sqrt{\text{Hz}}$/nH at 70 K. The value remains roughly constant for temperatures below 73 K. Using the responsivity of the SQUID magnetometer made on the same substrate ($dV/dB = 0.154$ µV/fT), we can estimate the magnetic field noise level the SQUID would have had if it had been coupled to that pickup loop. The magnetic field noise level would in that case have been 55 fT/$\sqrt{\text{Hz}}$ at 81 K, 39 fT/$\sqrt{\text{Hz}}$ at 78 K, and 27 fT/$\sqrt{\text{Hz}}$ at 70 K. Cooling the sensor can thus significantly improve the magnetic field noise level. Optimization

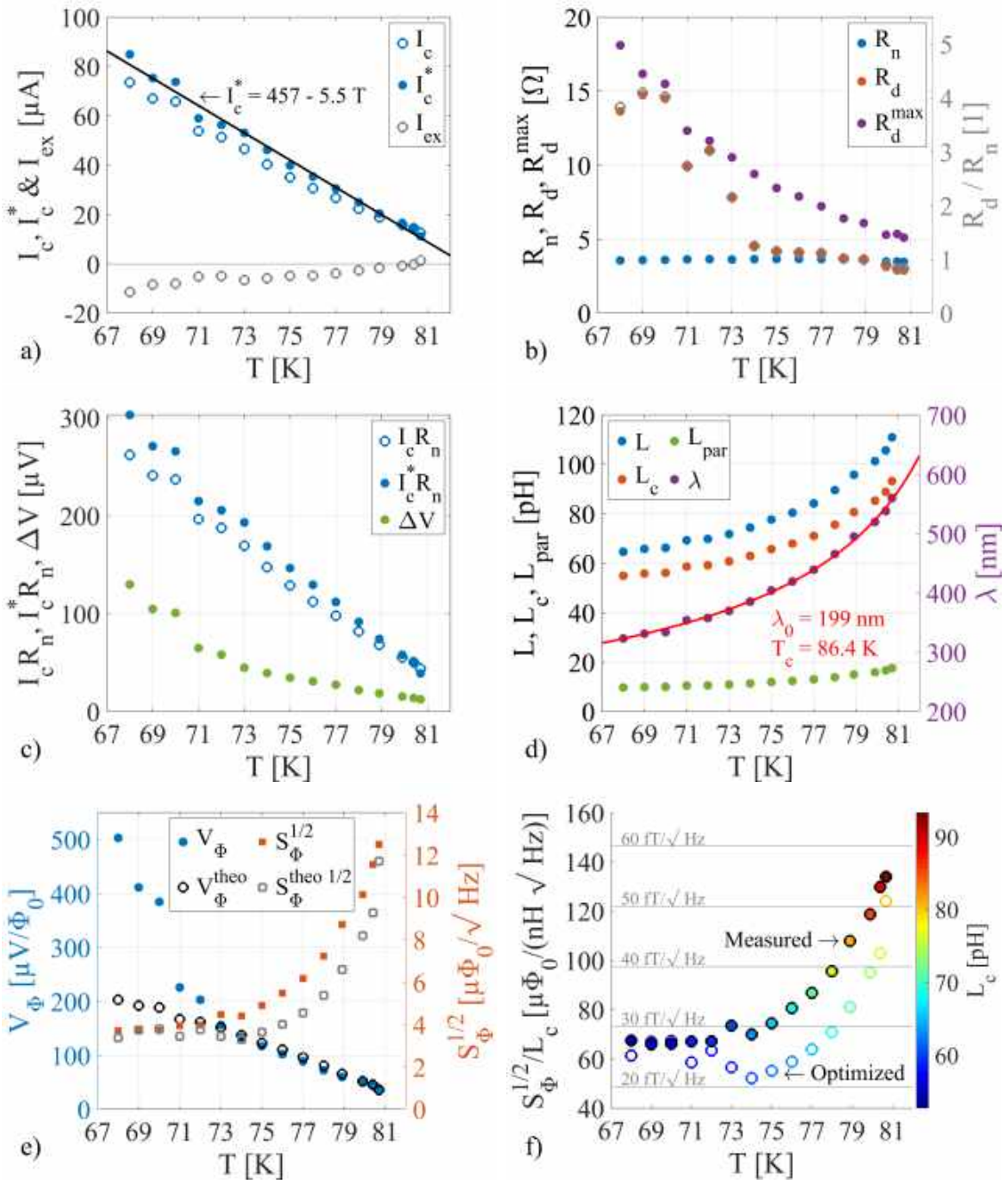

Figure 4.16: Temperature dependence of different SQUID parameters. a) Critical current (blue, empty), reduced critical current (blue, filled), and excess current (grey). The black line is a linear fit for $I_c^*(T)$. b) Left: Normal resistance (blue), dynamic resistance at the operation point (orange), and maximal dynamical resistance (purple). Right: R_d/R_n (grey, generally overlaps with the orange dots) c) I_cR_n (blue, empty), $I_c^*R_n$ (blue, filled), and voltage modulation depth (green). d) Left: SQUID inductance (blue), coupling inductance (orange), and parasitic inductance (green). Right: London penetration depth (purple) with fit using Eq. (2.38) (red). e) Left: Measured (blue) and theoretical (black, empty) transfer function. Right: Measured (orange) and theoretical (grey) flux noise. f) Measured $S_\Phi^{1/2}/L_c$ (filled circles) and optimized theoretical $S_\Phi^{1/2}/L_c$ (empty circles). The color corresponds to the coupling inductance.

of the coupling inductance while keeping all other parameters constant may lead to even lower noise levels – at least down to 74 K where a corresponding magnetic field noise level of 21 fT/$\sqrt{\text{Hz}}$ is predicted (see empty markers in Fig. 4.16f). The optimal L_c values are slightly lower than the real ones, suggesting that the SQUID loop length should be shortened.

4.6 Conclusion and outlook

In this chapter, the design, characterization, and optimization of our single layer SQUID magnetometers with a directly coupled pickup loop and grain boundary junctions for the 7-channel system was described. One of the first steps to make the sensor suitable for densely-packed multi-channel on-scalp MEG was to find a suitable feedback method. Direct injection of current into the SQUID loop was identified as the best on-chip feedback method with feedback flux crosstalk below 0.5%.

Direct injection turned out to be more than just a feedback method as it also allowed for inductance measurements. These measurements revealed that the kinetic inductance contributions in our SQUIDs vary strongly with film quality and temperature. Determination of all SQUID parameters by combining measurements and inductance simulations led to excellent agreement between experimental results and theoretical predictions. This allowed us to perform an in-depth magnetometer optimization. The SQUID and the pickup loop could thereby be optimized separately by minimizing $S_\Phi^{1/2}/L_c$ for the SQUID and maximizing A_p/L_p for the pickup loop. While the minimum in $S_\Phi^{1/2}/L_c$ as a function of L_c is rather broad, achieving low L_{par} and high quality junctions with fairly low critical currents is essential for reaching the lowest possible magnetic field noise values. Furthermore, the introduction of a CeO_2 buffer layer turned out to be a key element for more reproducible fabrication of low noise magnetometers. This is because the buffer layer decreased both I_{ex} and J_c, which made it easier to achieve the required low critical currents. Moving from the narrow linewidth pickup loop to a wide pickup loop allowed us to increase A_p/L_p. The optimized pickup loop design furthermore no longer requires any on-chip bonds, which is an advantage in an on-scalp MEG system.

The three best fabricated magnetometers all achieve a magnetic field noise level of 44 fT/$\sqrt{\text{Hz}}$ at 78 K. Based on the best test SQUIDs fabricated and the optimized pickup loop design, a magnetic field noise level just below 30 fT/$\sqrt{\text{Hz}}$ at 78 K is possible for this magnetometer type and junction technology. Future efforts should focus on increasing the reproducibility with which high quality junction with low critical currents can be fabricated. Fabricating test SQUIDs in the center of the substrate and then picking the optimal junction width and SQUID loop length to fabricate the final magnetometer did not allow us to obtain the same results for the magnetometer as for the test SQUIDs. The film and grain boundary quality is thus not uniform enough for this approach. Fabricating wide junctions and trimming them with argon ion milling may be a suitable alternative as this process has been found to be well controllable, although it takes time.

The effective area used to calibrate magnetometers was found to strongly vary with temperature because of the kinetic inductance contribution to L_c. An alternative

calibration method based on the responsivity and direct injection feedback was therefore developed that allowed for reliable temperature-independent one-time sensor calibration. Before we realized this, A_{eff} was considered a design dependent constant. Such wrong calibration led to underestimation of the magnetometer noise levels and to the conclusion that it is easy to reach noise levels below 50 fT/$\sqrt{\text{Hz}}$ [201]. While these noise levels are now reality, reproducibly fabricating such magnetometers is challenging.

The magnetic field noise level can be further decreased by pumping on the liquid nitrogen bath to reduce the operation temperature. For the example SQUID shown here, the corresponding magnetic field noise was 55 fT/$\sqrt{\text{Hz}}$ at 81 K, 39 fT/$\sqrt{\text{Hz}}$ at 78 K, and 27 fT/$\sqrt{\text{Hz}}$ at 70 K, meaning that the effect is significant. Since we also pump on the 7-channel cryostat, the sensor optimization should really be performed at the temperature the magnetometers should later be operated at. However, a SQUID could be characterized in the dipstick within an hour, while placing a SQUID in the cryostat and pumping on the vacuum usually took a full day. With the new test cryostat, the preparation time is reduced to around 4 hours. This enables more in-depth studies of the temperature dependence – not just of the noise, but also of the London penetration depth.

5

On-scalp MEG system development

This chapter presents the 7-channel on-scalp MEG system made using the bicrystal magnetometers detailed in the previous chapter. The system is described in Paper C. Here I give a summary and more details on the cryostat, the sensors and wiring, and the operation and performance of the system including crosstalk and noise. Next, biomedical measurements done with the system are summarized. Finally, the advantages and shortcomings of the 7-channel system are discussed, as well as implications on the next system, which is being built at the moment.

5.1 7-channel on-scalp MEG system

The 7-channel on-scalp MEG system was designed with two main goals in mind: small sensor-to-head standoff distance for improved signal levels and dense sensor packing for high spatial sampling. This was mainly achieved by designing the cryostat and the sensors including their wiring appropriately. The cryostat was designed by Justin Schneiderman and Lars Jönsson. Lars also built the cryostat, which was ready to be wired, filled with sensors, and characterized at the beginning of my PhD. I mainly worked on the sensors and together with fellow PhD student Christoph Pfeiffer on the 7-channel system characterization, troubleshooting, and operation optimization.

5.1.1 7-channel cryostat

Photographs of the cryostat are shown in Fig. 5.1. The cryostat contains a 0.9 liter nitrogen tank inside a vacuum enclosure, both of which are made of glass-fiber reinforced epoxy. Thermal insulation is provided by the vacuum space and several layers of superinsulation surrounding the nitrogen tank. Two strips of activated charcoal are attached to the sides of the nitrogen tank for additional cryopumping on the vacuum volume when the system is cold (see Fig. 5.1b).

For good thermal contact to the nitrogen bath, the sensors are mounted on sapphire wedges glued to a 44 mm diameter sapphire disk that is fixed into the sidewall of the nitrogen tank (see Fig. 5.1b-d). Thanks to the side-mounting, a wide

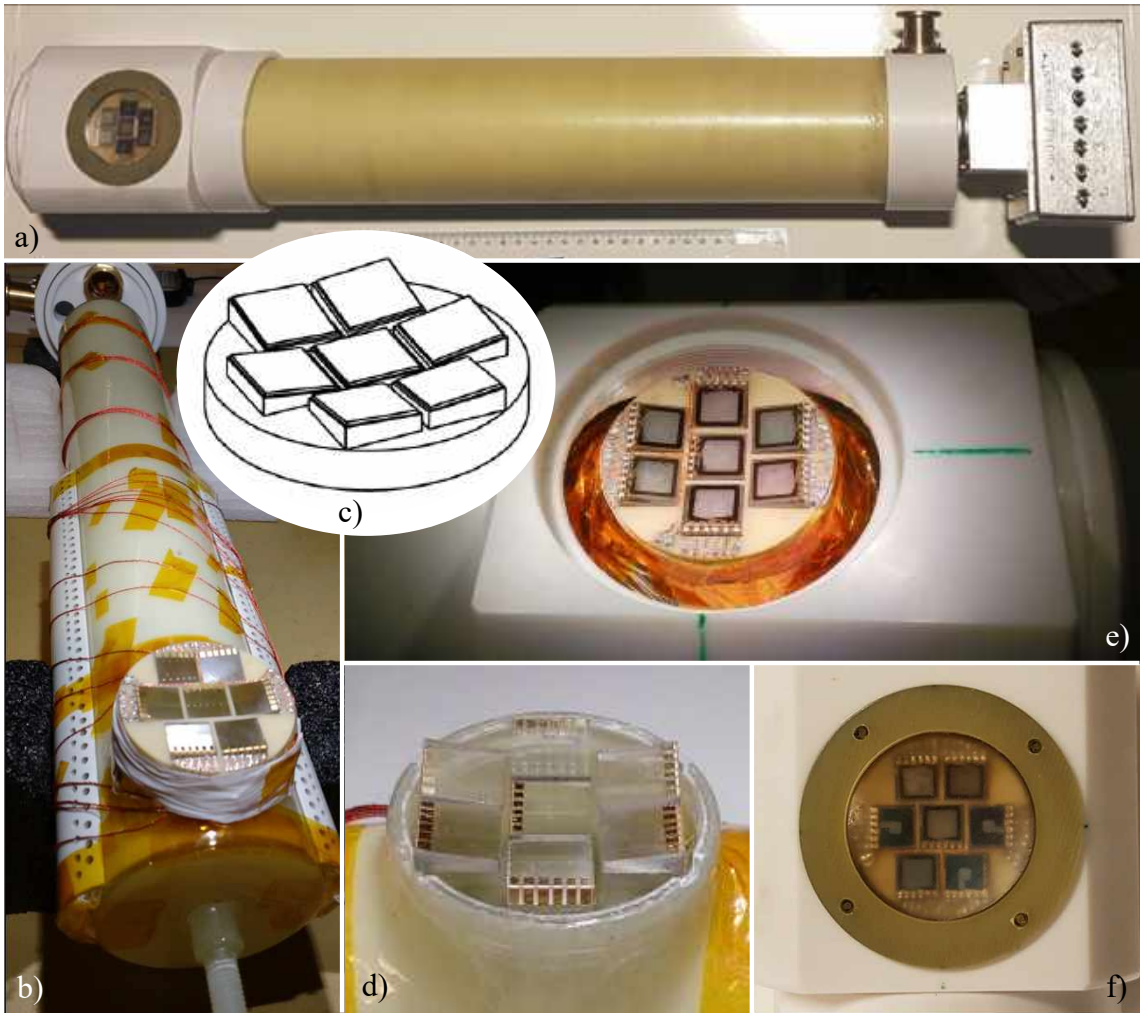

Figure 5.1: Photographs of the cryostat. a) The assembled cryostat with the sensors behind the vacuum window on the left, the cryostat body in the center, and inlets and breakout box to connect the SQUID electronics on the right. b) The nitrogen tank without the vacuum enclosure. Attached to the side are two strips of activated charcoal for cryopumping the vacuum enclosure. The sapphire disk with the wedges seals the nitrogen tank. c) Illustration of the wedge layout. d) The sapphire wedges glued to the sapphire disk. e) The magnetometers glued to the sapphire wedges and connected to the wires. f) The sensors with the vacuum window screwed in.

range of positions around the head can be covered without spilling the nitrogen. The seven 11 mm × 11 mm wedges are arranged in a dense hexagonal pattern with 1 mm edge-to-edge distance. The wedges are tilted towards the center to align to the surface of a sphere with 8 cm radius, which roughly corresponds to the average curvature of the adult head. A 0.4 mm thin concave window matching the curvature of the sensors seals the vacuum enclosure above the magnetometers. The distance between the sensors and the subject's head can be adjusted down to 1 mm with a screw connection.

The base temperature of ∼80 K on the sapphire wedges can be reduced to 70.1 K when pumping to ∼150 mbar on the liquid nitrogen bath through the nitrogen inlet. With a single filling, the cryostat remains cold (<80 K) for 16 hours. The temperature on the outside of the window at a distance 1-2 mm from the cold magnetometers is 6 °C in a 19 °C room temperature environment. When a person places his or her head to the window, the window's temperature rises within less than 30 s to match that of the head and thereafter does not feel cold. Due to the weak thermal link, the temperature of the sensors barely changes, however, it is advisable to fine-tune the SQUIDs and lock them in a FLL after the cryostat has been positioned to the subject's head. In case of bad vacuum, water vapor condensates on the window, which means that the cryostat needs to be warmed up and further pumping of the vacuum volume is required.

5.1.2 Sensors and wiring

The 7-channel system was populated step wise with the characterized single layer SQUID magnetometers described in the previous chapter. Several magnetometers from earlier batches were replaced by better magnetometers made later, which is why the system first only contained magnetometers with 1 mm wide pickup loop (see Fig. 5.2a) and later also some with 3.1 mm wide pickup loops (see Fig. 5.2b).

To avoid having to bond between the magnetometer chip and the gold metallization on the sapphire wedge, over-the-edge contacts as shown in Fig. 5.2c were fabricated. These contacts allow us to make the electrical connection using droplets of conducting silver glue. The over-the-edge contact pads are made by first manually rounding the substrate edge with the side contact pads. Next, a mask consisting of hand painted photoresist or appropriately cut kapton tape is made. Then a 15 nm titanium layer is sputtered, followed by a 100 nm gold layer, and finally the mask is removed.

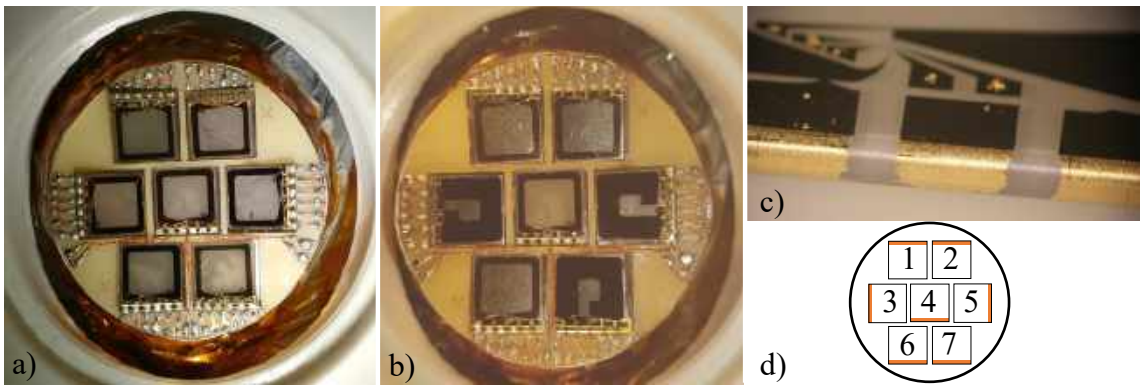

Figure 5.2: Photographs of the high-T_c SQUID magnetometers in the 7-channel cryostat. a) Earlier setup with only 1 mm wide pickup loop magnetometers. b) Present setup as presented in Paper C. c) Rounded substrate edge with over-the-edge gold contact pads. d) Numbering of the 7 magnetometer channels. The orange line indicates the edge contact pads.

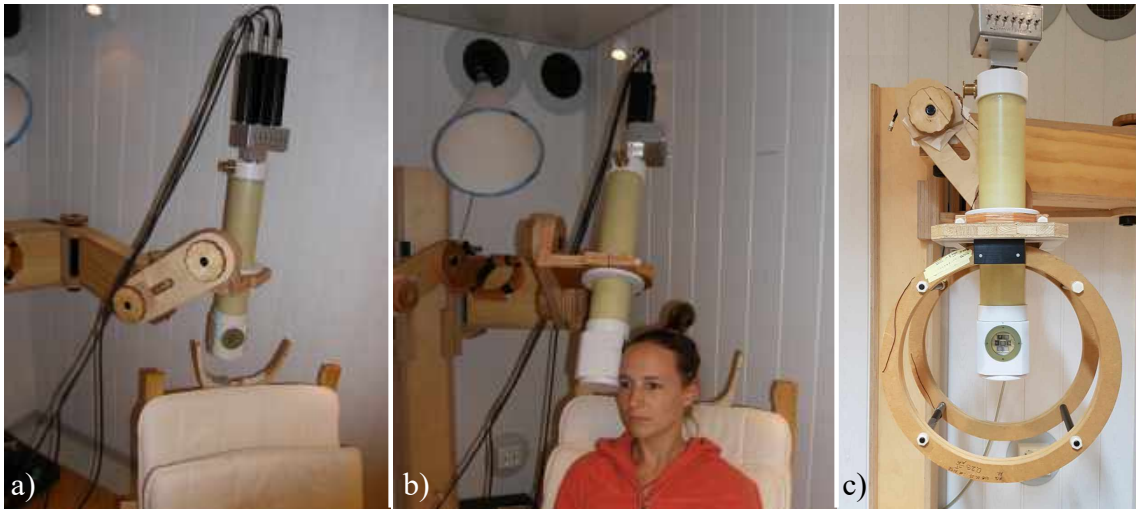

Figure 5.3: Photographs of the 7-channel system operation. a) The system, with the three SQUID electronics boxes connected to the breakout box, mounted on the wooden support structure. b) Cryostat placement for MEG measurements on the author. c) The Helmholtz coil used for calibration and magnetic field cancellation during cooldown.

On each chip, the SQUID with the better performance is connected to the side bond pads with very shallow bonds using a wedge bonder. Such bonds are also made for the direct injection feedback and for the heaters placed inside the pickup loop. The latest magnetometer design does not require any on-chip bonds, which eliminates the chance of bonds disconnecting and minimizes the standoff distance.

The 7 magnetometers are controlled and read out by three 3-channel SEL-1 SQUID electronics units – the same electronics as used for characterization. The electronics units are connected to a breakout box containing shunt resistors and diodes at the top end of the cryostat as shown in Fig. 5.3a. Six wires – three twisted pairs – lead to each chip: two for biasing and reading out the SQUID, two for the direct injection feedback, and two for the heater. The wires are wound around the nitrogen tank for thermal anchoring and lead to a printed circuit board (PCB) on the sapphire disk. On the PCB, short copper traces lead to the outer wedges, while the inner wedge is connected with three twisted pairs as visible in Fig. 5.2a&b. The connection between the PCB and the metallization on the wedge is made with silver wires and conducting silver glue.

The SEL-1 SQUID electronics has a gain of 4000, which is not enough for MEG measurements. Christoph Pfeiffer therefore built a dedicated amplifier and filter system that allows one to pick an additional gain of 4, 20 or 200, a high-pass filter with a cutoff frequency of 0.1 Hz, 1 Hz or 10 Hz, and a low-pass filter with a cutoff frequency of 100 Hz, 500 Hz, 1 kHz or 5 kHz [202]. The amplified and filtered MEG signal is then recorded with a NI-USB6259 data acquisition system from National Instruments (NI), Austin, USA.

5.1.3 Operation and performance of the 7-channel system

For system characterization and measurements, the 7-channel cryostat is mounted on a wooden articulated armature inside the MSR as shown in Fig. 5.3a&b. This allows both for secure and low vibration positioning during the cooldown and measurements, as well as freely adjustable cryostat placement to the subject's head during MEG recordings. The armature is made of wood to avoid magnetic disturbances and has already been used with the single channel cryostats [40].

Nitrogen is transferred from a pressurized dewar to the cryostat through a transfer tube. The filling is controlled by a person in the MSR. The cooldown procedure is important for the noise and will be described in more detail later. Once the cryostat is filled, the transfer is stopped, the transfer tube removed (once unfrozen), and the nitrogen inlet connected to the pump to reduce the temperature of the nitrogen bath as described in §4.5. The pumping pressure is typically chosen to be around 350 mbar corresponding to an on-chip temperature of around 72 K. At this temperature the voltage modulation depth of all SQUIDs is increased as compared to higher temperatures, and the bias current with the highest modulation depth does not exceed the electronics limit of 250 µA in any SQUID. The optimal bias currents vary strongly between the SQUIDs: for example from 3 to 236 µA in a typical measurement as presented in Paper C. The bias current giving the highest modulation depth and the feedback current necessary to couple one flux quantum into the SQUID loop are determined in every cooldown, however, the values are close to the ones specified in Paper C. We will now focus on the characterization of the system in terms of crosstalk, calibration, and noise.

Crosstalk

Feedback flux crosstalk was measured for all magnetometer pairs in the 7-channel system. One flux quantum was applied to the feedback of an exciting magnetometer in open loop configuration and the amount of flux coupled into the other sensors in FLL mode was measured. The full feedback flux crosstalk matrix is given in Paper C. Except for three magnetometer pairs, all pairwise feedback flux crosstalk values are below 0.2%. We attribute the increased crosstalk in these three pairs to wire crosstalk. This is especially clear for the wires carrying the feedback current to the central sensor (Ch4) and passing in between channels 3 and 6 (see Fig. 5.2). We considered this type of crosstalk low enough not to compensate for it.

Feedback flux crosstalk was not the only type of crosstalk encountered. A second type of crosstalk was found to arise from the ac bias reversal. The bias currents induce flux into neighboring magnetometers, which switches with the bias reversal frequency. This problem was solved by using synchronized clocks and a single bias reversal frequency (we pick 40 kHz). In this case the magnetic field from the bias currents switches between two states and just causes an additional flux bias. The flux bias Φ_b needs to be adjusted anyway, but in the case of a multi-channel system, one first needs to set all bias currents and put all channels into AC-bias reversal mode before adjusting Φ_b. Changing the bias current of one sensor may require readjustment of Φ_b in all sensors.

Lastly, crosstalk can arise from the mutual inductance between the pickup loops [203]. An external field B_i at sensor i creates a circulating current $I_i = B_i A_p^i / L_p^i$ in magnetometer i with a pickup loop effective area A_p^i and inductance L_p^i. This circulating current can couple into another magnetometer j through the mutual inductance M_{ji} of the two pickup loops and appears there as a magnetic field $B_{ji} = M_{ji} I_i / A_p^j$. The magnetic field crosstalk due to the mutual inductance between the pickup loops can thus be defined as:

$$C_{ji}^B = \frac{B_{ji}}{B_i} = \frac{M_{ji}}{L_p^i} \frac{A_p^i}{A_p^j} = k_{ji} \sqrt{\frac{L_p^j}{L_p^i}} \frac{A_p^i}{A_p^j}, \tag{5.1}$$

where the mutual inductance $M_{ji} = k_{ji}\sqrt{L_p^j L_p^i}$ and k_{ji} is the coupling coefficient. Simulated values for the magnetometers currently in the 7-channel system are given in Table 5.1. The mutual inductance simulation takes the sensor design, position, and orientation into account, but assumes a planar layout due to the reduced dimensionality of the simulation. For a magnetometer pair with the same pickup loop design one obtains $C_{ji}^B = C_{ij}^B$, otherwise the two values can differ. Magnetometers with a wide pickup loop cause less crosstalk than their narrow linewidth counterparts. As expected, the central sensor both experiences and causes the most crosstalk. Knowledge of this crosstalk matrix allows one to calculate the real external magnetic fields $\boldsymbol{B} = (B_1 \cdots B_7)^T$ from the measured values $\boldsymbol{B'} = (B'_1 \cdots B'_7)^T$ using $\boldsymbol{B'} = (C + I)\boldsymbol{B}$, where I is the identity matrix.

This third type of crosstalk can be eliminated by cancelling the circulating current in the pickup loop with the feedback applied for operation in a FLL [203]. However, this can not be achieved using direct injection of current as the directly injected current can take two paths: either through the SQUID loop, where the circulating current is cancelled as desired, or through the larger part of the pickup loop, where the circulating current is instead increased. To cancel the circulating current everywhere in the pickup loop, a feedback coil that is coupled to the pickup loop is needed. This has been successfully implemented in low-T_c SQUID systems with flux transformers [203–205]. In contrast, the feedback methods for multi-channel high-T_c SQUID

Table 5.1: Simulated magnetic field crosstalk C_{ji}^B in a 7-channel system magnetometer j (rows) due to the circulating current in the pickup loop of magnetometer i (columns) in percent. Wide loop magnetometers are marked bold, as are $|C_{ji}^B|$ values larger than 1%.

j \i	Ch1	Ch2	**Ch3**	Ch4	**Ch5**	Ch6	**Ch7**	Sum
Ch1	-	**-1.86**	-0.61	**-1.34**	-0.12	-0.18	-0.06	-4.16
Ch2	**-1.86**	-	-0.11	**-1.34**	-0.61	-0.12	-0.08	-4.13
Ch3	**-1.17**	-0.22	-	**-1.64**	-0.08	**-1.16**	-0.11	-4.39
Ch4	**-1.34**	**-1.34**	-0.86	-	-0.85	**-1.18**	-0.53	-6.09
Ch5	-0.23	**-1.16**	-0.08	**-1.65**	-	-0.22	-0.53	-3.87
Ch6	-0.18	-0.12	-0.61	**-1.18**	-0.11	-	-0.87	-3.07
Ch7	-0.11	-0.17	-0.11	**-1.02**	-0.53	**-1.69**	-	-3.64
Sum	-4.89	-4.87	-2.38	-8.17	-2.30	-4.55	-2.18	[%]

systems presented in Ref. [189] and Paper A only aimed at minimizing feedback flux crosstalk, but they do not eliminate crosstalk due to the mutual inductances of the pickup loops.

Nonetheless, it is sensible to use direct injection feedback for single layer high-T_c SQUID magnetometers since it allows for temperature-independent sensor calibration as shown in Paper B. The mutual inductance crosstalk can instead be accounted for using the crosstalk matrix as described above. The matrix entries do not depend on temperature because the kinetic inductance contribution to the total pickup loop inductance is below 2%. Since we were not aware of mutual inductance crosstalk and its magnitude at the point Paper C was published, this type of crosstalk was not accounted for in the measurements.

Calibration

The responsivity dV/dB is used to temperature-independently calibrate the sensors as described in §4.5.2 and Paper B. The responsivity measurement was repeated with the sensors placed inside the 7-channel system. Since the sensors are tilted with respect to each other, the orientation of the Helmholtz coil was varied and the maximal responsivity corresponding to alignment of the sensor normal with the applied field was selected. The measured values are given in Table 5.2 and were within 0.5% over multiple cooldowns and for different applied magnetic fields (0.2-10 nT peak-to-peak).

Comparing the responsivities measured in the cryostat to those in the dipstick shows differences of up to 20.4%, see Table 5.2. Three reasons can explain these differences. First, mutual inductance crosstalk decreases the measured responsivity. This can be accounted for using the last (Sum) column in Table 5.1 because a homogeneous magnetic field B is applied, resulting in the corrected responsivities shown in Table 5.2. Second, flux focusing by neighboring YBCO films increases the measured responsivity. This explains the largely increased responsivity of the central sensor (channel 4) that has the most YBCO films around it. Third, the exact position where the direct injection feedback current is applied changes the responsivity. In the dipstick measurements the direct injection was applied as close to the SQUID as possible to minimize the error in determining L_c. In the cryostat the connections are made to the side contact pads with silver glue.

Noise

Lastly, we look at the noise performance of the magnetometers in the 7-channel system. Fig. 5.4 shows the magnetic field noise spectra of all 7 magnetometers measured in FLL mode with synchronized ac bias reversal. To avoid underestimation of the noise, the measured responsivities without the mutual inductance corrections are used. The white noise levels are between 50 and 130 fT/$\sqrt{\text{Hz}}$ and the 1/f corner frequency is around 8 Hz.

In the dipstick with the superconducting shield (and at a higher operation temperature), the measured noise levels were between 44 and 80 fT/$\sqrt{\text{Hz}}$ for these 7 magnetometers. For comparison, the dipstick noise trace from the 44 fT/$\sqrt{\text{Hz}}$ magnetometer (channel 2) is shown in black. Generally, the low frequency noise

Table 5.2: Measured responsivities dV/dB of the magnetometers in the 7-channel cryostat (first row) and in the dipstick (second row). The third row states the percentual increase/decrease in the responsivities in the cryostat as compared to the dipstick. The forth row gives the responsivities in the 7-channel cryostat corrected for mutual inductance crosstalk.

Channel	1	2	3	4	5	6	7
Shin	19L	16R	P20R	9R	P21L	17L	24R
dV/dB cryostat [µV/fT]	0.124	0.124	0.154	0.130	0.154	0.119	0.151
dV/dB dipstick [µV/fT]	0.126	0.117	0.152	0.108	0.144	0.124	0.141
Change cryostat-dipstick	-1.6%	6.0%	1.3%	20.4%	6.9%	-4.0%	7.1%
Corrected dV/dB [µV/fT]	0.129	0.129	0.161	0.138	0.160	0.123	0.156

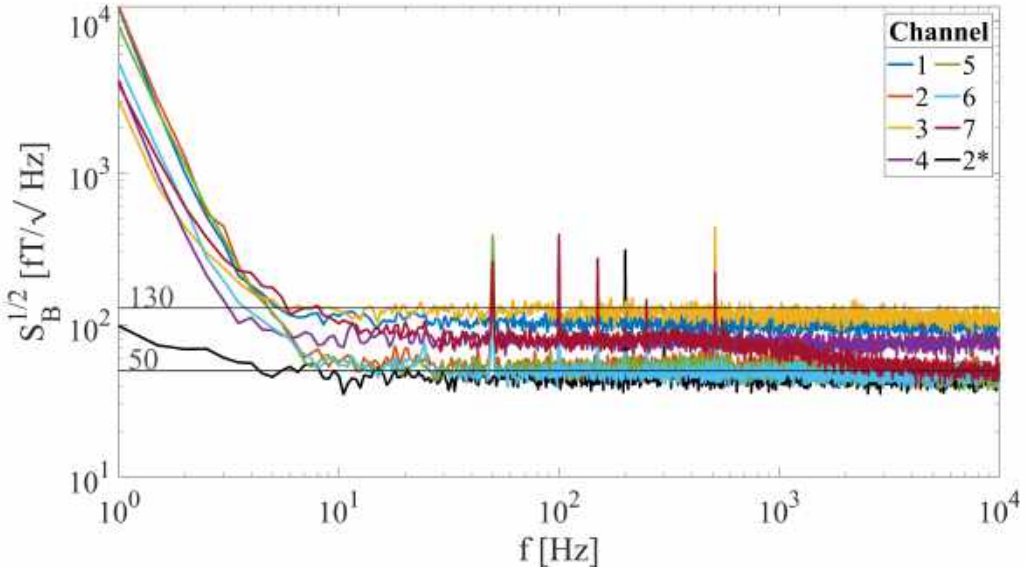

Figure 5.4: Magnetic field noise spectra of the magnetometers in the 7-channel system. For comparison the spectra of the channel 2 magnetometer measured in the dipstick with superconducting shield is plotted in black (indicated as 2*).

and the 1/f corner frequency is higher when no superconducting shield is used, as is necessarily the case for the 7-channel cryostat when in operation. The SQUIDs are also more likely to trap flux when cooled without the superconducting shield. This leads to increased noise levels that may decrease to lower values at higher frequency like in the case of channel 7 in Fig. 5.4.

The risk of trapping flux while cooling can be decreased by reducing the background magnetic field to as close to zero as possible. This is what is done with the superconducting shield, however, such a shield is not available for the 7-channel cryostat. We instead use the Helmholtz coil to zero the remnant magnetic field in the MSR as shown in Fig. 5.3c. The field is measured with a fluxgate and was found to have an amplitude of up to 10 nT. Once the SQUIDs are cold, the compensation field is slowly ramped down and the coil is removed. The noise traces in Fig. 5.4 were

measured after cooling with background field compensation. Additionally, we have found that cooling the magnetometers slowly (around one hour to fill the cryostat) can lead to less flux trapping. The cryostat is thereby tilted slightly such that the windows with the SQUIDs faces upwards and the sensors are first cooled with nitrogen gas. Lastly, we minimize the number of times the MSR door is opened to avoid trapping flux.

5.2 Applications

The 7-channel high-T_c SQUID-based on-scalp MEG system was used for three different types of applications. First, proof-of-principle MEG recordings were made at Chalmers to demonstrate the feasibility of our 7-channel system for on-scalp MEG. These recordings are published in Paper C. Second, MEG measurements with both the 7-channel system and a commercial full-head low-T_c SQUID-based MEG system were made and compared. These benchmarking recordings were performed at NatMEG, the Swedish national facility for magnetoencephalography at Karolinska Institute in Stockholm, and are described in Paper III, Paper IV, and Paper V. Lastly, the system was also used at Chalmers for other biomagnetic measurements than MEG, which shows that future projects involving the 7-channel system are not necessarily limited to MEG.

5.2.1 Proof-of-principle MEG recordings

To show that we can measure brain activity with the 7-channel system, we recorded induced alpha activity and auditory evoked fields, which are two simple and well established paradigms. The recordings were performed in our 2-layer MSR on a single subject each, with informed consent. The measurements were conducted in compliance with national legislation and the code of ethical principles (Declaration of Helsinki) and were approved by the regional ethical authority in Gothenburg, Sweden (dnr 1143-16). Details on the measurements can be found in Paper C and in Christoph Pfeiffer's thesis [202] – he was the one who led these two measurements.

Induced alpha activity

Same as D. Cohen [17], we chose alpha activity for the first MEG measurements with the 7-channel system because such activity can simply be induced by closing the eyes and is of high signal amplitude. For each trial, the subject was asked to keep his eyes closed for 30 s and then look at a picture of a forest for 30 s. Instructions to switch between *eyes closed* and *eyes open* were given verbally, and a total of 30 1-min-trials were recorded. The cryostat was aimed at the back of the subject's head where the highest signal magnitude can be expected. Fig. 5.5a shows the averaged time-frequency spectrum of the 30 trials recorded with channel 6. The alpha activity with a spectral density of more than 400 $\mathrm{fT}/\sqrt{\mathrm{Hz}}$ around 10 Hz is clearly suppressed once the subject opens his eyes. The suppression is even visible on a single trial level when applying a bandpass filter from 8 to 12 Hz, see Fig. 5.5b. The signal strength

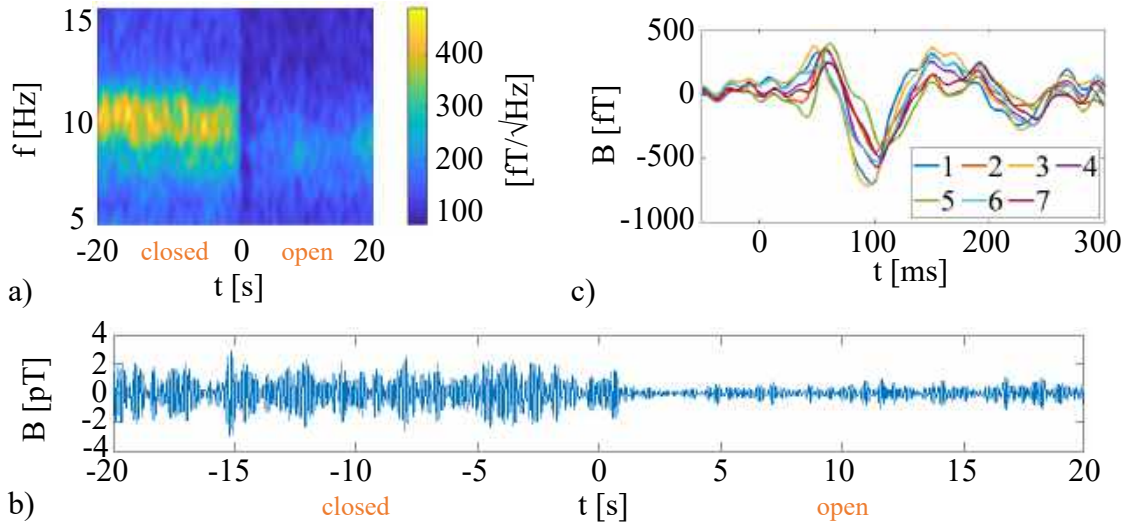

Figure 5.5: a) Time-frequency plot of induced alpha activity averaged over 30 trials and measured with channel 6. b) Single time trace of induced alpha activity measured with channel 6. c) Averaged auditory evoked fields from all 7 channels.

of the recorded alpha activity is similar to what has been recorded earlier with a single-channel high-T_c SQUID system [40].

Auditory evoked fields

As a second proof-of-principle measurement, another subject was presented with 1200 single tone stimulations to the right ear, while the cryostat was placed slightly above the left ear. The tones had a frequency of 1 kHz, a duration of 400 ms, and were presented every second with ±10 ms jitter. To avoid habituation, one in a set of five stimulations was replaced by a 1.2 kHz odd-ball tone. The measured brain activity from the 1 kHz tones was than processed and averaged as detailed in Paper C, and is shown in Fig. 5.5c. A strong negative peak in the magnetic field signal called *N100m* appears at roughly 100 ms after the start of the tone. The amplitude of this peak is with around 700 fT strongest in channels 1 and 3. This is slightly higher, but comparable to the ∼600 fT that have been measured with a single-channel high-T_c SQUID system on another subject [167].

5.2.2 Benchmarking MEG recordings

The next step after the successful proof-of-principle measurements was to compare MEG recordings from the 7-channel high-T_c SQUID system to those from a conventional low-T_c SQUID system. These benchmarking recordings were done in collaboration with neuroscientists at NatMEG in Stockholm. Their low-T_c MEG system is an Elekta Neuromag TRIUX (Elekta Oy, Helsinki, Finland, now Megin Oy) housed inside a 2-layer MSR. The system contains 306 sensors arranged in triplets consisting of a magnetometer and two orthogonal planar gradiometers that are placed at 102 different locations covering the full head. Typical white noise levels for the magnetometers are 3.5 fT/$\sqrt{\text{Hz}}$ and for the gradiometers 3.5 fT/(cm$\sqrt{\text{Hz}}$) [25]. The

sensor triplets have an average spacing of 35 mm and are located on average 18 mm from the room temperature surface [25].

In most cases our 7-channel high-T_c SQUID system cannot compete against this commercial system with its superior sensor noise levels and full head coverage. The main purpose was therefore to focus on the benefits of being one order of magnitude closer to the head and having higher spacial sampling. Since the high-T_c SQUID system covers only a small area, the chosen paradigm was first recorded with the low-T_c SQUID system, the brain activity of interest was then localized, and the expected field distribution on the scalp calculated to guide the placement of the high-T_c SQUID system [61]. It is worth noting that the field patterns are more focal closer to the sources and a radial projection to the scalp surface is normally not enough to find the extrema in the magnetic field distribution [61].

Earlier measurements presented in Paper II with a single-channel high-T_c SQUID system showed that sensor-level comparisons of recorded brain responses to electrical median nerve stimulations typically exhibited the expected signal amplitude increase when measuring closer to the brain. The measurements also reveled that a method to accurately assess the locations and orientations of the on-scalp MEG sensors is necessary. Such a method is implemented and evaluated in Paper III using the 7-channel system and will be described shortly. Subsequently, two studies that aim at exploring the benefits of on-scalp MEG as compared to conventional MEG are summarized. These studies are presented in Paper IV and Paper V, and indicate that our on-scalp MEG system allows retrieval of information unavailable to conventional MEG. Photographs from the MEG measurements with both the low-T_c and the high-T_c SQUID-based systems are shown in Fig. 5.6.

On-scalp MEG sensor localization

Localization of the sources in the brain creating the magnetic fields sampled on the subject's scalp requires precise knowledge of the sensor positions with respect to landmarks on the subject's head. In conventional MEG, the head is localized relative to the known sensor array layout using magnetic dipole-like coils attached to the head. For on-scalp MEG, the sensor positions and orientations are adjusted to each individual head and can thus vary. It therefore makes sense to instead localize the sensors relative to the head by inverting the conventional head localization procedure as suggested in Ref. [206]. We implemented the method using 10 magnetic dipole-like coils (see Fig. 5.6c&d for a photograph) and achieve, with 1 s long field recordings, a position accuracy better than 2 mm and an orientation accuracy better than 3°. Since the 7-channel system is a rigid structure, the sensor localization procedure can be improved using the known design to decrease the position and orientation uncertainty to less than 1 mm and 1°, respectively. It is furthermore possible to also extract the sensor responsivities, although this requires careful calibration of the magnetic dipole-like coils and crosstalk needs to be taken into account as described in §5.1.3 in the subsection on *Calibration*. Finally, the sensor localization method is used to perform source localization of the brain response to stimulation of the median nerve. The resulting equivalent current dipole fit based on high-T_c SQUID recordings from four different positions with 6 sensors each (one sensor had trapped flux) was within 4.2 mm of the one obtained with the Elekta system. As discussed

Figure 5.6: Photographs from the MEG measurements at NatMEG in Stockholm. a) The Elekta Neuromag TRIUX low-T_c SQUID-based full-head MEG system in the background and our 7-channel high-T_c SQUID-based system on the wooden fixture. b) Subject in the low-T_c SQUID system. c) EEG cap with EEG electrodes (with red cables), magnetic dipole-like coils for sensor localization highlighted in green, and red markings for cryostat positioning. d) Close-up photograph of the magnetic dipole-like coils. e) Subject prepared for a high-T_c SQUID recording. f) Subject during a high-T_c SQUID recording as seen through the MSR camera.

in Paper III, this lays well within the 3-11 mm variability found between different low-T_c MEG systems and recordings.

Discrimination accuracy for stimulation of phalanges

In Paper IV we compare the discrimination accuracy for neural activity patterns obtained from stimulating five different phalanges of the right hand. We hypothesized that on-scalp MEG might be able to resolve the very close sources better than conventional MEG thanks to the closer proximity and higher spatial sampling, thus allowing for better classification. However, we found that the discrimination accuracy was not better when focusing on activity in proximity of the P60m component, which is a large characteristic peak appearing around 60 ms after the stimulation onset.

Unexpectedly, we observed better classification performance for the on-scalp MEG system than the conventional system when looking at the time interval 10 to 20 ms after stimulation onset. This interval corresponds to the P16 peak in EEG that is normally not observed in conventional MEG, thus suggesting that on-scalp MEG may be sensitive to sources invisible to conventional MEG.

Detection of interictal epileptiform discharges

Detection of epileptic activity is an established clinical application of MEG [14]. MEG has been found to be better at detecting interictal epileptiform discharges (IEDs) than EEG with IEDs detected in 72 % of a set of epilepsy patients using MEG compared to 61 % for EEG [207]. In Paper V we present the first-ever on-scalp MEG recordings on a epilepsy patient and evaluate the potential added value of using on-scalp MEG. One hour measurements of resting state activity were recorded with both the full-head low-T_c SQUID system and the 7-channel high-T_c SQUID system centered at the positive IED peak-field position as determined from the low-T_c SQUID recording. In both cases, EEG was recorded simultaneously. In the low-T_c SQUID recording, 24 IEDs were detected, of which 8 were only seen by MEG and not EEG. Using a novel machine learning-based IED detection algorithm, 47 IEDs could be identified in the noisier on-scalp MEG data, of which 31 were only detected by MEG. Our on-scalp MEG system thus allowed identification of almost twice as many IEDs as the conventional system, hence showing that on-scalp MEG may improve non-invasive epilepsy evaluation.

5.2.3 Other biomagnetic measurements

SQUIDs can be used to measure magnetic signals originating from other organs than the brain such as the heart (magnetocardiography), peripheral nerves (magnetoneurography), liver (liver susceptometry), lungs (magnetopneumography), stomach (magnetogastrography), and intestine (magnetoenterography) [208]. In principle, our 7-channel system could be used for these applications as well. We have performed magnetocardiography (MCG) and fetal MCG measurements inside our magnetically shielded room using the 7-channel on-scalp MEG system.

Magnetocardiography

MCG is used routinely in some hospitals to identify abnormalities in the heart's electrical potential waveform and diagnose heart diseases [209]. A 7-channel high-T_c SQUID-based MCG system has furthermore been built more than 20 years ago [210]. Using gradiometers, it was shortly after even possible to measure in unshielded environments, which means that the system cost can be reduced immensely as no MSR is required [211, 212].

We performed MCG measurements in student labs to demonstrate the SQUID's ability to sense magnetic fields. Compared to brain signals, the heart signal is much easier to detect: we measured peak-to-peak signal amplitudes of up to 100 pT using the 7-channel system. Results vary between individuals and depend on the system placement.

Fetal magnetocardiography

During my pregnancy with Felicia we also tested if it was possible to detect her heartbeat signal with the 7-channel system. This was a pilot investigation that was initiated out of my own curiosity and I was aware of the risks. Due to the passive and non-invasive nature of the magnetic field measurement performed during fetal MCG, the procedure can generally be regarded as safe, and the potential risk to the mother and the fetus are understood to be minimal.

For the measurements I held the cryostat to my abdomen and tried not to breath during the short measurement sequences as breathing causes a large drift in the magnetic field signal. A measured heartbeat signal is shown in Fig. 5.7. Both the fetal and maternal heartbeat are clearly visible. The fetal heartbeat signal is weaker than the maternal one, and has a higher rate: here 130 bpm compared to 66 bpm. This data was taken at a gestational age of 31 weeks and 2 days. Both heartbeat signals were visible in the raw trace, however, to make the peaks more visible, the drift was subtracted and a moving average was performed. Using more advanced signal processing, it is possible to denoise the signal and even separate the fetal and the maternal heart signal [208, 213].

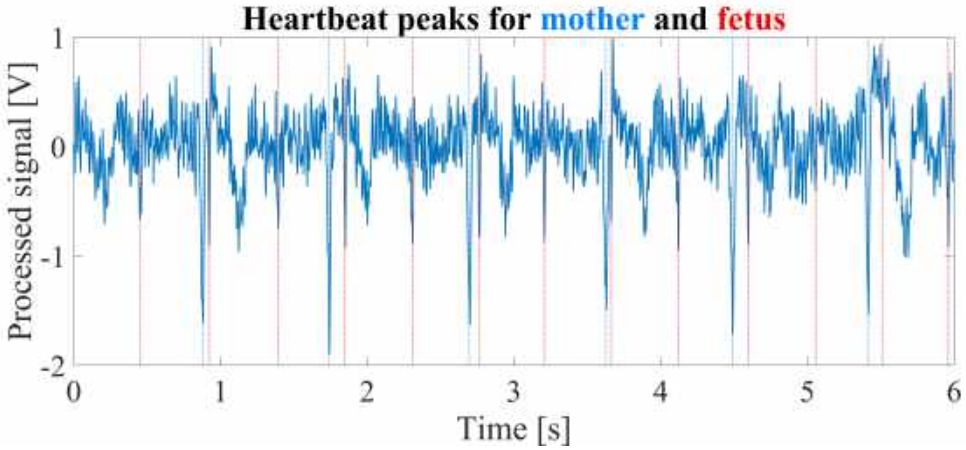

Figure 5.7: Fetal MCG signal at a gestational age of 31 weeks and 2 days. The vertical blue lines mark the heartbeat peaks for the mother and red lines for the fetus.

Fetal MCG can help with the early detection of congenital heart anomalies and allows one to study the progress of the disease intra-uterine [214]. Furthermore, it can be used to classify fetal arrhythmias [209, 214]. The feasibility of a high-T_c SQUID-based fetal MCG system that can be operated in unshielded environment and using a cryocooler was investigate in Ref. [215], however, they concluded that the SQUID sensitivity was not good enough when operated without shielding. Recently, an OPM-based fetal MCG system using a person-sized, cylindrical shield instead of an MSR was presented [216]. Such a shield could also be an option for high-T_c SQUIDs.

5.3 Future high-T_c SQUID-based MEG system

The biomedical applications described in the previous section proved that the 7-channel on-scalp MEG system is a useful tool. Its main benefits are the excellent standoff distance and the dense spacial sampling. As discussed in Paper C, the standoff distance of 1-3 mm is much smaller than the 6 mm or more of other reported multi-channel MEG systems [49, 50, 217], and the center-to-center distances between adjacent sensors of 12.0 mm vertically and 13.4 mm diagonally are smaller than the spacing of at least 13-15 mm in the said systems. Furthermore, the high-T_c SQUID system can be operated in a standard MSR without the need for continuous active field cancellation as is required for on-scalp MEG OPMs [49, 50], and the SQUIDs boost an intrinsically high bandwidth of several kHz, which is only limited by the readout electronics. Additionally, the system is portable and has a long enough hold time for a long day of measurements.

Nonetheless, several improvements for the design of a next generation high-T_c SQUID-based on-scalp MEG system emerged. First, more channels for a larger coverage are desirable. This would allow reduction of the need to move the system and perform multiple recordings to spatially sample the area of interest. A cryostat that can house 21 high-T_c SQUID magnetometers is being built at the moment. The idea is to use both the 7-channel system and the 21-channel system simultaneously, and ultimately reach full-head coverage with several such modules. To facilitate dense packing of the individual cryostats, the sensors of the 21-channel system are placed at the bottom face of the cryostat and not on the side as for the 7-channel system.

Second, while the sensor noise levels were sufficient for MEG recordings, lower noise levels are in any case beneficial. Reaching noise levels of 10 fT/$\sqrt{\text{Hz}}$ or less for YBCO SQUID magnetometers requires either larger substrates (at least 20 mm × 20 mm [152]) or flux transformers. Since larger substrates go against the idea of dense spacial sampling, we aim to use flux transformers in the next generation system. The development of high-T_c SQUID magnetometers with inductively coupled flux transformers for the on-scalp MEG system is described in the next chapter. The design of these new magnetometers should include a feedback method that allows cancellation of the mutual inductance crosstalk and appropriate sensor calibration needs to be investigated.

Third, a more compact readout electronics with 10 channels was bought from Cryoton Co. Ltd., Moscow, Russia. The electronics is a flux modulation readout electronics and includes all necessary amplifiers and data acquisition for operation as a MEG system. It furthermore allows direct compensation of crosstalk. The readout electronics can furthermore be extended in a modular way, which is advantageous for scaling up to full head coverage.

Fourth, replacing sensors should be made easier by making the disk to which the sensors are glued removable. This also allows wire bonding of the glued sensors, which was possible with the side-mounted 7-channel system, but very tedious. The disk including the tilted wedges has now been made from one piece of Shapal, a machinable aluminum nitride ceramic with good thermal conductivity.

Fifth, an alternative approach for the operation of the heaters is needed. Using heaters to warm SQUIDs above the transition temperature to release trapped flux is very helpful as it does not require the full system to be warmed up. However, we have found that using the heating mechanism of the Magnicon electronics can lead to even more trapped flux. This is because the sensors are heated sequentially by applying a voltage of 15 V to each heater with a resistance of 50-100 Ω, leading to a large heater current of 0.3 A that couples flux into neighboring magnetometers. The average power generated by the heater can be reduced by using pulse-width modulation, meaning the heater is turned on every 0.55 ms for a specified duration of less than 0.55 s. However, in our case a lower but continuous current would be beneficial, including the option to heat several magnetometers at the same time.

6

Next generation high-T_c SQUID magnetometers

Two options for replacing the single layer YBCO SQUID magnetometers based on bicrystal grain boundary junctions were investigated in parallel to the fabrication, optimization, and implementation of the said magnetometers in the 7-channel system.

The first alternative is magnetometers based on Dayem bridge junctions instead of bicrystal grain boundary junctions. These devices were fabricated and studied in detail by my fellow PhD students Minshu Xie [167] and Edoardo Trabaldo [218], while I helped with device characterization, design adjustments, and interpretation of results. Here I summarize the main results obtained, which have been published in Paper D and Paper E, and discuss the benefits and drawbacks of this junction type. Several of the identified problems could be solved, and Dayem bridge junctions are starting to become a viable option for single layer magnetometers as shown in Paper E.

The second alternative is YBCO SQUID magnetometers with an inductively coupled pickup loop. With multilayer flux transformers it is possible to reach lower noise levels than for single layer devices with an equally large pickup loop, but their fabrication is more challenging. The flux transformers used in this thesis were fabricated by my colleague Maxim Chukharkin, while I fabricated and optimized the associated bicrystal grain boundary junctions-based washer SQUIDs, as well as prototype multilayer input coils. I here present the main results achieved for flux transformer magnetometers, and describe some important findings from simulations of these devices in more detail. The section ends with a conclusion and outlook.

6.1 Dayem bridge junction-based magnetometers

The investigation of the possibility of fabricating low-noise magnetometers based on Dayem bridge junctions instead of bicrystal grain boundary junctions was triggered by the low flux noise achieved with a YBCO Dayem bridge junction-based nanoSQUID in our group [219]. The nanoSQUIDs described in the paper incorporate two parallel nanowires with a cross section down to 50 nm $\times$ 50 nm and a length of 100 nm to

200 nm separated by a distance of 100 nm to 1000 nm. The total flux noise of a nanoSQUID with a geometrical area of 0.1 µm^2 was measured to be 1.2 µ$\Phi_0/\sqrt{\text{Hz}}$ above 10 kHz and at 8 K [219]. Removing the amplifier noise of 1 µ$\Phi_0/\sqrt{\text{Hz}}$ gives an intrinsic SQUID noise of only 0.7 µ$\Phi_0/\sqrt{\text{Hz}}$ above 10 kHz. However, the noise was measured without bias current reversal and large 1/f-like noise was found. In retrospect it is clear that the low flux noise achieved in Ref. [219] is mainly due to the low operation temperature of 8 K and the small inductance of the nanoSQUID, and should not be assumed to be a general property of these Dayem bridge junctions. Nonetheless, the flux noise is significantly lower than the 80 µ$\Phi_0/\sqrt{\text{Hz}}$ at 4.2 K measured earlier for a YBCO Dayem bridge-based nanoSQUID [118], meaning that the excess noise of the junctions could be considerably reduced.

6.1.1 Early YBCO Dayem bridge-based magnetometers

Due to their minuscule effective area, bare nanoSQUIDs have a poor magnetic field sensitivity. To increase the effective area of the YBCO nanoSQUIDs without affecting the flux noise, Arzeo *et al.* directly coupled the 200 nm × 1 µm nanoSQUID loop to circular pickup loops with 40 µm to 400 µm diameter [220]. With the largest pickup loop, an effective area of 63 µm^2 could be obtained, which resulted in an intrinsic white magnetic field noise of 66 pT$/\sqrt{\text{Hz}}$ at 5 K [220].

In Paper D we study different Dayem bridge-based magnetometer designs to further increase the effective area. The measurements are now performed at 77 K and the SQUIDs are operated in a flux-locked loop with ac bias reversal to cancel critical current fluctuations. The first type of magnetometer studied is again a magnetometer with a directly coupled pickup loop, now with a square shape to match the substrate, a side length of 300 µm to 7500 µm, and a linewidth of 50 µm. We find that A_{eff} increases with pickup loop side length as predicted by the inductance and effective area simulation. Since the effective area can be improved by also enlarging the coupling inductance L_c between SQUID and pickup loop, we use the hairpin SQUID design shown in Fig. 6.1a&b, which allows us to increase L_c by varying the SQUID slit length while keeping the parasitic inductance of the nanowires and electrode low and roughly constant. One of the main problems is that the nanowire junctions have a significant parasitic kinetic inductance contribution at 77 K, leading to a simulated total parasitic inductance $L_{par} = 106$ pH using $\lambda = 520$ nm. Increasing the SQUID slit length from 2 µm to 32 µm results in the expected linear increase in A_{eff}, however, the voltage modulation depth also drops from an already low 5 µV to below 1 µV because of the large SQUID inductance L. As a compromise, a SQUID slit length of 8 µm is used, resulting in $L_c = 59$ pH, $L = 165$ pH, a voltage modulation depth of 4 µV, and a flux noise of 55 µ$\Phi_0/\sqrt{\text{Hz}}$ at 77 K. With the largest pickup loop (side length 7.5 mm), an effective area $A_{eff} = 0.09$ mm^2 is achieved, leading to a total magnetic field noise level of 1.2 pT$/\sqrt{\text{Hz}}$ at 77 K. The noise spectrum is flat down to 10 Hz thanks to ac bias reversal.

The good agreement between simulated and measured values demonstrates that the inductance and effective area simulation method is a useful tool. The results presented in Paper D acted as a starting point for my optimization of YBCO SQUID magnetometers with a directly coupled pickup loop but grain boundary Josephson

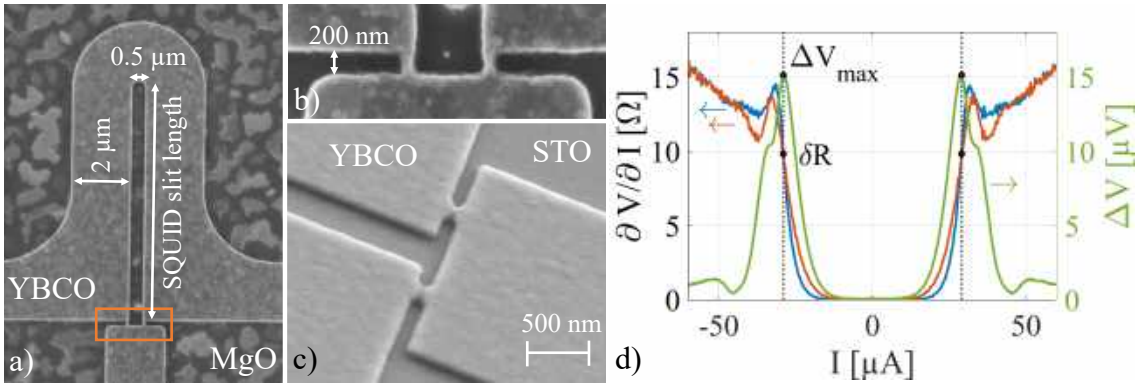

Figure 6.1: a) SEM image of a Dayem bridge-based hairpin SQUID with the junction area marked in orange. b) SEM image of the junction area using traditional Dayem bridge junctions as in Paper D. c) SEM image of the junction area using grooved Dayem bridge junctions as in Paper E. d) Left: Differential resistance $\partial V/\partial I$ for the I-V curves corresponding to integer flux (blue) and half-integer flux (orange) in the SQUID loop as a function of bias current I. Right: Voltage modulation depth ΔV as a function of bias current. The SQUID is operated at the bias current with the largest voltage modulation ΔV_{max} marked by a line. The differential resistance of the orange and blue curve coincide at that bias current, and is used to define δR. SEM images a) and b) are from Minshu Xie, and SEM image c) from Edoardo Trabaldo.

junctions. Same as for those junctions, the optimal SQUID slit length could also be determined by minimizing $S_\Phi^{1/2}/L_c$, although the minimum is expected to be broad. Furthermore, the very narrow pickup loop used here (linewidth 50 µm) is not optimal as discussed in §2.5. Using a wide pickup loop with $A_p/L_p \approx 5$ mm^2/nH in combination with the 8-µm-SQUID described above should reduce the total magnetic field noise level to below 400 fT/$\sqrt{\text{Hz}}$.

In Paper D we instead chose to study a second type of magnetometer: Dayem bridge-based SQUIDs with an inductively coupled flux transformer. This allowed us to increase A_{eff} to 0.46 mm^2 and decrease the magnetic field noise to 240 fT/$\sqrt{\text{Hz}}$ – the lowest value for a YBCO Dayem bridge-based device at that time. This type of device will be discussed in more detail in §6.2.2.

Besides the large L_{par} due to the kinetic inductance of the Dayem bridge junctions, the SQUID performance is limited by the large SQUID critical current $I_c \approx 100$ µA for two parallel nanowires with a cross section of 50 nm × 50 each. This leads to a large $\beta_L > 5$, far from the optimal $\beta_L \approx 1$. Furthermore, the gold capping layer used to protect the nanowires during ion milling [219, 221] reduces the resistance of the junctions and thus also the voltage modulation depth.

6.1.2 Grooved Dayem bridge-based magnetometers

These three problems are solved by the novel grooved Dayem bridge junctions developed by Edoardo Trabaldo [222]. A groove in the middle of the Dayem bridge reduces the critical current by a factor of 10 or more and also leads to a higher

junction resistance – the latter also due to omission of the gold capping layer. This allows one to increase the nanowire width (for example from 50 nm to 150 nm), which reduces the parasitic kinetic inductance. The groove is fabricated in the same lithography step as the Dayem bridge (and the rest of the magnetometer) by simply leaving a 40-50 nm gap in the carbon mask where the groove should be, thus not requiring any special alignment [222]. Redeposition of material in the very narrow nanogap during the argon ion milling reduces the etching rate in the gap and thus produces the groove in the nanowire. The junction critical current I_0 can be adjusted by varying the nanogap size: for a 200 nm long nanowire, a 50 nm gap results in $I_0 \approx 10$ µA [222]. A scanning electron microscopy (SEM) image of the junction area of a grooved Dayem bridge-based SQUID is shown in Fig. 6.1c.

In Paper E we study the properties of grooved Dayem bridge-based SQUIDs and present magnetometers with a directly coupled pickup loop made from this type of SQUID. The same SQUID design as for the traditional Dayem bridge-based SQUIDs described before is used (see Fig. 6.1a), but now the slit length can be significantly increased while still obtaining a large modulation depth and much lower noise. For a SQUID with a slit length of 30 µm and a SQUID critical current $I_c \approx 30$ µA, we measure a coupling inductance $L_c = 103$ pH with direct injection, a voltage modulation depth of 16.5 µV, and a flux noise of 10.6 $\mu\Phi_0/\sqrt{\text{Hz}}$ at 77 K. This SQUID was directly coupled to a 8.7 mm × 9.0 mm pickup loop with a linewidth of 2 mm and achieved an effective area $A_{eff} = 0.35$ mm^2 leading to a total magnetic field noise level of 63 $\text{fT}/\sqrt{\text{Hz}}$ above 3 Hz and at 77 K. This is the lowest magnetic field noise level achieved with a Dayem bridge-based magnetometer so far and is comparable to what we achieve with bicrystal grain boundary-based magnetometers.

In contrast to grain boundary junctions, the SQUID resistance when using Dayem bridge junctions is characterized by a bias-dependent differential (or dynamic) resistance and not a single and well-defined RSJ-like resistance parameter R_n [120]. The differential resistance of the aforementioned SQUID is plotted as a function of bias current in Fig. 6.1d. Instead of asymptotically decreasing towards R_n for high bias currents, the differential resistance increases, which could indicate heating effects or a flux-flow regime [218]. This aspect makes fitting of the I-V curve to extract R_n, I_c, and I_{ex} impossible. We instead estimate I_c with a voltage criterion and use the differential resistance δR at the bias current with the largest voltage modulation depth ΔV_{max} (i.e. the operation point) for some limited theoretical description of the voltage modulation depth. As for bicrystal grain boundary SQUIDs, the differential resistance of the two I-V curves corresponding to integer and half-integer flux in the SQUID loop coincide at the bias current where ΔV_{max} is obtained, see Fig. 6.1d.

In Paper E the temperature dependence of I_c, δR, ΔV_{max}, and the critical current modulation depth ΔI_c is furthermore studied. Most relevant for the use as an on-scalp MEG magnetometer is possibly that the voltage modulation depth first increases when the temperature is decreased from 84 K (T_c of the junctions) to 65 K, then decreases when being further cooled to 55 K, after which ΔV_{max} increases again. The peak at 65 K can be understood from the temperature dependence of δR and ΔI_c, which seem to describe $V_{max} \approx \Delta I_c \delta R$ rather well. In §4.5 we found that δR increases for grain boundary SQUIDs when the SQUID is cooled from 81 K

to 68 K[1]. In contrast, δR decreases in this temperature range for grooved Dayem bridge-based SQUIDs. More measurements are necessary to see how this affects the magnetic field noise level.

6.1.3 Conclusion and outlook

The obtained results show that grooved Dayem bridge-based magnetometers are starting to become a viable alternative to their bicrystal grain boundary-based counterparts. The total magnetic field noise level of 63 fT/$\sqrt{\text{Hz}}$ at 77 K is just slightly higher than that of the best bicrystal grain boundary-based magnetometers I have made for the 7-channel system. Further optimization of the pickup loop as described in §4.4.4 should result in magnetic field noise levels around 40 fT/$\sqrt{\text{Hz}}$ – based on the best grooved Dayem bridge-based magnetometer presented with $S_\Phi^{1/2}/L_c = 103$ μΦ$_0$/$\sqrt{\text{Hz}}$/nH. At the moment, 32 SQUIDs are coupled to the same pickup loop, which increases the pickup loop inductance and thus restricts its performance. A large number of SQUIDs is made to increase the chance of obtaining a good SQUID, which is unfortunately not that simple. Mass fabrication of grooved Dayem bridge-based magnetometers is nevertheless more reasonable than that of bicrystal grain boundary-based magnetometers as the substrates are much cheaper and no alignment to any structure on the substrate is necessary, thus simplifying the fabrication procedure. However, compared to bicrystal grain boundary junctions, the Dayem bridge junctions we tested are far more likely to be destroyed by electrostatic discharge. Furthermore, the noise performance when cooled without a superconducting shield still needs to be investigated. How suitable the grooved Dayem bridge-based magnetometers are for practical operation in a on-scalp MEG system is therefore still an open question.

6.2 SQUID magnetometers with flux transformers

We now switch to magnetometers with an inductively coupled flux transformer. Devices based on both bicrystal grain boundary junctions and Dayem bridge junctions have been studied. I will described the two in this order and then move on to presenting the conclusions from inductance and coupling simulations.

6.2.1 Magnetometers with bicrystal grain boundary junctions

Our YBCO SQUID magnetometers with an inductively coupled flux transformer are made using two substrates: one for the washer SQUID and one for the flux transformer. The SQUID chip contains only a single layer YBCO film, while the flux transformer chip contains two YBCO layers separated by an insulating STO layer as described in §3.4. This allows selection of the best combination of SQUID and flux transformer for assembly as a flip-chip magnetometer.

[1]Note that δR for grooved Dayem bridge-based SQUIDs is the same as the dynamic resistance R_d used for grain boundary junction-based SQUIDs earlier.

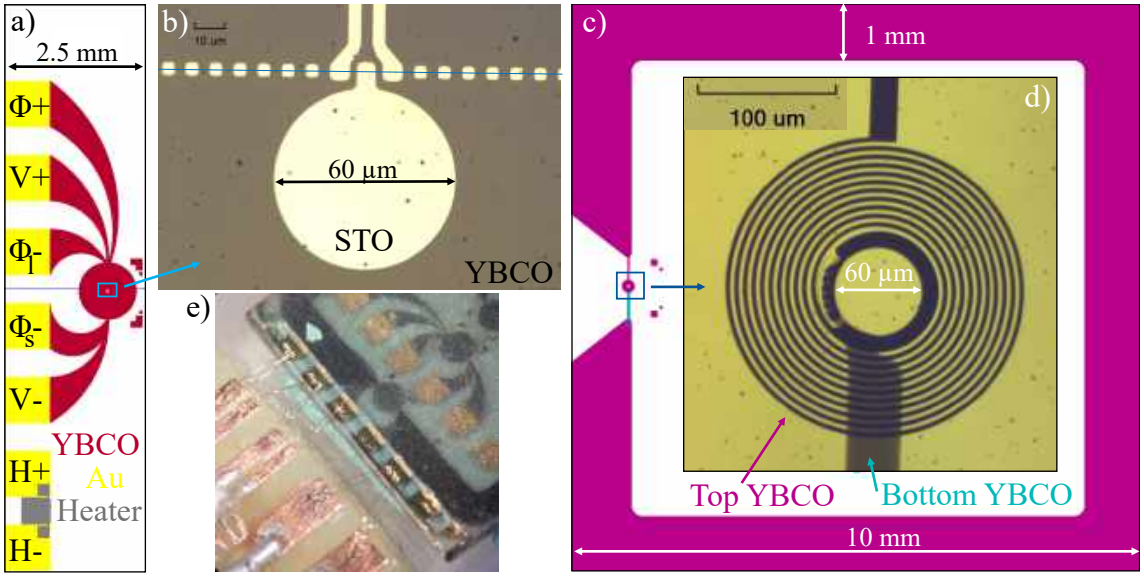

Figure 6.2: Design and images of our flip-chip bicrystal SQUID magnetometer with an inductively coupled flux transformer. a) Design of the SQUID chip with the YBCO in dark red, the gold contact pads in yellow, and the heater in grey. The bicrystal grain boundary is indicated by the blue line. b) Micrograph of the SQUID loop with a diameter of 60 µm. Holes are patterned into the YBCO film along the grain boundary marked by a blue line. c) Design of the flux transformer chip with the bottom YBCO layer in turquoise and the top YBCO in purple. d) Micrograph of the flux transformer input coil with the bottom YBCO in light grey and the top YBCO in dark grey. e) Photograph of the assembled magnetometer with the flux transformer chip on top of the SQUID chip. The SQUID chip has not been cut yet, so additional (unused) SQUIDs and bond pads are visible on the inside of the flux transformer pickup loop.

Design

The design of our YBCO flip-chip flux transformers was developed by Maxim Chukharkin and we adjusted it together to make it suitable for operation in an on-scalp MEG system. We fabricate four 2.5 mm × 10 mm SQUID chips with the design shown in Fig. 6.2a from a 10 mm × 10 mm STO bicrystal substrate. After fabrication, the SQUID chips can be separated using a diamond wire saw. This reduces the number of bicrystals needed by a factor of four compared to the single layer bicrystal SQUID magnetometers.

The main component of every SQUID chip is the washer SQUID with 1 mm outer diameter. The SQUID loop shown in more detail in Fig. 6.2b has a diameter of 60 µm and the Josephson junctions are formed where the YBCO film crosses the grain boundary at the edge of the SQUID loop. We pattern 6 µm × 6 µm holes along the grain boundary to reduce the chance of trapping flux.

Gold contact pads on the edge of the SQUID chip are used for SQUID biasing ($V+$ and $V-$), feedback ($\Phi+$, Φ_l- or Φ_s-), and the heater ($H+$ and $H-$). The feedback for operation in a flux-locked loop is currently implemented with direct injection, either using the long path around the full SQUID loop (from $\Phi+$ to Φ_l-)

or the short path around half the SQUID loop (from $\Phi+$ to Φ_s-). Both connection schemes were found to be suitable for providing the feedback with the Magnicon SQUID electronics, with the long path giving stronger feedback coupling.

The design of the flux transformer chip is shown in Fig. 6.2c. The square flux transformer pickup loop has outer dimensions of 10 mm × 10 mm – just like the STO substrate – and a linewidth of 1 mm. The spiral input coil shown in more detail in Fig. 6.2d has an inner diameter of 60 µm matching the SQUID loop. The input coil consists of 11.5 turns with a linewidth and spacing of 3 µm each. The linewidth of the innermost turn is increased to 12 µm, which increases the mutual inductance between SQUID loop and input coil [184]. Only the 40 µm wide structure connecting the innermost turn of the input coil to the pickup loop is made from the bottom YBCO layer, the rest of the input coil and the pickup loop are made from the top YBCO layer. This allows fabrication of the input coil with tightly spaced turns.

An image of an assembled magnetometer is shown in Fig. 6.2e with the flux transformer chip above the (not yet cut) SQUID chip. The alignment of the input coil to the SQUID loop is done manually under a microscope with the help of a micro-manipulation stage. The two substrates are separated by photoresist and glued together at the edges with BF-6 glue. The flux transformer chip does not cover the contact pads of the SQUID chip, thus allowing us to wire bond to the SQUID chip from above. The bonds can be made shallow such that the flux transformer substrate limits the standoff distance when using the magnetometer in an on-scalp MEG system.

Performance

Several SQUID chips were fabricated and similar problems were encountered as for the single layer SQUID magnetometers. The early SQUIDs made without a CeO_2 buffer layer suffered from a large critical current, which resulted in a large β_L, low modulation, and a large flux noise. The CeO_2 buffer layer could again solve this problem. Furthermore, I found that washer SQUIDs made from around 200 nm thick YBCO films exhibited less low frequency flux noise than those made from 150 nm thin films, which is likely due to stronger flux pinning in thick YBCO films.

We will now have a closer look at the magnetometer with which we reached a white noise level of below 11 $\mathrm{fT}/\sqrt{\mathrm{Hz}}$ at 78 K. The washer SQUID of that magnetometer was made from a 225 nm YBCO film with a CeO_2 buffer layer and contains two 2.4 µm wide Josephson junctions. Measured in the dipstick at $\sim$ 78 K, we obtain a SQUID critical current I_c = 106 µA, an excess current I_{ex} = 17 µA, and a normal resistance R_n = 1.5 Ω. The bare washer SQUID has a maximal voltage modulation depth of 12 µV and a total white flux noise of 20 $\mu\Phi_0/\sqrt{\mathrm{Hz}}$. Coupling the washer SQUID to the flux transformer increases the modulation depth to 18 µV and decreases the total white flux noise to 8.8 $\mu\Phi_0/\sqrt{\mathrm{Hz}}$. This is because the flux transformer input coil screens part of the SQUID inductance [64]. The effective area of the assembled magnetometer was measured to be 1.67 mm^2 corresponding to a flux-to-field transformation coefficient of 1.24 nT/Φ_0. The equivalent total magnetic field noise spectra of this magnetometer is shown in Fig. 6.3 in orange and was measured inside a superconducting shield. The white noise level is below 11 $\mathrm{fT}/\sqrt{\mathrm{Hz}}$ and the 1/f noise knee is around 250 Hz. The low frequency noise knee is

generally at higher frequencies for these magnetometers, as compared to our single layer ones. We attribute this to excess low frequency noise in the via [184] and the much larger SQUID washer size (diameter 1 mm) in comparison with the ∼4 µm linewidth SQUIDs used for single layer magnetometers. Nonetheless, comparing this magnetometer with the best single layer magnetometer I have fabricated shows that the flux transformer magnetometer outperforms the single layer magnetometer for frequencies above 20 Hz. The performance of this magnetometer is comparable to the 8-10 fT/$\sqrt{\text{Hz}}$ white magnetic field noise level reported for the best flux transformer magnetometers made on 10 mm × 10 mm substrates [32, 142].

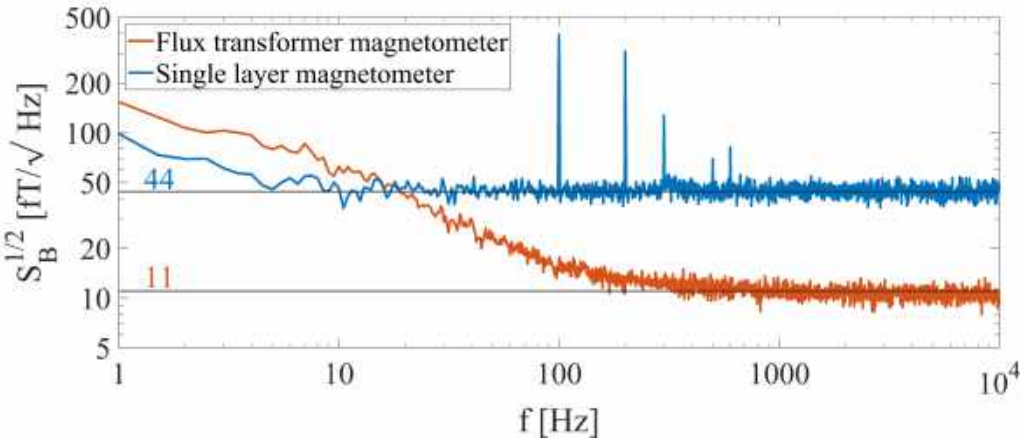

Figure 6.3: Magnetic field noise spectra of a YBCO SQUID magnetometer with an inductively coupled pickup loop (orange) measured in the dipstick at ∼78 K inside a superconducting shield. For comparison, the noise trace from the best single layer YBCO SQUID magnetometer with a directly coupled pickup loop is given in blue.

6.2.2 Magnetometers with Dayem bridge junctions

We will now switch to flux transformer SQUID magnetometers based on Dayem bridge junctions. Minshu Xie identified two main problems for the earlier Dayem bridge junctions that lead to very weak coupling between the washer SQUID and the flux transformer input coil [167]. First, the 50 nm thin YBCO film used to fabricate these junctions provides very little flux focusing. Second, there is a large mismatch between the SQUID hole size (diameter ∼ 5 µm) and the inner diameter of the flux transformer input coil (∼ 60 µm). The earlier needs to be small to keep the SQUID inductance low to achieve suitable flux noise, while the minimum size of the latter is restricted by the minimum size of the interlayer via connection. Note that the first problem is also relevant for the grooved Dayem bridge junctions, while the second problem is less important as the SQUID hole can be made significantly larger.

The coupling could be significantly improved using a two-level coupling approach presented in Paper D and shown in Fig. 6.4a. In this approach the flux transformer input coil is coupled to a washer-type pickup loop that is directly coupled to the SQUID loop. The effective area of such a magnetometer is a combination of that of a directly coupled pickup loop (see Eq. (2.32)) and an inductively coupled flux

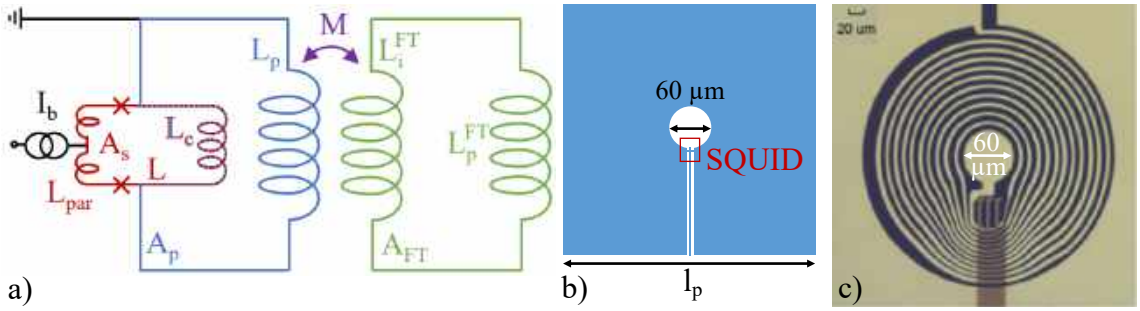

Figure 6.4: a) Equivalent circuit for the two-level coupling approach used for Dayem bridge-based magnetometers with an inductively coupled flux transformer. The effective areas of the SQUID (red and purple for L_c), washer type pickup loop (blue and purple for L_c), and the flux transformer pickup loop (green) are A_s, A_p, and A_{FT}, respectively. The SQUID with inductance L has a coupling inductance L_c to the washer-type pickup loop. The inductances of the washer-type pickup loop, the flux transformer input coil, and the flux transformer pickup loop are L_p, L_i^{FT}, and L_p^{FT}, respectively. The mutual inductance M between the flux transformer input coil and the washer-type pickup loop is given by $M = k\sqrt{L_p L_i^{FT}}$, where k is the coupling coefficient. b) Design of the square washer-type pickup loop with a central hole diameter of 60 µm and side length l_p between 300 µm and 2 mm. The SQUID design is the same as that for a magnetometer with a directly coupled pickup loop shown in Fig. 6.1a. c) Micrograph of the flux transformer input coil used. The rest of the flux transformer has the same design as shown in Fig. 6.2c.

transformer (see Eq. (2.33)) [167]:

$$A_{eff} = -A_s + \frac{L_c}{L_p} A_p + \frac{L_c}{L_p} \frac{k\sqrt{L_p L_i^{FT}}}{L_i^{FT} + L_p^{FT}} \cdot A_{FT}, \tag{6.1}$$

with the symbols defined in Fig. 6.4a. The first two terms can typically be neglected due to the small effective areas of the SQUID and washer-type pickup loop in comparison to the flux transformer pickup loop. Assuming that the coupling coefficient k does not depend on L_i^{FT}, the largest A_{eff} is achieved for $L_i^{FT} = L_p^{FT} =: L_{FT}$:

$$A_{eff} \approx \frac{k}{2} \frac{L_c}{\sqrt{L_p L_{FT}}} \cdot A_{FT}. \tag{6.2}$$

In Paper D we study the effective area of Dayem bridge-based magnetometers with such a two-level coupling approach. For the SQUID, the same design as for single layer devices is used (see Fig. 6.1a) with a SQUID slit length of 8 µm. The directly coupled washer-type pickup loop is shown in Fig. 6.4b and we vary the side length l_p between 300 µm and 2 mm. The flux transformer has the same pickup loop design as for bicrystal junctions (Fig. 6.2c), but an earlier input coil design as shown in Fig. 6.4b. In this design Maxim Chukharkin moved the via away from the SQUID loop to reduce low frequency noise, which explains the varying linewidth. The inner hole of the flux transformer and the washer-type pickup loop are both 60 µm.

The assembled magnetometers exhibited effective areas between 0.33 mm^2 and 0.46 mm^2. Since L_p is mainly dependent on the inner hole size, L_p and thus A_{eff} vary

only slightly with l_p as shown by the simulated values for A_{eff}. The variation in the measured A_{eff} can mainly be explained by the coupling coefficient k varying between magnetometers, which is a consequence of the manual alignment and the varying distance between the two substrates. Comparing simulations with the measured values gives an average $k = 0.37$.

The magnetometer with the largest effective area of 0.46 mm^2 exhibited a total white magnetic field noise level of 240 fT/$\sqrt{\text{Hz}}$, which was the best magnetic field noise level for a Dayem bridge-based magnetometer at 77 K at that time. In the meantime, Trabaldo *et al.* fabricated a magnetometer based on grooved Dayem bridge junctions using the same 2-level coupling approach and flux transformer, and achieved a total white magnetic field noise level of 60 fT/$\sqrt{\text{Hz}}$ [223]. The sensor has a comparable effective area with $A_{eff} = 0.41$ mm^2, but performs better because of the lower flux noise.

6.2.3 Flux transformer magnetometer simulation

The coupling between the flux transformer input coil and the washer SQUID can be studied in more detail with the inductance simulation method, which allows us to obtain several useful conclusions in terms of how to improve the magnetometer design without having to fabricate a large set of samples. The good agreement between simulated and measured effective areas found in Paper D makes the predictions from the simulation trustworthy. I will here present the results from the simulation of the traditional one-level coupling as used for bicrystal grain boundary junctions and described in §2.5.2, and not the two-level used for Dayem bridge junctions. Nonetheless, the conclusions are also relevant for grooved Dayem bridge junctions as the goal is to use the one-level coupling for this junction type as well. Furthermore, the effect of the film thickness on the coupling will be investigated.

First, I would like to point out that the pickup loop of our flux transformers has already been optimized with the goal of achieving the largest magnetometer effective area A_{eff}. As described in §2.5.2, the largest A_{eff} is obtained for matched flux transformer input coil and pickup loop inductance ($L_i = L_p = L_{FT}$) under the assumption that the coupling coefficient k between the SQUID washer and the input coil does not depend on L_i. According to Eq. (2.34), A_{eff} is proportional to $A_p/\sqrt{L_{FT}}$. The pickup loop effective area A_p can be estimated by $A_p = Dd$ [19, 187], where D is the outer diameter of the square loop and d the inner, while L_p can be estimated using the formulas given in Appendix B. Maxim Chukharkin found that it is possible to use the full substrate size without any noticeable increase in the low frequency noise, hence the maximal $D = 10$ mm is chosen. Maximizing $A_p/\sqrt{L_{FT}}$ as a function of pickup loop linewidth w gives an optimal $w \approx 1$ mm. In practice, the square loop needs to be cut open to place the input coil. For the design shown in Fig. 6.2c, the simulation predicts $L_p = 20.3$ nH and $A_p = 77.4$ mm^2. The input coil should be designed to have the same inductance $L_i = 20.3$ nH, which is not trivial as the SQUID washer screens part of the input coil inductance as the following simulations will show.

We start by studying the coupling using the current input coil and SQUID washer design shown in Fig. 6.2. To simplify the simulation, only two superconducting

layers are used: one for the top YBCO containing the spiral input coil (and not the bottom YBCO return line[2]) and one for the SQUID washer without the holes along the grain boundary or the connections to the contact pads. As default values, the YBCO film thickness of the SQUID washer is set to $t_{SQ} = 200$ nm, that of the input coil to $t_{FT} = 200$ nm, the London penetration depth to $\lambda = 400$ nm, and the separation of the two superconducting layers to $s = 3$ µm. The latter is an estimation of the separation we achieve for our flip-chip magnetometers. The simulation predicts $L = 123$ pH, $L_i = 15.8$ pH, and $k = 0.57$, which with Eq. (2.33) gives $A_{eff} = 1.69$ mm^2 corresponding to a flux-to-field transformation coefficient of 1.22 nT/Φ_0. This is very close to the measured values.

Decreasing the outer diameter of the washer SQUID from 1 mm to 220 µm – the outer diameter of the input coil – slightly improves the performance: $k = 0.61$ and $A_{eff} = 1.85$ mm^2. The smaller washer is not only preferable from a coupling point of view, but may also lead to an improved low frequency noise performance because smaller washers can be cooled in higher fields without trapping flux. The following simulations are done using this smaller washer as it reduces simulation duration significantly.

To illustrate the coupling and the induced current flows, the amplitude of the sheet current density j in the SQUID washer with a circulating current of 10 µA in the SQUID loop and a current of 10 µA in the input coil is shown in Fig. 6.5. The current flowing clockwise in the input coil induces a counterclockwise current in the SQUID washer just above. As this induced current is intercepted by the SQUID slit, the current needs to find some way to close on itself. Most of this return current flows around the perimeter of the SQUID loop as shown by the dark red color, while some of the return current flows along the outer perimeter of the washer.

The effect of varying the distance s between the SQUID washer and the flux transformer input coil is summarized in Table 6.1. Moving the SQUID washer and the input coil closer together screens both the SQUID inductance L and the input coil inductance L_i. This is due to the geometric inductance contribution decreasing. The effect is more significant for L_i. For a separation of 3 µm, the simulation predicts $L_i = 15.7$ nH, which is less than $L_p = 20.3$ nH to which the input coil inductance should be matched. The input coil size should therefore be increased by adding more turns. As expected, the coupling and A_{eff} increase with decreasing separation, which speaks for an integrated instead of a flip-chip magnetometer. For an integrated magnetometer, the SQUID washer and the input coil are made on the same chip and the separation is defined by the thickness of the thin insulating layer. Integrated magnetometers will be discussed in more detail in §6.2.4.

For flip-chip devices, another important aspect is the effect of alignment errors on k and A_{eff}. Offsetting the input coil by 10 µm towards the left, the right, up, or down with respect to the SQUID washer as orientated in Fig. 6.5 was found to lead to only small changes in k and A_{eff}. The coupling coefficient varies between 0.58 and 0.62, and A_{eff} between 1.76 mm^2 and 1.86 mm^2. Moving the flux transformer downwards with respect to the SQUID washer even increases k and A_{eff}. Since 10 µm is a rather large offset, neither k nor A_{eff} should be significantly affected by the

[2]Simulations with 3 superconducting layers including the return line showed almost no change in the coupling, but take a lot more time.

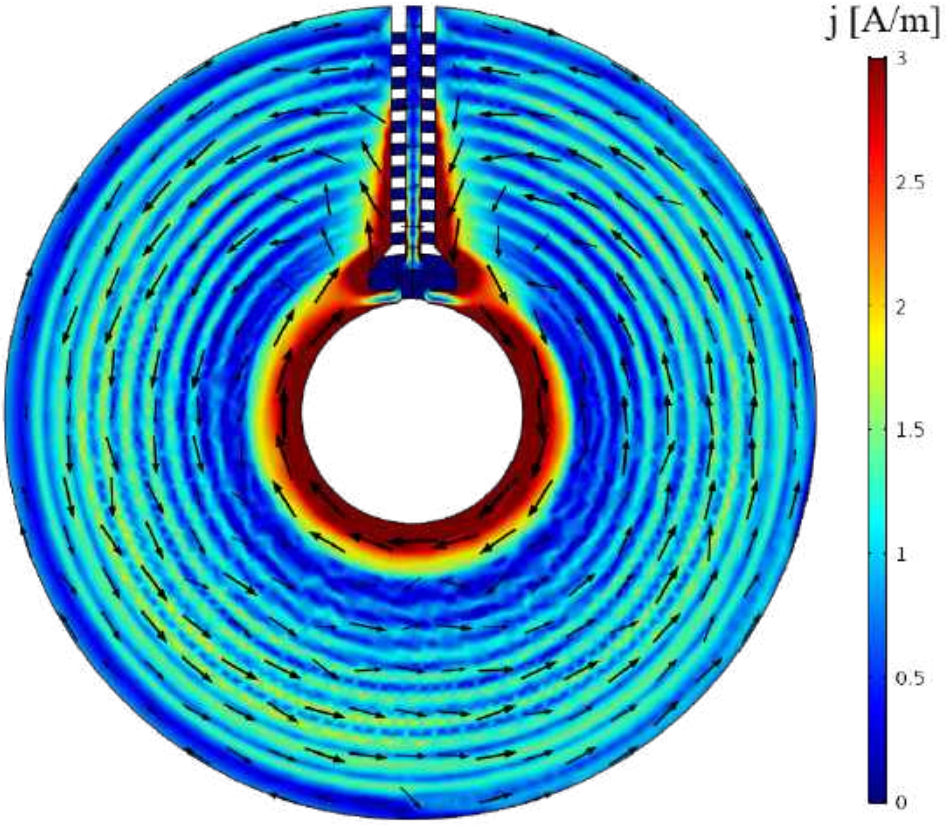

Figure 6.5: Simulation of the amplitude of the sheet current density j in the SQUID washer with a circulating current of 10 µA in the SQUID loop and a clockwise flowing current of 10 µA in the input coil (below the SQUID washer) as boundary conditions. The arrows show the direction of the current flow in the SQUID washer.

Table 6.1: Effect of varying the distance s between the SQUID washer and the flux transformer input coil on the SQUID inductance L, the input coil inductance L_i, the coupling coefficient k, the magnetometer effective area A_{eff}, and the corresponding flux-to-field transformation coefficient ${A_{eff}}^{-1}$.

s [µm]	L^{Kin} [pH]	L^{Geo} [pH]	L [pH]	L_i^{Kin} [nH]	L_i^{Geo} [nH]	L_i [nH]	k	A_{eff} [mm^2]	${A_{eff}}^{-1}$ [nT/Φ_0]
0.1	30	93	124	2.6	12.0	14.6	0.69	2.07	1.00
0.3	30	94	124	2.5	12.2	14.7	0.69	2.05	1.01
1	29	97	126	2.5	12.5	15.0	0.66	1.99	1.04
3	**28**	**99**	**128**	**2.4**	**13.3**	**15.7**	**0.61**	**1.85**	**1.12**
10	28	100	128	2.2	15.2	17.4	0.49	1.51	1.37
30	28	100	128	1.9	17.7	19.7	0.30	0.92	2.25
100	28	100	129	1.8	19.2	21.0	0.07	0.23	8.99

manual alignment – at least in the washer plane. Varying the pressure applied when joining the two chips together can still lead to significant differences as described by the dependence on s.

Next, we focus on the effect of varying the SQUID washer film thickness t_{SQ}. The results from the simulation are summarized in Table 6.2. The largest change appears in the kinetic inductance contribution to the SQUID inductance for t_{SQ} below 200 nm. Also the coupling coefficient decreases considerably. However, because of the much larger SQUID inductance, the effective area actually increases slightly for thinner SQUID washers. Nonetheless, the magnetic field noise is expected to be significantly larger for the SQUIDs with thin washers because the flux noise strongly increases with SQUID inductance.

Table 6.2: Effect of varying the SQUID washer film thickness t_{SQ} on the SQUID inductance L, the input coil inductance L_i, the coupling coefficient k, the magnetometer effective area A_{eff}, and the corresponding flux-to-field transformation coefficient ${A_{eff}}^{-1}$.

t_{SQ} [nm]	L^{Kin} [pH]	L^{Geo} [pH]	L [pH]	L_i^{Kin} [nH]	L_i^{Geo} [nH]	L_i [nH]	k	A_{eff} [mm^2]	${A_{eff}}^{-1}$ [nT/Φ_0]
30	176	104	280	3.2	14.5	17.7	0.43	1.94	1.07
50	107	103	210	3.0	14.0	17.0	0.49	1.91	1.08
100	55	101	156	2.7	13.6	16.2	0.56	1.88	1.10
200	**28**	**99**	**128**	**2.4**	**13.3**	**15.7**	**0.61**	**1.85**	**1.12**
300	19	98	118	2.2	13.3	15.5	0.63	1.84	1.13
400	15	97	112	2.1	13.2	15.4	0.64	1.83	1.13

The SQUID loop inductance can be reduced by decreasing the SQUID loop diameter. For a SQUID with $t_{SQ} = 200$ nm, decreasing the SQUID loop diameter from 60 µm to 40 µm decreases the SQUID inductance from 128 pH to 94 pH, but also k from 0.61 to 0.48 and A_{eff} from 1.85 mm^2 to 1.70 mm^2. Adjusting the input coil design may help improve the coupling. The optimal SQUID loop diameter and inductance is at this point not clear and further simulations – and also measurements – are required. Furthermore, the SQUID loop design can not only be adjusted by varying the circular hole diameter. It is also an option to place the junctions on the outside of the SQUID washer [187]. The SQUID slit then contributes to the total SQUID inductance, however, the flux transformer also screens part of this inductance. This SQUID design has been found to lead to a stronger coupling than with the junctions placed inside [64, 187]. Placing the junctions outside of the washer has the additional advantage that the grain boundary does not cross the entire washer width.

6.2.4 Conclusion and outlook

Using an inductively coupled flux transformer, a white magnetic field noise level below 11 fT/$\sqrt{\text{Hz}}$ at 78 K could be reached for a flip-chip high-T_c SQUID magnetometer based on bicrystal grain boundary junctions. While low frequency noise is generally a

larger problem in multilayer devices, this device outperformed the best magnetometer made for the 7-channel system for frequencies above 20 Hz. Reducing the pickup loop size may help improve the low frequency noise performance without reducing the effective area. The simulation tool can furthermore be used to improve the SQUID and input coil design without having to fabricate a large number of samples. Such optimization is still ongoing.

The performance of Dayem bridge-based magnetometers could also be improved using a flux transformer. However, the thin (50 nm) film used to fabricate these junctions results in larger noise levels than for bicrystal grain boundary-based magnetometers. The problem could be partly solved by employing a two-level coupling approach. Future magnetometers should preferably rely on the traditional one-level coupling and include thicker films – possibly by having different thicknesses for the SQUID washer and the junction area as investigated by Minshu Xie [167].

The presented bicrystal grain boundary-based magnetometer design is suitable for operation in an on-scalp MEG system. However, the contact pad layout and the feedback method should be readjusted before the sensor is used in the new 21-channel system. The new flux modulation electronics from Cryoton requires a four-point scheme for SQUID biasing, meaning that 8 contact pads are required. As described in §5.1.3, the direct injection feedback is not suitable for cancelling crosstalk arising from the mutual inductance of neighboring flux transformer pickup coils and should therefore be replaced by a feedback coil coupled to the pickup loop as in Refs. [204, 205]. This feedback coil can be made on the SQUID chip.

In principle, an integrated magnetometer would be preferable over a flip-chip magnetometer in an on-scalp MEG system for several reasons. First, only one chip would need to be cooled. For the flip-chip magnetometer we choose to have the SQUID chip below the flux transformer chip as it is more important to reach lower temperatures on the SQUID chip to improve the flux noise, while the flux transformer just needs to be superconducting. Second, the sensor-to-room temperature standoff distance can be made smaller for an integrated device. The thickness of the top chip in a flip-chip device increases the minimal possible sensor-to-room temperature standoff distance. Third, having just one chip is more convenient and no manual alignment is required. Nonetheless, the simulation predicts that manual alignment errors hardly affect the magnetometer performance. Fourth, the separation of the two superconducting layers is much smaller, leading to better coupling as the simulation shows.

In the first half of my PhD I made two prototype integrated magnetometers with a very similar design as for the flip-chip devices. Micrographs of these devices have been shown in Fig. 3.11a-c&f. The prototype integrated magnetometers were made on single crystal STO substrates and therefore only contained the microbridges but no Josephson junctions. The purpose of the devices was to test the fabrication procedure and check the vias connecting the two superconducting layers. The fabrication worked well and the vias showed critical currents above 10 mA, which means that the flux transformer can sustain circulating currents from magnetic fields above 1 µT. The washer SQUID was made in the bottom YBCO layer and the flux transformer input coil in the top superconducting layer. The SQUID washer was used as the return line for the input coil. The SQUID loop and the microbridges for the junctions

were patterned in the very last step by etching through the insulating STO layer and the bottom YBCO layer. This is done because the bottom layer is polished by CMP to achieve shallow slopes, which are unwanted for the SQUID loop and totally destroy the microbridges. The polishing makes the SQUID washer rather thin ($t_{SQ} \approx 100$ nm), which means that the SQUID inductance of this integrated device is higher and the coupling smaller than that of a flip-chip magnetometer with equivalent design. The thin SQUID washer may also show more low frequency excess noise. It is therefore not clear if an integrated device fabricated with CMP actually outperforms a flip-chip device. Furthermore, integrated devices often suffer from resonances caused by a parasitic capacitance between the input coil and the SQUID washer [64]. As the SQUID performance varies a lot between devices, the flip-chip approach is at this stage more promising.

7

Kinetic inductance magnetometers

This chapter summarizes the results obtained for KIMs. The high-T_c KIM project was done in collaboration with Visa Vesterinen and his group at VTT (Finland), who presented the first KIM [60]. The high-T_c KIMs were fabricated at Chalmers according to his designs. After preliminary dc transport measurements, the first KIMs were sent to Finland for further characterization. In autumn 2017, Visa Vesterinen visited Chalmers for two months, where we measured and characterized KIMs together using a vector network analyzer (VNA) and his KIM readout electronics board. KIMs fabricated after his visit could be checked with the VNA before being sent to VTT for responsivity and noise measurements. The main results have been published in Paper F. We demonstrate the first high-T_c KIMs, which reach a noise level of 4 pT/$\sqrt{\text{Hz}}$ at 10 kHz. The chapter concludes with ways to improve the performance.

7.1 Design

The KIM chip contains a superconducting loop, a capacitor, a coupling capacitor, and contact pads to connect the KIM to the transmission line. The general design is shown in Fig. 7.1a.

For a low magnetic field noise and a high responsivity, a large area superconducting loop with a narrow linewidth w and a thin film t is required. YBCO film deposition in our PLD system limits the substrate size to 10 mm × 10 mm. Since the film on the edge of the sample is typically of lower quality, and photolithography close to the edges is difficult, we pick a loop size of 8 mm × 8 mm. The corners of the loop are rounded to avoid current crowding, which can lead to lower critical currents.

Only a few devices featuring several centimeter long YBCO lines with linewidths $\lesssim$ 10 µm have been reported before – such structures are challenging to fabricate due to the high risk of defects [224]. A prototype high-T_c KIM (called KIM0) was therefore made with a linewidth w = 10 µm from a relatively thick YBCO film, t = 225 nm, grown on a sapphire substrate with a YSZ and CeO_2 buffer layer. Such a 10 µm linewidth loop has an estimated geometric loop inductance L_g = 45.3 nH based on Eq. (B.4) – independent of film thickness. Assuming λ = 400 nm, the kinetic loop inductance can be estimated using Eq. (2.37) as L_{k0} = 2.9 nH, leading to

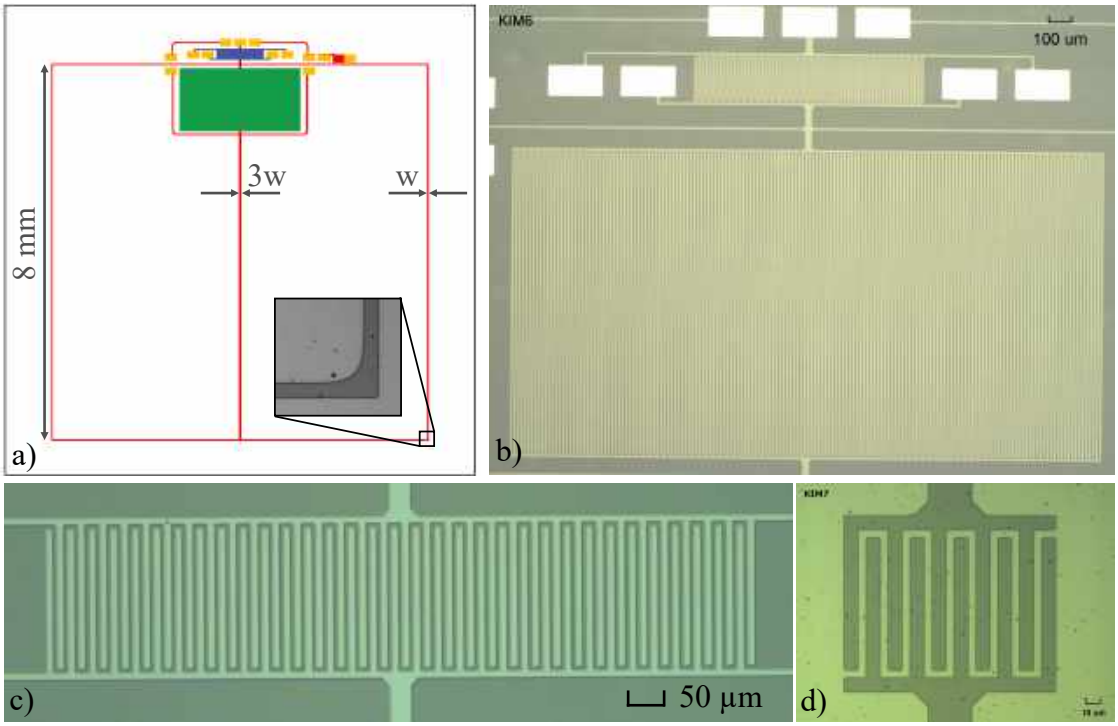

Figure 7.1: a) KIM design on a 10 mm × 10 mm substrate. The capacitor (green), the coupling capacitor (blue), and the remaining YBCO (red) is fabricated from a single YBCO layer on top of which the gold bond pads (yellow rectangles) are fabricated. The inset shows a micrograph of the rounded corners. b) Micrograph of the capacitor and coupling capacitor area. c) Micrograph of a coupling capacitor on a MgO substrate. d) Micrograph of the capacitor on the STO substrate.

a kinetic inductance fraction $\alpha_k = 0.06$. Reaching a high kinetic inductance fraction α_k can be challenging, since λ is smaller in YBCO than in NbN, where $\lambda \approx 1100$ nm was estimated for the KIM in Ref. [60]. Lines with smaller cross sections are thus necessary and KIMs with smaller t or w were fabricated after the prototype KIM.

Both the shunt capacitor and the coupling capacitor are formed from interdigitated fingers of width 10 µm and gap 5 µm as shown in Fig. 7.1b-d. The line connecting the shunt capacitor to the loop is 3 times as wide as the loop in order to reduce the parasitic inductance L_{par} while keeping the line narrow to avoid flux trapping. For the resonance frequency we aimed at around 250 MHz, which is well above the signal frequencies of interest, in the frequency band of the cold amplifier and the readout board, and low enough to allow the resonator to be modelled as a lumped element according to Eq. (2.53): $\sqrt{A} = 8 \text{ mm} \ll \lambda_c \approx 0.5$ m. The capacitor size is varied with loop width to achieve $f_r \approx 250$ MHz: the shunt capacitor has $C = 13.4 - 16.8$ pF, while the coupling capacitor has $C_c = 0.5 - 0.9$ pF. The resulting resonance frequency, however, strongly depends on the actual kinetic inductance contribution.

7.2 Fabricated devices

Half a year after the successful fabrication of the prototype KIM0, a new batch of KIMs with thinner films was fabricated. Since the YBCO film growth was continuously optimized on MgO substrates, while no films were grown on Al_2O_3, KIMs were made on MgO instead, which has similar rf loss properties (see §3.1).

Fabrication of functioning KIMs with 30-50 nm thickness turned out to be more challenging than anticipated, which is why several similar devices were fabricated with slightly varying methods as summarized in Table 7.1. While the first 50-nm-KIM showed promising resistance measurements, the first 30-nm-KIM was not superconducting at 77 K. The next two 30-nm-KIMs were then made using an in-situ gold layer for protection since this gold layer had been identified as crucial when fabricating thin nanowires [221]. Due to concerns that the gold layer may affect the rf properties of the KIM, the in-situ gold layer of KIM4 was etched away with 4 min argon ion milling. However, neither of the two devices functioned, and the 30-nm-KIM was discontinued.

The first 50-nm-KIM exhibited a fundamental resonance, however, the response to flux was slow, which indicates a small residual resistance in the loop. Two additional 50-nm-KIMs were fabricated; KIM5 showed no response to flux because one of the

Table 7.1: Design parameters of the fabricated KIM devices. The mask used for photolithography is either photoresist (PR) or carbon (C). We assume $\lambda = 400$ nm for the designed L_{k0}, and α_k is based on this value. The first tick in status describes if resistance measurements indicate that the device should work at 77 K, the second tick indicates if a fundamental resonance could be identified, and the third tick describes if the resonance shifts when a dc magnetic field is applied at 77 K. The snowflake indicates slow flux response at 77 K. In Paper F, KIM0 is called KIM A, KIM6 is KIM B, and KIM9 is KIM C.

Name	Sub-strate	Mask	In-situ gold	Gold pads	t [nm]	w [µm]	L_g [nH]	L_{k0} [nH]	α_k	Status
KIM0	Al_2O_3	PR	No	Yes	225	10	45.3	2.9	0.06	✓✓✓
KIM1	MgO	PR	No	Yes	50	10	45.3	12.9	0.22	✓✓❄
KIM2	MgO	PR	No	Yes	30	10	45.3	21.4	0.32	✗
KIM3	MgO	PR	Yes	Yes	30	10	45.3	21.4	0.32	✓✗
KIM4	MgO	PR	Etched	Yes	30	10	45.3	21.4	0.32	✓✗
KIM5	MgO	PR	No	Yes	50	10	45.3	12.9	0.22	✗✓✗
KIM6	MgO	PR	No	Yes	50	10	45.3	12.9	0.22	✓✓❄
KIM7	STO	PR	No	Yes	225	5	49.7	5.7	0.10	✗
KIM8	MgO	C	No	No	50	Test lines of different widths				
KIM9	MgO	C	No	No	75	10	45.3	8.6	0.16	✓✓✓
KIM10	MgO	C	No	No	50	10	45.3	12.9	0.22	✗
KIM11	MgO	C	No	No	50	5	49.7	25.7	0.34	✓
KIM12	MgO	C	No	No	50	10	45.3	12.9	0.22	✗
KIM13	MgO	C	No	No	50	3	53.0	42.9	0.45	✓

loop arms was disconnected, while KIM6 showed the same slow flux response as KIM1.

The next KIMs were to be fabricated during Visa Vesterinen's visit, but unfortunately the YBCO PLD system was down during that time. As YBCO films on STO were available from earlier film optimization, a KIM was made on STO even though STO has a large permittivity and high rf losses. The capacitors were made much smaller as shown in Fig. 7.1d. However, this KIM did not work because the STO turned semiconducting from the ion milling, and no resonance could be identified.

Next, a 50 nm thick sample was fabricated that contained test lines with different linewidths placed at varying distances from the substrate edge. The idea was to check if the film is better in the center and what the minimum linewidth was. The lines were patterned using a carbon mask since good results were achieved with this mask type for SQUIDs. This turned out to be a successful approach: even the 3-µm-wide line 1 mm from the edge (i.e. where the KIM loop usually is) showed good dc transport properties, as will be described later.

Subsequently, two 10-µm-linewidth devices were made with 75 nm and 50 nm thick films, respectively. The 75-nm-KIM worked well, while the 50-nm-KIM had a defect in the loop that was clearly visible with optical microscopy.

Finally, three more 50-nm-KIMs were made, this time with varying linewidths: 3, 5 and 10 µm. The linewidth of the 3-µm-KIM varies from 2.6 - 6.0 µm and is on average around 4.6 µm. Resistance measurements indicate that the 10-µm KIM had a short, possibly in the capacitor, while the results from the other two KIMs look promising. No resonance measurements have been made for these two KIMs so far, but their α_k should be much larger than that of the other KIMs.

7.3 DC transport characterization

Resistance measurements can be used to determine if the KIM is superconducting at 77 K, what the T_c is, and if any of the loop arms is disconnected. Except for KIM2, all KIMs were superconducting at 77 K. The critical temperature of the film before patterning and the final device can differ as shown in Fig. 7.2a. It is noteworthy that T_c not always decreases, but in some cases increases as for KIM1 and for KIM4 after the gold was etched away.

The test lines on KIM8 confirmed that the film closer to the substrate edge has a lower T_c than in the center, however, the difference was only roughly 1 K as plotted in Fig. 7.2b. Making the loop size smaller is thus not necessary. Narrower lines have slightly lower T_c, but the difference is also minimal. Comparing all KIMs shows that thicker samples tend to have higher T_c, however, the biggest difference in T_c comes from the generally higher film quality achieved in the second half of my PhD.

The test lines showed an average resistivity of $\rho = 2.8$ µΩm at 300 K, which can be used to calculated the expected resistance of the two loop arms in parallel. If one of the loop arms is disconnected, the total resistance nearly doubles. This forebodes that the KIM will not respond to flux as there is no superconducting loop, which is illustrated by KIM5 with R(300 K) = 170 kΩ as compared to KIM6 with R(300 K) = 110 kΩ. In Table 7.1 the first tick in status indicates the prediction from the described resistance measurements. Lastly, the resistivity of KIM1, KIM5, and KIM6

is with $\rho = 4.5$-5.4 µΩm at 300 K elevated, while the resistance of the other KIMs can be well described using $\rho = 2.8$ µΩm. Higher resistivity may be an indication of lower film quality and explain the slow flux response observed.

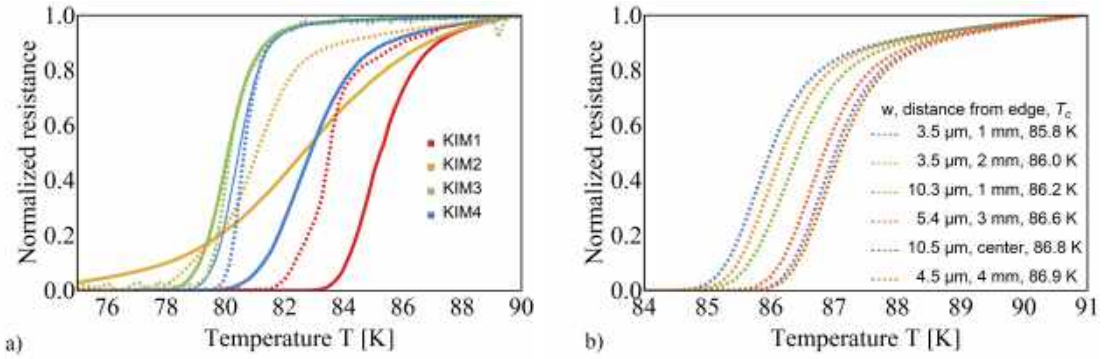

Figure 7.2: Normalized resistance as a function of temperature around T_c. a) KIM1-4 measured before patterning the film (dashed lines) and the final device (solid line). For KIM4 the thin solid line shows the transition before the gold was etched away. b) Test lines on sample KIM8 with different linewidths w placed at different distances from the edge as indicated in the legend.

7.4 Resonance characterization

For rf characterization at Chalmers, the KIM is glued onto the PCB shown in Fig. 7.3a. The PCB contains an rf readout transmission line to which the KIM is connected through bondwires, a 3-turn copper coil for applying a dc magnetic field, and a single-turn copper coil for applying an rf magnetic field. The mutual inductance between the KIM loop and the dc bias coil was calculated to be 20 nH, and 5.3 nH for the rf coil. The sample holder is placed inside a dipstick that contains an rf input line with a 20 dB attenuator, a Russian amplifier for a frequency range of 0.2 to 2 GHz and with a temperature-dependent gain of 25 to 33 dB, a thermometer attached to the amplifier, and an rf output line. The sample holder is placed in between the attenuator and the amplifier. To shield the sample from external magnetic fields, a high-permeability magnetic shield is used. Transmission measurements are performed with a vector network analyzer (VNA) ZNB20 from Rohde & Schwarz, Hamburg, Germany. The sample is cooled by immersing the dipstick into liquid nitrogen or helium.

Fig. 7.4 shows the fundamental KIM resonance of KIM6 measured at 77 K. The complex S21 transmission data is fitted with Eq. (2.51) to extract the resonance frequency f_r, the internal quality factor Q_i, the external quality factor Q_e, and the total quality factor Q_t. For KIM6 we obtain $f_r = 253.716$ MHz, $Q_i = 3332$, $Q_e = 3237$, and $Q_t = 1642$, meaning that the resonator is close to critically coupled ($Q_i \approx Q_e$). The fundamental resonance could be found for 5 devices at 77 K as specified in Table 7.1 by the second tick.

Visa Vesterinen furthermore found that the bias coils on the PCB lead to stray coupling and that the choice of coupling configuration affects Q_i and Q_e, and to

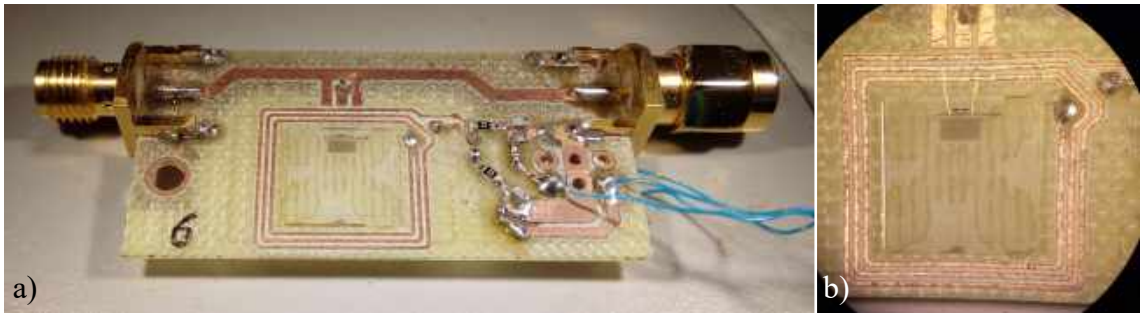

Figure 7.3: a) Photograph of the PCB for rf characterization in the dipstick at Chalmers. The rf transmission line is at the top of the PCB. The KIM is placed inside the 3-turn dc bias coil. The rf coil is on the backside of the PCB. The four blue wires are used to apply a signal to the coils. b) Close-up of the KIM surrounded by the dc bias coil.

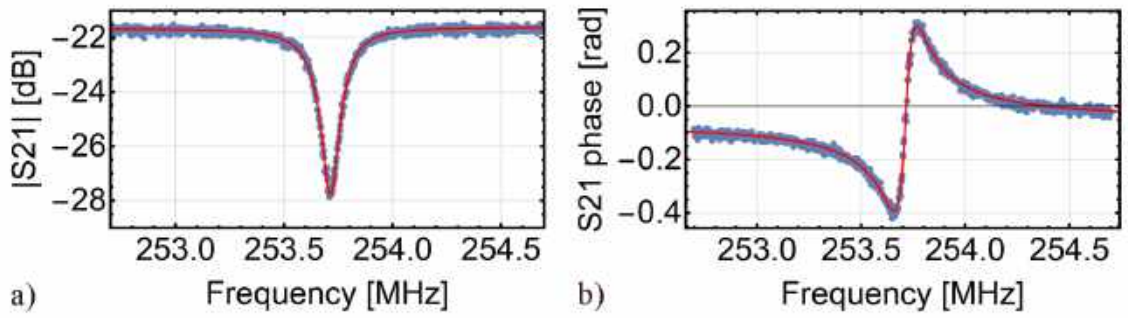

Figure 7.4: Fundamental KIM resonance for KIM6 measured at 77 K with a) showing the absolute value of S21 and b) the phase as a function of frequency. The red line is the best fit of Eq. (2.51) to the data (blue points).

a lower extent f_r. We therefore tested four different coupling configurations as described in detail in the supplement of Paper F. The traditional coupling where a bondwire connects the rf feedline to the coupling capacitor and another bondwire connects the resonator to the ground was found to give the lowest Q_i and Q_e (2500 and 350 for KIM0 at 77 K). Leaving away the ground bondwire – thus letting the rf return current flow through the bias coils – leads to the highest Q_i and Q_e (4300 and 15700 for KIM0 at 77 K). The coupling can be increased by bypassing the coupling capacitor (i.e. bonding between the feedline and directly after the coupling capacitor) leading to similar Q_i values and lower Q_e (4200 and 3900 for KIM0 at 77 K). This configuration was used for KIM6 in the measurement presented above.

7.4.1 Magnetic field response

Once the fundamental resonance is identified, a magnetic field can be applied using the dc coil to determine whether the KIM works as a magnetometer. At 77 K, KIM0 and KIM9 reacted to magnetic field, while the thinner KIM1 and KIM6 only reacted to an oscillating magnetic field of 1 kHz indicating a small residual resistance in the loop. Since the magnetic field response of KIM0 and KIM9 at 77 K is presented in

Paper F, I here show the magnetic field response of KIM6 at 4.8 K where the normal KIM behavior is also observed for this KIM.

Fig. 7.5a-c shows how the resonance moves to lower frequencies when applying a static magnetic field B_0. The maximal frequency shift $\Delta f_r = 0.587$ MHz is reached at a field of 44 µT and for larger fields the resonance no longer shifts to lower frequencies. In contrast to the low-T_c KIMs presented in Refs. [60, 168, 169], our high-T_c KIMs do not reset but instead trap flux. This is because the current in the KIM loop first exceeds the threshold current for flux entry (see Eq. (2.28)) and not the critical current. Flux trapping leads to a hysteretic behaviour – when the magnetic field applied to the coil is again reduced, the maximal frequency is generally obtained at another applied magnetic field than 0. This property can be used to select a dc bias point with high responsivity without having to apply a current to the dc bias coil.

Applying a magnetic field not only decreases f_r, but also Q_i as shown in Fig. 7.5d. This decrease can be quite significant as in this case.

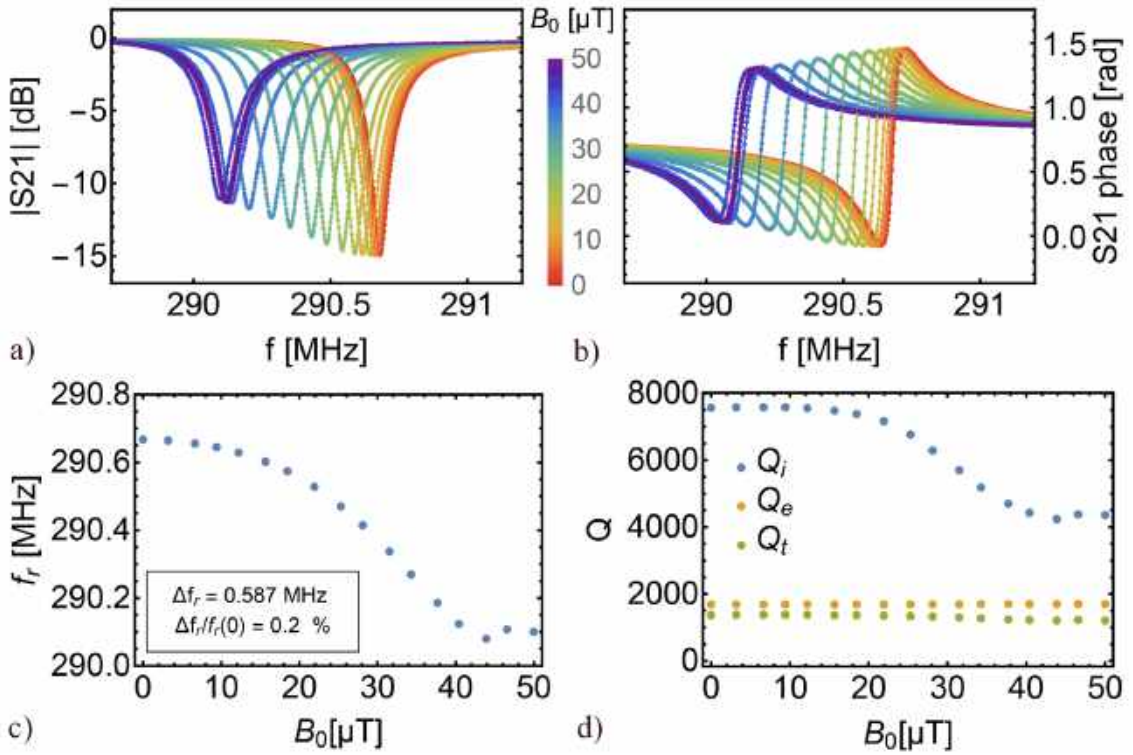

Figure 7.5: Magnetic field response of KIM6 at 4.8 K. a) Absolute value of the transmission S_{21} as a function of frequency for different applied magnetic fields B_0 given in color. Measured values are marked with dots and the best fit to each curve is given as a line. b) The same for the phase of S_{21}. c) Dependence of the fitted resonance frequency on B_0. d) Dependence of the quality factors Q_i (blue), Q_e (orange), and Q_t (green) on B_0.

7.4.2 Temperature dependence

As the kinetic inductance depends quadratically on the London penetration depth, the resonance frequency varies strongly with temperature. To study this in more

detail, we measured the transmission at various temperatures for two samples (KIM0 and KIM6) while the sample slowly warmed up after taking it out of the liquid helium or nitrogen bath. The data is again fitted to extract f_r, Q_i, Q_e, and Q_t. The resonance frequency, but also the internal quality factor, are especially sensitive to temperature close to T_c, see Paper F. For KIM0 the sensitivity of f_r to T is -0.64 MHz/K at 77 K. In Paper F we estimate that a 1 mK change in temperature produces the same voltage swing as a 57 nT change in magnetic field. A stable operation temperature is thus essential for sensitive magnetic field measurements. According to Visa Vesterinen, using temperature stabilization is common practice in their lab to solve this problem for low-T_c kinetic inductance sensors. A similar solution is required for high-T_c KIMs if they should be operated in an on-scalp MEG system.

From the temperature dependence data it is also possible to estimate the kinetic inductance fraction α_k using the resonance frequency at low temperature and 77 K. At 77 K we obtain for KIM0 $\alpha_k = 0.06$, for KIM6 $\alpha_k = 0.4$, and for KIM9 $\alpha_k = 0.16$. While the values for KIM0 and KIM9 are as estimated in Table 7.1 where $\lambda = 400$ nm is assumed, the α_k for KIM6 is almost a factor 2 larger than predicted, thus indicating a larger λ and worse film quality.

7.4.3 Duffing oscillator behaviour

Increasing the rf carrier power leads to a higher responsivity, but also to a distortion of the resonance until it eventually bifurcates [173]. This Duffing oscillator type of behaviour is due to the kinetic inductance nonlinearity which shifts the resonance towards lower frequencies in a power-dependent manner. Fig 7.6 shows the Duffing oscillator behaviour measured for KIM6 at 4.8 K with the cold amplifier turned off to avoid its saturation. A clear decrease in resonance frequency can be seen for increasing rf carrier power. The onset of bifurcation is at around -16 dBm and the "jump" in $|S_{21}|$ increases for larger readout power. The change in the resonance shape needs to be taken into account when increasing the rf carrier power to increase the responsivity. Generally, the maximum input power is limited by the readout electronics and not the bifurcation.

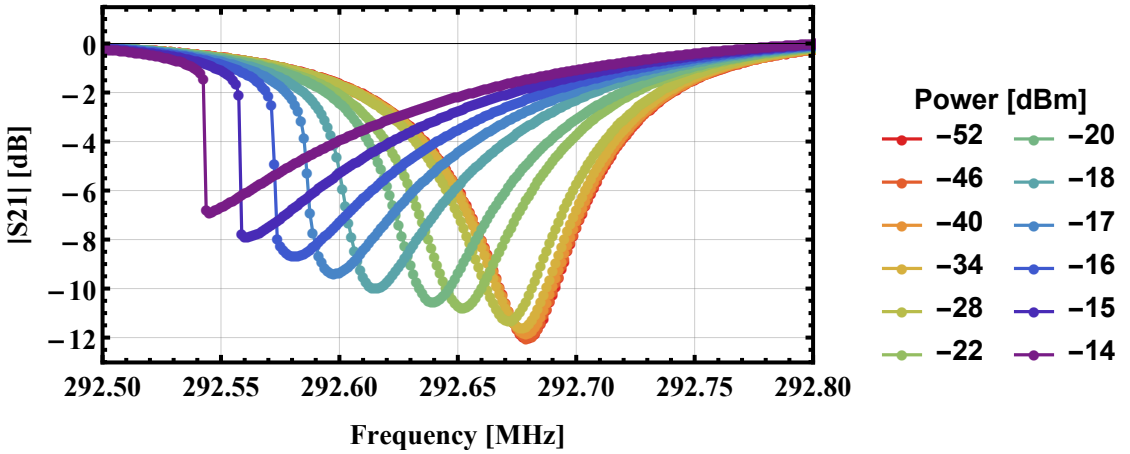

Figure 7.6: Duffing oscillator behaviour for KIM6 measured at 4.8 K. Measured values are marked with dots. The frequency is swept upwards.

7.5 Magnetometer performance

Magnetometer characterization in terms of responsivity and noise was done with the KIM readout circuit described in §2.7.4. Most relevant for on-scalp MEG are the measurements at 77 K. Such measurements were performed by Visa Vesterinen at VTT for the two KIMs that showed the proper magnetic field response, KIM1 and KIM9, and have been published in Paper F, where also the detailed wiring diagrams are shown. KIM1 is named sample A and KIM9 sample B in the paper. I here present the main results.

7.5.1 Response to magnetic field

We begin by studying the resonance lineshape and its response to magnetic field by applying a dc magnetic field B_0 and sweeping the frequency of a weak rf readout tone across the resonance. Fig. 7.7a&b shows how the resonance moves to lower frequencies with increasing B_0. For sample A the resonance shifts 140 kHz and for sample C 50 kHz. Both samples trap flux and do not reset - sample A at 28 µT and sample C at 9 µT. The best fits show that sample A is overcoupled with $Q_e = 350$ and $Q_i \leq 2500$, while sample C is close to critically coupled with $Q_e = 3500$ and $Q_i \leq 3750$. Sample A was measured using the traditional coupling configuration, while the ground connection was left away when measuring sample C.

The change in total inductance L_{tot} with applied magnetic field can be assessed by the normalized inductance $L_{tot}(B_0)/L_{tot}(0) = f_r^2(0)/f_r^2(B_0)$ and is shown in Fig.

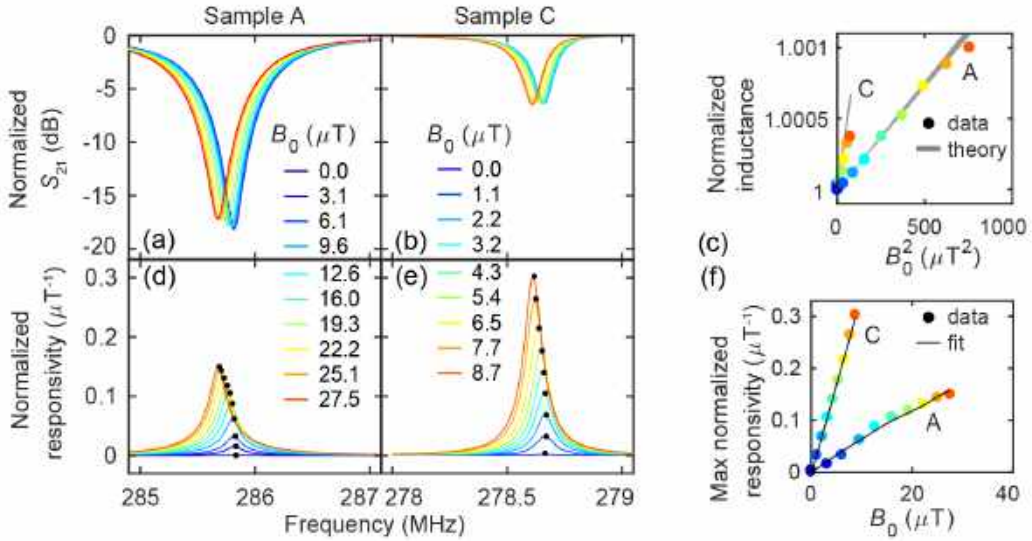

Figure 7.7: a) & b) Normalized transmission S_{21} as a function of frequency for different applied magnetic fields B_0 for the two samples. c) Normalized inductance $L_{tot}(B_0)/L_{tot}(0)$ as a function of B_0^2. d) & e) Normalized responsivity $|\frac{\partial V}{\partial B_0}/V|$ as a function of frequency and applied magnetic field B_0. For each B_0 the maximal normalized responsivities is marked with a black dot and plotted in f) as a function of B_0. Figure adapted from Paper F.

7.7c). The normalized inductance is proportional to B_0^2 and increases faster for sample C mainly because of its higher α_k – see Paper F for more details.

To measure the responsivity, a weak (140 nT or 30 nT) ac probe tone at a frequency of 1 kHz is applied additionally to the dc magnetic field. For every frequency of interest, the modulated output voltage is ensemble averaged and the responsivity $|\partial V/\partial B_0|$ is extracted. Fig. 7.7d&e shows the normalized responsivity $|\frac{\partial V}{\partial B_0}/V|$, which is convenient to compare the two magnetometers. The normalized responsivity as a function of frequency has a Lorentzian lineshape that peaks on resonance. The responsivity vanishes for $B_0 = 0$ µT as expected, and increases with increasing B_0. Since the circulating current I_s is roughly proportional to B_0 according to Eq. (2.47), the maximal normalized responsivity shown in Fig. 7.7f grows linearly with B_0 as predicted by Eq. (2.54).

7.5.2 Noise

Finally, we focus on the noise of our KIMs at 77 K. An operation point with high responsivity is chosen and one-second-long time traces of the output voltage V are recorded. The voltage noise spectrum is obtained by performing a FFT on each time trace. Several such voltage noise spectra are averaged to reduce the uncertainty in the noise estimate. The magnetic field noise spectrum is then obtained by dividing the averaged voltage noise by the responsivity which is determined using a weak ac probe tone at 1 kHz.

As described in §2.7.3, the responsivity grows linearly with the input voltage V_{in}. To prevent saturation of the readout electronics, the rf carrier cancellation circuit is activated – see §2.7.4. Fig. 7.8 shows the magnetic field noise spectra obtained for the two KIMs at high readout power, where the white noise level is lowest. Both

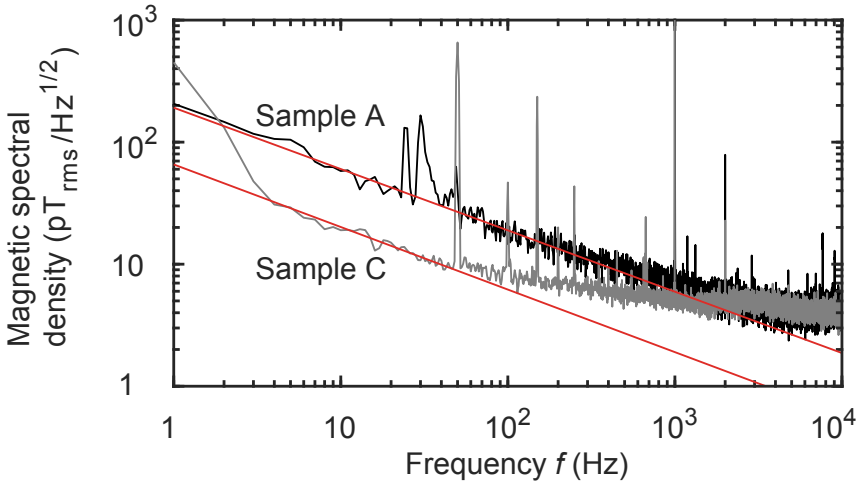

Figure 7.8: Magnetic field noise spectra for KIM0 (Sample A) and KIM9 (Sample C) measured at 77 K with a high readout power (-19 dBm for sample A and -46 dBm for sample C). Both KIMs reach a white noise level of 4 pT/$\sqrt{\text{Hz}}$. The low frequency noise is proportional to f^{-p} with a best-fit exponent $p = 0.5$, thus indicating 1/f noise. Figure published in Paper F.

KIMs reach a noise level of 4 pT/$\sqrt{\text{Hz}}$ at 10 kHz. The low frequency noise, however, grows with increasing readout power and dominates the spectrum at these high readout powers. The origin of this noise is not fully understood, but it is not direct magnetic field noise as operating points with vanishing responsivity show similar low frequency voltage noise.

7.6 Conclusion and outlook

This chapter presented the first high-T_c KIMs operating at 77 K. The lowest white magnetic field noise level reached is 4 pT/$\sqrt{\text{Hz}}$ at 10 kHz, which is too high for operation in a on-scalp MEG system, especially also because of the large low frequency noise. Nonetheless, it is still unclear where the low frequency noise comes from and further investigation of the noise sources may help lower the noise. Possible candidates include critical current fluctuations or inductance fluctuations, hopping of trapped flux vortices, and temperature fluctuations.

The kinetic inductance fraction α_k is, with up to 0.16 for a device functioning at 77 K, rather small, which also limits the responsivity. Achieving a higher α_k was attempted with thinner films and narrower linewidths. However, fabrication of such long, thin, and narrow lines from YBCO proved to be challenging, although the device fabrication could be improved using a carbon mask for patterning the lines. An alternative approach to increase α_k is to implement narrow constrictions as is done for some low-T_c KIMs [168, 169]. This would also reduce I_c and allow for periodical resets. KIMs that reset can furthermore be operated in higher background fields. The KIMs demonstrated here were operated in background fields of up to 28 µT at 77 K (and 50 µT at 4.8 K), which is close to the Earth's magnetic field. To get the KIM to reset without constrictions requires very narrow linewidths: Eq. (2.28) suggests that to reach $I_c < I_T$ requires linewidths of less than 5 µm for a film with a current density of $J = 10^7$ A/cm^2 at 77 K. Making just part of the KIM loop very narrow facilitates the fabrication of a device with high α_k that resets.

Lastly, one of the main advantages of KIMs is that they can be multiplexed. This opportunity has yet to be investigated for high-T_c KIMs.

8

Conclusion and outlook

The main objectives of my PhD project were to develop and optimize high-temperature superconducting magnetometers suitable for operation in a multi-channel on-scalp MEG system, and to verify their suitability in a 7-channel on-scalp MEG system. For the magnetometers to be suitable, four central requirements need to be fulfilled. First, they need to exhibit low magnetic field noise in the frequency range of interest. Second, the sensors need to allow for a small standoff distance and dense spatial sampling. Third, it needs to be possible to fabricate several such sensors and a high reproducibility is therefore wanted. Fourth, accurate sensor calibration and low crosstalk between sensors are needed for the measured signals to be trustworthy.

The first two requirements involve a trade-off between low noise, high spatial sampling, and possibly low standoff distance. Both the standoff distance and the spatial sampling density were already more or less defined when I started my PhD. The 7-channel cryostat was designed to have a variable standoff distance that can be reduced from a few mm down to around 1 mm. The sensor spacing was set by the substrate size of 10 mm $\times$ 10 mm and a gap of 2 mm for wiring. As described in §4.1, this is a reasonable choice as the sensor spacing should be roughly equal to the distance to the sources [42, 43].

This reduces the question to what noise levels are required. State-of-the-art low-T_c MEG magnetometers have magnetic field noise levels of a few fT/$\sqrt{\text{Hz}}$ [25]. Although it is possible to reach such low noise levels with high-T_c SQUID magnetometers, it is a difficult task and requires larger substrates [99, 156]. Simulations show that the reduced standoff distance of 1 mm allows for quite an increase in the sensor noise level: a full-head on-scalp MEG system with a standoff distance of 1 mm and a sensor noise of 50 fT/$\sqrt{\text{Hz}}$, for example, is predicted to be able to extract more information than a state-of-the-art low-T_c MEG system [44, 47]. However, the claim that full-head on-scalp MEG systems outperform state-of-the-art MEG systems [43–47] still needs to be experimentally proven. Lower noise levels are undeniably an advantage – as long as the spatial sampling and the standoff distance are not affected much.

One of the main tasks was therefore to understand what limits the magnetic field noise levels of our single layer high-T_c SQUID magnetometers with bicrystal grain

boundary junctions. This task was, however, complicated by the large spread in magnetometer performance found for almost the same sensor design. The realization that the varying kinetic inductance contribution is partly responsible for the spread was a key element for solving this problem. Determination of all SQUID parameters by combining measurements and inductance simulations led to excellent agreement between experimental results and theoretical predictions. This allowed us to perform an in-depth magnetometer optimization, which showed that achieving high quality junctions with fairly low critical currents ($\lesssim 30$ µA) in combination with the optimized pickup loop design is crucial for reaching the lowest possible magnetic field noise for this technology. High quality junctions with low critical currents could be more easily obtained using a CeO_2 buffer layer, which also reduced excess currents. The use of a CeO_2 buffer layer also crucially meant that magnetometers with low magnetic field noise could be more reproducibly fabricated – an important step to fulfill the third requirement. The best fabricated single layer high-T_c SQUID magnetometers with bicrystal grain boundary junctions achieve a magnetic field noise level of 44 fT/$\sqrt{\text{Hz}}$ at 78 K. Based on the performance of the best test SQUIDs fabricated and the optimized pickup loop design, the lowest possible magnetic field noise for this technology is just under 30 fT/$\sqrt{\text{Hz}}$ at 78 K. Lowering the operation temperature can lead to even lower noise levels. Preferably, optimization is performed at the temperature the magnetometers should be operated at. Future efforts to further improve this noise performance should mainly focus on increasing the reproducibility of fabricating high quality junctions with fairly low critical currents.

Direct injection of current into the SQUID loop played a large role in fulfilling the fourth requirement. It allowed us to realize that the coupling inductance has a large kinetic inductance contribution that leads to a temperature-dependent effective area. A temperature-independent magnetometer calibration method could be developed using direct injection of current as a feedback method. This type of feedback furthermore allowed for low sensor-to-sensor feedback flux crosstalk (below 0.5%).

Based on these sensors, a 7-channel on-scalp MEG system was constructed. With a dense (2 mm edge-to-edge) hexagonal head-aligned array, the system achieves a small sensor-to-head standoff distance of 1-3 mm and dense spatial sampling. The magnetic field noise levels are typically 50-130 fT/$\sqrt{\text{Hz}}$ and the sensor-to-sensor feedback flux crosstalk is below 0.6%. While this was not the only type of crosstalk encountered, the crosstalk from ac bias reversal could be relatively simply removed by using synchronized clocks, and the crosstalk from the mutual inductance of the pickup loops could be simulated and can be compensated. Verification of the simulated mutual inductance crosstalk matrix is still a task for future work.

The suitability of the 7-channel on-scalp MEG system for recording brain activity was demonstrated in several MEG measurements. Moreover, the 7-channel system even allowed retrieval of information unavailable to conventional MEG as shown in Paper IV and Paper V. The epilepsy study performed in Paper V is furthermore a real application with clinical relevance. I hope this direction will be investigated in more detail in the future as the results are very promising.

For future multi-channel on-scalp MEG systems, three alternative types of high-temperature superconducting magnetometers were investigated. First, Dayem bridge junction-based magnetometers with a directly coupled pickup loop were characterized.

The best device based on the novel grooved Dayem bridge junctions achieved a magnetic field noise level of 63 fT/$\sqrt{\text{Hz}}$. Single layer magnetometers with grooved Dayem bridge junctions are thus starting to become a viable alternative to the bicrystal grain boundary junction-based magnetometers of the same type. This would allow us to get rid of the expensive bicrystal substrates. However, the sensors still need to be adjusted such that they can be operated in an on-scalp MEG system, reproducible fabrication of magnetometers with low noise needs to be achieved, and the suitability of the sensors for operation in a MEG system (mainly in terms of low frequency noise performance) needs to be evaluated. Most of the conclusions obtained for bicrystal grain boundary junction-based devices can directly be applied for this junction type as well.

Second, magnetometers with inductively coupled multilayer flux transformer were made. The best device was based on bicrystal grain boundary junctions and reached a white magnetic field noise level below 11 fT/$\sqrt{\text{Hz}}$. Although the low frequency noise is higher, the device outperformed the best single layer device for frequencies above 20 Hz. Also in this case, operation in the MSR without the use of a superconducting shield needs to be tested. For use in an on-scalp MEG system, the problem with crosstalk arising from the mutual inductance of the pickup loops needs to be solved using a feedback coil coupled to the flux transformer pickup loop, and accurate magnetometer calibration still needs to be guaranteed. Optimization of the design using simulations is ongoing.

Third, the potential of kinetic inductance magnetometers (KIMs) was investigated. We demonstrated the first high-T_c KIMs, which could be operated in fields of 9-28 µT and achieved a noise level of 4 pT/$\sqrt{\text{Hz}}$ at 10 kHz. This noise level – and especially the low frequency noise – is too high for application in an on-scalp MEG system. However, the field is still in its infancy and the origin of the noise requires further investigation. The KIM is especially interesting for multi-channel systems because it allows for multiplexed readout.

The future development of high-temperature superconducting magnetometers in our group focuses on flux transformer magnetometers because lower noise levels can be reached. Preferably, SQUIDs based on grooved Dayem bridge junctions can be used. However, at this point it is not clear if such devices can reach the excellent noise level of 11 fT/$\sqrt{\text{Hz}}$ achieved with a bicrystal grain boundary junction-based device. Optimization of the design using simulations and investigation of the possibility of fabricating grooved Dayem bridge-based SQUIDs with thicker washers will give an answer to this question. The development of a 21-channel on-scalp MEG cryostat is ongoing. With both the 7-channel and the 21-channel system the benefits of on-scalp MEG can be further explored, which will hopefully allow the retrieval of more new information from brain activity and thus enable new neuroscience discoveries and improved treatments for brain diseases.

Bibliography

[1] F. A. Azevedo, L. R. Carvalho, L. T. Grinberg, J. M. Farfel, R. E. Ferretti, R. E. Leite, W. J. Filho, R. Lent, and S. Herculano-Houzel: "Equal numbers of neuronal and nonneuronal cells make the human brain an isometrically scaled-up primate brain". *J. Comp. Neurol.* **513**, 5, 532–541 (2009). DOI: 10.1002/cne.21974.

[2] B. Pakkenberg and H. J. G. Gundersen: "Neocortical neuron number in humans: Effect of sex and age". *J. Comp. Neurol.* **384**, 2, 312–320 (1997). DOI: 10.1002/(SICI)1096-9861(19970728)384:2<312::AID-CNE10>3.0.CO;2-K.

[3] Y. Tang, J. R. Nyengaard, D. M. De Groot, and H. J. G. Gundersen: "Total regional and global number of synapses in the human brain neocortex". *Synapse*, **41**, 3, 258–273 (2001). DOI: 10.1002/syn.1083.

[4] M. E. Raichle: "A brief history of human brain mapping". *Trends Neurosci.* **32**, 2, 118–126 (2009). DOI: 10.1016/j.tins.2008.11.001.

[5] K. J. Friston: "Modalities, Modes, and Models in Functional Neuroimaging". *Science*, **326**, 5951, 399–403 (2009). DOI: 10.1126/science.1174521.

[6] W. A. Gibby: "X-Ray Computed Tomography". *Neuroimaging: Clinical and Physical Principles*. Ed. by R. A. Zimmerman, W. A. Gibby, and R. F. Carmody. New York, NY: Springer New York (2000). Pages 3–24. DOI: 10.1007/978-1-4612-1152-5_1.

[7] G. de Marco and I. Peretti: "Magnetic Resonance Imaging: Basic Principles and Applications". *The Neuroimaging of Brain Diseases: Structural and Functional Advances*. Ed. by C. Habas. Cham: Springer International Publishing (2018). Pages 1–25. DOI: 10.1007/978-3-319-78926-2_1.

[8] R. P. Lystad and H. Pollard: "Functional neuroimaging: a brief overview and feasibility for use in chiropractic research". eng. *J. Can. Chiropr. Assoc.* **53**, 19421353, 59–72 (2009). URL: https://www.ncbi.nlm.nih.gov/pmc/articles/PMC2652631/.

[9] G. H. Glover: "Overview of Functional Magnetic Resonance Imaging". *Neurosurg. Clin. N. Am.* **22**, 2, 133–139 (2011). DOI: 10.1016/j.nec.2010.11.001.

[10] N. K. Logothetis: "What we can do and what we cannot do with fMRI". *Nature*, **453**, 7197, 869–878 (2008). DOI: 10.1038/nature06976.

[11] M. Hämäläinen, R. Hari, R. J. Ilmoniemi, J. Knuutila, and O. V. Lounasmaa: "Magnetoencephalography - theory, instrumentation, and applications to noninvasive studies of the working human brain". *Rev. Mod. Phys.* **65**, 413–497 (1993). DOI: 10.1103/RevModPhys.65.413.

[12] S. Murakami and Y. Okada: "Contributions of principal neocortical neurons to magnetoencephalography and electroencephalography signals". *J. Physiol.* **575**, 3, 925–936 (2006). DOI: 10.1113/jphysiol.2006.105379.

[13] S. Baillet: "Magnetoencephalography for brain electrophysiology and imaging". *Nat. Neurosci.* **20**, 327 (2017). DOI: 10.1038/nn.4504.

[14] R. Hari, S. Baillet, G. Barnes, R. Burgess, N. Forss, J. Gross, M. Hämäläinen, O. Jensen, R. Kakigi, F. Mauguière, N. Nakasato, A. Puce, G.-L. Romani, A. Schnitzler, and S. Taulu: "IFCN-endorsed practical guidelines for clinical magnetoencephalography (MEG)". *Clin. Neurophysiol.* **129**, 8, 1720–1747 (2018). DOI: 10.1016/j.clinph.2018.03.042.

[15] Y. C. Okada, A. Lahteenmäki, and C. Xu: "Experimental analysis of distortion of magnetoencephalography signals by the skull". *Clin. Neurophysiol.* **110**, 2, 230–238 (1999). DOI: 10.1016/S0013-4694(98)00099-6.

[16] R. Hari and R. Salmelin: "Magnetoencephalography: From SQUIDs to neuroscience: Neuroimage 20th Anniversary Special Edition". *Neuroimage*, **61**, 2, 386–396 (2012). DOI: 10.1016/j.neuroimage.2011.11.074.

[17] D. Cohen: "Magnetoencephalography: Evidence of Magnetic Fields Produced by Alpha-Rhythm Currents". *Science*, **161**, 3843, 784–786 (1968). DOI: 10.1126/science.161.3843.784.

[18] R. C. Jaklevic, J. Lambe, A. H. Silver, and J. E. Mercereau: "Quantum Interference Effects in Josephson Tunneling". *Phys. Rev. Lett.* **12**, 159–160 (1964). DOI: 10.1103/PhysRevLett.12.159.

[19] J. Clarke and A. I. Braginski, eds.: *The SQUID Handbook: Fundamentals and Technology of SQUIDs and SQUID Systems*. Vol. 1. Wiley-VCH Verlag GmbH & Co. KGaA (2006). DOI: 10.1002/3527603646.

[20] D. Cohen: "Magnetoencephalography: Detection of the Brain's Electrical Activity with a Superconducting Magnetometer". *Science*, **175**, 4022, 664–666 (1972). DOI: 10.1126/science.175.4022.664.

[21] J. Knuutila: "Instrumentation development: From MEG recording to functional mapping". *International Congress Series*, **1300**, 7–10 (2007). DOI: 10.1016/j.ics.2006.12.084.

[22] J. E. T. Knuutila, A. I. Ahonen, M. S. Hämäläinen, M. J. Kajola, P. P. Laine, O. V. Lounasmaa, L. T. Parkkonen, J. T. A. Simola, and C. D. Tesche: "A 122-channel whole-cortex SQUID system for measuring the brain's magnetic fields". *IEEE T. Magn.* **29**, 6, 3315–3320 (1993). DOI: 10.1109/20.281163.

[23] A. I. Ahonen, M. S. Hämäläinen, M. J. Kajola, J. E. T. Knuutila, P. P. Laine, O. V. Lounasmaa, L. T. Parkkonen, J. T. Simola, and C. D. Tesche: "122-channel SQUID instrument for investigating the magnetic signals from the human brain". *Phys. Scr.* **1993**, T49A, 198 (1993). DOI: 10.1088/0031-8949/1993/T49A/033.

[24] J. Vrba, K. Betts, M. Burbank, T. Cheung, A. A. Fife, G. Haid, P. R. Kubik, S. Lee, J. McCubbin, J. McKay, D. McKenzie, P. Spear, B. Taylor, M. Tillotson, D. Cheyne, and H. Weinberg: "Whole cortex, 64 channel SQUID biomagnetometer system". *IEEE Trans. Appl. Supercon.* **3**, 1, 1878–1882 (1993). DOI: 10.1109/77.233314.

[25] Elekta: *Elekta Neuromag TRIUX - Technical specifications*. (2011). URL: www.natmeg.se/onewebmedia/NM23083B-A%20Elekta%20Neuromag%20TRIUX%20datasheet.pdf.

[26] C. Wang, L. Sun, B. Lichtenwalter, B. Zerkle, and Y. Okada: "Compact, ultra-low vibration, closed-cycle helium recycler for uninterrupted operation of MEG with SQUID magnetometers". *Cryogenics*, **76**, 16–22 (2016). DOI: 10.1016/j.cryogenics.2016.03.007.

[27] C. Wang, A. Olesh, and Y. H. Lee: "An Ultra-low Vibration Helium Reliquefier for Dual-Helmet Magnetoencephalography (MEG)". *IOP Conference Series: Materials Science and Engineering*, **502**, 012137 (2019). DOI: 10.1088/1757-899x/502/1/012137.

[28] Y. Zhang, Y. Tavrin, M. Mueck, A. Braginski, C. Heiden, S. Hampson, C. Pantev, and T. Elbert: "Magnetoencephalography using high temperature rf SQUIDs". English. *Brain Topogr.* **5**, 4, 379–382 (1993). DOI: 10.1007/BF01128694.

[29] I. K. Kominis, T. W. Kornack, J. C. Allred, and M. V. Romalis: "A subfemtotesla multichannel atomic magnetometer". *Nature*, **422**, 6932, 596–599 (2003). DOI: 10.1038/nature01484.

[30] V. Shah, S. Knappe, P. D. D. Schwindt, and J. Kitching: "Subpicotesla atomic magnetometry with a microfabricated vapour cell". *Nat. Photon.* **1**, 649– (2007). DOI: 10.1038/nphoton.2007.201.

[31] M. S. Dilorio, K.-Y. Yang, and S. Yoshizumi: "Biomagnetic measurements using low-noise integrated SQUID magnetometers operating in liquid nitrogen". *Appl. Phys. Lett.* **67**, 13, 1926–1928 (1995). DOI: 10.1063/1.114570.

[32] D. Drung, F. Ludwig, W. Müller, U. Steinhoff, L. Trahms, H. Koch, Y. Q. Shen, M. B. Jensen, P. Vase, T. Holst, T. Freltoft, and G. Curio: "Integrated $YBa_2Cu_3O_{7-x}$ magnetometer for biomagnetic measurements". *Appl. Phys. Lett.* **68**, 10, 1421–1423 (1996). DOI: 10.1063/1.116100.

[33] H.-J. Barthelmess, M. Halverscheid, B. Schiefenhovel, E. Heim, M. Schilling, and R. Zimmermann: "Low-noise biomagnetic measurements with a multichannel dc-SQUID system at 77 K". *IEEE Trans. Appl. Supercon.* **11**, 1, 657–660 (2001). DOI: 10.1109/77.919430.

[34] M. Faley, U. Poppe, R. D. Borkowski, M. Schiek, F. Boers, H. Chocholacs, J. Dammers, E. Eich, N. Shah, A. Ermakov, V. Slobodchikov, Y. Maslennikov, and V. Koshelets: "Magnetoencephalography using a Multilayer high-T_c DC SQUID Magnetometer". *Phys. Procedia*, **36**, 66–71 (2012). DOI: 10.1016/j.phpro.2012.06.131.

[35] J. Dammers, H. Chocholacs, E. Eich, F. Boers, M. Faley, R. E. Dunin-Borkowski, and N. Jon Shah: "Source localization of brain activity using helium-free interferometer". *Appl. Phys. Lett.* **104**, 21, 213705 (2014). DOI: 10.1063/1.4880097.

[36] H. Xia, A. Ben-Amar Baranga, D. Hoffman, and M. V. Romalis: "Magnetoencephalography with an atomic magnetometer". *Appl. Phys. Lett.* **89**, 21, (2006). DOI: 10.1063/1.2392722.

[37] C. Johnson, P. D. D. Schwindt, and M. Weisend: "Magnetoencephalography with a two-color pump-probe, fiber-coupled atomic magnetometer". *Appl. Phys. Lett.* **97**, 24, 243703 (2010). DOI: 10.1063/1.3522648.

[38] C. N. Johnson, P. D. D. Schwindt, and M. Weisend: "Multi-sensor magnetoencephalography with atomic magnetometers". *Phys. Med. Biol.* **58**, 17, 6065–6077 (2013). DOI: 10.1088/0031-9155/58/17/6065.

[39] K. Kim, S. Begus, H. Xia, S.-K. Lee, V. Jazbinsek, Z. Trontelj, and M. V. Romalis: "Multi-channel atomic magnetometer for magnetoencephalography: A configuration study". *Neuroimage*, **89**, 143–151 (2014). DOI: 10.1016/j.neuroimage.2013.10.040.

[40] F. Öisjöen, J. F. Schneiderman, G. A. Figueras, M. L. Chukharkin, A. Kalabukhov, A. Hedström, M. Elam, and D. Winkler: "High-T_c superconducting quantum interference device recordings of spontaneous brain activity: Towards high-T_c magnetoencephalography". *Appl. Phys. Lett.* **100**, 132601 (2012). DOI: 10.1063/1.3698152.

[41] T. H. Sander, J. Preusser, R. Mhaskar, J. Kitching, L. Trahms, and S. Knappe: "Magnetoencephalography with a chip-scale atomic magnetometer". *Biomed. Opt. Express*, **3**, 5, 981–990 (2012). DOI: 10.1364/BOE.3.000981.

[42] A. I. Ahonen, M. S. Hamalainen, R. J. Ilmoniemi, M. J. Kajola, J. E. T. Knuutila, J. T. Simola, and V. A. Vilkman: "Sampling theory for neuromagnetic detector arrays". *IEEE T. Bio-Med. Eng.* **40**, 9, 859–869 (1993). DOI: 10.1109/10.245606.

[43] J. Iivanainen, A. Mäkinen, R. Zetter, M. Stenroos, R. J. Ilmoniemi, and L. Parkkonen: "Sampling theory for spatial field sensing: Application to electro- and magnetoencephalography". *arXiv preprint*, 1912.05401, (2019). URL: https://arxiv.org/abs/1912.05401.

[44] J. F. Schneiderman: "Information content with low- vs. high-T_c SQUID arrays in MEG recordings: The case for high-T_c SQUID-based MEG". *J. Neurosci. Methods*, **222**, 42–46 (2014). DOI: 10.1016/j.jneumeth.2013.10.007.

[45] E. Boto, R. Bowtell, P. Krüger, T. M. Fromhold, P. G. Morris, S. S. Meyer, G. R. Barnes, and M. J. Brookes: "On the Potential of a New Generation of Magnetometers for MEG: A Beamformer Simulation Study". *PLoS One*, **11**, 8, 1–24 (2016). DOI: 10.1371/journal.pone.0157655.

[46] J. Iivanainen, M. Stenroos, and L. Parkkonen: "Measuring MEG closer to the brain: Performance of on-scalp sensor arrays". *Neuroimage*, **147**, Supplement C, 542–553 (2017). DOI: 10.1016/j.neuroimage.2016.12.048.

[47] B. Riaz, C. Pfeiffer, and J. F. Schneiderman: "Evaluation of realistic layouts for next generation on-scalp MEG: spatial information density maps". *Sci. Rep.* **7**, 1, 6974– (2017). DOI: 10.1038/s41598-017-07046-6.

[48] A. Borna, T. R. Carter, J. D. Goldberg, A. P. Colombo, Y.-Y. Jau, C. Berry, J. McKay, J. Stephen, M. Weisend, and P. D. D. Schwindt: "A 20-channel magnetoencephalography system based on optically pumped magnetometers". *Phys. Med. Biol.* **62**, 23, 8909 (2017). DOI: 10.1088/1361-6560/aa93d1.

[49] E. Boto, N. Holmes, J. Leggett, G. Roberts, V. Shah, S. S. Meyer, L. D. Muñoz, K. J. Mullinger, T. M. Tierney, S. Bestmann, G. R. Barnes, R. Bowtell, and M. J. Brookes: "Moving magnetoencephalography towards real-world applications with a wearable system". *Nature*, **555**, 657 (2018). DOI: 10.1038/nature26147.

[50] J. Iivanainen, R. Zetter, M. Grön, K. Hakkarainen, and L. Parkkonen: "On-scalp MEG system utilizing an actively shielded array of optically-pumped magnetometers". *Neuroimage*, **194**, 244–258 (2019). DOI: 10.1016/j.neuroimage.2019.03.022.

[51] R. M. Hill, E. Boto, M. Rea, N. Holmes, J. Leggett, L. A. Coles, M. Papastavrou, S. Everton, B. A. Hunt, D. Sims, J. Osborne, V. Shah, R. Bowtell, and M. J. Brookes: "Multi-Channel Whole-Head OPM-MEG: Helmet Design and a Comparison with a Conventional System". *bioRxiv*, (2020). DOI: 10.1101/2020.03.12.989129.

[52] D. Budker and M. Romalis: "Optical magnetometry". *Nat. Phys.* **3**, 4, 227–234 (2007). DOI: 10.1038/nphys566.

[53] D. Drung: "High-T_c and low-T_c dc SQUID electronics". *Supercond. Sci. Technol.* **16**, 12, 1320 (2003). DOI: 10.1088/0953-2048/16/12/002.

[54] J. M. Taylor, P. Cappellaro, L. Childress, L. Jiang, D. Budker, P. R. Hemmer, A. Yacoby, R. Walsworth, and M. D. Lukin: "High-sensitivity diamond magnetometer with nanoscale resolution". *Nat. Phys.* **4**, 810– (2008). DOI: 10.1038/nphys1075.

[55] L. Rondin, J.-P. Tetienne, T. Hingant, J.-F. Roch, P. Maletinsky, and V. Jacques: "Magnetometry with nitrogen-vacancy defects in diamond". *Rep. Prog. Phys.* **77**, 5, 056503 (2014). DOI: 10.1088/0034-4885/77/5/056503.

[56] E. Abe and K. Sasaki: "Tutorial: Magnetic resonance with nitrogen-vacancy centers in diamond—microwave engineering, materials science, and magnetometry". *J. Appl. Phys.* **123**, 16, 161101 (2018). DOI: 10.1063/1.5011231.

[57] R. Jahns, R. Knöchel, H. Greve, E. Woltermann, E. Lage, and E. Quandt: "Magnetoelectric sensors for biomagnetic measurements". *2011 IEEE International Symposium on Medical Measurements and Applications*. (2011). 107–110. DOI: 10.1109/MeMeA.2011.5966676.

[58] M. Pannetier, C. Fermon, G. L. Goff, J. Simola, and E. Kerr: "Femtotesla Magnetic Field Measurement with Magnetoresistive Sensors". *Science*, **304**, 5677, 1648–1650 (2004). DOI: 10.1126/science.1096841.

[59] P. Campiglio, L. Caruso, E. Paul, A. Demonti, L. Azizi-Rogeau, L. Parkkonen, C. Fermon, and M. Pannetier-Lecoeur: "GMR-Based Sensors Arrays for Biomagnetic Source Imaging Applications". *IEEE T. Magn.* **48**, 11, 3501–3504 (2012). DOI: 10.1109/TMAG.2012.2198632.

[60] J. Luomahaara, V. Vesterinen, L. Grönberg, and J. Hassel: "Kinetic inductance magnetometer". *Nat. Commun.* **5**, 4872 (2014). DOI: 10.1038/ncomms5872.

[61] M. Xie, J. Schneiderman, M. Chukharkin, A. Kalabukhov, B. Riaz, D. Lundqvist, S. Whitmarsh, M. Hamalainen, V. Jousmaki, R. Oostenveld, and D. Winkler: "Benchmarking for on-scalp MEG sensors". *IEEE Trans. Biomed. Eng.* **64**, 6, 1270–1276 (2016). DOI: 10.1109/TBME.2016.2599177.

[62] J. Clarke and A. I. Braginski, eds.: *The SQUID Handbook: Applications of SQUIDs and SQUID Systems*. Vol. 2. Wiley-VCH Verlag GmbH & Co. KGaA (2006). DOI: 10.1002/9783527609956.

[63] T. V. Duzer and C. W. Turner: *Principles of Superconductive Devices and Circuits*. 2nd ed. Bibliyografya Ve Indeks. Upper Saddle River, New Jersey 07458: Prentice Hall PTR (1999). URL: https://books.google.se/books?id=uoViQgAACAAJ.

[64] D. Koelle, R. Kleiner, F. Ludwig, E. Dantsker, and J. Clarke: "High-transition-temperature superconducting quantum interference devices". *Rev. Mod. Phys.* **71**, 631–686 (1999). DOI: 10.1103/RevModPhys.71.631.

[65] C. Granata and A. Vettoliere: "Nano Superconducting Quantum Interference device: A powerful tool for nanoscale investigations". *Phys. Rep.* **614**, 1–69 (2016). DOI: 10.1016/j.physrep.2015.12.001.

[66] D. van Delft and P. Kes: "The discovery of superconductivity". *Phys. Today*, **63**, 9, 38–43 (2010). DOI: 10.1063/1.3490499.

[67] H. K. Onnes: "Further experiments with liquid helium. C. On the change of electric resistance of pure metals at very low temperatures, etc. IV. The resistance of pure mercury at helium temperatures". *Comm. Phys. Lab. Univ. Leiden*, 120b, (1911).

[68] H. K. Onnes: "Further experiments with liquid helium. G. On the electrical resistance of pure metals, etc. VI. On the sudden change in the rate at which the resistance of mercury disappears." *Comm. Phys. Lab. Univ. Leiden*, 124c, (1911).

[69] G. Webb, F. Marsiglio, and J. Hirsch: "Superconductivity in the elements, alloys and simple compounds". *Physica C: Superconductivity and its Applications*, **514**, 17–27 (2015). DOI: 10.1016/j.physc.2015.02.037.

[70] W. Meissner and R. Ochsenfeld: "Ein neuer Effekt bei Eintritt der Supraleitfähigkeit". *Naturwissenschaften*, **21**, 44, 787–788 (1933). DOI: 10.1007/BF01504252.

[71] F. London, H. London, and F. A. Lindemann: "The electromagnetic equations of the supraconductor". *Proceedings of the Royal Society of London. Series A - Mathematical and Physical Sciences*, **149**, 866, 71–88 (1935). DOI: 10.1098/rspa.1935.0048.

[72] A. Abrikosov: "The magnetic properties of superconducting alloys". *J. Phys. Chem. Solids*, **2**, 3, 199–208 (1957). DOI: 10.1016/0022-3697(57)90083-5.

[73] V. Ginzburg and L. Landau: "On the Theory of Superconductivity". *Zh. Eksp. Teor. Fiz.* **20**, 1064, (1950). English translation in: V. L. Ginzburg: "On Superconductivity and Superfluidity". Springer Berlin Heidelberg (2009). DOI: 10.1007/978-3-540-68008-6_4.

[74] J. Bardeen, L. N. Cooper, and J. R. Schrieffer: "Microscopic Theory of Superconductivity". *Phys. Rev.* **106**, 162–164 (1957). DOI: 10.1103/PhysRev.106.162.

[75] J. Bednorz and K. Müller: "Possible high T_c superconductivity in the BaLaCuO system". English. *Zeitschrift für Physik B Condensed Matter*, **64**, 2, 189–193 (1986). DOI: 10.1007/BF01303701.

[76] M. K. Wu, J. R. Ashburn, C. J. Torng, P. H. Hor, R. L. Meng, L. Gao, Z. J. Huang, Y. Q. Wang, and C. W. Chu: "Superconductivity at 93 K in a new mixed-phase Y-Ba-Cu-O compound system at ambient pressure". *Phys. Rev. Lett.* **58**, 908–910 (1987). DOI: 10.1103/PhysRevLett.58.908.

[77] A. Schilling, M. Cantoni, J. D. Guo, and H. R. Ott: "Superconductivity above 130 K in the Hg-Ba-Ca-Cu-O system". *Nature*, **363**, 6424, 56–58 (1993). DOI: 10.1038/363056a0.

[78] R. Wesche: "High-Temperature Superconductors". *Springer Handbook of Electronic and Photonic Materials*. Ed. by S. Kasap and P. Capper. Cham: Springer International Publishing (2017). Chap. 50, Pages 1225–1256. DOI: 10.1007/978-3-319-48933-9_50.

[79] J. Nagamatsu, N. Nakagawa, T. Muranaka, Y. Zenitani, and J. Akimitsu: "Superconductivity at 39 K in magnesium diboride". *Nature*, **410**, 6824, 63–64 (2001). DOI: 10.1038/35065039.

[80] Y. Kamihara, H. Hiramatsu, M. Hirano, R. Kawamura, H. Yanagi, T. Kamiya, and H. Hosono: "Iron-Based Layered Superconductor: LaOFeP". *J. Am. Chem. Soc.* **128**, 31, 10012–10013 (2006). DOI: 10.1021/ja063355c.

[81] Y. Kamihara, T. Watanabe, M. Hirano, and H. Hosono: "Iron-Based Layered Superconductor La[O1-xFx]FeAs (x = 0.05-0.12) with T_c = 26 K". *J. Am. Chem. Soc.* **130**, 11, 3296–3297 (2008). DOI: 10.1021/ja800073m.

[82] J.-F. Ge, Z.-L. Liu, C. Liu, C.-L. Gao, D. Qian, Q.-K. Xue, Y. Liu, and J.-F. Jia: "Superconductivity above 100 K in single-layer FeSe films on doped $SrTiO_3$". *Nat. Mater.* **14**, 3, 285–289 (2015). DOI: 10.1038/nmat4153.

[83] A. P. Drozdov, P. P. Kong, V. S. Minkov, S. P. Besedin, M. A. Kuzovnikov, S. Mozaffari, L. Balicas, F. F. Balakirev, D. E. Graf, V. B. Prakapenka, E. Greenberg, D. A. Knyazev, M. Tkacz, and M. I. Eremets: "Superconductivity at 250 K in lanthanum hydride under high pressures". *Nature*, **569**, 7757, 528–531 (2019). DOI: 10.1038/s41586-019-1201-8.

[84] M. Somayazulu, M. Ahart, A. K. Mishra, Z. M. Geballe, M. Baldini, Y. Meng, V. V. Struzhkin, and R. J. Hemley: "Evidence for Superconductivity above 260 K in Lanthanum Superhydride at Megabar Pressures". *Phys. Rev. Lett.* **122**, 027001 (2019). DOI: 10.1103/PhysRevLett.122.027001.

[85] F. Peng, Y. Sun, C. J. Pickard, R. J. Needs, Q. Wu, and Y. Ma: "Hydrogen Clathrate Structures in Rare Earth Hydrides at High Pressures: Possible Route to Room-Temperature Superconductivity". *Phys. Rev. Lett.* **119**, 107001 (2017). DOI: 10.1103/PhysRevLett.119.107001.

[86] H. Weinstock, ed.: *Applications of Superconductivity*. Vol. 365. NATO ASI Series (Series E: Applied Sciences). Springer, Dordrecht (2000). DOI: 10.1007/978-94-017-0752-7_1.

[87] W. V. Hassenzahl, D. W. Hazelton, B. K. Johnson, P. Komarek, M. Noe, and C. T. Reis: "Electric power applications of superconductivity". *Proc. IEEE*, **92**, 10, 1655–1674 (2004). DOI: 10.1109/JPROC.2004.833674.

[88] J. Waldram: *Superconductivity of Metals and Cuprates*. Bristol and Philadelphia: Institute of Physics Publishing (1996).

[89] B. S. Deaver and W. M. Fairbank: "Experimental Evidence for Quantized Flux in Superconducting Cylinders". *Phys. Rev. Lett.* **7**, 43–46 (1961). DOI: 10.1103/PhysRevLett.7.43.

[90] R. Doll and M. Näbauer: "Experimental Proof of Magnetic Flux Quantization in a Superconducting Ring". *Phys. Rev. Lett.* **7**, 51–52 (1961). DOI: 10.1103/PhysRevLett.7.51.

[91] B. Josephson: "Possible new effects in superconductive tunnelling". *Physics Letters*, **1**, 7, 251–253 (1962). DOI: 10.1016/0031-9163(62)91369-0.

[92] P. W. Anderson and J. M. Rowell: "Probable Observation of the Josephson Superconducting Tunneling Effect". *Phys. Rev. Lett.* **10**, 230–232 (1963). DOI: 10.1103/PhysRevLett.10.230.

[93] S. Shapiro: "Josephson Currents in Superconducting Tunneling: The Effect of Microwaves and Other Observations". *Phys. Rev. Lett.* **11**, 80–82 (1963). DOI: 10.1103/PhysRevLett.11.80.

[94] M. T. Levinsen, R. Y. Chiao, M. J. Feldman, and B. A. Tucker: "An inverse ac Josephson effect voltage standard". *Appl. Phys. Lett.* **31**, 11, 776–778 (1977). DOI: 10.1063/1.89520.

[95] D. E. McCumber: "Effect of ac Impedance on dc Voltage-Current Characteristics of Superconductor Weak-Link Junctions". *J. Appl. Phys.* **39**, 7, 3113–3118 (1968). DOI: 10.1063/1.1656743.

[96] W. C. Stewart: "Current-voltage characteristics of Josephson junctions". *Appl. Phys. Lett.* **12**, 8, 277–280 (1968). DOI: 10.1063/1.1651991.

[97] B. Chesca, R. Kleiner, and D. Koelle: "SQUID Theory". *The SQUID Handbook*. Ed. by J. Clarke and A. I. Braginski. Vol. I. John Wiley & Sons, Ltd (2005). Chap. 2, Pages 29–92. DOI: 10.1002/3527603646.ch2.

[98] R. H. Koch, C. P. Umbach, G. J. Clark, P. Chaudhari, and R. B. Laibowitz: "Quantum interference devices made from superconducting oxide thin films". *Appl. Phys. Lett.* **51**, 3, 200–202 (1987). DOI: 10.1063/1.98922.

[99] M. I. Faley, J. Dammers, Y. V. Maslennikov, J. F. Schneiderman, D. Winkler, V. P. Koshelets, N. J. Shah, and R. E. Dunin-Borkowski: "High-T_c SQUID biomagnetometers". *Supercond. Sci. Technol.* **30**, 8, 083001 (2017). DOI: 10.1088/1361-6668/aa73ad.

[100] R. Gross, P. Chaudhari, M. Kawasaki, M. B. Ketchen, and A. Gupta: "Low noise $YBa_2Cu_3O_{7-\delta}$ grain boundary junction dc SQUIDs". *Appl. Phys. Lett.* **57**, 7, 727–729 (1990). DOI: 10.1063/1.103600.

[101] D. Dimos, P. Chaudhari, and J. Mannhart: "Superconducting transport properties of grain boundaries in $YBa_2Cu_3O_7$ bicrystals". *Phys. Rev. B*, **41**, 4038–4049 (1990). DOI: 10.1103/PhysRevB.41.4038.

[102] H. Hilgenkamp and J. Mannhart: "Grain boundaries in high-T_c superconductors". *Rev. Mod. Phys.* **74**, 485–549 (2002). DOI: 10.1103/RevModPhys.74.485.

[103] C. P. Foley, E. E. Mitchell, S. K. H. Lam, B. Sankrithyan, Y. M. Wilson, D. L. Tilbrook, and S. J. Morris: "Fabrication and characterisation of YBCO single grain boundary step edge junctions". *IEEE Trans. Appl. Supercon.* **9**, 2, 4281–4284 (1999). DOI: 10.1109/77.783971.

[104] E. E. Mitchell and C. P. Foley: "YBCO step-edge junctions with high I_cR_n". *Supercond. Sci. Technol.* **23**, 6, 065007 (2010). DOI: 10.1088/0953-2048/23/6/065007.

[105] M. I. Faley, D. Meertens, U. Poppe, and R. E. Dunin-Borkowski: "Graphoepitaxial high-T_c SQUIDs". *J. Phys.: Conf. Ser.* **507**, 4, 042009 (2014). DOI: 10.1088/1742-6596/507/4/042009.

[106] M. I. Faley, U. Poppe, H. Soltner, C. L. Jia, M. Siegel, and K. Urban: "Josephson junctions, interconnects, and crossovers on chemically etched edges of $YBa_2Cu_3O_{7-x}$". *Appl. Phys. Lett.* **63**, 15, 2138–2140 (1993). DOI: 10.1063/1.110565.

[107] S. Adachi, K. Hata, T. Sugano, H. Wakana, T. Hato, Y. Tarutani, and K. Tanabe: "Preparation of multilayer films for integrated high-T_c SQUIDs with ramp-edge Josephson junctions". *Physica C*, **468**, 15, 1936–1941 (2008). Proceedings of the 20$^{\text{th}}$ International Symposium on Superconductivity (ISS 2007) DOI: 10.1016/j.physc.2008.05.171.

[108] S. Adachi, A. Tsukamoto, T. Hato, J. Kawano, and K. Tanabe: "Recent Developments of High-T_c Electronic Devices with Multilayer Structures and Ramp-Edge Josephson Junctions". *IEICE Trans. Electron.* **E95.C**, 3, 337–346 (2012). DOI: 10.1587/transele.E95.C.337.

[109] M. J. Zani, J. A. Luine, R. W. Simon, and R. A. Davidheiser: "Focused ion beam high T_c superconductor dc SQUIDs". *Appl. Phys. Lett.* **59**, 2, 234–236 (1991). DOI: 10.1063/1.105976.

[110] N. Bergeal, X. Grison, J. Lesueur, G. Faini, M. Aprili, and J. P. Contour: "High-quality planar high-T_c Josephson junctions". *Appl. Phys. Lett.* **87**, 10, 102502 (2005). DOI: 10.1063/1.2037206.

[111] S. A. Cybart, C. Y., W. J., B. H. Wehlin, M. K. Ma, C. Huynh, and D. C.: "Nano Josephson superconducting tunnel junctions in $YBa_2Cu_3O_{7-\delta}$ directly patterned with a focused helium ion beam". *Nat. Nanoechnol.* **10**, 7, 598–602 (2015). DOI: 10.1038/nnano.2015.76.

[112] B. Müller, M. Karrer, F. Limberger, M. Becker, B. Schröppel, C. Burkhardt, R. Kleiner, E. Goldobin, and D. Koelle: "Josephson Junctions and SQUIDs Created by Focused Helium-Ion-Beam Irradiation of $YBa_2Cu_3O_7$". *Phys. Rev. Applied*, **11**, 044082 (2019). DOI: 10.1103/PhysRevApplied.11.044082.

[113] G. J. Clark, A. D. Marwick, R. H. Koch, and R. B. Laibowitz: "Effects of radiation damage in ion-implanted thin films of metal-oxide superconductors". *Appl. Phys. Lett.* **51**, 2, 139–141 (1987). DOI: 10.1063/1.98594.

[114] E. Y. Cho, Y. W. Zhou, J. Y. Cho, and S. A. Cybart: "Superconducting nano Josephson junctions patterned with a focused helium ion beam". *Appl. Phys. Lett.* **113**, 2, 022604 (2018). DOI: 10.1063/1.5042105.

[115] J. Müller, S. Weiss, R. Gross, R. Kleiner, and D. Koelle: "Voltage-flux-characteristics of asymmetric dc SQUIDs". *IEEE Trans. Appl. Supercon.* **11**, 1, 912–915 (2001). DOI: 10.1109/77.919493.

[116] P. W. Anderson and A. H. Dayem: "Radio-Frequency Effects in Superconducting Thin Film Bridges". *Phys. Rev. Lett.* **13**, 195–197 (1964). DOI: 10.1103/PhysRevLett.13.195.

[117] J. Schneider, H. Kohlstedt, and R. Wördenweber: "Nanobridges of optimized $YBa_2Cu_3O_7$ thin films for superconducting flux-flow type devices". *Appl. Phys. Lett.* **63**, 17, 2426–2428 (1993). DOI: 10.1063/1.110496.

[118] J. Schneider, M. Mück, and R. Wördenweber: "dc SQUIDs based upon $YBa_2Cu_3O_7$ nanobridges". *Appl. Phys. Lett.* **65**, 19, 2475–2477 (1994). DOI: 10.1063/1.113037.

[119] S. Nawaz, R. Arpaia, F. Lombardi, and T. Bauch: "Microwave Response of Superconducting $YBa_2Cu_3O_{7-\delta}$ Nanowire Bridges Sustaining the Critical Depairing Current: Evidence of Josephson-like Behavior". *Phys. Rev. Lett.* **110**, 167004 (2013). DOI: 10.1103/PhysRevLett.110.167004.

[120] M. V. Pedyash, D. H. A. Blank, and H. Rogalla: "Superconducting quantum interference devices based on YBaCuO nanobridges". *Appl. Phys. Lett.* **68**, 8, 1156–1158 (1996). DOI: 10.1063/1.115708.

[121] R. L. Fagaly: "Superconducting quantum interference device instruments and applications". *Rev. Sci. Instrum.* **77**, 10, 101101 (2006). DOI: 10.1063/1.2354545.

[122] K. Enpuku, Y. Tsujita, K. Nakamura, T. Sasayama, and T. Yoshida: "Biosensing utilizing magnetic markers and superconducting quantum interference devices". *Supercond. Sci. Technol.* **30**, 5, 053002 (2017). DOI: 10.1088/1361-6668/aa5fce.

[123] C. Tesche and Clarke.J.: "dc SQUID: Noise and Optimalization". *J. Low Temp. Phys.* **29**, 3/4, 301–331 (1977). DOI: 10.1007/BF00655097.

[124] W.-T. Tsang and T. V. Duzer: "dc analysis of parallel arrays of two and three Josephson junctions". *J. Appl. Phys.* **46**, 10, 4573–4580 (1975). DOI: 10.1063/1.321397.

[125] J. Clarke and R. H. Koch: "The Impact of High-Temperature Superconductivity on SQUID Magnetometers". *Science*, **242**, 4876, 217–223 (1988). DOI: 10.1126/science.242.4876.217.

[126] A. W. Kleinsasser: "Excess currents and voltages in superconducting junctions". *Appl. Phys. Lett.* **62**, 2, 193–195 (1993). DOI: 10.1063/1.109312.

[127] F. Tafuri and J. R. Kirtley: "Weak links in high critical temperature superconductors". *Rep. Prog. Phys.* **68**, 11, 2573–2663 (2005). DOI: 10.1088/0034-4885/68/11/r03.

[128] K. Enpuku, Y. Shimomura, and T. Kisu: "Effect of thermal noise on the characteristics of a high T_c superconducting quantum interference device". *J. Appl. Phys.* **73**, 11, 7929–7934 (1993). DOI: http://dx.doi.org/10.1063/1.353946.

[129] K. Enpuku, G. Tokita, and T. Maruo: "Inductance dependence of noise properties of a high-T_c dc superconducting quantum interference device". *J. Appl. Phys.* **76**, 12, 8180–8185 (1994). DOI: 10.1063/1.357870.

[130] Y. Greenberg: "Theory of the voltage–current characteristics of high T_c asymmetric DC SQUIDs". *Physica C*, **383**, 4, 354–364 (2003). DOI: 10.1016/S0921-4534(02)01344-8.

[131] K. Enpuku, T. Maruo, and T. Minotani: "Effect of large dielectric constant of $SrTiO_3$ substrate on the characteristics of high T_c dc superconducting quantum interference device". *J. Appl. Phys.* **80**, 2, 1207–1213 (1996). DOI: 10.1063/1.362858.

[132] R. Voss, R. Laibowitz, A. Broers, S. Raider, C. Knoedler, and J. Viggiano: "Ultra low noise Nb DC SQUIDs". *IEEE T. Magn.* **17**, 1, 395–399 (1981). DOI: 10.1109/TMAG.1981.1060901.

[133] J. Blomgren, T. Eriksson, E. Tarte, and D. Winkler: "Noise properties of an YBCO SQUID". *Physica C*, **368**, 1–4, 191–195 (2002). DOI: 10.1016/S0921-4534(01)01165-0.

[134] M. I. Faley, U. Poppe, K. Urban, and R. L. Fagaly: "Noise analysis of DC SQUIDs with damped superconducting flux transformers". *J. Phys.: Conf. Ser.* **234**, 4, 042009 (2010). DOI: 10.1088/1742-6596/234/4/042009.

[135] K. Enpuku, G. Tokita, T. Maruo, and T. Minotani: "Parameter dependencies of characteristics of a high T_c dc superconducting quantum interference device". *J. Appl. Phys.* **78**, 5, 3498–3503 (1995). DOI: 10.1063/1.359983.

[136] S. K. H. Lam, R. Cantor, J. Lazar, K. E. Leslie, J. Du, S. T. Keenan, and C. P. Foley: "Low-noise single-layer $YBa_2Cu_3O_{7-x}$ dc superconducting quantum interference devices magnetometers based on step-edge junctions". *J. Appl. Phys.* **113**, 12, (2013). DOI: 10.1063/1.4798345.

[137] M. Kawasaki, P. Chaudhari, and A. Gupta: "1/f noise in $YBa_2Cu_3O_{7-\delta}$ superconducting bicrystal grain-boundary junctions". *Phys. Rev. Lett.* **68**, 1065–1068 (1992). DOI: 10.1103/PhysRevLett.68.1065.

[138] K. Enpuku, S. Kuriki, and S. Tanaka: "Vortex Electronis and SQUIDs". *Vortex Electronis and SQUIDs*. Springer Berlin Heidelberg (2003). Chap. High-T_c SQUIDs, Pages 141–184. DOI: 10.1007/978-3-540-44876-1_5.

[139] M. J. Ferrari, M. Johnson, F. C. Wellstood, J. J. Kingston, T. J. Shaw, and J. Clarke: "Magnetic flux noise in copper oxide superconductors". *J. Low Temp. Phys.* **94**, 1, 15–61 (1994). DOI: 10.1007/BF00755416.

[140] C. Katzer, C. Stahl, P. Michalowski, S. Treiber, F. Schmidl, P. Seidel, J. Albrecht, and G. Schütz: "Gold nanocrystals in high-temperature superconducting films: creation of pinning patterns of choice". *New J. Phys.* **15**, 11, 113029 (2013). DOI: 10.1088/1367-2630/15/11/113029.

[141] R. Wördenweber: "Engineering of superconductors and superconducting devices using artificial pinning sites". *Physical Sciences Reviews*, **2**, 8, (2017). DOI: 10.1515/psr-2017-8000.

[142] E. Dantsker, S. Tanaka, and J. Clarke: "High-T_c super conducting quantum interference devices with slots or holes: Low 1/f noise in ambient magnetic fields". *Appl. Phys. Lett.* **70**, 15, 2037–2039 (1997). DOI: 10.1063/1.118776.

[143] R. H. Koch, J. Z. Sun, V. Foglietti, and W. J. Gallagher: "Flux dam, a method to reduce extra low frequency noise when a superconducting magnetometer is exposed to a magnetic field". *Appl. Phys. Lett.* **67**, 5, 709–711 (1995). DOI: 10.1063/1.115282.

[144] H. Oyama, S. Kuriki, and M. Matsuda: "Effects of flux dam on low-frequency noise in high-T_c SQUID magnetometers". *IEEE Trans. Appl. Supercon.* **11**, 1, 1331–1334 (2001). DOI: 10.1109/77.919596.

[145] K. Enpuku, D. Kuroda, D. Tokimizu, and T. Q. Yang: "Suppression of thermally activated flux entry through a flux dam in high T_c superconducting quantum interference device magnetometer". *J. Appl. Phys.* **92**, 8, 4751–4757 (2002). DOI: 10.1063/1.1510165.

[146] J. Z. Sun, W. J. Gallagher, and R. H. Koch: "Initial-vortex-entry-related magnetic hysteresis in thin-film SQUID magnetometers". *Phys. Rev. B*, **50**, 13664–13673 (1994). DOI: 10.1103/PhysRevB.50.13664.

[147] M. Matsuda, Y. Murayama, S. Kiryu, N. Kasai, S. Kashiwaya, M. Koyanagi, T. Endo, and S. Kuriki: "Directly-coupled DC-SQUID magnetometers made of Bi-Sr-Ca-Cu oxide films". *IEEE Trans. Magn.* **27**, 2, 3043–3046 (1991). DOI: 10.1109/20.133851.

[148] D. Koelle, A. H. Miklich, F. Ludwig, E. Dantsker, D. T. Nemeth, and J. Clarke: "dc SQUID magnetometers from single layers of $YBa_2Cu_3O_{7-x}$". *Appl. Phys. Lett.* **63**, 16, 2271–2273 (1993). DOI: 10.1063/1.110526.

[149] A. H. Miklich, D. Koelle, E. Dantsker, D. T. Nemeth, J. J. Kingston, R. F. Kromann, and J. Clarke: "Bicrystal YBCO DC SQUIDs with low noise". *IEEE Trans. Appl. Supercon.* **3**, 1, 2434–2437 (1993). DOI: 10.1109/77.233947.

[150] L. P. Lee, J. Longo, V. Vinetskiy, and R. Cantor: "Low-noise $YBa_2Cu_3O_{7-\delta}$ direct-current superconducting quantum interference device magnetometer with direct signal injection". *Appl. Phys. Lett.* **66**, 12, 1539–1541 (1995). DOI: 10.1063/1.113639.

[151] F. Ludwig, J. Beyer, D. Drung, S. Bechstein, and T. Schurig: "High-performance high-T_c SQUID sensors for multichannel systems in magnetically disturbed environment". *IEEE Trans. Appl. Supercon.* **9**, 2, 3793–3796 (1999). DOI: 10.1109/77.783853.

[152] R. Cantor, L. P. Lee, M. Teepe, V. Vinetskiy, and J. Longo: "Low-noise, single-layer $YBa_2Cu_3O_{7-x}$ DC SQUID magnetometers at 77 K". *IEEE Trans. Appl. Supercon.* **5**, 2, 2927–2930 (1995). DOI: 10.1109/77.403205.

[153] V. N. Glyantsev, Y. Tavrin, W. Zander, J. Schubert, and M. Siegel: "The stability of dc and rf SQUIDs in static ambient fields". *Supercond. Sci. Technol.* **9**, 4A, A105–A108 (1996). DOI: 10.1088/0953-2048/9/4a/027.

[154] J. Jaycox and M. Ketchen: "Planar coupling scheme for ultra low noise DC SQUIDs". *IEEE Trans. Magn.* **17**, 1, 400–403 (1981). DOI: 10.1109/TMAG.1981.1060902.

[155] M. B. Ketchen and J. M. Jaycox: "Ultra-low-noise tunnel junction dc SQUID with a tightly coupled planar input coil". *Appl. Phys. Lett.* **40**, 8, 736–738 (1982). DOI: 10.1063/1.93210.

[156] M. I. Faley, U. Poppe, K. Urban, D. N. Paulson, and R. L. Fagaly: "A New Generation of the HTS Multilayer DC-SQUID Magnetometers and Gradiometers". *J. Phys.: Conf. Ser.* **43**, 1, 1199 (2006). DOI: 10.1088/1742-6596/43/1/292.

[157] M. M. Khapaev: "Extraction of inductances of plane thin film superconducting circuits". *Supercond. Sci. Technol.* **10**, 6, 389 (1997). DOI: 10.1088/0953-2048/10/6/002.

[158] J. Lee and T. R. Lemberger: "Penetration depth of$YBa_2Cu_3O_7$ films determined from the kinetic inductance". *Appl. Phys. Lett.* **62**, 19, 2419–2421 (1993). DOI: 10.1063/1.109383.

[159] H. J. M. ter Brake, W. A. M. Aarnink, P. J. van den Bosch, J. W. M. Hilgenkamp, J. Flokstra, and H. Rogalla: "Temperature dependence of the effective sensing area of high-T_c dc SQUIDs". *Supercond. Sci. Technol.* **10**, 7, 512 (1997). DOI: 10.1088/0953-2048/10/7/009.

[160] T. Kisu, T. Iinuma, K. Enpuku, K. Yoshida, K. Yamafuji, and M. Takeo: "Magnetic penetration depth and critical current in YBaCuO thin films". *IEEE Trans. Appl. Supercon.* **3**, 1, 2961–2964 (1993). DOI: 10.1109/77.234023.

[161] H. Terai, M. Hidaka, T. Satoh, and S. Tahara: "Direct-injection high-T_c dc-SQUID with an upper $YBa_2Cu_3O_{7-x}$ ground plane". *Appl. Phys. Lett.* **70**, 20, 2690–2692 (1997). DOI: 10.1063/1.118995.

[162] H. Li, E. Y. Cho, H. Cai, Y. Wang, S. J. McCoy, and S. A. Cybart: "Inductance Investigation of $YBa_2Cu_3O_{7-\delta}$ Nano-Slit SQUIDs Fabricated With a Focused Helium Ion Beam". *IEEE Trans. Appl. Supercon.* **29**, 5, 1–4 (2019). DOI: 10.1109/TASC.2019.2898692.

[163] J. Zmuidzinas: "Superconducting Microresonators: Physics and Applications". *Annual Review of Condensed Matter Physics*, **3**, 1, 169–214 (2012). DOI: 10.1146/annurev-conmatphys-020911-125022.

[164] A. J. Annunziata, D. F. Santavicca, L. Frunzio, G. Catelani, M. J. Rooks, A. Frydman, and D. E. Prober: "Tunable superconducting nanoinductors". *Nanotechnology*, **21**, 44, 445202 (2010). DOI: 10.1088/0957-4484/21/44/445202.

[165] M. M. Khapaev, A. Y. Kidiyarova-Shevchenko, P. Magnelind, and M. Y. Kupriyanov: "3D-MLSI: software package for inductance calculation in multilayer superconducting integrated circuits". *IEEE Trans. Appl. Supercon.* **11**, 1, 1090–1093 (2001). DOI: 10.1109/77.919537.

[166] M. M. Khapaev: "Inductance extraction of multilayer finite-thickness superconductor circuits". *IEEE Trans. Microw. Theory.* **49**, 1, 217–220 (2001). DOI: 10.1109/22.900014.

[167] M. Xie: "Development of high-T_c SQUID magnetometers for on-scalp MEG". PhD thesis. Chalmers University of Technology 2017. URL: research.chalmers.se/en/publication/?id=252588.

[168] A. S. Kher: "Superconducting Nonlinear Kinetic Inductance Devices". PhD thesis. California Institute of Technology 2017. DOI: 10.7907/Z9JQ0Z1F.

[169] A. T. Asfaw, E. I. Kleinbaum, T. M. Hazard, A. Gyenis, A. A. Houck, and S. A. Lyon: "SKIFFS: Superconducting Kinetic Inductance Field-Frequency Sensors for sensitive magnetometry in moderate background magnetic fields". *Appl. Phys. Lett.* **113**, 17, 172601 (2018). DOI: 10.1063/1.5049615.

[170] A. Megrant, C. Neill, R. Barends, B. Chiaro, Y. Chen, L. Feigl, J. Kelly, E. Lucero, M. Mariantoni, P. J. J. O'Malley, D. Sank, A. Vainsencher, J. Wenner, T. C. White, Y. Yin, J. Zhao, C. J. Palmstrøm, J. M. Martinis, and A. N. Cleland: "Planar superconducting resonators with internal quality factors above one million". *Appl. Phys. Lett.* **100**, 11, 113510 (2012). DOI: 10.1063/1.3693409.

[171] A. Bruno, G. de Lange, S. Asaad, K. L. van der Enden, N. K. Langford, and L. DiCarlo: "Reducing intrinsic loss in superconducting resonators by surface treatment and deep etching of silicon substrates". *Appl. Phys. Lett.* **106**, 18, 182601 (2015). DOI: 10.1063/1.4919761.

[172] M. S. Khalil, M. J. A. Stoutimore, F. C. Wellstood, and K. D. Osborn: "An analysis method for asymmetric resonator transmission applied to superconducting devices". *J. Appl. Phys.* **111**, 5, 054510 (2012). DOI: 10.1063/1.3692073.

[173] L. J. Swenson, P. K. Day, B. H. Eom, H. G. Leduc, N. Llombart, C. M. McKenney, O. Noroozian, and J. Zmuidzinas: "Operation of a titanium nitride superconducting microresonator detector in the nonlinear regime". *J. Appl. Phys.* **113**, 10, 104501 (2013). DOI: 10.1063/1.4794808.

[174] I. Gergis, P. Kobrin, J. Cheung, E. Sovero, C. Lastufka, D. Deakin, and J. Lopez: "Temperature dependence of the microwave surface resistance of YBCO thin films from microstrip resonator measurements". *Physica C*, **175**, 5-6, 603–606 (1991). DOI: 10.1016/0921-4534(91)90272-z.

[175] M. A. Lindeman, J. A. Bonetti, B. Bumble, P. K. Day, B. H. Eom, W. A. Holmes, and A. W. Kleinsasser: "Arrays of membrane isolated yttrium-barium-copper-oxide kinetic inductance bolometers". *J. Appl. Phys.* **115**, 23, 234509 (2014). DOI: 10.1063/1.4884437.

[176] V. Vesterinen: "Microwave-coupled superconducting devices for sensing and quantum information processing". PhD thesis. VTT Technical Research Centre of Finland 2015. URL: http://www.vtt.fi/inf/pdf/science/2015/S96.pdf.

[177] J. van Rantwijk, M. Grim, D. van Loon, S. Yates, A. Baryshev, and J. Baselmans: "Multiplexed Readout for 1000-Pixel Arrays of Microwave Kinetic Inductance Detectors". *IEEE Trans. Microw. Theory.* **64**, 6, 1876–1883 (2016). DOI: 10.1109/TMTT.2016.2544303.

[178] Shinkosha: *Crystals for a bright future - General catalog.* (2012). URL: shinkosha.com/english/catalog/SC_2012_eng_web.pdf.

[179] J. Krupka, R. G. Geyer, M. Kuhn, and J. H. Hinken: "Dielectric properties of single crystals of Al_2O_3, $LaAlO_3$, $NdGaO_3$, $SrTiO_3$, and MgO at cryogenic temperatures". *IEEE T. Microw. Theory.* **42**, 10, 1886–1890 (1994). DOI: 10.1109/22.320769.

[180] R. K. Singh and D. Kumar: "Pulsed laser deposition and characterization of high-T_c $YBa_2Cu_3O_{7-x}$ superconducting thin films". *Materials Science and Engineering: R: Reports*, **22**, 4, 113–185 (1998). DOI: 10.1016/S0927-796X(97)00019-3.

[181] P. Benzi, E. Bottizzo, and N. Rizzi: "Oxygen determination from cell dimensions in YBCO superconductors". *J. Cryst. Growth*, **269**, 2, 625–629 (2004). DOI: 10.1016/j.jcrysgro.2004.05.082.

[182] X. D. Wu, R. C. Dye, R. E. Muenchausen, S. R. Foltyn, M. Maley, A. D. Rollett, A. R. Garcia, and N. S. Nogar: "Epitaxial CeO_2 films as buffer layers for high-temperature superconducting thin films". *Appl. Phys. Lett.* **58**, 19, 2165–2167 (1991). DOI: 10.1063/1.104994.

[183] S. E. Russek, S. C. Sanders, A. Roshko, and J. W. Ekin: "Surface degradation of superconducting $YBa_2Cu_3O_{7-\delta}$ thin films". *Appl. Phys. Lett.* **64**, 26, 3649–3651 (1994). DOI: 10.1063/1.111192.

[184] M. L. Chukharkin: "Fabrication and noise properties of high-T_c SQUIDs with multilayer superconducting flux transformers". PhD thesis. Chalmers University of Technology 2013. URL: https://research.chalmers.se/en/publication/180478.

[185] M. Chukharkin, A. Kalabukhov, J. F. Schneiderman, F. Öisjöen, O. Snigirev, Z. Lai, and D. Winkler: "Noise properties of high-T_c superconducting flux transformers fabricated using chemical-mechanical polishing". *Appl. Phys. Lett.* **101**, 042602 (2012). DOI: 10.1063/1.4738782.

[186] D. Grundler, B. David, R. Eckart, and O. Dössel: "Highly sensitive $YBa_2Cu_3O_7$ dc SQUID magnetometer with thin-film flux transformer". *Appl. Phys. Lett.* **63**, 19, 2700–2702 (1993). DOI: 10.1063/1.110399.

[187] F. Ludwig, E. Dantsker, D. Koelle, R. Kleiner, A. Miklich, and J. Clarke: "Multilayer magnetometers based on high-T_c SQUIDs". *Appl. Supercond.* **3**, 7, 383–398 (1995). Electronic Applications of High Temperature Superconductors DOI: 10.1016/0964-1807(95)00078-X.

[188] M. I. Faley, U. Poppe, K. Urban, D. N. Paulson, T. N. Starr, and R. L. Fagaly: "Low noise HTS dc-SQUID flip-chip magnetometers and gradiometers". *IEEE Trans. Appl. Supercon.* **11**, 1, 1383–1386 (2001). DOI: 10.1109/77.919609.

[189] M. Faley, I. Gerasimov, O. Faley, H. Chocholacs, J. Dammers, E. Eich, F. Boers, N. Shah, A. Sobolev, V. Slobodchikov, Y. Maslennikov, V. Koshelets, and R. Dunin-Borkowski: "Integration Issues of Graphoepitaxial High-T_c SQUIDs Into Multichannel MEG Systems". *IEEE Trans. Appl. Supercon.* **25**, 3, 1–5 (2015). DOI: 10.1109/TASC.2014.2365098.

[190] S. Wunderlich, F. Schmidl, L. Dorrer, H. Schneidewind, and P. Seidel: "Improvement of sensor performance of high-T_c thin film planar SQUID gradiometers by ion beam etching". *IEEE Trans. Appl. Supercon.* **9**, 1, 71–76 (1999). DOI: 10.1109/77.763258.

[191] J. Du, S. K. H. Lam, D. L. Tilbrook, and C. P. Foley: "Trimming of step-edge junctions for improvement of SQUID performance". *Supercond. Sci. Technol.* **15**, 1, 165–169 (2001). DOI: 10.1088/0953-2048/15/1/330.

[192] R. Gross, L. Alff, A. Beck, O. M. Froehlich, D. Koelle, and A. Marx: "Physics and technology of high temperature superconducting Josephson junctions". *IEEE Trans. Appl. Supercon.* **7**, 2, 2929–2935 (1997). DOI: 10.1109/77.621919.

[193] J. V. Migacz and M. E. Huber: "Thermal annealing of Nb/Al-AlO_x/Nb Josephson junctions". *IEEE Trans. Appl. Supercon.* **13**, 2, 123–126 (2003). DOI: 10.1109/TASC.2003.813661.

[194] A. Vettoliere, B. Ruggiero, M. Valentino, P. Silvestrini, and C. Granata: "Fine-Tuning and Optimization of Superconducting Quantum Magnetic Sensors by Thermal Annealing". *Sensors*, **19**, 17, (2019). DOI: 10.3390/s19173635.

[195] T. Minotani, S. Kawakami, Y. Kuroki, and K. Enpuku: "Properties of Josephson Junction Fabricated on Bicrystal Substrate with Different Misorientation Angles". *Jpn. J. Appl. Phys.* **37**, Part 2, No. 6B, L718–L721 (1998). DOI: 10.1143/jjap.37.l718.

[196] E. Dantsker, S. Tanaka, P. A. Nilsson, R. Kleiner, and J. Clarke: "Low excess flux noise in $YBa_2Cu_3O_{7-x}$ dc SQUIDs cooled in static magnetic fields". *IEEE Trans. Appl. Supercon.* **7**, 2, 2772–2775 (1997). DOI: 10.1109/77.621812.

[197] Dortmund Data Bank: *Vapor Pressure of Nitrogen.* (Retrieved 13.10.2019). URL: http://www.ddbst.com/en/EED/PCP/VAP_C1056.php.

[198] Wikipedia: *Vapor pressures of the elements (data page).* (Retrieved 13.10.2019). URL: https://en.wikipedia.org/wiki/Vapor_pressures_of_the_elements_(data_page).

[199] P. Hales, H. Jones, S. Milward, and S. Harrison: "Investigation into the use of solid nitrogen to create a "Thermal Battery" for cooling a portable high-temperature superconducting magnet". *Cryogenics*, **45**, 2, 109–115 (2005). DOI: 10.1016/j.cryogenics.2004.04.011.

[200] D. Grundler, B. David, and O. Doessel: "Experimental investigation of the kinetic inductance in $YBa_2Cu_3O_7$ square washer superconducting quantum interference devices". *J. Appl. Phys.* **77**, 10, 5273–5277 (1995). DOI: 10.1063/1.359279.

[201] F. Öisjöen: "High-T_c SQUIDs for biomedical applications: immunoassays, MEG, and ULF-MRI". PhD thesis. Chalmers University of Technology 2011. URL: https://research.chalmers.se/en/publication/148623.

[202] C. Pfeiffer: "On-scalp MEG using high-T_c SQUIDs: Measuring brain activity with superconducting magnetometers". PhD thesis. Chalmers University of Technology 2019. URL: https://research.chalmers.se/en/publication/512577.

[203] H. ter Brake, F. Fleuren, J. Ulfrnan, and J. Flokstra: "Elimination of flux-transformer crosstalk in multichannel SQUID magnetometers". *Cryogenics*, **26**, 12, 667–670 (1986). DOI: 10.1016/0011-2275(86)90166-9.

[204] C. Granata, A. Vettoliere, and M. Russo: "Improved superconducting quantum interference device magnetometer for low cross talk operation". *Appl. Phys. Lett.* **88**, 21, 212506 (2006). DOI: 10.1063/1.2206556.

[205] C. Granata, A. Vettoliere, M. Luiso, and M. Russo: "Integrated SQUID sensors for low cross-talk multichannel systems". *J. Phys.: Conf. Ser.* **43**, 1, 1235 (2006). DOI: 10.1088/1742-6596/43/1/301.

[206] C. Pfeiffer, L. M. Andersen, D. Lundqvist, M. Hämäläinen, J. F. Schneiderman, and R. Oostenveld: "Localizing on-scalp MEG sensors using an array of magnetic dipole coils". *PLoS One*, **13**, 5, 1–21 (2018). DOI: 10.1371/journal.pone.0191111.

[207] S. Knake, E. Halgren, H. Shiraishi, K. Hara, H. Hamer, P. Grant, V. Carr, D. Foxe, S. Camposano, E. Busa, T. Witzel, M. Hämäläinen, S. Ahlfors, E. Bromfield, P. Black, B. Bourgeois, A. Cole, G. Cosgrove, B. Dworetzky, J. Madsen, P. Larsson, D. Schomer, E. Thiele, A. Dale, B. Rosen, and S. Stufflebeam: "The value of multichannel MEG and EEG in the presurgical evaluation of 70 epilepsy patients". *Epilepsy Res.* **69**, 1, 80–86 (2006). DOI: 10.1016/j.eplepsyres.2006.01.001.

[208] K. Sternickel and A. I. Braginski: "Biomagnetism using SQUIDs: status and perspectives". *Supercond. Sci. Technol.* **19**, 3, S160 (2006). URL: http://stacks.iop.org/0953-2048/19/i=3/a=024.

[209] T. Inaba, Y. Nakazawa, K. Yoshida, Y. Kato, A. Hattori, T. Kimura, T. Hoshi, T. Ishizu, Y. Seo, A. Sato, Y. Sekiguchi, A. Nogami, S. Watanabe, H. Horigome, Y. Kawakami, and K. Aonuma: "Routine clinical heart examinations using SQUID magnetocardiography at University of Tsukuba Hospital". *Supercond. Sci. Technol.* **30**, 11, 114003 (2017). DOI: 10.1088/1361-6668/aa8c26.

[210] H. J. M. ter Brake, N. Janssen, J. Flokstra, D. Veldhuis, and H. Rogalla: "Multichannel heart scanner based on high-T_c SQUIDs". *IEEE Trans. Appl. Supercon.* **7**, 2, 2545–2548 (1997). DOI: 10.1109/77.621758.

[211] K. A. Kouznetsov, J. Borgmann, and J. Clarke: "High-T_c second-order gradiometer for magnetocardiography in an unshielded environment". *Appl. Phys. Lett.* **75**, 13, 1979–1981 (1999). DOI: 10.1063/1.124891.

[212] Y. Zhang, G. Panaitov, S. G. Wang, N. Wolters, R. Otto, J. Schubert, W. Zander, H.-J. Krause, H. Soltner, H. Bousack, and A. I. Braginski: "Second-order, high-temperature superconducting gradiometer for magnetocardiography in unshielded environment". *Appl. Phys. Lett.* **76**, 7, 906–908 (2000). DOI: 10.1063/1.125625.

[213] S. Yu and R. T. Wakai: "Maternal MCG Interference Cancellation Using Splined Independent Component Subtraction". *IEEE Trans. Biomed. Eng.* **58**, 10, 2835–2843 (2011). DOI: 10.1109/tbme.2011.2160635.

[214] M. J. Peters, J. G. Stinstra, S. Uzunbajakau, and N. Srinivasan: "Fetal Magnetocardiography". *Advances in Electromagnetic Fields in Living Systems*. Ed. by J. C. Lin. Boston, MA: Springer US (2005). Pages 1–40. DOI: 10.1007/0-387-24024-1_1.

[215] H. ter Brake, A. Rijpma, J. Stinstra, J. Borgmann, H. Holland, H. Krooshoop, M. Peters, J. Flokstra, H. Quartero, and H. Rogalla: "Fetal magnetocardiography: clinical relevance and feasibility". *Physica C*, **368**, 1, 10–17 (2002). DOI: 10.1016/S0921-4534(01)01132-7.

[216] S. Strand, W. Lutter, J. F. Strasburger, V. Shah, O. Baffa, and R. T. Wakai: "Low-Cost Fetal Magnetocardiography: A Comparison of Superconducting Quantum Interference Device and Optically Pumped Magnetometers". *Journal of the American Heart Association*, **8**, 16, e013436 (2019). DOI: 10.1161/JAHA.119.013436.

[217] T. P. L. Roberts, D. N. Paulson, E. Hirschkoff, K. Pratt, A. Mascarenas, P. Miller, M. Han, J. Caffrey, C. Kincade, B. Power, R. Murray, V. Chow, C. Fisk, M. Ku, D. Chudnovskaya, J. Dell, R. Golembski, P. Lam, L. Blaskey, E. Kuschner, L. Bloy, W. Gaetz, and J. C. Edgar: "Artemis 123: development of a whole-head infant and young child MEG system". *Front. Hum. Neurosci.* **8**, (2014). DOI: 10.3389/fnhum.2014.00099.

[218] E. Trabaldo: "Noise and electrical properties of YBCO nanostructures". PhD thesis. Chalmers University of Technology 2020. URL: https://research.chalmers.se/en/publication/515677.

[219] R. Arpaia, M. Arzeo, S. Nawaz, S. Charpentier, F. Lombardi, and T. Bauch: "Ultra low noise $YBa_2Cu_3O_{7-\delta}$ nano superconducting quantum interference devices implementing nanowires". *Appl. Phys. Lett.* **104**, 072603 (2014). DOI: 10.1063/1.4866277.

[220] M. Arzeo, R. Arpaia, R. Baghdadi, F. Lombardi, and T. Bauch: "Toward ultra high magnetic field sensitivity $YBa_2Cu_3O_{7-\delta}$ nanowire based superconducting quantum interference devices". *J. Appl. Phys.* **119**, 17, 174501 (2016). DOI: 10.1063/1.4948477.

[221] S. Nawaz, R. Arpaia, T. Bauch, and F. Lombardi: "Approaching the theoretical depairing current in $YBa_2Cu_3O_{7-\delta}$ nanowires". *Physica C*, **495**, 33–38 (2013). DOI: 10.1016/j.physc.2013.07.011.

[222] E. Trabaldo, C. Pfeiffer, E. Andersson, R. Arpaia, A. Kalaboukhov, D. Winkler, F. Lombardi, and T. Bauch: "Grooved Dayem Nanobridges as Building Blocks of High-Performance $YBa_2Cu_3O_{7-\delta}$ SQUID Magnetometers". *Nano Lett.* **19**, 3, 1902–1907 (2019). DOI: 10.1021/acs.nanolett.8b04991.

[223] E. Trabaldo, C. Pfeiffer, E. Andersson, M. Chukharkin, R. Arpaia, D. Montemurro, A. Kalaboukhov, D. Winkler, F. Lombardi, and T. Bauch: "SQUID Magnetometer Based on Grooved Dayem Nanobridges and a Flux Transformer". *IEEE Trans. Appl. Supercon.* **30**, 7, 1–4 (2020). DOI: 10.1109/TASC.2020.3004896.

[224] W. Hattori, T. Yoshitake, and S. Tahara: "A 5-μm-wide 18-cm-long low-loss $YBa_2Cu_2O_{7-\delta}$ coplanar line for future multichip module technology". *IEEE Trans. Appl. Supercon.* **8**, 3, 97–103 (1998). DOI: 10.1109/77.712140.

[225] K. Yoshida, M. S. Hossain, T. Kisu, K. Enpuku, and K. Yamafuji: "Modeling of Kinetic-Inductance Coplanar Striplin with NbN Thin Films". *Jpn. J. Appl. Phys.* **31**, Part 1, No. 12A, 3844–3850 (1992). DOI: 10.1143/jjap.31.3844.

[226] R. Cantor: "Dc SQUIDs: Design, Optimization and Practical Applications". *SQUID Sensors: Fundamentals, Fabrication and Applications*. Ed. by H. Weinstock. Dordrecht: Springer Netherlands (1996). Pages 179–233. DOI: 10.1007/978-94-011-5674-5_4.

[227] S. Mohan, M. del Mar Hershenson, S. Boyd, and T. Lee: "Simple accurate expressions for planar spiral inductances". *IEEE J. Solid-St. Circ.* **34**, 10, 1419–1424 (1999). DOI: 10.1109/4.792620.

[228] M. Zahn: *Electromagnetic Field Theory: A Problem Solving Approach*. Massachusetts Institute of Technology: MIT OpenCourseWare (2008). URL: https://ocw.mit.edu/resources/res-6-002-electromagnetic-field-theory-a-problem-solving-approach-spring-2008/textbook-contents/.

A

List of symbols

Symbols – Superconductivity

$\boldsymbol{A}$	Vector potential
$\boldsymbol{B}$	Magnetic field (magnetic flux density measured in tesla)
B_T	Threshold field for trapping vortices during cooling
δ	Superconducting phase
e^*	Effective charge
$\boldsymbol{E}$	Electric field
ϵ_r	Relative permittivity
f	Frequency
H_c	Critical field
H_{c1}	Lower critical field
H_{c2}	Upper critical field
I_T	Threshold current for massive flux entry
$\boldsymbol{J}$	Superconducting current density
$\boldsymbol{J_m}$	Current density of the m^{th} superconducting layer
j_m	Sheet current density of the m^{th} superconducting layer
λ	London penetration depth
λ_p	Pearl penetration depth
m^*	Effective mass
n	Oxygen content in YBCO
n_s	Superfluid density
$\boldsymbol{p}$	Momentum
p	Hole doping in YBCO
Φ	Magnetic flux
Ψ	Superconducting order parameter
T_c	Critical temperature
u_m	Stream function for the m^{th} superconducting layer
$\boldsymbol{v_s}$	Superconducting pair velocity
ξ	Coherence length

Symbols – Josephson junctions and SQUID magnetometers

A_{eff}	Magnetometer effective area
A_p	Pickup loop effective area
A_s	SQUID effective area
α_I	SQUID critical current asymmetry parameter
α_L	SQUID inductance asymmetry parameter
α_R	SQUID normal resistance asymmetry parameter
β_c	Stewart-McCumber parameter
β_L	Screening parameter or inductance parameter
C	Capacitance
C_{ji}	Feedback flux crosstalk
C_{ji}^B	Magnetic field crosstalk due to mutual inductance between pickup loops
d	Pickup loop inner hole diameter
D	Pickup loop outer diameter
δ	Superconducting phase difference across a junction
Δi_c	Normalized critical current modulation depth
ΔI_{inj}	Periodicity of the injected current
ΔV	(Maximal) SQUID voltage modulation
Δv	Normalized (maximal) SQUID voltage modulation
$\Delta\tau$	Timestep for Runge-Kutta method
$\partial V/\partial B$	Responsivity in FLL mode
E_{Geo}	Energy stored in the magnetic field defining the geometric inductance
E_{Kin}	Kinetic energy of the charge carriers defining the kinetic inductance
Γ	Noise parameter
I	Current
i	Normalized current
I_0	Critical current of a Josephson junction
I_b	Bias current
I_c	SQUID critical current
I_c^*	Reduced SQUID critical current
i_c	Normalized SQUID critical current
I_{ex}	Excess current
I_f	Feedback current
I_{inj}	Current directly injected into the SQUID loop
I_N	Nyquist noise current
i_N	Normalized Nyquist noise current
I_s	Superconducting current (supercurrent)
J	Circulating current in a SQUID
j	Normalized circulating current in a SQUID
J_c	Junction critical current density
k	Coupling coefficient (for mutual inductance)
L	SQUID inductance
L_c	SQUID coupling inductance
L_{FT}	Matched flux transformer input coil and pickup loop inductance
L^{Geo}	Geometric inductance contribution

l_{JJ}	Length of the microbridge forming the JJ
L^{Kin}	Kinetic inductance contribution
L_i	Flux transformer input coil inductance
L_p	Pickup loop inductance
L_{par}	SQUID parasitic inductance
l_{sq}	SQUID loop length
M	Mutual inductance
M_f	Mutual inductance between SQUID and feedback coil
M_m	Magnetic moment
ω_c	Characteristic frequency
Φ_a	Applied magnetic flux
ϕ_a	Normalized applied magnetic flux
Φ_a	Total flux threading the SQUID loop
Φ_b	Flux bias for FLL operation with ac bias reversal
R	Resistance, in case of JJs and SQUIDs: normal resistance of a JJ
R_d	Dynamic resistance of a SQUID at the point of operation
R_f	Feedback resistance
R_n	Normal resistance of a SQUID
$S_B^{1/2}$	Total equivalent magnetic field noise amplitude spectral density ("Magnetic field noise")
$S_\Phi^{1/2}$	Total equivalent flux noise amplitude spectral density ("Flux noise")
$S_V^{1/2}$	Total voltage noise amplitude spectral density ("Voltage noise")
$S_{V,el}^{1/2}$	Electronics contribution to voltage noise amplitude spectral density
$S_{V,sq}^{1/2}$	Intrinsic SQUID voltage noise amplitude spectral density
$S_{V,FFL}^{1/2}$	Voltage noise amplitude spectral density in FLL mode
S_V	Voltage noise power spectral density
s_V	Normalized voltage noise power spectral density
t	Film thickness
τ	Normalized time
θ	Misorientation angle bicrystal substrate
V	Voltage
v	Normalized voltage
$\bar{V}$	Average voltage across the JJ or SQUID
$\bar{v}$	Normalized average voltage across the JJ or SQUID
V_b	Voltage bias for FLL operation
V_n^{res}	Voltage of resonance due to standing wave along the SQUID slit
V_{out}	Output voltage in FLL
V_Φ	Flux-to-voltage transfer function
V_Φ^{FLL}	Flux-to-voltage transfer function in FLL mode
w_{el}	Width of the electrode
w_{JJ}	Width of the microbridge forming the JJ
w_{sl}	Width of the SQUID slit
w_{sq}	Linewidth of the SQUID loop

Symbols – KIMs

A	Area of the superconducting loop
α_k	Kinetic inductance fraction
B_0	Average orthogonal field to the superconducting loop
C	Capacitance of the capacitor
C_c	Capacitance of the coupling capacitor
Δf	Resonance width (FWHM)
Δf_r	Maximal resonance frequency shift with applied magnetic field
$\partial V/\partial B_0$	Responsivity
f_r	Resonance frequency
I^*	Current nonlinearity parameter
I_{rf}	RF current in the loop
I_s	Screening current
L	Inductance of the superconducting loop
L_g	Geometric inductance of the superconducting loop
L_k	Kinetic inductance of the superconducting loop
L_{k0}	Kinetic inductance of the superconducting loop with $I_s = 0$
L_{par}	Parasitic inductance of the central line
L_{tot}	Total resonator inductance
λ_c	Carrier wavelength
Φ_a	Flux threading the superconducting loop
Q_c	Complex-valued coupling quality factor used for fitting $S_{21}(f)$
Q_e	External or coupling quality factor
Q_i	Internal quality factor
Q_t	Total or loaded quality factor of the resonator
R_i	Resistance describing the superconductor losses
ρ	Resisitivity
S_{21}	Transmission parameter
t	Film thickness
V	Output voltage
V_{in}	Input voltage
w	Linewidth of the superconducting loop
Z	Impedance of the resonator
Z_0	Characteristic impedance

B

Inductance formulas

SQUID loop

The geometric inductance of a thin coplanar stripline of length l with spacing s between the strips of width w is given by [225]:

$$L_c^{Geo} \approx \mu_0 \frac{K(k)}{K(k')} l, \tag{B.1}$$

where μ_0 is the vacuum permeability and $K(k)$ is the complete elliptic integral of the first kind with a modulus $k = s/(s+2w)$ and $k' = \sqrt{1-k^2}$.

SQUID magnetometer pickup loop

The geometric inductance of a thin-film square pickup loop with inner side length d and linewidth w is [226]:

$$L_p \approx 1.25\mu_0 d \qquad \text{for } \frac{d}{w} < 1, \tag{B.2a}$$

$$L_p \approx \frac{2}{\pi}\mu_0 d \left[ln\left(5 + \frac{d}{w}\right) + 0.25 \right] \qquad \text{for } 1 < \frac{d}{w} < 10, \tag{B.2b}$$

$$L_p \approx \frac{2}{\pi}\mu_0 (d+w) \left[ln\left(1 + \frac{d}{w}\right) + 0.5 \right] \qquad \text{for } \frac{d}{w} > 10. \tag{B.2c}$$

Flux transformer input coil

The geometric inductance of a spiral coil with n turns of width w and spacing s can be approximated by the current sheet expression [227]:

$$L_i \approx \frac{\mu_0 n^2 d_{avg} c_1}{2} \left(ln(c_2/\rho) + c_3\rho + c_4\rho^2 \right), \tag{B.3}$$

where d_{out} is the outer coil diameter, d_{in} is the inner coil diameter, $d_{avg} = 0.5(d_{out}+d_{in})$ is the average diameter, $\rho = (d_{out} - d_{in})/(d_{out} + d_{in})$ is the fill ratio, and c_1 to c_4 are coefficients found in Table B.1.

Table B.1: Coefficients for the current sheet approximation.

Layout	c_1	c_2	c_3	c_4
Square	1.27	2.07	0.18	0.13
Hexagonal	1.09	2.23	0.00	0.17
Octagonal	1.07	2.29	0.00	0.19
Circular	1.00	2.46	0.00	0.20

KIM

The geometric inductance of a thin square loop with outer side length D and very narrow linewidth w is [228]:

$$L_g \approx \frac{2\mu_0 D}{\pi}\left[sinh^{-1}\left(\frac{2D}{w}\right) - 1\right]. \tag{B.4}$$